UNIVERSIDAD DISTRITAL
FRANCISCO JOSÉ DE CALDAS

REVISTA Ingeniería

Four-monthly scientific journal

2026

Volume 31 Issue 1 ISSN 0121-750X E-ISSN 2344-8393

REVISTA Ingeniería

Volume 31 • Issue 1 • Year 2026 • ISSN 0121-750X • E-ISSN 2344-8393

Four-monthly Scientific Journal

UNIVERSIDAD DISTRITAL FRANCISCO JOSÉ DE CALDAS

Carrera 7 No. 40-53
Edificio Administrativo
Facultad de Ingeniería
Bogotá, Colombia
Correo revista:
revingenieria.ud@udistrital.edu.co

https://revistas.udistrital.edu.co/index.php/reving

Focus and Scope

The *Ingeniería* journal is an open-access academic-scientific online publication specialized in knowledge related to the fields of Engineering and Technology, according to the classification of scientific areas established by the Organization for Economic Cooperation and Development (OECD). Its main goal is to disseminate and promote debates about advances in research and development in the diverse areas of Engineering and Technology. We focus on disseminating original and unpublished articles in English that are relevant at both the national and international level. We seek to provide a platform to share knowledge and foster collaboration between researchers and professionals in the field. The journal does not request any Article Processing Charges (APC), as it is directly funded by Universidad Distrital Francisco José de Caldas. Moreover, the journal operates following a double-blind review process, thus ensuring the impartiality and quality of the published works. The journal is published in a continuous fashion and follows a Four-monthly

Open Access Policy

The *Ingeniería* journal provides free access to its content. This free access is granted under the principle of making research freely available to the public, which en-courages a greater exchange of global knowledge.

Article Processing Charges

No publication fees are charged to the authors or their institutions, nor are any payments made to expert peer reviewers or associate or adjunct editors. The *Ingeniería* journal is funded by Universidad Distrital Francisco José de Caldas, its Faculty of Engineering, and its Central Research Office.

Indexed in

Scopus	SciELO
Publindex Colombia Categoría B	Redalyc
Directorio Latindex	Fuente Académica Premier (EBSCO)
Applied Science & Technology Source Ultimate (EBSCO)	Emerging Sources Citation Index Bibliographic Bases (SC)
Fuente Académica Plus (EBSCO)	OpenAlex
Catálogo 2.0 Latindex	DOAJ
Dialnet	ROAD
Google Scholar Metrics	PKP Index
MIAR	

Peer-reviewers in this issue

Antonio Luchetta
University of Florence, Italy

Carlos Francisco Simões Gomes
Universidade Federal Fluminense, Brazil

Diana Stella Garcia Miranda
Universidad Nacional de Colombia, Colombia

Diego Julián Rodriguez
Universidad Nacional de Colombia, Colombia

Gilberto Santos
Polytechnic Institute of Cávado and Ave, Portugal

Guillermo Valencia-Palomo
Instituto Tecnológico de Hermosillo, Mexico

Henry Leonardo Lopez Salamanca
Institutos Lactec, Divisão de Sistemas Elétricos
Universidade Federal do Paraná

Jose Guillermo Guarnizo Marin
Universidad Distrital Francisco José de Caldas, Colombia

Marcio Pereira Basilio
Universidade Federal Fluminense, Brazil

Marko D. Orošnjak
University of Luxembourg, Luxembourg

Mireia Faus
Universitat de València, Spain

Mostafa Ahmed
Technical University of Munich, Germany

Muhammad Abu Talha
American International University–Bangladesh, Bangladesh

Osvaldo Luiz Gonçalves Quelhas
Universidade Federal Fluminense, Brazil

Sanjay Bhasin
University of Buckingham, United Kingdom

Sergio A. Useche
Universitat de València, Spain

Shigeru Kuchii
National Institute of Technology, Kitakyushu College, Japan

Walter Julián Gil-González
Universidad Tecnológica de Pereira, Colombia

Yasmany Damián García-Ramírez
Universidad Técnica Particular de Loja, Ecuador

Table of Contents

UNIVERSIDAD DISTRITAL
FRANCISCO JOSÉ DE CALDAS

Ingeniería

https://revistas.udistrital.edu.co/index.php/reving/issue/view/1320

DOI: https://doi.org/10.14483/23448393.25002

Editorial

Voltage Stability and Jacobian Determinant in Power Systems: Analysis, Indicators, and Practical Monitoring Tools

Oscar Danilo Montoya[1], Juan Diego Pulgarín Rivera[2], and Carlos Andrés Torres-Pinzón[2]

[1]Compatibility and Electromagnetic Interference group, Department of Engineering, Universidad Distrital Francisco José de Caldas; Electrical engineer, Master of Electrical Engineering, and PhD in Engineering, Colombia

[2]Compatibility and Electromagnetic Interference group, Department of Engineering, Universidad Distrital Francisco José de Caldas; Electrical Engineer, Master of Engineering (Automation), and PhD in Engineering, Colombia

Voltage stability is a fundamental aspect of power system reliability, which refers to an electrical network's ability to maintain acceptable voltage levels under normal operating conditions and various types of disturbances [1]. This involves complex, nonlinear power flow equations that capture the intricate relationships between bus voltages, phase angles, and power injections across the system [2]. As demand and system conditions change, maintaining voltage stability becomes increasingly challenging, and failure to do so can lead to voltage collapse and widespread blackouts [3]. Therefore, understanding and monitoring the factors that influence voltage stability are crucial for ensuring the secure, reliable, and efficient operation of modern power grids.

Editorial

1. Power flow equations

Consider a power system with n buses. The complex power injected at bus i is $S_i = P_i + j\,Q_i$, which is related to the bus voltage $V_i \angle \delta_i$ and the admittance matrix Y_{ij}. The active and reactive power flow equations are presented below [4].

$$P_i = V_i \sum_{j=1}^{n} V_j \left(G_{ij} \cos\left(\delta_i - \delta_j\right) + B_{ij} \sin\left(\delta_i - \delta_j\right)\right), \forall i \in N \quad (1)$$

$$Q_i = V_i \sum_{j=1}^{n} V_j \left(G_{ij} \sin\left(\delta_i - \delta_j\right) + B_{ij} \cos\left(\delta_i - \delta_j\right)\right), \forall i \in N \quad (2)$$

* Correspondence: odmontoyag@udistrital.edu.co

where:

- V_i and δ_i are the magnitude and angle of the voltage at bus *i*,
- G_{ij} and B_{ij} represent the conductance and susceptance elements of the admittance matrix Y_{ij}.
- *N* denotes the set containing all the nodes in the transmission network.

1.1 Jacobian matrix and voltage stability

The power flow equations can be vectorially expressed as follows [5]:

$$F(x) = 0,$$

where $x = [\delta_2, \ldots, \delta_n, V_2, \ldots, V_n]^T$. Linearizing around an operating point yields

$$\Delta F = J\Delta x,$$

where J is the Jacobian matrix, which comprises the partial derivatives J

$$J = \begin{bmatrix} \frac{\partial P}{\partial \delta} \frac{\partial P}{\partial P} \\ \frac{\partial Q}{\partial \delta} \frac{\partial Q}{\partial V} \end{bmatrix}$$

2. Voltage stability and Newton-Raphson power flow divergence

The stability of a power system as it approaches its operating limits is closely associated with the behavior of the Newton-Raphson power flow method. Under normal conditions, this iterative technique converges rapidly to a solution, indicating a stable operating point [5]. However, as the system load increases toward its stability boundary, the power flow solutions tend to become more sensitive, and the Newton-Raphson method may fail to converge [6].

This divergence in the power flow solution is a practical indicator that the system is nearing a voltage collapse or severe voltage instability. This occurs when the Jacobian matrix J, derived from the linearization of the nonlinear power flow equations, approaches singularity [3]. As the load increases, |J|, *i.e.*, the determinant of the Jacobian, tends to decrease, reflecting the system's diminishing ability to maintain voltage stability.

When |J| approaches zero, the power flow equations become unsolvable with the iterative method, signifying that the system is at or beyond its stability margin [7]. This non-convergence signals that the system cannot support further load increases without risking voltage collapse.

Monitoring the convergence behavior of the power flow alongside the evolution of the Jaco- bian determinant provides valuable early warning signals. With this information, operators can implement preventive control actions—such as reactive power compensation or system reconfigu- ration—in order to avoid instability and ensure a secure operation.

Remark 1 *A divergence of the Newton-Raphson power flow method indicates that* $|J| \to 0$*, and that a voltage collapse may occur, highlighting the critical link between solution convergence, the Jacobian determinant, and voltage stability. Recognizing these signs early allows for timely interventions aimed at preventing voltage collapse and maintaining system reliability [1].*

The next section presents a simple yet effective MATLAB/Matpower tool to evaluate this behav- ior, facilitating a practical assessment of system stability limits.

3. Matpower tool for monitoring power flow divergence under load increases

To practically demonstrate how increasing system load impacts the solvability of power flow equa- tions and, consequently, a system's voltage stability, a MATLAB/Matpower code is presented be- low [8]. This tool incrementally raises the load in a predefined case (*e.g.*, *case9*) and monitors the success or failure of the power flow solution at each step. Failure to converge indicates a potential approach to the system's stability limit, often associated with voltage collapse.

```
clc;
step = 0.001;
max_load_multiplier = 5;
start_multiplier = 1;   % Assuming original load is at 1
% Loop over load multipliers load_multiplier=start_
multiplier;
for k = start_multiplier:step:max_load_multiplier
    % Create a copy to avoid modifying original case
    % Scale load (columns 3 and 4 of bus matrix: Pd and Qd) mpc =
    loadcase('case9');   % Load the case
    mpc.bus(:, 3:4) = k * mpc.bus(:, 3:4);
    % Run power flow once per load level results =
    runpf(mpc);
    if results.success
        disp(['Success at load multiplier: ', num2str(k)]);
        % Optional: Store results if needed
    else
        disp(['Failure at load multiplier: ', num2str(k-step)]);
        break;
    end
end
```

This analysis revolves around the use of a straightforward yet powerful method to determine the load levels at which power flow equations lose solvability. These points are critical since they indicate an approach to voltage instability, which is a major concern in power system operation. Operators can utilize these insights for preventive measures, thereby ensuring grid reliability.

4. Numerical assessment

Table II summarizes the maximum loadability limits for several IEEE test systems:

Table II. Maximum loadability for IEEE feeders

IEEE system	Maximum load multiplier	Approx. loadability (% of original value)
IEEE 9-Bus	2.373	237.3
IEEE 14-Bus	4.004	400.4
IEEE 30-Bus	3.657	365.7
IEEE 57-Bus	1.785	178.5
IEEE 118-Bus	1.816	181.6

4.1 Results analysis

- **Maximum load multiplier.** This value indicates how many times the original load can be handled by the system before becoming unstable.
  - For example, the IEEE 9-bus system can sustain approximately 2.373 times its initial load, while the IEEE 14-bus system can handle about 4.004 times.
  - Larger systems like the IEEE 118-bus feeder support up to approximately 1.816 times the original load, reflecting different stability margins across system sizes.
- **Approximate loadability (% of the original load).** This value represents the maximum load that the system can support relative to its initial load.
  - The IEEE 14-bus system exhibits the highest loadability (400.4%), indicating a signifi- cant load margin.
  - Conversely, the IEEE 57-bus feeder's maximum loadability is about 178.5%, suggesting a more constrained margin.

4.2 Main findings

- **Loadability variations across systems.** Smaller systems like the IEEE 9-bus and 14-bus feeders have a higher relative load capacity compared to larger systems such as the IEEE 57-bus grid, highlighting differences regarding their inherent system stability.

- **Practical implications.** Load multipliers provide crucial thresholds for operators to prevent voltage collapse. When the load approaches these limits, system reinforcement or control actions become necessary.
- **System size and stability margin.** Generally, larger systems tend to exhibit a lower loadabil- ity, which underscores the importance of robust stability monitoring in large interconnected grids.

5. Conclusion

Analyzing a power system's maximum loadability and the behavior of the Jacobian determinant provides crucial insights with regard to voltage stability margins. As the system load increases, the Jacobian matrix approaches singularity, which is signified by the determinant $|\mathbf{J}| \to 0$. This condi- tion indicates that the power flow equations are nearing their solvability limit, and that the system is close to voltage collapse. Monitoring these indicators in real time can serve as an early-warning mechanism, allowing operators to implement preventive control actions such as reactive power support, reconfiguration, or load shedding to maintain stability and avoid catastrophic failures.

Understanding the relationship between the Jacobian determinant and system stability not only aids in operational decision-making; it can also inform system planning processes. By quantifying load margins, utilities can identify vulnerabilities and prioritize infrastructure upgrades or control strategies that effectively enlarge the stability region. Furthermore, incorporating these assessments into operation routines enhances resilience by providing a clear measure of how close the system is to its operating limits, thereby supporting the implementation of proactive measures that help to ensure a reliable and secure power delivery under increasing demand or unforeseen disturbances.

6. Acknowledgments

This research received support from the Ibero-American Program of Science and Technology for Development (CYTED), through Thematic Network 723RT0150, *i.e.*, *Red para la integracio´n a gran escala de energ´ıas renovables en sistemas ele´ctricos* (RIBIERSE-CYTED).

References

[1] P. Kessel and H. Glavitsch, "Estimating the voltage stability of a power system," *IEEE Trans. Power Delivery*, vol. 1, no. 3, pp. 346–354, 1986. [Online]. Available: https://doi.org/10.1109/tpwrd.1986.4308013 1, 2

[2] T. Cutsem and C. Vournas, *Voltage stability of electric power systems*. USA: Springer, 1998. [Online]. Available: https://doi.org/10.1007/978-0-387-75536-6

[3] Y. Tang, *Voltage stability analysis of power system*. Singapore: Springer, 2021. [Online]. Available: https://doi.org/10.1007/978-981-16-1071-41

[4] O. D. Montoya, W. Gil-González, A. Arias-Londoño, A. Rajagopalan, and J. C. Hernández, "Voltage stability analysis in medium-voltage distribution networks using a second-order cone approximation," *Energies*, vol. 13, no. 21, p. 5717, Nov. 2020. [Online]. Available: https://doi.org/10.3390/en13215717

[5] B. Sereeter, C. Vuik, and C. Witteveen, "On a comparison of Newton–Raphson solvers for power flow problems," *J. Comp. App. Math.*, vol. 360, pp. 157–169, Nov. 2019. [Online]. Available: https://doi.org/10.1016/j.cam.2019.04.007

[6] V. Ajjarapu and C. Christy, "The continuation power flow: A tool for steady state voltage stability analysis," *IEEE Trans. Power Syst.*, vol. 7, no. 1, pp. 416–423, 1992. [Online]. Available: https://doi.org/10.1109/59.141737

[7] F. Hong, J. Chen, and J. Zuo, "Power flow unsolvable cases adjustment method based on grid static voltage stability," in *2011 Int. Conf. Adv. Power Syst. Autom. Protect.*, Oct. 2011, pp. 2066–2071. [Online]. Available: https://doi.org/10.1109/apap.2011.6180773

[8] K. Buayai, K. Chinnabutr, P. Intarawong, and K. Kerdchuen, "Applied matpower for power system optimization research," *Energy Proc.*, vol. 56, pp. 505–509, 2014. [Online]. Available: https://doi.org/10.1016/j.egypro.2014.07.185

UNIVERSIDAD DISTRITAL
FRANCISCO JOSÉ DE CALDAS

Ingeniería

https://revistas.udistrital.edu.co/index.php/reving/issue/view/1320

DOI: https://doi.org/10.14483/23448393.22627

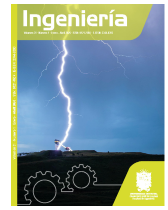

Research

Regression Analysis of Principal Ship Attributes for Purse Seiners in the Concept Design Stage

Análisis de regresión de los atributos principales de barcos pesqueros de cerco en la etapa de diseño conceptual

Dennys De La Torre[1], and Dheybi Cervan[2]

[1]U1Grupo de Investigación de Transporte Multidisciplinario, Universidad Nacional de Ingeniería, Av. Túpac Amaru 210 – Lima, Perú
[2]Facultad de Ingeniería Mecánica, Av. Túpac Amaru 210 – Lima, Perú

Abstract

Context: In the ship concept design stage, naval architects must estimate the principal attributes of a vessel before the final definition of hull proportions and detailed arrangements. These estimates are essential for assessing feasibility, performance, and operational capability. However, reliable vessel-specific predictive tools are often unavailable for certain vessel categories.
Method: A database of 130 American-type semi-industrial purse with RSW systems was employed to develop practical regression-based power-law models for estimating key ship attributes directly from principal hull dimensions.
Results: The results show that the main volumetric and power attributes exhibit strong and consistent scaling relationships with the principal dimensions, yielding moderate to high determination coefficients, while the fuel and water capacities report a weak geometric dependence. The proposed regression equations demonstrate improved predictive performance when compared to existing formulations reported in the literature for semi-industrial purse seiners.
Conclusions: This work provides a set of vessel-specific, empirically grounded regression tools tailored to American-type semi-industrial purse seiners, which can be directly applied during the ship concept design stage to support rapid and informed decision-making. This study complements previous analyses focused on hull geometric ratios by addressing a distinct and application-oriented design problem that deals with attribute estimation rather than geometric proportion selection.

Keywords: ship dimensions, fishing vessels, hull statistics, ship concept design stage, regression analysis

Article history

Received: October 28th, 2024

Modified: October 28th, 2025

Accepted: December 22nd, 2025

Ing, vol. 31, no. 1, 2026, e22627

* Correspondence: ddelatorrec@uni.edu.pe

Resumen

Contexto: En la etapa de diseño conceptual del buque, los arquitectos navales deben estimar los atributos principales de una embarcación antes de la definición final de las proporciones del casco y de realizar arreglos detallados. Estas estimaciones son esenciales para evaluar la factibilidad, el desempeño y la capacidad operativa. Sin embargo, no se suele disponer de herramientas predictivas confiables y específicas para determinadas categorías de embarcaciones.
Método: Se empleó una base de datos de 130 embarcaciones cerqueras semiindustriales de tipo americano con sistemas RSW para desarrollar modelos prácticos basados en regresión de tipo ley de potencia, a fin de estimar los atributos clave del buque directamente de las dimensiones principales del casco.
Resultados: Los resultados muestran que los principales atributos volumétricos y de potencia presentan relaciones de escalamiento fuertes y consistentes con las dimensiones principales, con coeficientes de determinación moderados a altos, mientras que las capacidades de combustible y agua reportan una débil dependencia geométrica. Las ecuaciones de regresión propuestas demuestran un mejor desempeño predictivo en comparación con las formulaciones existentes que figuran en la literatura para cerqueros semiindustriales.
Conclusiones: Este trabajo proporciona un conjunto de herramientas de regresión específicas para este tipo de embarcaciones, las cuales han sido empíricamente fundamentadas y adaptadas a los cerqueros semiindustriales tipo americano, y pueden aplicarse directamente durante la etapa de diseño conceptual del buque para una toma de decisiones rápida e informada. Al abordar un problema de diseño distinto y orientado a la aplicación, este estudio complementa análisis previos que emplean las relaciones geométricas del casco, centrándose en la estimación de atributos más que en la selección de proporciones geométricas.

Palabras clave: dimensiones del buque, embarcaciones pesqueras, estadística del casco, etapa de diseño conceptual del buque, análisis de regresión

Contents

1. Introduction

Ship concept design documents present typical data for various vessel types, in addition to defining their main linear dimensions (length, breadth, and depth) as functions of owner-specified attributes—*e.g.*, the fish hold capacity for fishing vessels. Hull statistics provide meaningful estimated regression equations to predict ship attributes as a function of linear ship dimensions. Investigations on hull statistics have been a prominent research topic in recent years.

In the literature, [1] analyzed a database of 260 non-sister container ships built between 1979 and 2022. They developed simple regression formulas and compared them against existing equivalents in the literature, demonstrating superior trend approximation. This study updated a set of simple and multivariable regression models, achieving a higher goodness of fit than previous works. These formulas were designed for ease of use, allowing designers to apply them directly in ship concept design and multi-attribute design procedures.

[2] utilized an open dataset of 54 in-service cruise ships delivered since 2000. Their study demonstrated the application of supervised statistical learning methods to analyze key cruise ship characteristics. Furthermore, it established a practical formula to support naval architects in the preliminary design phase for estimating gross tonnage.

[3] presented preliminary design formulas developed using a database of container ships built since 2015. Their formulas establish associations between the main dimensions—*i.e.*, length between perpendiculars (*Lpp*), breadth, draught, and depth—and key operational attributes: deadweight, TEU capacity, and ship speed.

While our previous study, titled *Effect of Ship Size on the Hull Dimension Ratios of Purse Seiners* [4] focused on the influence of vessel size on geometric hull proportions (L/B, L/D, B/D) from an explanatory perspective, this work addresses a fundamentally different design problem: the prediction of the main ship attributes required at the ship concept design stage. In [4], hull dimension ratios were treated as response variables and analyzed to interpret stability, speed, and seakeeping qualities in the preliminary design stage. In this work, hull ratios are not treated as primary outcomes; instead, the response variables are operational and volumetric vessel attributes directly required by designers at the ship concept design stage. Consequently, the statistical analysis in this manuscript serves a predictive and instrumental role rather than an explanatory one.

[5] introduced a procedure for determining the optimal characteristics of multi-purpose cargo vessels (MPCVs) at the preliminary design stage. Their method is based on the statistical analysis of a database compiled from reliable MPCV designs built over the past three decades. Using the resulting diagrams and formulas, designers can derive ship dimensions directly from a required deadweight (key input).

[6] developed an artificial neural network (ANN) model to predict the main particulars of chemical tankers during the preliminary design stage. This model utilizes deadweight and vessel speed as inputs, generating predictions for the overall length, the length between perpendiculars, the breadth, the draught, and the freeboard as outputs. Their results demonstrate that the model determines the initial main particulars with a high degree of accuracy when compared to actual ship data.

[7] employed statistical methods to analyze representative ship samples, establishing the relationship between gross tonnage (GT) and vessel size. This analysis yielded a regression equation that quantifies the GT-size relationship for typical Grand Canal vessels, in accordance with the specifications outlined in the Standard for the Main Dimensions of Ships in the Grand Canal.

[8] presented a plot of depth *vs.* breadth for several vessel types, which corresponds to lines of constant breadth-to-depth ratio. The analysis identified a distinct group—comprising fishing vessels and cargo ships where depth is constrained by stability—exhibiting a characteristic breadth/depth ratio of approximately 1.65.

[9] presented a collection of design diagrams derived from statistical and regression analyses of principal ship design attributes across various vessel types. This compilation synthesizes formulations and regressions developed by thesis students from the National Technical University of Athens (NTUA) and the staff of the NTUA Ship Design Laboratory, utilizing data sourced from the IHS Fairplay World Shipping Encyclopedia. For fishing vessels, the diagrams contrast power against length between perpendiculars, reefer capacity volume (in ft^3) against length between perpendiculars, reefer capacity volume against breadth, and reefer capacity volume against depth. The regression formulas used the determination coefficient (R^2) to indicate the goodness of fit [10].

[11] investigated the main attributes of seiners, fishing tackle, and trawlers by conducting regression analysis based on data from more than 2000 fishing vessels provided by the Ministry of Agriculture and Rural Affairs of China. For seiners, they obtained relationships of attributes against the main dimensions, or between GT and length and power and length, with an R^2 higher than 0.69.

[12] analyzed the principal dimensions and attributes of fishing vessels certified by the Russian Maritime Register of Shipping (RMRS). Their study examined over a thousand vessels of varying specifications. By applying analytical methods, they established relationships between key dimensions and attributes, such as GT *vs.* displacement and breadth *vs.* displacement.

Larger fishing vessels are appearing in the world's fishing fleet, in response to the need to save more time for catches, improve the use of energy, fish larger species, and stay longer at sea. Ship designers necessitate exhaustive and extensive hull statistics and estimated regression equations to obtain principal attributes and dimensions. However, these statistics and equations are commonly unavailable for a given vessel type. This research was motivated by a pronounced gap in the systematic documentation of principal dimensions and key attributes for American-type semi-industrial purse seiners within the existing literature. Such application-driven statistical analyses have been increasingly recognized as valuable when tailored to specific vessel categories, particularly those that are underrepresented in global design databases. The objective of this study is not to analyze hull ratios as design outcomes, but to develop practical, vessel-specific regression tools that allow naval architects to estimate power, tonnage, and fish hold capacity directly from principal dimensions during the first loop of the design spiral.

This work reports statistics, conducts regression analyses, and makes comparisons with existing formulas while using a database of 130 vessels from the Peruvian fishing fleet, which was published by PRODUCE [13] and DICAPI [14]. This work aimed to determine the relationships between the main ship dimensions of a purse seiner, such as length (L), breadth (B), and depth (D), and attributes like power, fuel, water, gross tonnage (GT), net tonnage (NT), and reefer volume or fish hold capacity (FHC).

Although our regression methodology is intentionally classical and based on simple power-law models, the contribution is not methodological but applicative. The novelty lies in the use of an updated and homogeneous database of American-type semi-industrial purse seiners for the systematically deriving vessel-specific regression formulas, in addition to a quantitative comparison with existing design equations. This provides naval architects with empirically grounded, fleet-representative relationships tailored to fishing vessel categories that have been scarcely addressed in the statistical hull-statics literature [15].

2. Methods

2.1 Vessel database

This research used data on purse seiners obtained from the vessel registry of the Peruvian Government's Ministry of Production (PRODUCE [13]), as well as from the General Directorate of Captaincies and Coast Guard (DICAPI [14]). To perform statistical analyses, we used a collection of 130 semi-industrial purse seiners (Table I) with a section plan approximately as described in [16]. The ships, registered from 1996 to 2020, have a refrigerated seawater (RSW) conservation system. These semi-industrial purse seiners are of the American type, with the bridge and accommodation forward and the working deck aft. We conducted regressions, correlation analyses, and comparisons to investigate the interaction between ship attributes and dimensions. It should be acknowledged that the database used herein is the same as that used in [4]. This reuse follows the international editorial guidelines for derived publications, as the research questions, dependent variables, analytical objectives, and engineering applications are clearly differentiated. This manuscript does not present duplicate results; it reutilizes the data to address a separate and practically relevant design problem.

Table I. Main attributes and dimensions in the purse seiner database

Main characteristic	Symbol	SI Units	Minimum	Maximum
Length	L	m	21.7	77.0
Breadth	B	m	6.0	14.5
Depth	D	m	2.6	8.6
Power	Power	kW	230	2289
Fuel capacity	Fuel	gal.	360	52 500
Water capacity	Water	gal.	80	29 800
Gross tonnage	GT		21.82	1006
Net tonnage	NT		72.45	224
Fish hold capacity	FHC	m^3	89.83	868

The initial dataset was extracted from the complete registry of the Peruvian fishing fleet. The vessels were filtered based on whether they included RSW systems. P*ower*, NT, *GT*, and *FHC data* were fully available for all selected vessels. The fuel and water tank capacities, which are not mandatory fields in the Peruvian fishing vessels database, were manually completed using information retrieved from the public records of the DICAPI. As a result, some vessels lack entries for *fuel* and *water capacity*. These missing values were maintained to reflect the actual availability of documented information, *i.e.*, only 59% of the records for fuel capacity and 54% for water capacity.

No observations were removed. To assess data quality, an outlier screening was performed using standardized Z-scores ($|z|>3$). All detected outliers correspond to real vessels with extreme but plausible physical characteristics (larger tonnage, higher installed power, or unusually high tank capacities), as shown in Fig. 1. Since these values represent the true variability in the fleet rather than measurement errors, they were preserved in the analysis.

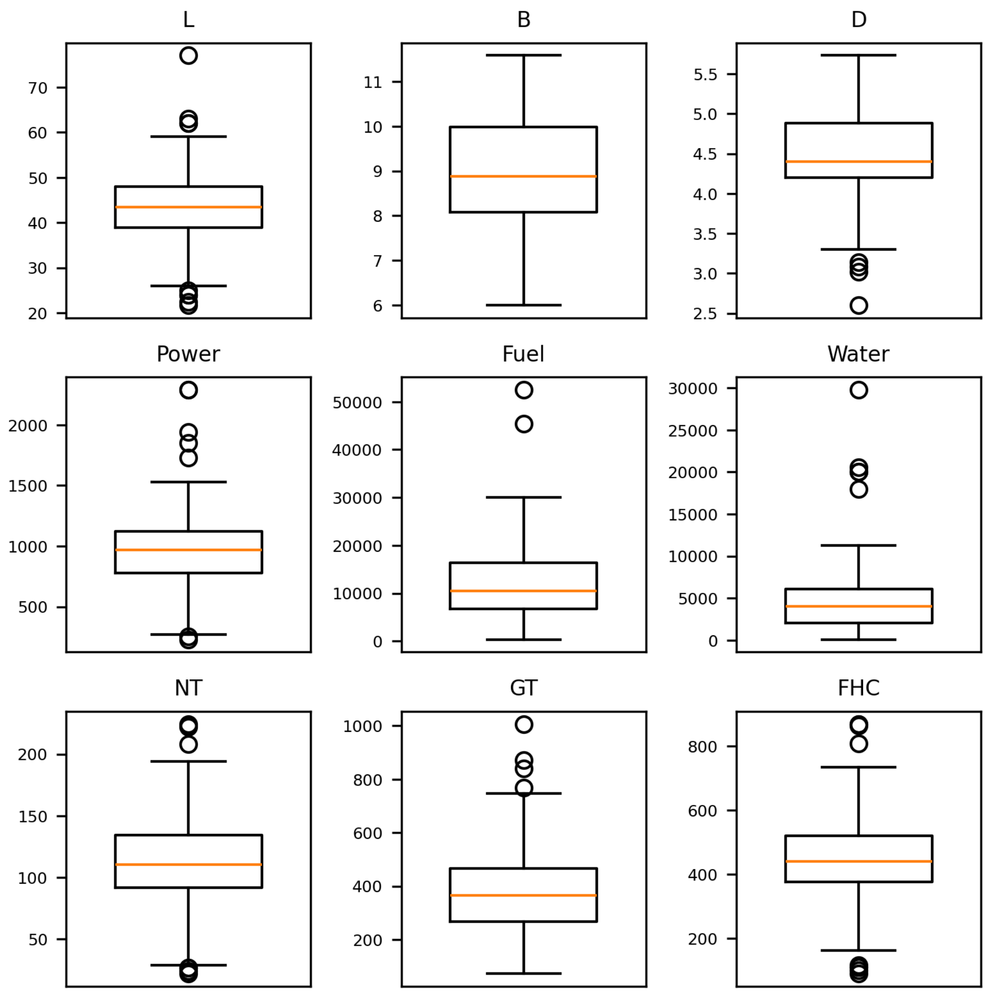

Figure 1. Boxplot for all variables showing outliers

2.2 Regression analysis methodology

Owner requirements are translated into technical characteristics during the ship concept design stage. This is the first loop of the design spiral. The design stage corresponds to the preliminary estimation of the main attributes (power, GT, NT, FHC, and range, as expressed by the fuel and water capacity, among others). To aid the designer in choosing the main attributes, a compilation of hull statistics for the most relevant dimensions must be available. For fishing vessels, this would include the principal dimensions *vs.* the GT, the NT, the FHC, and the fuel and water capacity.

The ship's linear dimensions are L, B, and D. L is the main linear dimension of the ship, which includes the overall length L, the length between perpendiculars Lpp, and the water line length Lwl. All these lengths are roughly the same, but L is generally found in public registries. B is the molded vessel breadth, measured at the midship station. D is the height between the molded baseline and the molded depth line of the uppermost deck at the side of the midship section [17]. Naval architects choose these linear dimensions while considering the geometric restrictions of the port. Then, they use them to select the ship's attributes by means of estimated regression equations. Similarly, when the designer requires a linear dimension for a given volume attribute (*e.g.*, GT), he or she can use the same estimated regression equations to determine it.

Fundamentally, a fishing vessel is a volume carrier, not a deadweight carrier [18]. The volume attributes related to fishing vessels are FHC, GT, and NT. FHC refers to the refrigerated fish hold volume, GT denotes the total enclosed volume of the vessel, and NT only represents the cargo volume and the passenger spaces.

Estimated regression equations are used to predict the response variable values as a function of a predictor variable. These equations are usually the result of simple regressions. We conducted simple regressions with the following form:

$$Y = aX^b \tag{1}$$

All power-law regressions were obtained using the classical log-log linearization approach [19], *i.e.*, applying an ordinary least-squares fit to the transformed variables, or $\ln y$ and $\ln x$. This procedure is consistent with the methodology used in hull-scaling studies and preliminary design formulations in naval architecture. The coefficient of determination is often quantified and compared to assess the accuracy of simple regressions:

$$R^2 = 1 - \frac{\sum_{i=1}^{n} \left(y_i - y_i^* \right)^2}{\sum_{i=1}^{n} \left(y_i - \overline{y} \right)^2} \tag{2}$$

where y_i denotes the values of n observations, y_i^* the predicted values, and $\overline{y}$ the mean value.

3. Results

3.1 Ship statistics

Normality tests (Shapiro-Wilk, D'Agostino-Pearson, and Anderson-Darling, with a 95% confidence level) showed that no variables follow a normal distribution. Breadth is the closest to normality. This behavior, characterized by skewness, kurtosis, and long-tailed histograms, is typical of heterogeneous fishing fleets, where technological variation, vessel age dispersion, and operational heterogeneity produce non-symmetric distributions. As a consequence, the median was considered to be a more representative measure of central tendency than the mean for all variables. It should be noted that the lack of normality does not invalidate the regression analysis, since normality is required for model residuals rather than for the raw variables themselves [19], and simple potential regression remains appropriate for uncovering structural scaling relationships in conceptual ship design.

Table II shows that the ship attributes do not exhibit a normal distribution. This table also includes the *p*-value of the Shapiro-Wilk normality test, rejecting normality of the variables for a 95% confidence level. The distribution of B is the closest to normality.

Fig. 2 reports that, in this vessel category, power ranges between 750 and 1250 kW. There are a few ships with levels higher than 1500 kW in the Peruvian fishing fleet. The average power is about 1000 kW. Fig. 3 shows that the fuel ranges between 800 and 1100 gallons. This variable does not have a normal distribution, but the distribution peak marks a high concentration near its median. A high concentration of ships is also found around the medians for L, power, fuel, water, NT, GT, FHC, and D.

The Peruvian fishing fleet ranges from about 33 to 55 m in length, 8.8 to 9.2 m in breadth, 4.4 to 4.6 m in depth, 750 to 1250 kW, 8000 to 11000 gal fuel capacity, 1000 to 5000 gal water capacity, 300 to 500 GT, 100 to 120 NT, and 300 to 500 m^3 FHC. In addition, a few large vessels belong to another category, with lengths over 60 m, power values over 1500 kW, fuel capacities over 20 000 gal, water capacities over 9000 gal, NT over 175, GT over 600, and FHC over 600 m^3.

Table II. Descriptive statistics for the ship attributes of American-type semi-industrial purse seiners in the Peruvian fleet

Statistic	Length (m)	Breadth (m)	Depth (m)	Power (kW)	Fuel (gal)	Water (gal)	Net tonnage	Gross tonnage	FHC (m^3)
Mean	43.5	9.0	4.4	965	12939	5196	113.7	376.5	446
Standard error	0.8	0.1	0.05	30.4	1091	642	3.62	14.5	12.3
Median	43.3	8.9	4.4	969	10500	4000	110.5	366.5	440
Mode	40.5	8.9	4.4	969	12000	5000	127.0	248.3	450
Standard deviation	8.7	1.1	0.55	346	9572	5371	41.36	164.72	140
Sample variance	75.9	1.2	0.3	11985	91E6	28E6	1710.9	27134	1974
Kurtosis	1.55	-0.34	0.9	2.65	4.00	7.4	4.17	1.6	1.49
Skewness	0.21	-0.01	-0.4	0.99	1.64	2.51	0.94	0.83	0.13
Shapiro-Wilk	0	0.035	0	0	0	0	0	0	0
Range	52.3	6.6	3.1	2059	52140	29720	290.81	934.2	779

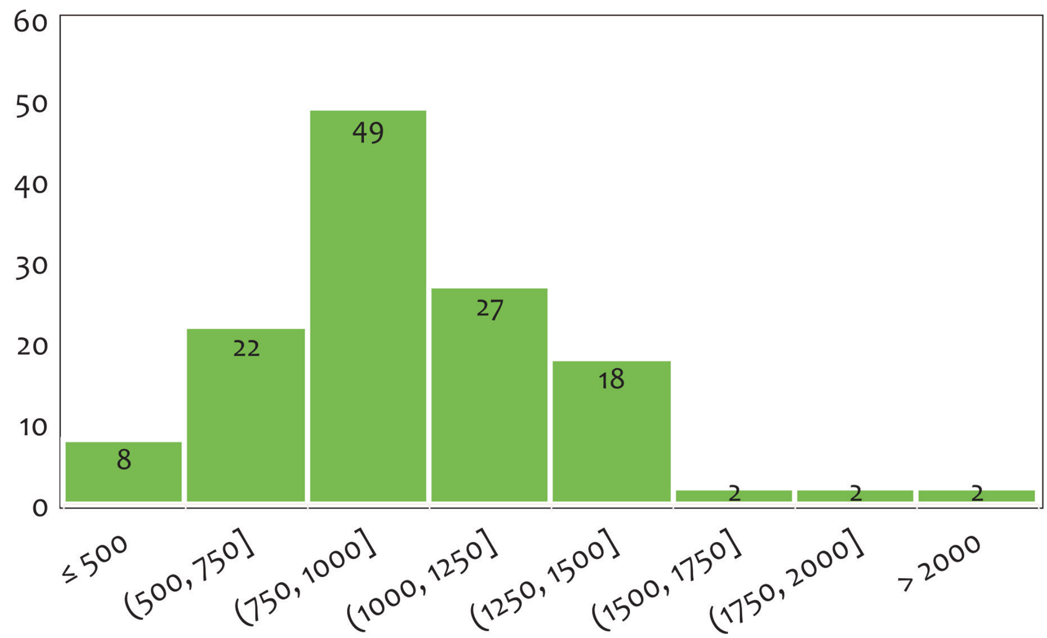

Figure 2. Power histogram of American-type, semi-industrial purse seiners

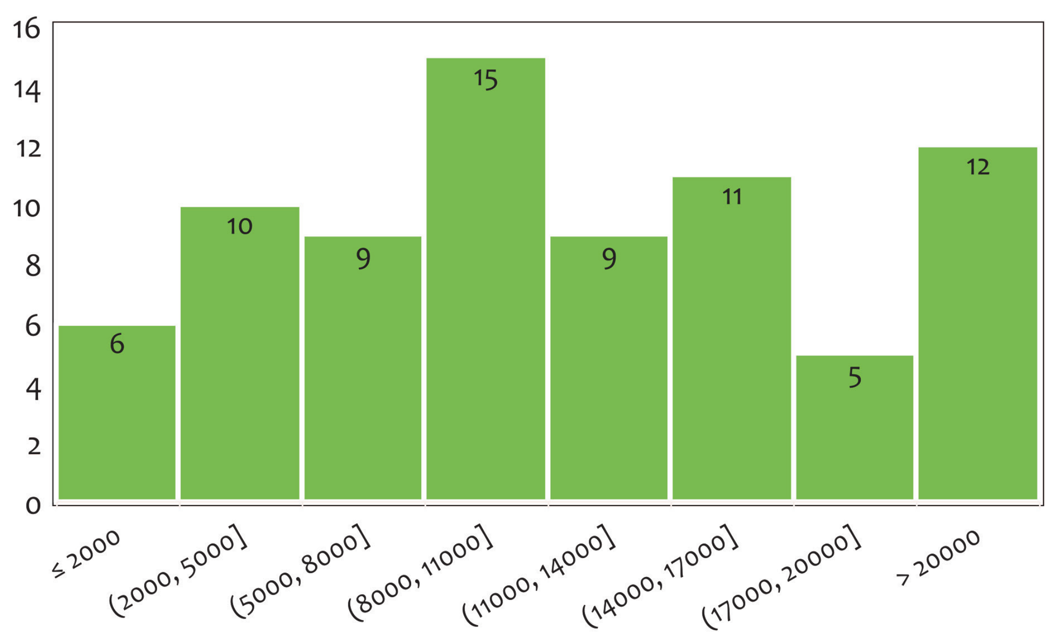

Figure 3. Fuel histogram of American-type, semi-industrial purse seiners

3.2 Regression analysis

Note that the response variables are power, fuel capacity, water capacity, GT, NT, and FHC, and the predictor variables are L, B, and D. Table III presents the estimated regression equations and the determination coefficients (R^2) for all variables. The regression equations rely on simple potential regression. The determination coefficients are higher than 0.64 for all response variables except fuel and water. Since $R^2 > 0.64$, it could be said that the predictor variables explain 64% of the variance in power, GT, NT, and FHC. The estimated regression equations for fuel and water capacity yield values with high variation.

Fig. 4 shows a strong positive relationship between power and L. The data points are uniformly dispersed about the trend line. The data points concentrate between 30 and 55 m, and between 750 and 1250 kW. Fig. 5 shows a strong positive association between GT and L. This association has an R^2 of nearly 1. L explains 91% of the variation in GT. A power function closely approximates the GT-L relationship, as the data points adhere to the regression curve. Fig. 6, the scatter plot of NT *vs.* L, also reveals a strong relationship. L explains 75% of the variation in NT. The data points align closely with the regression line. Moreover, Fig. 7 shows a strong positive association between FHC and L. L explains 74% of the variation in FHC. The data samples closely fit the regression curve.

Table III. Regression analysis coefficients for the attributes of American-type semi-industrial purse seiners

	Power (kW)		**Fuel (gal)**		**Water (gal)**	
	Estimated equation	R^2	**Estimated equation**	R^2	**Estimated equation**	R^2
Length (m)	$3.44 \cdot L^{1.48}$	0.68	$2.73 \cdot L^{2.15}$	0.24	$2.76 \cdot L^{1.86}$	0.13
Breadth (m)	$3.78 \cdot B^{2.5}$	0.69	$7.67 \cdot B^{3.23}$	0.18	$14.12 \cdot B^{2.47}$	0.08
Depth (m)	$29.1 \cdot D^{2.32}$	0.64	$39.3 \cdot D^{3.69}$	0.25	$35.5 \cdot D^{3.03}$	0.12
	Net tonnage		**Gross tonnage**		**FHC (m^3)**	
	Estimated equation	R^2	**Estimated equation**	R^2	**Estimated equation**	R^2
Length (m)	$0.19 \cdot L^{1.69}$	0.75	$0.11 \cdot L^{2.16}$	0.91	$1.09 \cdot L^{1.59}$	0.74
Breadth (m)	$0.30 \cdot B^{2.67}$	0.67	$0.20 \cdot B^{3.39}$	0.80	$1.59 \cdot B^{2.55}$	0.67
Depth (m)	$2.00 \cdot D^{2.67}$	0.72	$3.24 \cdot D^{3.14}$	0.74	$9.34 \cdot D^{2.57}$	0.74

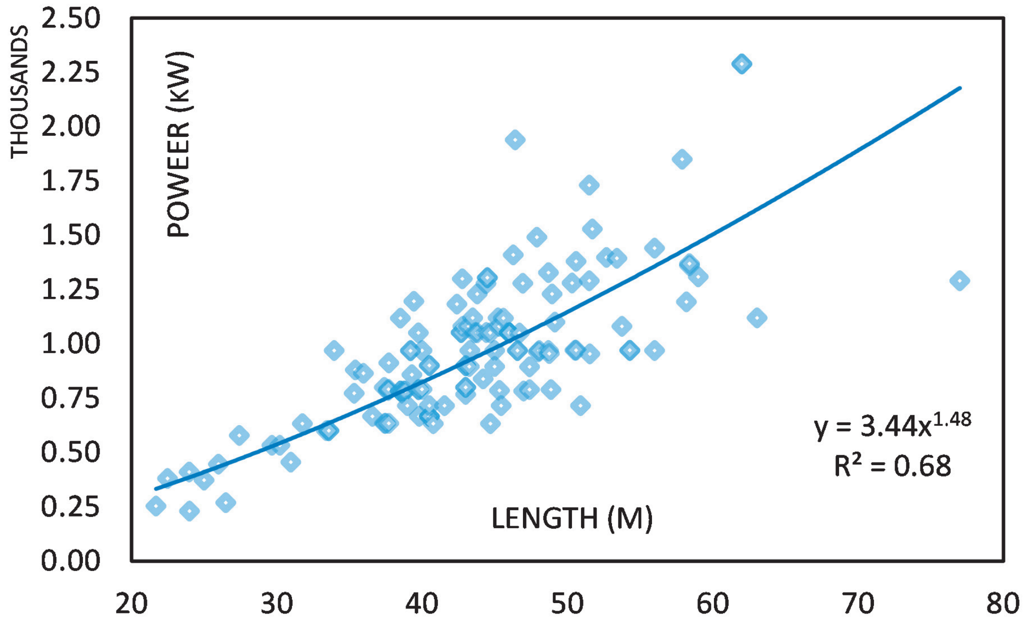

Figure 4. Power *vs.* length scatter plot and regression equation of for the American-type semi-industrial purse seiners in the Peruvian fleet

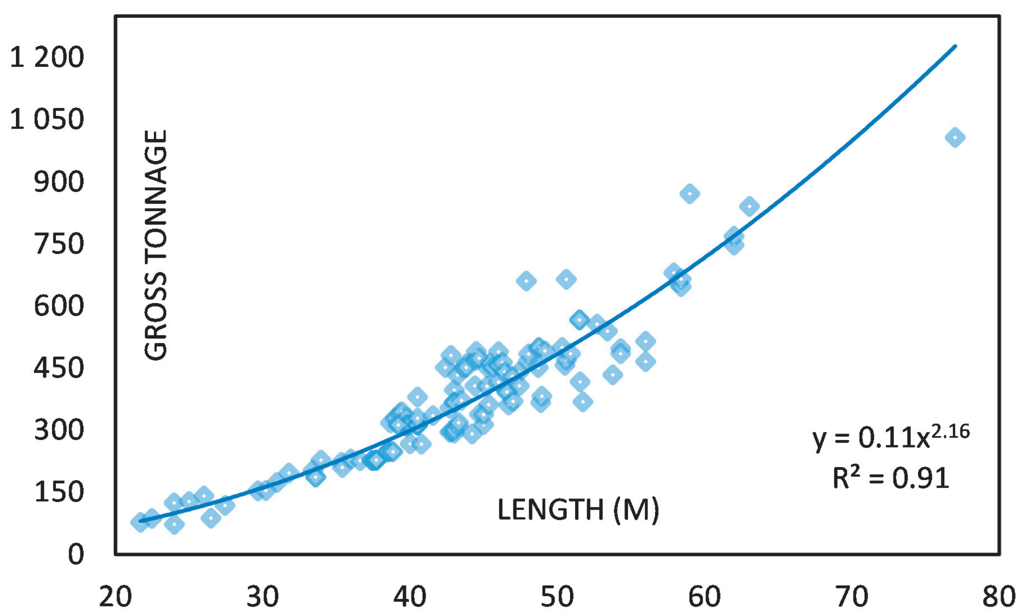

Figure 5. GT *vs.* L scatter plot and regression equation of for the American-type semi-industrial purse seiners in the Peruvian fleet

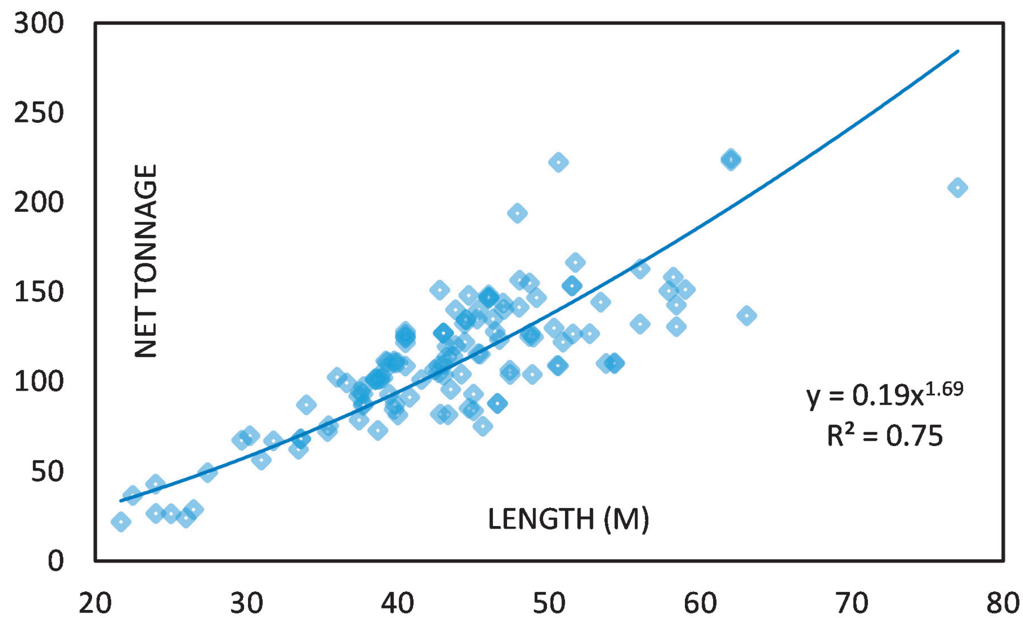

Figure 6. NT *vs.* L scatter plot and regression equation of for the American-type semi-industrial purse seiners in the Peruvian fleet

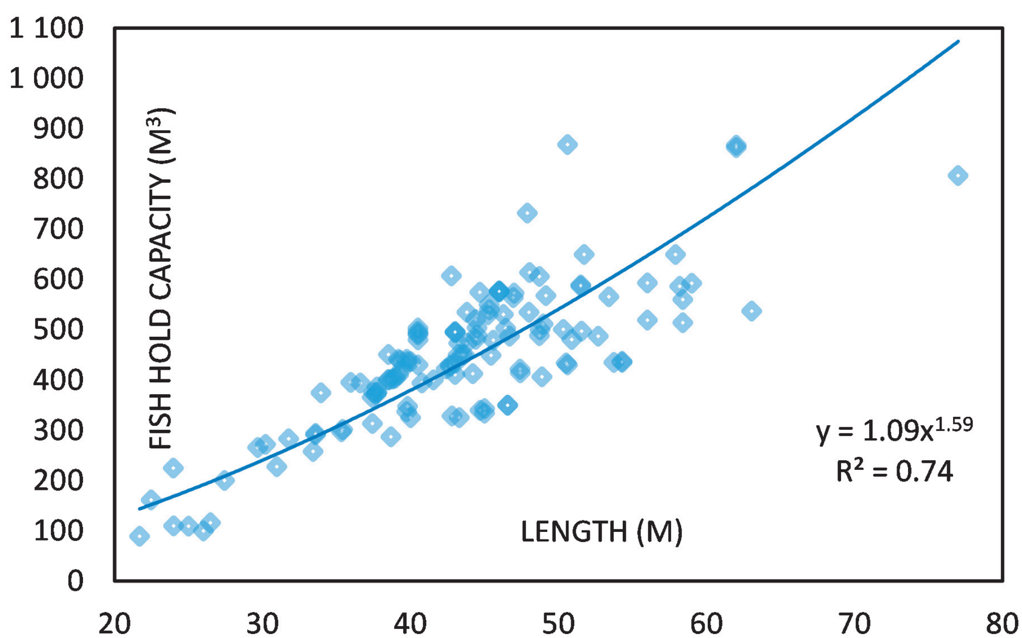

Figure 7. FHC vs. L scatter plot and regression equation of for the American-type semi-industrial purse seiners in the Peruvian fleet

Although L, B, and D strongly influence structural, volumetric, and power-related attributes, the fuel and water capacities of purse seiners are less dependent on the ship's linear dimensions. These tanks are typically sized according to operational requirements—such as desired autonomy, fishing grounds, and mission profile—rather than hull geometry alone. As discussed in standard naval design literature, consumables like fuel and freshwater are mission-driven capacities defined primarily by endurance criteria, propulsion plant characteristics, fuel consumption [21], and the expected operational range, which may vary regardless of the vessel's main dimensions. Therefore, it is reasonable that the fuel and water capacities exhibit weak correlations with L, B, and D in analyzed dataset.

Table IV demonstrates that power capacity, GT, NT, and FHC are strongly dependent on vessel dimensions. Across the three predictors (length, breadth, and depth), these variables consistently show high coefficients of determination ($R^2 \approx 0.64-0.91$) and comparatively low error metrics, with root mean square error (RMSE) and mean absolute error (MAE) values corresponding to their data ranges. This indicates that their scaling behavior is largely governed by hull dimensions. In particular, tonnage measures and the hold capacity follow expected dimensional relationships, while the installed power increases predictably with vessel size, as a consequence of propulsion requirements and hydrodynamic resistance.

In contrast, the fuel and water capacities show very low R^2 values, combined with high RMSE and MAE, regardless of whether L, B, or D is used as the predictor variable. These error patterns demonstrate that the fuel and water capacities are not directly determined by principal dimensions but instead depend on mission-specific, operational, and regulatory factors, which vary regardless of hull scaling. As a result, their variability cannot be captured through simple geometric regression models.

Table IV. Power-law regression coefficients and error metrics (RMSE, MAE) for principal vessel attributes regressed against length, breadth, and depth

	Length (m)		**Breadth (m)**		**Depth (m)**	
	RMSE	**MAE**	**RMSE**	**MAE**	**RMSE**	**MAE**
Power (kW)	237.52	171.21	203.82	157.86	226.51	174.68
Fuel (gal)	9660.40	6326.25	9117.37	5927.89	8967.28	5795.70
Water (gal)	5459.11	3241.92	5439.20	3194.88	5345.40	3149.84
Net tonnage	23.92	18.62	21.18	16.85	19.85	14.18
Gross tonnage	62.20	45.42	85.43	58.26	98.48	70.29
FHC (m^3)	88.97	69.79	78.07	61.55	70.85	52.13

3.3 Model validation results

A statistical validation of the power-law models was performed to assess the three classical regression assumptions: (i) error normality, (ii) homoscedasticity, and (iii) residuals independence. The Shapiro-Wilk test was used for normality, the Breusch-Pagan test for homoscedasticity, and the Durbin-Watson statistic for independence.

The results indicate that residuals normality is not strictly satisfied for any of the variables. This does not affect the validity of the models, since normality is required for parametric inference rather than for predictive relationships, and power regressions in naval architecture are not typically used for hypothesis testing. For example, [22] and [23] use power regressions for predictions but not for hypothesis testing. Residuals independence was confirmed for all variables, with Durbin-Watson values close to 2.0. Heteroscedasticity was more pronounced for the fuel and water capacities, which is consistent with their weaker geometric dependence.

4. Discussion

The methodological approach adopted in this study is intentionally simple, relying on classical potential regressions that ensure interpretability and direct use in the concept ship design stage. The innovation, therefore, does not reside in the statistical technique itself, but in the development of updated, vessel-specific regression formulas for American-type semi-industrial purse seiners, a category for which systematic design data are largely absent. By integrating a recent fleet-wide database and benchmarking the resulting regressions against existing formulations in the literature, this study provides a refined and more accurate set of predictive relationships. These results aid in closing a documented gap in design knowledge and offer practical benefits for naval architects working with this class of fishing vessels.

4.1 Modern statistical techniques

Although modern statistical and machine learning-based techniques—such as multiple regression, artificial neural networks, or ensemble-based models—can offer predictive improvements, their use is not a standard requirement in ship *concept* design. At this early stage, naval architects rely primarily on low-dimensional empirical relationships derived from hull statistics, where proportionality laws, geometric similarity, and scaling behavior dominate the governing trends. The foundational literature emphasizes the long-established use of simple models for estimating ship main particulars and attributes, given their interpretability, robustness, and compatibility with classical naval architecture principles [19], [25]. Moreover, conceptual design decisions typically require transparent and physically meaningful formulations that can be applied quickly during iterative design loops, which favors simple power-law regressions over more complex black-box approaches [10]. Therefore, our use of simple regression methods aligns with standard and widely accepted practices in preliminary ship design.

4.2 Model validation

Power-law regression models of the form $Y = aX^b$ were estimated using log-log linear regression, following the standard procedure adopted in preliminary ship design tools. After fitting the models, their performance was assessed by means of the R^2, the RMSE, and the MAE on the original scale of the variables. For the main design attributes (power, GT, NT, and FHC), the resulting models exhibited moderate to high goodness of fit, with R^2 values ranging from approximately 0.64 to 0.91 and error levels compatible with the accuracy that is typically expected during the conceptual design stage. In addition, the residuals were inspected to check for systematic patterns, revealing no clear structural bias with respect to the predictor and indicating that the power-law form is adequate for capturing the dominant trends in the data. In contrast, the models for fuel and water capacity exhibited very low R^2 values and comparatively high dispersion, confirming that these attributes are poorly explained by principal dimensions alone and should be used with caution.

These validation steps confirm that power-law regressions are suitable as first-order predictors for key volumetric and tonnage attributes, while also highlighting the limitations of simple models for range-related variables such as fuel and water capacity.

4.3 Assessment of scaling models for preliminary design parameters

In addition to the classical power model $y = ax^b$, a nonlinear regression was also performed using the extended formulation, *i.e.*, $y = ax^b + c$, following the approach employed by [26]. Although this model introduces an additional degree of freedom, the estimated constant c resulted in a large negative value, revealing two issues:

i. The parameters lose physical interpretability, as the model predicts unrealistic offsets for small values of the independent variable.

ii. The constant term acts as a numerical compensator instead of representing a meaningful contribution to the vessel's geometric or scaling behavior.

Conversely, the classical power-law model produced stable coefficients and a monotonic trend consistent with well-established naval architectural scaling patterns [20], where hull-related attributes often follow proportionality laws of the form $y \propto x^b$. The absence of a constant term also preserves the log-linear transformability of the model, ensuring statistical robustness and allowing direct utilization in preliminary design contexts. Therefore, the power model $y = ax^b$ is considered to be an appropriate and physically meaningful representation for the analyzed characteristics.

4.4 Comparison with previous studies

Table V presents the estimated regression equations, derived from the database and formulations found in the literature [10], [11], for *power, FHC, and GT*. Figs. 8-10 compare the regression formulas for FHC from this study's database against those from [10]. For all dimension ranges, FHC's dependence on B and D follows a similar trend in both regressions. However, for L values exceeding 35 m, the estimated and referenced regressions for FHC exhibit two different trends. The database in [10], which included ships up to 130 m and 400 000 ft^3, yields a regression equation that overestimates values for the shorter vessels in our database. Fig. 11 shows that the estimated formulation for GT *vs.* L fits the present database well, but the equation in [11] overestimates the values of of GT when L is greater than 35 m. Fig. 12 shows that the equations in [10] and [11] can overestimate power values, but our regression equation provides a good approximation across all dimension ranges. Therefore, the regression equations for the analyzed database yield more precise estimations. Table VI reports the calculated R^2 for FHC, GT and power as a functions of ship dimensions. Although the R^2 values of the cited regression equations are higher than those of our database—except *FHC*=f(*D*)—, our estimated regression equations are appropriate for predicting the ship attributes of American-type semi-industrial purse seiners.

Table V. Comparison of estimated formulas of attributes of semi-industrial purse seiners

Present Database	Units	Papanikolau [10]	Bin *et al.* [11]
Power = $3.44 \cdot L^{1.48}$	kW *vs.* m	Power=$65.945 \cdot L_{pp}$ - 1266.22	Power=$50.19 \cdot L$-971
FHC = $38.40 \cdot L^{1.59}$	ft^3 *vs.* m	FHC = $7.9873 \cdot L_{pp}^{2.0778}$	
FHC = $56.33 \cdot B^{2.55}$	ft^3 *vs.* m	FHC = $15.144 \cdot B^{3.0943}$	
FHC = $329.68 \cdot D^{2.57}$	ft^3 *vs.* m	FHC = $774.89 \cdot D^{1.9626}$	
GT = $0.11 \cdot L^{2.16}$	GT *vs.* m		GT = $0.0057 \cdot L^{2.994}$

Table VI. Comparison of the R^2 values for the attributes of semi-industrial purse seiners

R^2	Power=f(L)	FHC=f(B)	FHC=f(D)	FHC=f(L)	GT=f(L)
Our database	0.68	0.67	0.74	0.74	0.91
Papanikolaou [10]	0.8481	0.8001	0.6557	0.8059	---
Bin *et al.* [11]	0.6929	---		---	0.9613

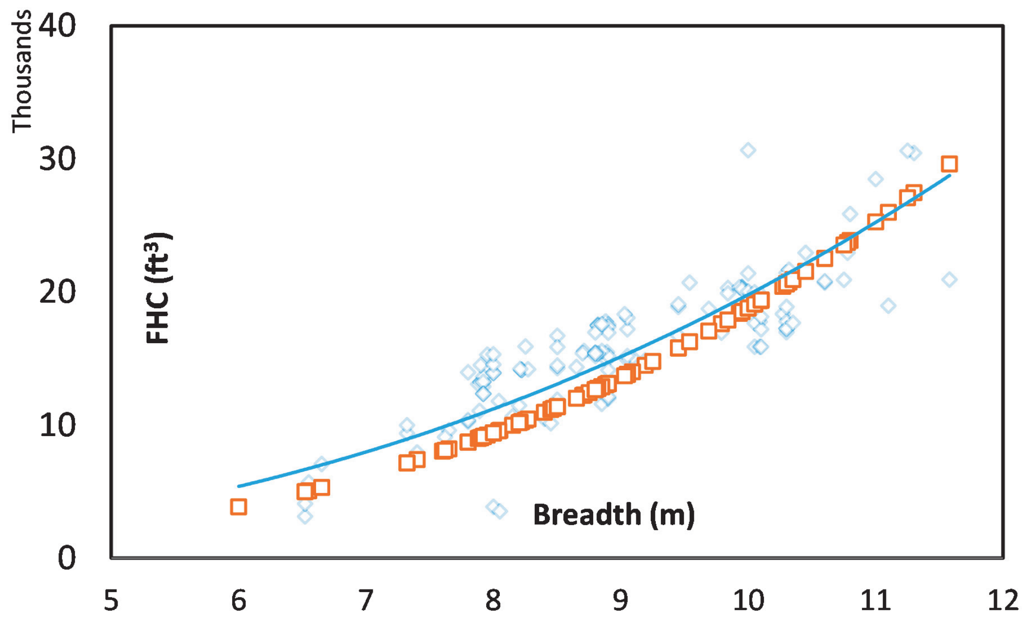

Figure 8. FHC *vs.* B comparison against previous studies. The blue line corresponds to our database, and the orange points to [10].

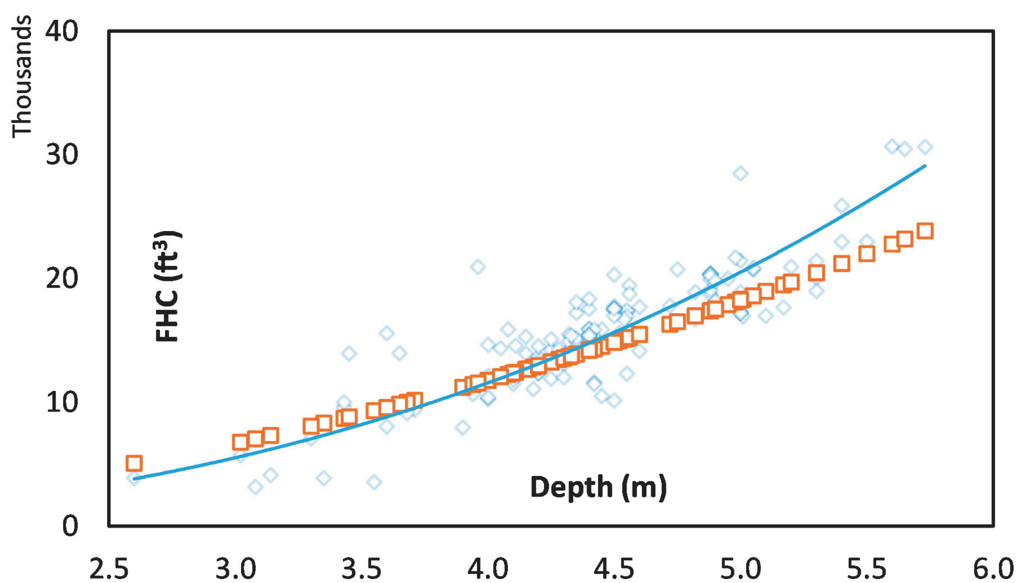

Figure 9. FHC *vs.* D comparison against previous studies. The blue line corresponds to our database, and the orange points to [10].

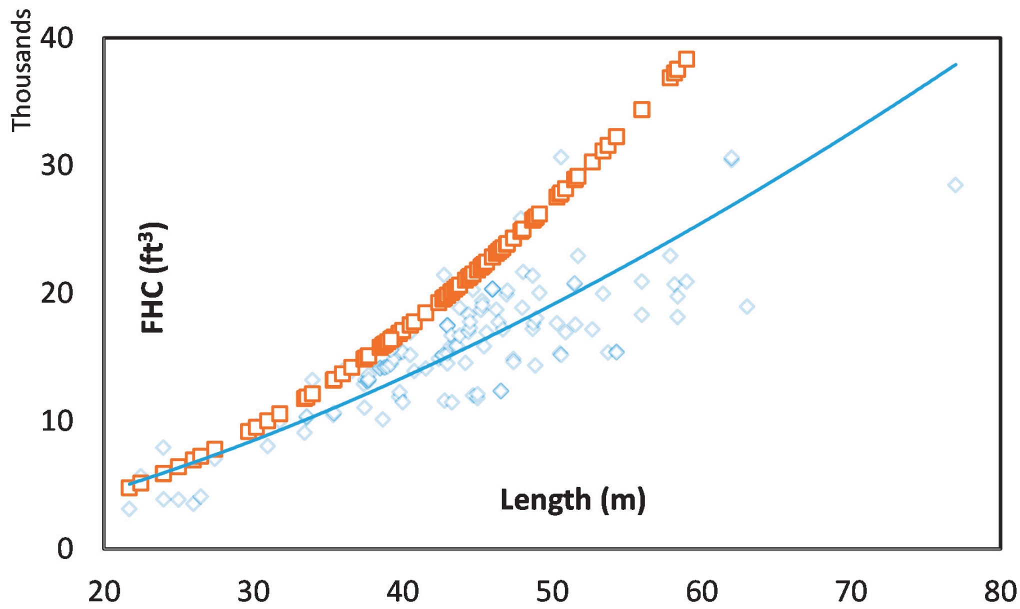

Figure 10. FHC *vs.* L comparison against previous studies. The blue line corresponds to our database, and the orange points to [10].

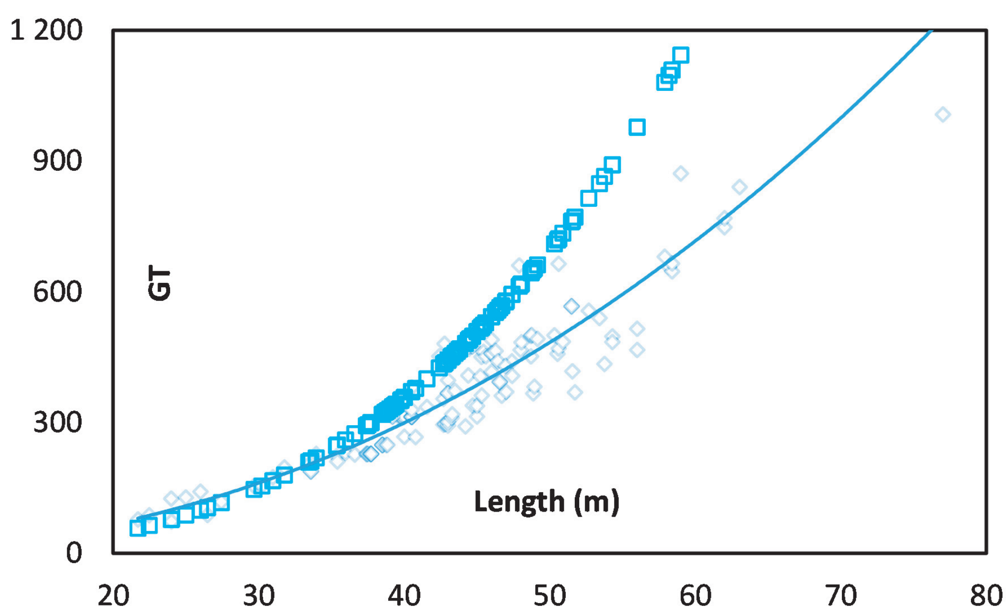

Figure 11. GT *vs.* L comparison against previous studies. The blue line corresponds to our database, and the orange points to [11].

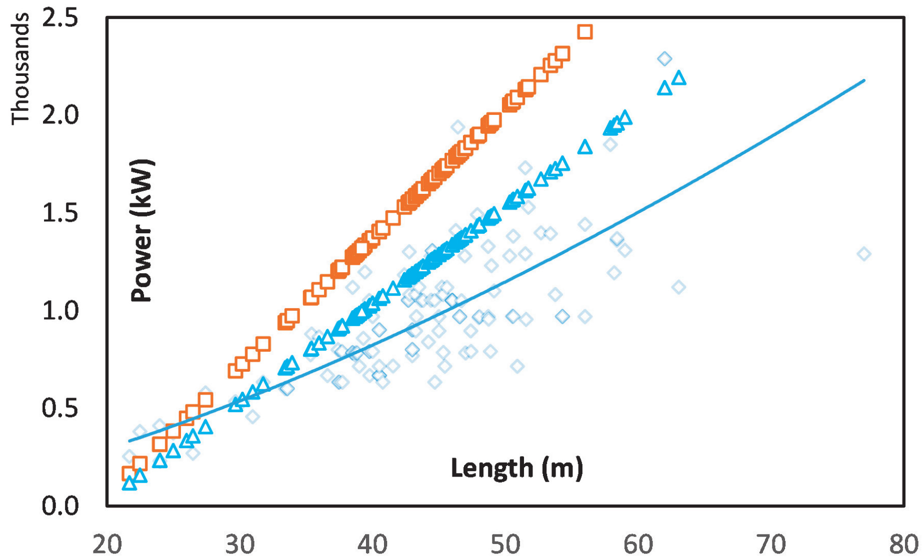

Figure 12. Power comparisons against previous studies. The blue line corresponds to our database, the orange points to [10], and the light blue points to [11].

The results of our regression analysis show that, when previously published formulas [10], [11] are applied to our dataset of Peruvian American-type semi-industrial purse seiners with RSW systems, the predicted key attributes are systematically higher than observed. This discrepancy can be attributed to the differences in the underlying populations: earlier works utilized broader fishing-vessel fleets, encompassing diverse gear types and operational profiles, whereas our dataset was limited to a highly specialized vessel class with distinct operational requirements and design optimizations (*e.g.*, mid-size RSW purse seiners). Therefore, the over-estimation is not indicative of a methodological error, but rather of the need to derive tailored regression models for specific vessel populations. These findings emphasize the value of focused empirical datasets in ship design regressions and the potential limitations faced when generalizing from broader fleets.

5. Conclusions

Designers can use the median for all linear dimensions and attributes during the early design of American-type semi-industrial purse seiners with an RSW systems. Although the medians and means of L, B, and D are close, statistically, B is the variable with the closest distribution to normality.

The Peruvian fishing fleet, specifically when it comes to American-type semi-industrial purse seiners with an RSW system, ranges from about 33 to 55 m in length, 8.8 to 9.2 m in breadth, 4.4 to 4.6 m in depth, 750 to 1250 kW, 8000 to 11 000 gal fuel capacity, 1000 to 5000 gal fuel capacity, 300 to 500 GT, 100 to 120 NT, and 300 to 500 m^3 FHC. Ships with lengths over 60 m, installed power over 1500 kW, fuel capacity over 20 000 gal, and water capacity over 9000 gal would belong to another category of ships: larger purse seiners with a tall tower to spot tuna or industrial purse seiners.

The combined interpretation of the RMSE, MAE, and R^2 confirms that the power-law regressions provide reliable estimations for GT, NT, FHC, and power. The fuel and water capacities exhibit very high RMSE and MAE values and should therefore be used with caution, as they are not primarily governed by geometric scaling.

The regression models developed in this study are specifically tailored to American-type semi-industrial purse seiners with RSW, a vessel class of high regional relevance. Because they are derived from a homogeneous and representative dataset, these models provide more accurate early-design predictions than some broader formulas in the literature. Their application supports more reliable dimensioning and capacity estimation in the conceptual design stage of this type of fleet.

In light of the present findings, our proposal for incorporating artificial intelligence and other advanced predictive techniques arises directly from the limitations identified in this analysis. Attributes such as the fuel and water capacity exhibited low determination coefficients under classical power-law regression, suggesting that their behavior may depend on nonlinear or multi-factor interactions not captured by single-dimension predictors. This motivates the exploration of data-driven approaches—such as multiple regression, robust regression, or machine learning models—to assess whether these methods can better represent complex operational or design dependencies. Thus, the recommendation for future integration of said techniques is not external to the study; it emerges naturally from the statistical patterns and modeling gaps observed in the analyzed dataset.

6. Acknowledgements

We would like to thank the Vice-Rectorate for Research of Universidad Nacional de Ingeniería, Lima, Peru, as well as the reviewers for their helpful comments.

7. Author contributions

Dennys de la Torre: conceptualization, methodology, data curation, writing (original draft)
Dheybi Cervan: visualization, research, revision.

8. Funding

This research received no external funding.

9. Data availability

The data will be made available upon request.

10. Conflict of interest

The authors declare that they have no known competing financial interests or personal relationships that could have appeared to influence the work reported in this paper.

11. Use of artificial intelligence

During this work, the authors did not employ any technologies associated with artificial intelligence.

References

[1] B. Rinauro, E. Begovic, F. Mauro, and G. Rosano, "Regression analysis for container ships in the early design stage," *Ocean Eng.*, vol. 292, art. 116499, Jan. 2024, https://doi.org/10.1016/j.oceaneng.2023.116499

[2] A. Lepore, L. Mocerino, B. Palumbo, E. Rizzuto, E. Rossi, and L. Vitiello, "A supervised statistical learning approach to the preliminary design of cruise ship Gross Tonnage," *Appl. Ocean Res.*, vol. 143, art. 103837, Feb. 2024, https://doi.org/10.1016/j.apor.2023.103837

[3] T. Cepowski and P. Chorab, "Determination of design formulas for container ships at the preliminary design stage using artificial neural network and multiple nonlinear regression," *Ocean Eng.*, vol. 238, art. 109727, Oct. 2021, https://doi.org/10.1016/j.oceaneng.2021.109727

[4] D. de la Torre, "Effect of ship size on the hull dimension ratios of purse seiners," *Ing. Investig.*, vol. 45, no. 1, art. e116364, 2025, https://doi.org/10.15446/ing.investig.116364

[5] M. Kalajdžić and N. Momčilović, "A step toward the preliminary design of seagoing multi-purpose cargo vessels," *Brodogradnja*, vol. 71, no. 2, pp. 75–89, Jun. 2020, https://doi.org/10.21278/brod71205

[6] S. Gurgen, I. Altin, and M. Ozkok, "Prediction of main particulars of a chemical tanker at preliminary ship design using artificial neural network," *Ships Offshore Struct.*, vol. 13, no. 5, pp. 459–465, Jul. 2018, https://doi.org/10.1080/17445302.2018.1425337

[7] X. Peng, H. Lei, and W. Zhong, "Research on estimation method of gross registered tonnage of ships in Grand Canal," in *Modeling Risk Management for Resources and Environment in China*, First., D. D. Wu and Y. Zhou, Eds., Berlin, Heidelberg: Springer Berlin Heidelberg, 2011, pp. 101–108, https://doi.org/10.1007/978-3-642-18387-4

[8] D. G. . M. Watson, *Practical ship design*, vol. 1. Oxford: Elsevier Science LTD, 1998.

[9] S&P Global, "IHS Fairplay World Shipping Encyclopedia version 12.01," 2011. [Online]. Available: https://www.spglobal.com/marketintelligence/en/mi/products/maritime-portal-desktop.html

[10] A. Papanikolaou, *Ship design. Methodologies of preliminary design*, 1st ed. Dordrecht: Springer Netherlands, 2014, https://doi.org/10.1007/978-94-017-8751-2

[11] H. Bin, L. Xiuwen, and R. Yuqing, "Statistics and analysis of main parameters of ocean fishing vessels in China," in *2020 5th Int. Conf. Electromech, Control Tech. Trans. (ICECTT)*, IEEE, May 2020, pp. 594–598, https://doi.org/10.1109/ICECTT50890.2020.00135

[12] O. E. Surov, M. V. Kitaev, E. E. Solovieva, V. A. Veselov, and D. V. Tyuftyaev, "Analysis of main dimensions and characteristics of fishing vessels," *Russ. J. Water Transp.*, vol. 2, no. 72, pp. 41–53, Sep. 2022, https://doi.org/10.37890/jwt.vi72.273

[13] Ministerio de la Producción, Gobierno del Perú, "Embarcaciones pesqueras." [Online]. Available: https://consultasenlinea.produce.gob.pe/ConsultasEnLinea/consultas.web/embarcacion

[14] Dirección General de Capitanías y Guardacostas del Perú, "Consulta datos de la nave." [Online]. Available: https://www.dicapi.mil.pe/consultas/naves-artefactos-navales

[15] H. M. Gaspar, "Data-driven ship design," in *17th Int. Conf. Comput. IT Appl. Marit. Ind.*, 2015, pp. 426–439. http://www.shiplab.hials.org/wp-content/uploads/2019/05/40_Gaspar.pdf

[16] L. J. C. Valerio Mena, V. N. Acosta Pastor, and V. A. Loarte Vicuña, "Determinación numérica de la resistencia al avance de buques," *TECNIA*, vol. 9, no. 2, pp. 61–68, Dec. 1999, https://doi.org/10.21754/tecnia.v9i2.324

[17] N. Hamlin, "Ship geometry," in *Principles of Naval Architecture*, 2nd ed., vol. I, E. V. Lewis, Ed. Jersey City, NJ, USA: The Society of Naval Architects and Marine Engineers, 1988, p. 19.

[18] B. Tibbitts, "Naval surface ships," in *Ship Design and Construction*, T. Lamb, Ed. Jersey City, NJ, USA: The Society of Naval Architects and Marine Engineers, 2003, pp. 28_1-28_11.

[19] J. Fox, *Applied regression analysis & generalized linear models*, 3rd ed. Thousand Oaks, CA, USA: SAGE Publications, 2016.

[20] D. Doane and L. Seward, *Applied statistics in business and economics*, 3rd ed. New York: McGraw-Hill, 2011.

[21] N. Bialystocki and D. Konovessis, "On the estimation of ship's fuel consumption and speed curve: A statistical approach," *J. Ocean Eng. Sci.*, vol. 1, no. 2, pp. 157–166, Apr. 2016, https://doi.org/10.1016/j.joes.2016.02.001

[22] H. Schneekluth and V. Bertram, *Ship design for efficiency and economy*, 2nd ed. Oxford, UK: Butterworth-Heinemann, 1998.

[23] C. B. Barrass, *Ship design and performance for masters and mates*. Oxford, UK: Elsevier Butterworth-Heinemann, 2004.

[24] P. Gale, "Concept design," in *Ship Design and Construction*, J. Lamb, Ed. Jersey City, NJ, USA: The Society of Naval Architects and Marine Engineers, 2003, pp. 5–9.

[25] K. Rawson and E. Tupper, *Basic ship theory. Vol. I*, 5th ed. Oxford, UK: Butterworth-Heinemann, 2001.

[26] M. L. Hakim, B. Nugroho, I. K. Suastika, and I. K. A. P. Utama, "Alternative empirical formula for predicting the frictional drag penalty due to fouling on the ship hull using the design of experiments (DOE) method," *Int. J. Technol.*, vol. 12, no. 4, art. 829, Oct. 2021, https://doi.org/10.14716/ijtech.v12i4.4692

Dennys De La Torre

He received a Naval Engineering degree from Universidad Nacional de Ingeniería, Lima, Peru, in 2004. He is a MSc in Investment Projects from the same university, as well as a PhD in Energy. He is a professor of ship dynamics with more than 15 years of teaching experience. He has experience in projects on board oil platforms and national and international shipyards. He is the manager of a boat design company and a research professor of the Vice-Rectorate of Research of Universidad Nacional de Ingeniería (lines of research: wave energy and ship dynamics).

Email: ddelatorrec@uni.edu.pe

Dheybi Cervan

He received his Mechanical-Electrical Engineering degree from Universidad Nacional de Ingeniería, Lima, Peru, as well as a MSc and PhD in Sciences with a mention in Energy. His main research interests include power systems reliability, data science, and artificial intelligence applications for industrial systems. He is a consultant with ten years of experience who provides specialized services to various companies and organizations in Peru's electrical and energy sectors. He is currently qualified as a researcher by CONCYTEC (National Council for Science, Technology and Technological Innovation). Additionally, he has teaching experience in Master's programs in Energy and Maintenance Engineering.

Email: dcervanp@uni.pe

UNIVERSIDAD DISTRITAL
FRANCISCO JOSÉ DE CALDAS

Ingeniería

https://revistas.udistrital.edu.co/index.php/reving/issue/view/1320

DOI: https://doi.org/10.14483/23448393.24130

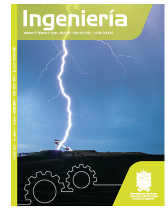

Research

R-SWARA and COPRAS Integration for Evaluating Third-Party Logistics Providers

Integración de R-SWARA y COPRAS para la evaluación de proveedores logísticos externos

Adhie Prayogo[1], and M. Mujiya Ulkhaq[2]

[1]Department of Industrial Engineering, Faculty of Engineering, Universitas Muria Kudus (Kudus, Indonesia)
[2]Department of Industrial Engineering, Faculty of Engineering, Diponegoro University (Semarang, Indonesia)

Abstract

Context: Evaluating third-party logistics (3PL) providers is a complex task since multiple criteria assessed by experts with potentially diverse perspectives are involved, leading to varying scores based on individual prioritizations. This study attempts to evaluate 3PL providers for a mid-sized fishery company in Jakarta, Indonesia, focusing on refrigerated transportation within cold chain logistics.

Method: A methodology integrating rough stepwise weight assessment ratio analysis (R-SWARA) and complex proportional assessment (COPRAS) is employed to address expert uncertainty and rank six providers based on seven criteria: security, punctuality, cost, delivery area, customer service, assurance, and logistics experience. R-SWARA assigns weights using rough set intervals, while COPRAS ranks providers.

Results: The integrated methods yield Vendor A as the top choice, with a utility degree of 100%, followed by Vendor D and others ranging from 96.7 to 98.4%. These rankings highlight the critical role of punctuality and security in refrigerated transportation, aligning with the fishery industry's need to ensure product freshness and reliability. A sensitivity analysis that varies the weight of punctuality by ± 20% confirms the ranking's stability, highlighting the methodology's robustness. The findings align with prior studies emphasizing performance and quality in logistics, while R-SWARA's use of intervals offers a novel approach to handling uncertainty.

Conclusions: The proposed method recommends Vendor A to ensure timely and secure seafood delivery, with implications for perishable goods logistics. The limitations include a small expert panel and a single-case focus, suggesting the need for future research with larger samples and broader applications. Another limitation of the proposed approach is its reliance on expert judgement for criteria weighting, as well as its sensitivity to the selected criteria and case context. Therefore, the findings should be interpreted as a decision support rather than universal rankings.

Keywords: third-party logistics, R-SWARA, COPRAS, multi-criteria decision-making, fishery industry, vendor selection

Article history

Received:
September 21st, 2025

Modified:
December 6th, 2025

Accepted:
February 25th, 2026

Ing, vol. 31, no. 1, 2026, e24130

* Correspondence: adhie.prayogo@umk.ac.id

Resumen

Contexto: Evaluar proveedores de logística tercerizada (3PL) es una tarea compleja, pues involucra múltiples criterios evaluados por expertos con perspectivas potencialmente diversas, lo que conduce a puntuaciones variables según las priorizaciones individuales. Este estudio busca evaluar proveedores 3PL para una empresa pesquera de tamaño medio en Yakarta, Indonesia, con enfoque en el transporte refrigerado dentro de la logística de cadena de frío.
Método: Se emplea una metodología que integra el análisis de razón de evaluación de pesos por etapas aproximado (R-SWARA) y la evaluación proporcional compleja (COPRAS) para abordar la incertidumbre de los expertos y clasificar seis proveedores en función de siete criterios: seguridad, puntualidad, costo, área de entrega, servicio al cliente, garantía y experiencia logística. R-SWARA asigna los pesos mediante intervalos de conjuntos aproximados, mientras que COPRAS clasifica a los proveedores.
Resultados: Los métodos integrados sitúan al Proveedor A como la mejor opción, con un grado de utilidad del 100 %, seguido del Proveedor D y otros, con valores que oscilan entre 96.7 y 98.4 %. Estas clasificaciones destacan el papel fundamental de la puntualidad y la seguridad en el transporte refrigerado, en concordancia con la necesidad de la industria pesquera de garantizar la frescura y confiabilidad del producto. Un análisis de sensibilidad que varía el peso de la puntualidad en ± 20 % confirma la estabilidad de la clasificación, subrayando la robustez de la metodología. Los hallazgos coinciden con estudios previos que enfatizan el desempeño y la calidad en la logística, mientras que el uso de intervalos de R-SWARA ofrece un enfoque novedoso para el manejo de la incertidumbre.
Conclusiones: El método propuesto recomienda al Proveedor A para garantizar una entrega de comida marina que sea oportuna y segura, con implicaciones para la logística de bienes perecederos. Las limitaciones incluyen un panel reducido de expertos y el enfoque en un solo caso, lo que sugiere la necesidad de futuras investigaciones con muestras más amplias y aplicaciones más generales. Otra limitación del enfoque propuesto es su dependencia del juicio experto para la ponderación de criterios, así como su sensibilidad a los criterios seleccionados y al contexto del caso. Por lo tanto, los hallazgos deben interpretarse como un apoyo a la toma de decisiones más que como clasificaciones universales.

***Palabras clave*:** logística tercerizada, R-SWARA, COPRAS, toma de decisiones multicriterio, industria pesquera, selección de proveedores

Contents

1. Introduction

Efficient logistics are the backbone of modern supply chains, but selecting the right third-party logistics (3PL) provider remains a critical challenge in competitive markets. Industries increasingly focus on boosting productivity while maintaining operational efficiency by partnering with reliable suppliers, vendors, and service providers [1]. This strategy allows companies to concentrate on core activities while delegating critical support functions (*e.g.*, transportation) to specialized experts [2], [3]. Transportation is vital for ensuring timely, cost-effective, and customer-aligned delivery of goods. Given its complexity and significance, many industries opt for 3PL providers to manage distribution [4]. Benefits like cost reduction, operational flexibility, and access to advanced technology and expertise further drive the adoption of 3PL strategies [5], [6].

Selecting an appropriate 3PL provider requires thorough analysis to avoid potential setbacks [7]. Organizations must first identify key criteria aligned with their operational priorities before evaluating vendors [8]. Previous studies highlight diverse criteria tailored to specific industries. For instance, [9] proposed criteria for fast-moving consumer goods (FMCG), including the freight cost per kilometer, fleet capacity, vehicle quality, driver quality, order acceptance rate, distance target achievement, flexibility, on-time delivery, financial strength, customer support, and training and development. [10] identified six criteria for 3PL selection in the oil and gas industry through expert interviews: cost, performance, services, intangible factors (*e.g.*, brand reputation and relationship trust), quality assurance, and IT systems. Similarly, [11] emphasized logistics costs, responsiveness, location, information technology, and service quality for FMCG 3PL providers. Cost and service quality are universal criteria, while industry-specific factors like flexibility in FMCG or intangible factors in oil and gas reflect distinct operational needs.

Evaluating 3PL providers is a complex task since multiple criteria assessed by experts with potentially diverse perspectives are involved, leading to varying scores based on individual prioritizations [12]. This challenge becomes even more critical in cold chain logistics, where delays and service failures can directly affect product freshness and quality, and where expert judgments often involve uncertainty and hesitation. To address this challenge, multi-criteria decision-making (MCDM) approaches employ weighting techniques to systematically evaluate vendors [13]. Several MCDM methods have been applied, including the analytical hierarchy process (AHP) and its extensions [10], [11], [14]–[16], fuzzy AHP [17]–[20], analytical network process (ANP) [21], stepwise weight assessment ratio analysis (SWARA) [22]–[26], decision-making trial and evaluation laboratory (DEMATEL) [12], [27], the preference ranking organization method for enrichment evaluations (PROMETHEE) [28] and a recent hybrid model combining entropy and critic: EC-PROMETHEE [29]. Experts assign scores to criteria, which are then evaluated using weights. To enhance robustness, prior studies have integrated these weighting approaches, with scoring methods such as the technique for order preference by similarity to the ideal solution (TOPSIS) [30]–[33], VIšekriterijumsko KOmpromisno Rangiranje (VIKOR) [14], [30], [34], [35], complex proportional assessment (COPRAS) [9], [12], [36], multi-objective optimization on the basis of ratio analysis (MOORA) [26], and additive ratio assessment (ARAS) [37], [38]. Combining weighting and scoring methods allows for a better approximation to the complexity of 3PL evaluation in comparison with the use of a single method.

The SWARA method has gained traction for determining criteria importance, but its reliance on precise expert evaluations makes it sensitive to variations, with imprecise or less knowledgeable opinions introducing vagueness [36], [39]. Recent systematic reviews and field assessments of MCDM methods highlight a growing trend towards hybrid framework for overcoming uncertainty and subjectivity [40], [41]. To address this, rough set theory has been integrated, using interval data with upper and lower bounds to account for uncertainty and reduce bias, unlike single-value assessments in traditional SWARA. This is called *R-SWARA* [13]. While prior studies often overlook expert uncertainty, this study advances 3PL evaluation by integrating R-SWARA with COPRAS.

To apply the proposed method, this study evaluates 3PL providers for a mid-sized fishery in Indonesia, focusing on refrigerated transportation to ensure product freshness in cold chain logistics. R-SWARA is employed to rank criteria assessed by experts, with rough set theory mitigating judgment uncertainty to enhance decision robustness. The COPRAS method then ranks vendors based on these weighted criteria. This technique was selected for its comprehensive ranking of alternatives and its ability to balance trade-offs across all criteria, including those of lower weight, which is critical in logistics systems. In comparison with TOPSIS and VIKOR, which require calculating the distance from the ideal solution, COPRAS allows the normalized criterion values to be multiplied directly by the corresponding rough weight without defuzzification, ensuring an uncertainty structure throughout the process. The utility degree in COPRAS also supports decision-makers in directly comparing overall performance levels, unlike PROMETHEE, with outranking flows from the pairwise comparisons. Our integrated methodology offers a replicable framework for industries requiring precise 3PL selection under uncertainty, such as perishable goods logistics.

The originality of this study lies in the proposed integration of R-SWARA and COPRAS into a single evaluation framework to support provider selection under uncertainty in the cold chain logistics sector. Specifically, R-SWARA is used to derive criteria weights while accommodating uncertainty in expert judgements, and COPRAS is then applied to generate an interpretable utility-based ranking across alternatives using both benefit and cost criteria. In addition, a sensitivity analysis is performed to examine the stability of the ranking with respect to changes in key criteria weights, strengthening the robustness of the proposed decision support approach. This combined approach provides transparent, decision-oriented prioritization for the studied context.

This paper is structured as follows. Section 2 reviews the proposed method, detailing the R-SWARA and COPRAS methods and their integration. Section 3 presents the case study, including data collection from experts and criteria selection for the fishery industry. The result of the case study is also provided in this section. Section 4 discusses findings and conclusions, comparing them to prior studies and addressing practical implications.

2. Methodology

This section outlines the methodology for evaluating 3PL providers using the R-SWARA-COPRAS integrated approach. Initially, the studied firm conducted a preliminary screening process to eliminate the 3PL providers that did not satisfy its standards, considering the nature of the products being transported—which require safety assurance, on-time delivery, and regulatory compliance. In this vein, the proposed methodology enabled a compensatory decision-making approach to rank the remaining feasible alternatives. The integrated methodology first applied R-SWARA to derive robust criterion weights, accounting for expert uncertainty through rough set intervals. These weights were then used in the COPRAS method to rank 3PL providers based on expert scores. Fig. 1 illustrates the integrated framework based on R-SWARA, COPRAS, and sensitivity analysis. This combination leverages R-SWARA's ability to handle subjective judgments and COPRAS's comprehensive ranking, making it suitable for complex logistics decisions. The computational procedures were conducted manually by strictly following the formulations. Repeated calculations and checks were performed to ensure accuracy and consistency.

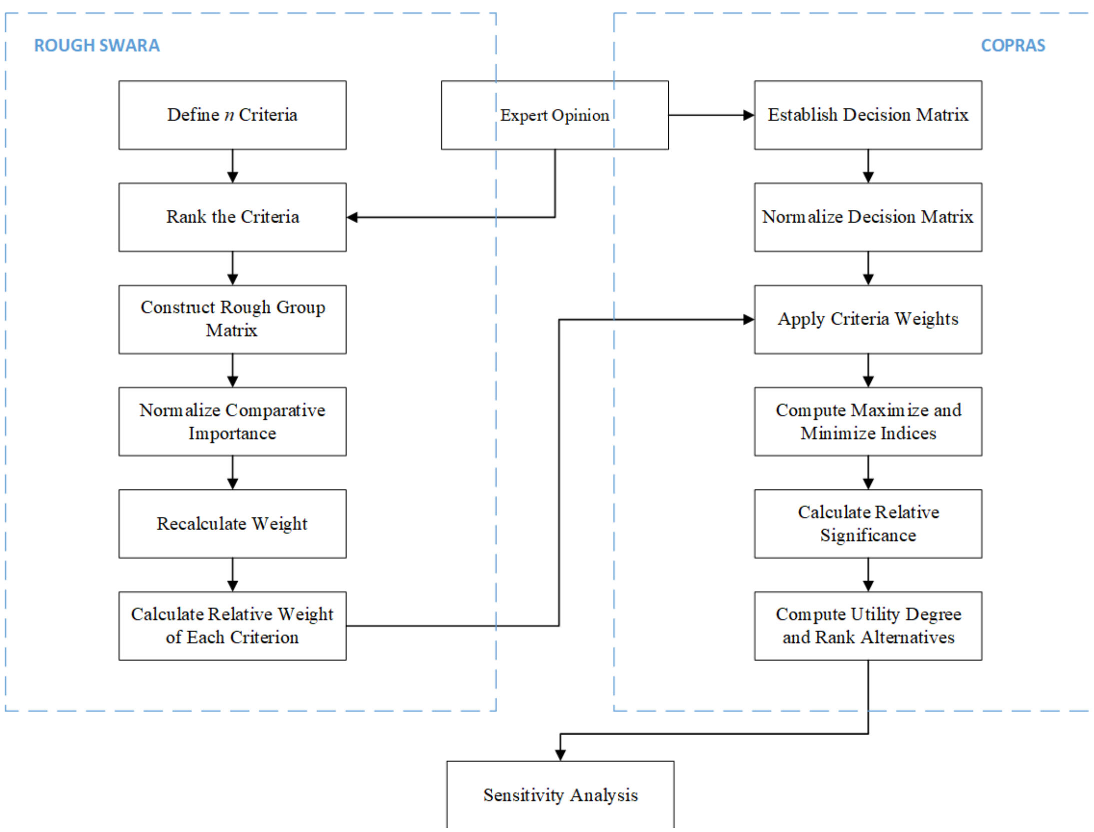

Figure 1. Flow process – R-SWARA and COPRAS

2.1 Phase 1: determining rough criteria weights using the R-SWARA method

SWARA, introduced by [42], allows experts to assign weights to criteria based on their relative importance. Unlike the AHP, SWARA is efficient for group decision-making, requiring experts to rank criteria and estimate their comparative significance. However, SWARA's reliance on precise expert judgments can introduce subjectivity and uncertainty [43]. To address this issue, [43] developed R-SWARA by integrating rough set theory, which uses interval data with upper and lower bounds to handle vague or conflicting subjective opinions. Their study validated R-SWARA in selecting wagons for internal transport, demonstrating a strong correlation with the rough best-worst method (BWM) and rough AHP in sensitivity analysis, thus confirming its robustness.

The R-SWARA method consists of the following steps [43]:

Step 1.1: defining the criteria

Let a set of n criteria be defined as: $C=\{C1,C2,\ldots,Cn\}$.

Step 1.2: ranking the criteria

A group of k experts then provides rankings of the criteria from most to least important. Let r_{ij} denote the ranking value assigned by expert i to criterion C_j.

Step 1.3: constructing a rough group matrix

Since experts may provide different values, each criterion is represented by a rough number (RN) as an interval rather than a single value. For each score r_{ij}, two limits are calculated: (i) the lower limit, which is the average of all scores that are lower than or equal to r_{ij}, and (ii) the upper limit, which is the average of all scores that are greater than or equal to r_{ij}. This is shown in Eqs. (1) and (2), respectively.

$$RN_{lower}=C_j^L=\frac{\sum_{r_{ij}\leq r_{ij}} r_{ij}}{N_L}\#\tag{1}$$

$$RN_{upper}=C_j^U=\frac{\sum_{r_{ij}\geq x_{ij}} r_{ij}}{N_U}\#\tag{2}$$

where N_L and N_U are number of scores lower than or equal to r_{ij} and the number of scores greater than or equal to r_{ij}, respectively. Therefore, for criterion C_j, the rough number is $RN\left(C_j\right)=\left[C_j^L,C_j^U\right]$.

Step 1.4: normalizing comparative importance

Once the rough numbers $RN(C_j)$ have been obtained for each criterion C_j, they are converted into comparative importance values s_j. Formally:

- For the most important criterion (ranked first), the comparative importance is fixed as $s_1 = [1, 1]$. This means that the top-ranked criterion is treated as the reference baseline.
- For every other criterion $j > 1$, the comparative importance is obtained by adding 1 to the rough number interval: $s_j = RN(C_j) + 1$.

Step 1.5: recalculating weights

After obtaining the comparative importance intervals s_j, the next step is to compute the recalculated coefficients q_j as follows:

- For the most important criterion (the reference baseline), the recalculated coefficient is fixed as $q_1 = [1, 1]$.
- For every subsequent criterion $j > 1$, the coefficient is computed iteratively by dividing the previous coefficient by the current comparative importance: $q_j = q_{j-1}/s_j$.

Step 1.6: calculating the relative weights

Once the recalculated coefficients q_j have been obtained, the final step is to normalize them to produce the relative rough weights w_j. This is formally expressed in Eq. (3):

$$w_j = \frac{q_j}{\sum_{i=1}^{n} q_j} \tag{3}$$

where both the numerator and the denominator are intervals, so the division is again performed using interval arithmetic. The normalization ensures that the weights sum to 1. Each $w_j = \left[w_j^L, w_j^U \right]$ $\left[w_j^L, w_j^U \right]$ is the final rough weight interval for criterion C_j, representing its relative importance after accounting for expert disagreement and uncertainty. These rough weights are then applied as inputs in the COPRAS method to evaluate and rank the alternatives under consideration.

2.2 Phase 2: evaluation of alternatives using COPRAS

The COPRAS method, proposed by [44], ranks alternatives by comparing their performance across multiple criteria, distinguishing between beneficial (maximizing) and cost (minimizing) criteria. The integrated R-SWARA-COPRAS method involves the following steps:

Step 2.1: defining alternatives and criteria

Let the alternatives be $A = \{A_1, A_2, \ldots, A_m\}$ and the criteria be $C = \{C_1, C_2, \ldots, C_n\}$. The criteria are partitioned into a beneficial set $J^+ \subseteq \{1, 2, \ldots, n\}$ and a non-beneficial set $J^- \subseteq \{1, 2, \ldots, n\}$, where $J^+ \cap J^- = \emptyset$ and $J^+ \cup J^- = \{1, 2, \ldots, n\}$.

Step 2.2: establishing the decision matrix

A decision matrix $X = \left[x_{ij}\right]_{m\times n}$ $X = \left[x_{ij}\right]_{m\times n}$ is created in which each alternative A_i is evaluated against each criterion C_j. The matrix entries x_{ij} represent expert-assigned performance scores for alternative A_i under criterion C_j. These scores can be individual expert values or aggregated through rough number logic, if multiple expert evaluations per entry are available. In this study, the individual expert scores were aggregated via the simple average.

Step 2.3: normalizing the decision matrix

The decision matrix is normalized to eliminate the influence of differing units across criteria. For each criterion j, the normalized value x_{ij}^* x_{ij}^* is computed using Eq. 4.

$$x_{ij}^* = \frac{x_{ij}}{\sum_{i=1}^{m} x_{ij}} \tag{4}$$

This ensures that each value is expressed as a proportion of the total performance under that criterion.

Step 2.4: applying the criterion weights

Let w_j be the weight of criterion C_j from R-SWARA. Next, the weighted normalized matrix $D = [d_{ij}]$ is defined as shown in Eq. (5)

$$d_{ij} = x_{ij}^* \times w_j \tag{5}$$

Step 2.5: Computing maximizing and minimizing indices

The next step is to separate the contributions of beneficial criteria (the higher the better) and non-beneficial criteria (the lower the better).

- Eq. (6) is used for the beneficial criteria J^+:

$$S_i^+ = \sum_{j\in J^+} d_{ij}, i = 1, 2, \ldots, m \tag{6}$$

- Eq. (7) is used for the non-beneficial criteria J^-:

$$S_i^- = \sum_{j\in J^-} d_{ij}, i = 1, 2, \ldots, m \tag{7}$$

Step 2.6: calculating the relative significance

Once the maximizing and minimizing indices have been calculated, COPRAS combines them into a single measure of performance for each alternative called the *relative significance* Q_i, as defined by Eq. (8)

$$Q_i = S_i^+ + \frac{\sum_{r=1}^{m} S_r^-}{S_i^- \cdot \sum_{r=1}^{m} \left(\frac{1}{S_r^-} \right)} \#(8) \quad (8)$$

Step 2.7: computing the utility degree and ranking the alternatives

Finally, the utility degrees U_i are computed by Eq. (9)

$$U_i = \frac{Q_i}{Q_r} \times 100\% \quad (9)$$

where Q_r is the best (maximum) relative significance among all alternatives. The alternative with the highest utility score (*i.e.*, $U_i = 100\%$) is considered to be the most preferred. Other alternatives are scaled proportionally relative to the most preferred one.

The proposed framework provides structured decision support, but it involves several assumptions and limitations. First, the weighting stage depends on expert judgement; although the method is designed to structure and aggregate these judgements, different expert panels may yield different weights and rankings. Second, the results are sensitive to the definition and operationalization of criteria (including the way in which benefit and cost criteria are specified) and to the quality of the input assessments. Third, the analysis reflects the context of the case and the set of evaluated alternatives. Consequently, the ranking should not be interpreted as universally generalizable beyond the study setting. Finally, as with many MCDM approaches, the method does not fully capture dynamic changes over time (*e.g.*, performance variability or market shocks) unless updated inputs are provided.

3. Results

To apply the proposed method, a case study was conducted to evaluate 3PL providers in the refrigerated transportation sector for a mid-sized fishery in Indonesia. We applied the integrated R-SWARA and COPRAS methodology outlined in Section 2 to select the most suitable 3PL provider who ensured product freshness in cold chain logistics. This case study details the selection of criteria, the expert panel, the data collection process, and the input data, providing the foundation for the analysis presented in Section 4.

3.1 Defining the criteria

The company aims to select a 3PL provider from six candidates (A, B, C, D, E, F) based on criteria tailored to cold chain logistics requirements. Based on the company's operational needs and prior literature [9]–[11], seven criteria were identified for 3PL evaluation:

- *Security (C1)* measures the provider's ability to ensure safe handling and protection of perishable goods against theft, damage, or contamination.
- *Punctuality (C2)* evaluates the provider's reliability in meeting delivery schedules, critical for minimizing spoilage in cold chain logistics.
- *Cost (C3)* assesses the total logistics cost, including transportation and handling fees, as a minimizing criterion.
- *Delivery area (C4)* gauges the provider's coverage and ability to serve diverse geographic markets, including remote regions.
- *Customer service (C5)* reflects the provider's responsiveness and communication quality in addressing client needs and issues.
- *Assurance (C6)* measures the provider's compliance with quality standards (*e.g.*, ISO certifications, cold chain protocols) and reliability guarantees.
- *Logistics experience (C7)* evaluates the provider's expertise and track record in refrigerated transportation for perishable goods.

3.2 Collecting the data

Three experts with extensive experience in fishery logistics were engaged to assess the evaluation criteria and alternative vendors. Although the number of experts was limited, it remained within the range of commonly reported in previous research works, involving panels of three [36], [45], [46], four [47], or five experts [48]–[50]. The three experts in the study possess experience and knowledge related to cold logistic providers (Table I), ensuring a reliable assessment. The data collection process ensured a diversity of perspectives while maintaining consistency through structured questionnaires, and it facilitated discussions to resolve ambiguities. The questionnaire was divided into two main sections. The first section aimed to determine the relative importance of each criterion. The experts ranked the criteria, with a lower score representing the most important and higher score indicating the least important. The result is shown in Table II. The second section focused on the performance evaluation of each 3PL parties. The experts scored the six 3PL providers (A, B, C, D, E, F) regarding each criterion via a 0-100 scale, based on historical performance data, service agreements, and site visits. The result is shown in Table III.

Table I. Expert background

Experts	Position	Work experience
1	Head of logistics division	3 years
2	Head of marketing division	4 years
3	Head of marketing division	4 years

Table II. Result of the ranking

No	Criteria	Weights			
		Expert 1	Expert 2	Expert 3	Average rank
1	C1 security	1	2	2	1.667
2	C2 punctuality	1	1	1	1.000
3	C3 cost	2	1	2	1.667
4	C4 delivery area	2	1	1	1.333
5	C5 customer service	1	2	1	1.333
6	C6 assurance	2	1	2	1.667
7	C7 logistics experience	2	2	2	2.000

Table III. 3PL provider scores

No	Criteria	3PL Provider's Score					
		A	B	C	D	E	F
		From Expert 1					
1	C1 security	91	87	89	88	85	90
2	C2 punctuality	94	85	91	95	93	87
3	C3 cost	90	80	83	89	87	94
4	C4 delivery area	85	89	87	93	94	90
5	C5 customer service	91	87	88	93	92	86
6	C6 assurance	88	90	94	89	87	89
7	C7 logistics experience	90	88	93	86	87	89
		From Expert 2					
1	C1 security	89	83	91	90	88	87
2	C2 punctuality	91	90	87	89	92	84
3	C3 cost	94	86	88	91	90	89
4	C4 delivery area	93	92	91	86	88	94
5	C5 customer service	89	86	86	91	90	87
6	C6 assurance	86	83	91	89	86	94
7	C7 logistics experience	97	89	89	90	91	89
		From Expert 3					
1	C1 security	93	89	87	91	92	90
2	C2 punctuality	89	90	94	86	82	89
3	C3 cost	87	87	86	93	92	91
4	C4 delivery area	94	91	93	88	85	83
5	C5 customer service	89	83	86	89	92	93
6	C6 assurance	94	92	93	91	83	86
7	C7 logistics experience	90	91	87	85	85	88

3.3 Result and discussion

The R-SWARA method was applied to determine the weights of the seven criteria identified. Using the expert ranks from Table I, the criteria were first ranked by averaging the ranks to establish a strict order. The order from the most to the least preferred can be presented as follows: C2 ≻ (C4 and C5; tie) ≻ (C1, C3, C6; tie) ≻ C7. Using Eqs. (1) and (2), the rough numbers for each criterion are calculated. For instance, criteria C4 = {2,1,1} has $\underline{Lim}(1)=1, \underline{Lim}(1)=\frac{1}{3}(2+1+1)=1.33$ and $\underline{Lim}(2)=\frac{1}{3}(2+1+1)=1.33, \underline{Lim}(2)=2$. Thus, $C_4^1=[1.33,2.00]$ and $C_4^2=C_4^3=[1.00,1.33]$. Therefore, $C_4^L=\frac{C_4^1+C_4^2+C_4^3}{n}=\frac{1.33+1.00+1.00}{3}=1.11$ and $C_4^L=\frac{C_4^1+C_4^2+C_4^3}{n}=\frac{2.00+1.33+1.33}{3}=1.55$. Using the same procedure, the rough numbers for each criterion are as follows: RN(C4) = [1.11,1.55], RN(C2) = [1.00,1.00], RN(C5) = [1.11,1.55], RN(C1) = [1.45,1.89], RN(C3) = [1.45,1.89], RN(C6) = [1.45,1.89], RN(C7) = [2.00,2.00]. The normalization of the matrix yielded the following rough numbers for each criterion: RN(C2) = [1, 1], RN(C4) = RN(C5) = [0.55, 0.775], RN(C1) = RN(C3) = RN(C6) = [0.725, 0.945].

Afterwards, the comparative importance (s_2) was set to [1, 1] for C2 and computed as $s_j + 1$ for others. For instance, RN(C4) = [0.55, 0.775] becomes RN(S4) = [1.55, 1.775]. The recalculated weight q_j and the relative weights are then computed using Eq. (3). For C4, $Q_4^L=\frac{1.00}{1.775}=0.563$ and $Q_4^U=\frac{1.00}{1.55}=0.645$. Thus, RN($Q_4$) = [0.563,0,645]. With the same equation, each criterion can be calculated. The result is shown in Table IV. The COPRAS method was then applied to rank the six 3PL providers using the averaged scores from Table III, with cost (C3) as a minimizing criterion and the others as beneficial ones. The normalized decision matrix x_{ij}^* is given in Table V. The results of the weighted normalized decision matrix, relative significance, and utility degrees are presented in Tables VI and VII.

Table IV. Result of the R-SWARA method

No	Criteria	*RN(C_j)*	s_j	q_j	w_j
1	C1 security	[0.725, 0.945]	[1.725, 1.945]	[0.797, 1.029]	[0.113, 0.175]
2	C2 punctuality	[1, 1]	[1, 1]	[1, 1]	[0.142, 0.170]
3	C3 cost	[0.725, 0.945]	[1.725, 1.945]	[0.887, 1.127]	[0.126, 0.192]
4	C4 delivery area	[0.55, 0.775]	[1.55, 1.775]	[0.563, 0.645]	[0.080, 0.110]
5	C5 customer service	[0.55, 0.775]	[1.55, 1.775]	[0.873, 1.145]	[0.124, 0.195]
6	C6 assurance	[0.725, 0.945]	[1.725, 1.945]	[0.887, 1.127]	[0.126, 0.192]
7	C7 logistics experience	[1, 1]	[2, 2]	[0.863, 0.973]	[0.122, 0.166]

Table V. Normalized decision matrix

No	Criteria	A	B	C	D	E	F
1	C1 security	0.171	0.162	0.167	0.168	0.166	0.167
2	C2 punctuality	0.170	0.165	0.169	0.168	0.166	0.162
3	C3 cost	0.170	0.158	0.161	0.171	0.168	0.172
4	C4 delivery area	0.168	0.168	0.168	0.165	0.165	0.165
5	C5 customer service	0.168	0.160	0.163	0.171	0.171	0.166
6	C6 assurance	0.167	0.165	0.173	0.168	0.160	0.168
7	C7 Logistics experience	0.173	0.167	0.168	0.163	0.164	0.166

Table VI. Weighted Normalized Decision Matrix

No	Criteria	A	B	C	D	E	F
1	C1 security	[0.019, 0.030]	[0.018, 0.028]	[0.019, 0.029]	[0.019, 0.029]	[0.019, 0.029]	[0.019, 0.029]
2	C2 punctuality	[0.024, 0.029]	[0.023, 0.028]	[0.024, 0.029]	[0.024, 0.029]	[0.024, 0.028]	[0.023, 0.027]
3	C3 cost	[0.021, 0.033]	[0.020, 0.030]	[0.020, 0.031]	[0.022, 0.033]	[0.021, 0.032]	[0.022, 0.033]
4	C4 delivery area	[0.013, 0.019]	[0.013, 0.019]	[0.013, 0.018]	[0.013, 0.018]	[0.013, 0.018]	[0.013, 0.018]
5	C5 customer service	[0.021, 0.033]	[0.020, 0.031]	[0.020, 0.032]	[0.021, 0.033]	[0.021, 0.033]	[0.021, 0.032]
6	C6 assurance	[0.021, 0.032]	[0.021, 0.032]	[0.022, 0.033]	[0.021, 0.032]	[0.020, 0.031]	[0.021, 0.032]
7	C7 logistics experience	[0.021, 0.029]	[0.020, 0.028]	[0.020, 0.028]	[0.020, 0.027]	[0.020, 0.027]	[0.020, 0.028]

Table VII. Relative significance and utility degrees

No	Alternatives	Q_i	U_i
1	A	[0.141, 0.203]	[100%, 100%]
2	B	[0.136, 0.196]	[96.5%, 96.6%]
3	C	[0.139, 0.200]	[98.5%, 98.6%]
4	D	[0.140, 0.201]	[99%, 99.3%]
5	E	[0.138, 0.199]	[97.9%, 98%]
6	F	[0.139, 0.200]	[98.5%, 98.6%]

As summarized in Table VIII, the findings align with prior studies on 3PL selection, particularly in emphasizing criteria like punctuality and security for perishable goods logistics, in order to ensure product freshness and reliability. The high weight assigned to punctuality underscores its importance in maintaining strict delivery schedules to prevent spoilage, while security reflects the necessity of protecting perishable goods from contamination or damage. For instance, [9] highlighted on-time delivery and vehicle quality as key factors in FMCG logistics, which share similarities with fisheries' cold chain requirements. Similarly, [10] identified performance and quality assurance as critical in the oil and gas industry, supporting the relevance of criteria like assurance (C6) and customer service (C5) in this study. However, unlike the aforementioned studies, which used single-value weights (*e.g.*, via AHP or TOPSIS), the integration of R-SWARA addresses expert subjectivity by incorporating rough set intervals, offering a methodological advancement over traditional approaches. This is consistent with [43], who demonstrated R-SWARA's robustness in handling uncertainty regarding transport-related decisions. The use of COPRAS further complements R-SWARA by providing a comprehensive ranking that balances trade-offs across all criteria, including the minimizing criterion cost (C3), which aligns with the emphasis placed by [11] on cost efficiency in FMCG logistics. The close utility degrees suggest competitive performance among vendors, but the leading provider's dominance reflects its balanced excellence across all criteria, particularly those critical to cold chain logistics.

Table VIII. Comparative table of related works

Study	Application	MCDM Methods	Criteria Emphasis	Uncertainty Modeling
This study	Fishery industry	rough SWARA, COPRAS	cost, assurance, punctuality, customer service	rough set theory
[9]	Fast-moving consumer goods	AHP, data envelopment analysis, COPRAS – G	freight cost/km driver's quality and acceptance rate/order	grey number
[10]	Oil and gas industry	AHP	cost, performance, services	-
[43]	Selection of railway wagons	rough SWARA, rough BWM, rough AHP	price of the wagon, load capacity, maintenance condition, manipulative convenience	rough set theory
[11]	Fast moving consumer goods	AHP	price, service quality	-

3.4 Sensitivity Analysis

To evaluate the robustness of the integrated R-SWARA and COPRAS methods for selecting 3PL providers for a mid-sized fishery in Jakarta, Indonesia, a sensitivity analysis was conducted by varying the weight of the highest-ranked criterion, punctuality (C2), established with a rough weight interval of [0.142, 0.170]. Punctuality was selected due to its critical role in cold chain logistics, as timely delivery is essential to prevent the spoilage of perishable seafood. The midpoint of C2's weight, calculated as (0.142 + 0.170) / 2 = 0.156, was adjusted by ± 20%, resulting in a reduced weight of 0.125 (80% of 0.156) and an increased weight of 0.187 (120% of 0.156). To maintain the normalization requirement (criterion weights must sum to 1), the weight difference of 0.031 was redistributed equally across the six remaining criteria: security ([0.113, 0.175]), cost ([0.126, 0.192]), delivery area ([0.080, 0.110]), customer service ([0.124, 0.195]), assurance ([0.126, 0.192]), and logistics experience ([0.122, 0.166]). In the reduced case, each criterion's midpoint weight increased by approximately 0.005 (0.031/6), whereas, in the increased case, each decreased by 0.005. The COPRAS method was then reapplied, recomputing the weighted normalized matrix, the maximizing and minimizing indices, the relative significance scores, and the utility degrees for the six 3PL providers (A, B, C, D, E, F).

In the reduced weight scenario (C2=0.125), the recalculated utility degrees were approximately as follows: Vendor A at 100%, Vendor D at 99.0%, Vendor C at 98.6%, Vendor F at 98.5%, Vendor E at 98.0%, and Vendor B at 96.9%. The ranking order remained stable (A > D > C > F > E > B), with slight increases in utility degrees for non-top vendors, as the reduced emphasis on punctuality, where Vendor A scored highly with an average of 91.33, slightly narrowed the performance gap. In the increased weight scenario (C2=0.187), the utility degrees were approximately as follows: Vendor A at 100%, Vendor D at

98.7%, Vendor C at 98.3%, Vendor F at 98.2%, Vendor E at 97.6%, and Vendor B at 96.5%. The ranking order was unchanged, with slightly decreased utility degrees due to the greater emphasis on punctuality, amplifying Vendor A's advantage. The tie between Vendors C and F persisted in both scenarios, reflecting their closely matched performance across criteria, particularly in customer service and delivery area.

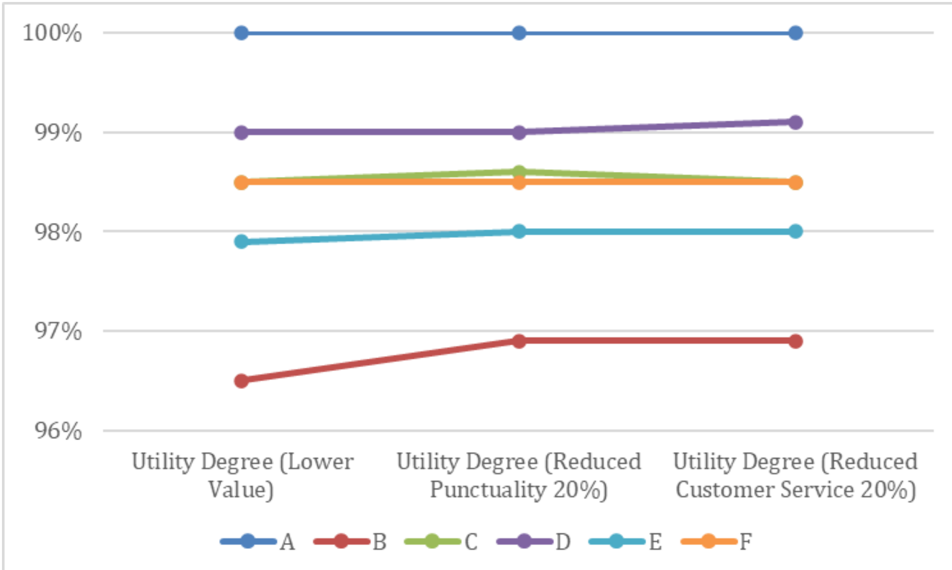

Figure 2. Sensitivity analysis

To further validate robustness, an additional sensitivity analysis varied the weights of customer service ([0.124, 0.195]) and delivery area ([0.080, 0.110]) by ± 20% simultaneously, redistributing the weight changes across the remaining criteria. The results consistently maintained the ranking order, with Vendor A at 100%, followed by D, C, F, E, and B, though utility degree gaps narrowed slightly (*e.g.*, D at 99.1%, C and F at 98.5% in the reduced case), as shown in Fig. 2. This stability, driven by R-SWARA's use of rough set intervals to capture expert uncertainty, aligns with the findings of [43], who demonstrated R-SWARA's reliability in transport-related decisions. However, extreme weight changes, such as ± 50% for punctuality, could potentially disrupt the tie between Vendors C and F, indicating sensitivity to significant shifts in critical criteria.

4. Conclusions

The findings of this study contribute to the literature on 3PL evaluation by addressing several limitations identified in previous research. Unlike conventional studies that rely on crisp expert inputs, the proposed framework incorporates uncertainty-aware weighting through R-SWARA, allowing expert hesitation and variability in judgments to be systematically represented. This particularly relevant in cold-chain logistics, where performance assessment involves complex trade-offs between punctuality, reliability, and service quality.

The originality of this study also lies in the integration of R-SWARA and COPRAS, which produces a utility-based ranking that remains transparent and interpretable for decision-makers. By avoiding reliance on distance-based ideal solutions, the COPRAS approach facilitates a direct comparison of alternatives and preserves the influence of all criteria, including those with relatively lower weights. The inclusion of sensitivity analysis further strengthens the robustness of the results, demonstrating that the ranking of 3PL providers remains stable under variations in key criteria weights.

In practical terms, these results offer actionable guidance for the fishery company. Vendor A's top ranking indicates that it is the most reliable choice for ensuring timely and secure delivery of seafood, critical for maintaining product quality and customer satisfaction in domestic and international markets. Vendor D's strong performance regarding customer service and delivery area suggests it as a viable alternative, particularly if cost negotiations or expanded market coverage are prioritized. The tie between Vendors C and F highlights their comparable suitability, potentially allowing the company to consider additional factors (*e.g.*, contract terms, scalability). The lower rankings of Vendors E and B, driven by weaker scores in punctuality and security, suggest that they may require improvements to meet cold chain standards. These findings can inform contract negotiations, performance monitoring, and strategic partnerships, ensuring alignment with the company's operational goals of minimizing spoilage and meeting stringent temperature controls (*e.g.*, 0-4°C for fresh fish). Furthermore, the study supports the studied fishery in promoting sustainable logistics practices by systematically comparing alternatives that align economic efficiency with environmental and social responsibility through reduced food losses, improved energy efficiency in refrigerated transport via punctual deliveries, and sustained product quality.

Despite its contributions, the study has limitations that warrant consideration. The reliance on three experts, while sufficient for R-SWARA's group decision-making, may limit the diversity of perspectives, potentially overlooking nuances in vendor performance. Future studies could involve a larger expert panel or incorporate stakeholder inputs (*e.g.*, customers, regulators) to enhance robustness. Additionally, this study assumes equal weighting of expert opinions, which may not account for varying levels of expertise, so weighted aggregation methods could be explored. The use of averaged vendor scores in COPRAS simplifies the analysis but may dilute the uncertainty handling of the rough set approach, suggesting a need for fully rough-based ranking in future work. Finally, the case study's focus on a single fishery in Indonesia limits generalizability, so applying the methodology to other perishable goods industries (*e.g.*, dairy, pharmaceuticals) could validate its broader applicability. Future research could also compare R-SWARA-COPRAS with other MCDM methods to assess relative performance or integrate real-time data (*e.g.*, GPS tracking, temperature logs) for dynamic 3PL evaluation.

5. Authors contribution

Adhie Prayogo contributed to the conceptualization, data curation, development of initial methodology, and writing the initial draft. M. Mujiya Ulkhaq supervised the overall research process and refined the methodology and the manuscript. Both authors have reviewed and approved the final manuscript and accept responsibility for its content.

6. Ethics Statement

The authors confirm that this study relies on expert assessments and secondary data and does not involve human subjects or sensitive information. Therefore, the study did not require approval from institutional review board or ethics committee.

7. Artificial Intelligence Statement

The authors used Grammarly for language editing and grammar correction. The authors reviewed and approved all revisions and take full responsibility for the content of the manuscript.

References

[1] P. Thompson, C. Okorie, and K. El Sakty, "An Exploratory Study of the Strategic Use of 3PLs for Cost Reduction and Customer Satisfaction in the Oil and Gas Industry: Nigerian Firms' Experience," *Manag. Res. Pract.*, vol. 13, no. 1, p. 27, 2019, [Online]. Available: https://jscm.au.edu/index.php/jscm/article/download/165/123

[2] M. Heiyantuduwa, W. M. N. N. Wannisingha, and T. Rupasinghe, "A Strategic Analysis of the use of Third Party Logistics Providers (3PLs) in Fast Moving Consumer Goods (FMCG) Industry: A Systematic Review of Literature," *Soc. Sci. Res. Netw.*, 2015. https://doi.org/10.2139/ssrn.2699881

[3] I. Vlachos and V. Polichronidou, "The role of Third-Party Logistics Providers in managing international supply chain triads," *Int. Conf. Logist. Oper. Manag.*, pp. 1–10, 2022. https://doi.org/10.1109/gol53975.2022.9820185

[4] X. Chen, G. Cai, and J.-S. J. Song, "The Cash Flow Advantages of 3PLs as Supply Chain Orchestrators," *Soc. Sci. Res. Netw.*, 2016. https://doi.org/10.2139/ssrn.2679357

[5] H. T. Mengistu, K. S. Dimitrov, and M. H. Qureshi, "Impact of 3PL Outsourcing on Supply Chain Management in Manufacturing Companies in Norway: Case Study Norsk Hydro," *J. Procure. Supply Chain*, vol. 7, no. 1, pp. 1–11, 2023. https://doi.org/10.53819/81018102t5174

[6] G. Turner, "A 3PL's role in perishable freight transportation," *J. Supply Chain Manag. Logist. Procure.*, vol. 2, no. 1, pp. 84–93, 2019.

[7] S. A. Baidoo-Baiden, "3PL Relationship Management Practices as a Cost Reduction Tool in the Supply Chain: A Case of Stellar Logistics," *Am. J. supply Chain Manag.*, vol. 7, no. 1, pp. 1–18, 2022. https://doi.org/10.47672/ajscm.1175

[8] S. Boakai and F. Samanlioglu, "An MCDM approach to third party logistics provider selection," *Int. J. Logist. Syst. Manag.*, vol. 44, no. 3, p. 283, 2023. https://doi.org/10.1504/ijlsm.2023.129365

[9] R. D. Raut, B. B. Gardas, S. Pushkar, and B. E. Narkhede, "Third-party logistics service providers selection and evaluation: A hybrid AHP-DEA-COPRAS-G group decision-making approach," *Int. J. Procure. Manag.*, vol. 12, no. 6, pp. 632–651, 2019. https://doi.org/10.1504/ijpm.2019.102936

[10] T. D. Nguyen and T. C. Le, "3PL provider selection in oil and gas industry using the analytic hierarchy process: A case study in oil-field services company X," vol. 9, no. 1, 2020. https://doi.org/10.46223/hcmcoujs.econ.en.9.1.176.2019

[11] K. Suroto and H. Hasbullah, "Third Party Logistics Selection in Fast Moving Consumer Goods using AHP Method: A Case Study at PT.PZC," 2022. https://doi.org/10.4108/eai.25-11-2021.2318835

[12] Y. Yuan, Z. Xu, and Y. Zhang, "The DEMATEL–COPRAS hybrid method under probabilistic linguistic environment and its application in Third Party Logistics provider selection," *Fuzzy Optim. Decis. Mak.*, pp. 1–20, 2021. https://doi.org/10.1007/s10700-021-09358-9

[13] A. Ulutaş and A. Topal, "A new hybrid model based on rough step-wise weight assessment ratio analysis for third-party logistics selection," *Soft Comput.*, pp. 1–12, 2021. https://doi.org/10.1007/s00500-021-06374-0

[14] C.-N. Wang, N.-A.-T. Nguyen, T.-T. Dang, and C.-M. Lu, "A compromised decision-making approach to third-party logistics selection in sustainable supply chain using fuzzy ahp and fuzzy vikor methods," *Mathematics* vol. 9, no. 8, p. 886, 2021. https://doi.org/10.3390/math9080886

[15] S. N. W. Pramono *et al.*, "Integrating the analytic hierarchy process and importance-performance analysis into ISO 14001 framework for assessing campus sustainability," *AIP Conf. Proc.*, vol. 1902, no. 1, p. 20035, 2017. https://doi.org/10.1063/1.5010652

[16] M. M. Ulkhaq, W. R. Wijayanti, D. A. Dilaga, A. A. Qadarullah, and F. Arfi, "Combining the Analytic Hierarchy Process and Importance-Performance Analysis to Assess Service Quality of m-Commerce: A Case of Indonesian m-Commerce," in *2021 IEEE 8th Int. Conf. Ind. Eng. App. (ICIEA)*, 2021, pp. 6–10. https://doi.org/10.1109/iciea52957.2021.9436718

[17] D. P. Sari, W. R. Wijayanti, A. Prayogo, M. Mujiya Ulkhaq, and D. I. Rinawati, "An integrated fuzzy AHP and TOPSIS model for evaluating the performance of raw material suppliers: A case study in lasem batik writing centre," *MATEC Web Conf.*, vol. 204, p. 2014, 2018. https://doi.org/10.1051/matecconf/201820402014

[18] M. M. Ulkhaq, R. L. Nartadhi, and P. Y. Akshinta, "Evaluating Service Quality of Korean Restaurants: A Fuzzy Analytic Hierarchy Approach," *Ind. Eng. Manag. Syst.*, vol. 15, no. 1, pp. 77–91, 2016. https://doi.org/10.7232/iems.2016.15.1.077

[19] M. M. Ulkhaq, A. D. Siamiaty, A. Handoko, S. A. Madjid, and D. 'Sa Nu, "The Fuzzy Analytic Hierarchy Process for Prioritizing the Sustainable Tourism Attitude Scale," *IOP Conf. Ser. Earth Environ. Sci.*, vol. 219, no. 1, p. 12012, Jan. 2019. https://doi.org/10.1088/1755-1315/219/1/012012

[20] W. R. Wijayanti, W. R. Dewi, F. Ardi, A. Fajri, M. M. Ulkhaq, and P. Y. Akshinta, "Combining the fuzzy AHP and TOPSIS to evaluate service quality of e-commerce website," in *Proc. 10th Int. Conf. Ed. Tech. Comp.*, 2018, pp. 397–402. https://doi.org/10.1145/3290511.3290514

[21] N. U. Handayani, D. P. Sari, M. M. Ulkhaq, and R. A. C. Fitriani, “The Analytic Network Process for Identifying the Potential Sub-Sectors of Creative Industry: Empirical Finding from Semarang, Indonesia,” *Rev. Gestão - RGSA*, vol. 18, no. 3, p. e05016, 2024. https://doi.org/10.24857/rgsa.v18n3-098

[22] E. Çakir, “Selecting Contractor Company in Urban Transformation Using SWARA - Gray Relationship Analysis Method,” *J. Int. Sci. Res.*, vol. 2, no. 6, pp. 79–95, 2017. https://doi.org/10.23834/isrjournal.327313

[23] H. E. Gürler, “Assessment of Third-Party Reverse Logistics Provider Through the SWARA-WASPAS Integrated Framework,” *Kahramanmaraş Sütçü İmam Üniversitesi Sos. Bilim. Derg.*, vol. 21, no. 1, pp. 204–217, 2024. https://doi.org/10.33437/ksusbd.1422598

[24] A. K. Narayanan and J. N, “Application of SWARA and TOPSIS Methods for Supplier Selection in a Casting Unit,” *Int. J. Eng. Res. Technol.*, vol. 7, no. 5, 2018, [Online]. Available: https://www.ijert.org/research/application-of-swara-and-topsis-methods-for-supplier-selection-in-a-casting-unit-ijertv7is050210.pdf

[25] V. V. A. Almeida, C. F. S. Gomes, L. H. C. Pinochet, and M. dos Santos, “Prioritization of investment order in Brazil among renewable energy sources: an analysis using the SWARA-MOORA-3NAG method,” *J. Model. Manag.*, vol. 20, no. 2, pp. 620–647, 2025. https://doi.org/10.1108/jm2-09-2023-0208

[26] P. G. Fernandes *et al.*, “Product Engineering Assessment of Subsea Intervention Equipment Using SWARA-MOORA-3NAG Method,” *Systems*, vol. 11, no. 3, 2023. https://doi.org/10.3390/systems11030125

[27] E. Adalı and A. Işik, “Integration of DEMATEL, ANP and DEA methods for third party logistics providers’ selection,” *Manag. Sci. Lett.*, vol. 6, no. 5, pp. 325–340, 2016. https://doi.org/10.5267/j.msl.2016.3.004

[28] S. Hasibuan and C. Jaqin, “Seleksi dan Penentuan Third Party Logistik Transportasi Produk Pelumas Menggunakan Metode TOPSIS dan PROMETHE,” *Oper. Excell.*, vol. 14, no. 3, p. 235, 2022. https://doi.org/10.22441/oe.2022.v14.i3.058

[29] M. P. Basilio, V. Pereira, and F. Yigit, “New Hybrid EC-Promethee Method with Multiple Iterations of Random Weight Ranges: Applied to the Choice of Policing Strategies,” *Mathematics*, vol. 11, no. 21, 2023. https://doi.org/10.3390/math11214432

[30] S. Shukla, S. Khare, T. Verma, M. Chhimwal, and G. Kumar, "Selection of Third-Party Reverse Logistics Partners Using Multi-criteria Decision Making: A Case Study of EV Industry," in *Recent Advances in Mechanical Engineering. ICRAMERD 2023*, S. Sahoo and N. Yedla, Eds. Singapore: Sprin. ger, 2024, pp. 209–219. https://doi.org/10.1007/978-981-97-1080-5_17

[31] M. M. Ulkhaq, P. Y. Akshinta, R. L. Nartadhi, and W. P. Susatyo Nugroho, “Assessing Sustainable Rural Community Tourism Using the AHP and TOPSIS Approaches under Fuzzy Environment,” *MATEC Web Conf.*, vol. 68, p. 9003, 2016. https://doi.org/10.1051/matecconf/20166809003

[32] M. M. Ulkhaq *et al.*, “Evaluating Hospital Service Quality: A Combination of the AHP and TOPSIS,” in *Proc. 2nd Int. Conf. Med. Health Infor.*, 2018, pp. 117–124. https://doi.org/10.1145/3239438.3239448

[33] M. M. Ulkhaq, W. R. Wijayanti, M. S. Zain, E. Baskara, and W. Leonita, "Combining the AHP and TOPSIS to evaluate car selection," in *Proc. 2nd Int. Conf. High Perf. Compil., Comp. Comm.*, 2018, pp. 112–117. https://doi.org/10.1145/3195612.3195628

[34] A. Jayant and P. Singh, "Application of AHP-VIKOR Hybrid MCDM Approach for 3pl Selection: A Case Study," *Int. J. Comp. App.*, no. 5, pp. 4–11, 2015. [Online]. Available: https://research.ijcaonline.org/icaet2015/number5/icaet4061.pdf

[35] R. Kumar, H. Singh, and J. S. Dureja, "An approach to analyze logistic outsourcing problem in medium-scale organization by CFPR and VIKOR," *J. Manuf. Technol. Manag.*, vol. 23, no. 7, pp. 885–898, 2012. https://doi.org/10.1108/17410381211267718

[36] E. Rosiana, A. K. Garside, and I. Amallynda, "Integration of Rough SWARA and COPRAS in the Performance Evaluation of Third-Party Logistics Providers," *JTI.*, vol. 22, no. 1, pp. 31–42, 2021. https://ejournal.umm.ac.id/index.php/industri/article/view/15823

[37] S. S. Goswami and D. K. Behera, "Developing Fuzzy-AHP-Integrated Hybrid MCDM System of COPRAS-ARAS for Solving an Industrial Robot Selection Problem," *Int. J. Decis. Support Syst. Technol.*, vol. 15, no. 1, pp. 1–38, 2023. https://doi.org/10.4018/ijdsst.324599

[38] S. K. Tembhare, A. K. Amar, and J. George, "Evaluating Alternatives Using ARAS Method Integrated with Entropy Weight Method for Vendor Selection in Supply Chain Management," *J. Emerg. Technol. Innov. Res.*, vol. 8, no. 2, pp. 1271–1275, 2021, [Online]. Available: https://www.jetir.org/view?paper=JETIR2102149

[39] S. Sremac, Ž. Stević, D. Pamučar, M. Arsić, and B. Matić, "Evaluation of a Third-Party Logistics (3PL) Provider Using a Rough SWARA–WASPAS Model Based on a New Rough Dombi Aggregator," *Symmetry (Basel).*, vol. 10, no. 8, p. 305, 2018. https://doi.org/10.3390/sym10080305

[40] M. P. Basílio, V. Pereira, H. G. Costa, M. Santos, and A. Ghosh, "A Systematic Review of the Applications of Multi-Criteria Decision Aid Methods (1977–2022)," *Electronics*, vol. 11, no. 11, 2022. https://doi.org/10.3390/electronics11111720

[41] M. P. Basilio, V. Pereira, and M. dos Santos, "Preface to the Special Issue 'Advanced Applications of Multi-Criteria Decision-Making Methods in Operational Research,'" *Mathematics*, vol. 13, no. 11, 2025. https://doi.org/10.3390/math13111888

[42] V. Keršuliene, E. K. Zavadskas, and Z. Turskis, "Selection of rational dispute resolution method by applying new step-wise weight assessment ratio analysis (Swara)," *J. Bus. Econ. Manag.*, vol. 11, no. 2, pp. 243–258, 2010. https://doi.org/10.3846/jbem.2010.12

[43] E. K. Zavadskas, Ž. Stević, I. Tanackov, and O. Prentkovskis, "A Novel Multicriteria Approach – Rough Step-Wise Weight Assessment Ratio Analysis Method (R-SWARA) and Its Application in Logistics," *Stud. Informatics Control*, vol. 27, pp. 97–106, 2018. https://doi.org/10.24846/v27i1y201810

[44] E. K. Zavadskas, A. Kaklauskas, and V. Sarka, "The New Method of Multicriteria Complex Proportional Assessment of Projects," *Technol. Econ. Dev. Econ.*, vol. 3, pp. 131–139, 1994.

[45] S. Jovčić and P. Průša, "A Hybrid MCDM Approach in Third-Party Logistics (3PL) Provider Selection," *Mathematics2*, vol. 9, no. 21, 2021. https://doi.org/10.3390/math9212729

[46] Ö. Bali and Ö. EROĞLU, "Assessment of 3PL Providers for Hazardous Materials," *J. Mil. Inf. Sci.*, vol. 2, no. 2, pp. 27–40, 2014. https://doi.org/10.17858/jmisci.38531

[47] S. Çıkmak, "Sustainable 3PL Service Provider Selection in the Pharmaceutical Industry Using Fuzzy-Based SWARA and MAIRCA Methods," *Abant Sos. Bilim. Derg.*, vol. 25, no. 1, pp. 306–333, 2025. https://doi.org/10.11616/asbi.1585792

[48] A. Ulutaş, "A grey hybrid model to select the optimal third-party logistics provider," *South African J. Ind. Eng.*, vol. 32, no. 1, 2021. https://doi.org/10.7166/32-1-2126

[49] S. Sremac, Ž. Stević, D. Pamučar, M. Arsić, and B. Matić, "Evaluation of a Third-Party Logistics (3PL) Provider Using a Rough SWARA–WASPAS Model Based on a New Rough Dombi Aggregator," *Symmetry (Basel).*, vol. 10, no. 8, 2018. https://doi.org/10.3390/sym10080305

[50] M. E. Akpınar, "Third-Party Logistics (3PL) Provider Selection Using Hybrid Model of SWARA and WASPAS," *Int. J. Pure Appl. Sci.*, vol. 7, no. 3, 2021. https://doi.org/10.29132/ijpas.972885

ADHIE PRAYOGO

He received his Bachelor's degree in Industrial Engineering from Diponegoro University, Indonesia, in 2018. He completed his Master's degree in Supply Chain Management at Széchenyi István University, Hungary, in 2022. He is currently a lecturer at the Department of Industrial Engineering, *Universitas Muria Kudus*, Indonesia. His research interests focus on the digitalization and optimization of Supply Chain Management, and transportation systems. Email: adhie.prayogo@umk.ac.id

M. MUJIYA ULKHAQ

He is an assistant professor in the Department of Industrial Engineering at Diponegoro University, Indonesia. He obtained his PhD in Analytics for economics and management at the University of Brescia, Italy. His research interests include performance management, service quality measurement, and data analytics. Email: ulkhaq@live.undip.ac.id

UNIVERSIDAD DISTRITAL
FRANCISCO JOSÉ DE CALDAS

Ingeniería

https://revistas.udistrital.edu.co/index.php/reving/issue/view/1320

DOI: https://doi.org/10.14483/23448393.22843

Research

Technical Feasibility Analysis of DC Microgrids in a Non-Interconnected Area

Análisis de viabilidad técnica de Microrredes DC en una zona no interconectada

Iván Felipe-Muñoz[1], and Maximiliano Bueno-López[2]

[1]Industrial Automation Engineering, Universidad del Cauca, Popayán, Colombia
[2]Professor at the Program of Electrical Technology, Universidad Tecnológica de Pereira, Pereira, Colombia

Abstract

Context: In recent times, access to electricity in non-interconnected areas has been a constant challenge. Therefore, this article evaluates the technical feasibility of implementing direct-current (DC) microgrids in these areas, focusing on food conservation. Our evaluation focuses on the region of Chacón Playa (Timbiquí) in the Cauca Pacific, Colombia.
Method: This work analyzes the advantages and disadvantages of DC microgrids vs. alternating-current (AC) systems, selecting a radial topology for its simplicity and expandability. A simulation is performed in MATLAB-Simulink with a control system based on the incremental conductance algorithm, which incorporates solar photovoltaic generation, battery backup, power converters, and a load composed of four DC coolers.
Results: The results and simulations show that DC microgrids are effective in meeting voltage and current demands in response to changes in solar radiation and power demand. Our findings highlight the ability of DC microgrids to provide a stable and efficient power supply suitable for food conservation in non-interconnected areas.
Conclusions: DC microgrids represent a viable solution to cover energy needs in isolated areas. This study supports their implementation as a sustainable and reliable alternative, opening new opportunities for the development of regulatory frameworks that facilitate the expansion of this type of technology in similar regions.

Keywords: DC microgrid, MATLAB, non-interconnected zones, distributed generation, incremental conductance

Article history

Received:
November 2nd, 2024

Modified:
December 9th, 2025

Accepted:
March 2nd, 2026

Ing, vol. 31, no. 1, 2026, e22843

* Correspondence: ifmunoz@unicauca.edu.co, m.bueno3@utp.edu.co

Resumen

Contexto: En los últimos tiempos, el acceso a la electricidad en zonas no interconectadas ha sido un desafío constante. Por ello, este artículo evalúa la viabilidad técnica de implementar microrredes de corriente continua (DC) en estas áreas, centrando su atención en la conservación de alimentos. Nuestra evaluación se enfoca en la región de Chancón Playa (Timbiquí) en el Pacífico del Cauca, Colombia.

Método: Este trabajo analiza las ventajas y desventajas de las microrredes DC frente a los sistemas de corriente alterna (AC), seleccionando una topología radial por su simplicidad y capacidad de expansión. Se desarrolla una simulación en MATLAB-Simulink con un sistema de control basado en el algoritmo de conductancia incremental, la cual incorpora generación solar fotovoltaica, respaldo de baterías, convertidores de potencia y una carga compuesta por cuatro refrigeradores DC.

Resultados: Los resultados y las simulaciones muestran que las microrredes DC son efectivas para satisfacer las demandas de tensión y corriente en respuesta a cambios en la radiación solar y en la demanda de potencia. Nuestros hallazgos destacan la capacidad de las microrredes DC para ofrecer un suministro de energía estable y eficiente, adecuado para la conservación de alimentos en zonas no interconectadas.

Conclusiones: Las microrredes DC representan una solución viable para cubrir las necesidades energéticas en zonas aisladas. Este estudio respalda su implementación como alternativa sostenible y confiable, abriendo nuevas oportunidades para el desarrollo de marcos regulatorios que faciliten la expansión de este tipo de tecnología en regiones similares.

***Palabras clave*:** microrred DC, MATLAB, zonas no interconectadas, generación distribuida, conductancia incremental

Contents

1. Introduction

In developing countries such as Colombia, the energy demand is steadily increasing. The emergence of new industries, ongoing technological advancements, and efforts towards economic reactivation to meet the needs of a growing population have led to a substantial rise in electricity consumption. Consequently, there is an urgent need to expand the electrical infrastructure, but persistent economic and social crises have played a critical role in delaying the implementation of projects aimed at achieving universal access to electricity. This challenge disproportionately affects rural areas, where its impacts are most pronounced. As a result, the disparity between urban and rural regions continues to widen [1], [2].

Today, many regions still lack access to electricity or are served by low-quality systems characterized by intermittent and unreliable supply. In these areas, the consequences are particularly severe since the absence of continuous and dependable electricity significantly hinders human development and constrains the social and economic progress of affected communities. These areas are known as *non-interconnected zones* (NIZ), covering approximately 52% of the national territory. Out of this total, almost 90% is made up of rural areas, while the remaining percentage corresponds to urban areas that obtain electricity access through isolated grids, diesel power plants and a few individual generation systems based on renewable sources. In rural areas, most of the electricity comes from diesel generators, representing about 85% [3]. These data underline a marked dependence on this fuel, according to statistics provided by the Institute for Planning and Promotion of Energy Solutions (IPSE) for NIZ in 2025.

The expansion of the interconnected power system to NIZ has been constrained by their remote location and difficult geographic access. Even in areas where grid extension has been achieved, service quality and reliability are not guaranteed. Consequently, local generation systems have been implemented to provide a limited electricity supply. However, these systems exhibit frequent operational failures, resulting in a high dependence on diesel-based generation to meet the daily demand. This reliance leads to elevated operating costs due to fuel price volatility and the logistical complexity of fuel transportation to remote regions, often accessible only by air or river [4]. Furthermore, diesel-based generation produces significant CO_2 emissions, contributing to climate change and environmental degradation.

In Colombia, small-scale distribution systems have been developed to operate as alternating-current (AC) microgrids with centralized local generation, providing stable operation in NIZ. These microgrids are designed to supply electricity in areas that are not linked to the national interconnected system, delivering a level of service comparable to that of the main grid [5]. Although these systems are technically capable of integrating renewable energy sources such as solar photovoltaic (PV), biomass, and micro-hydropower generation, most of them continue to rely predominantly on fossil fuel-based generators [6].

In light of the above, the energy transition has become a strategic priority for the Colombian government, aiming to reduce dependence on conventional fossil fuel-based generation systems, particularly diesel generators. To this effect, multiple initiatives and planning frameworks have been proposed to expand the national electricity coverage while promoting the integration of renewable energy sources. Programs such as the Indicative Plan for the Expansion of Electricity Coverage (PIEC) have incorporated, in addition to individual solutions, the deployment of isolated microgrids. These systems are characterized by a reduced reliance on conventional generation and an increased use of environmentally sustainable distributed energy resources [7]. In this context, microgrids based on a direct-current (DC) main bus have emerged as promising alternatives since they facilitate the integration of renewable generation sources with low or negligible greenhouse gas emissions.

The relevance of DC microgrids for supplying electricity to remote areas without access to the conventional power grid has been demonstrated in several studies. The high penetration of renewable energy sources and DC-based energy storage systems allows these microgrids to operate autonomously in isolation while avoiding pollutant emissions. Previous research includes comprehensive analyses of microgrid deployment in remote areas, concluding that DC microgrids exhibit higher efficiency than their AC counterparts [8]–[10].

Furthermore, other studies have highlighted that DC systems offer improved controllability due to the absence of reactive power and harmonic issues, in contrast to AC microgrids, which often depend on diesel generation or conventional grid support and require frequency regulation [11], [12].

In the context of Colombia's energy transition, however, the adoption of DC microgrids faces regulatory and technical challenges that must be addressed in order to ensure successful implementation. Recent advances in power electronics have enabled the development of converters that facilitate the direct integration of DC loads and generation units. This capability is particularly relevant for meeting essential energy needs in remote areas, such as lighting and food refrigeration [13].

In this scenario, DC microgrids play a crucial role. Their integration with clean generation sources and power converters, including reducers, boosters and bidirectional devices, allows directly incorporating DC loads [13], [14], which, though not widely adopted in the country, show potential for increasing efficiency and reducing losses, thus guaranteeing quality services in these regions while also satisfying their essential needs.

This paper presents a technical analysis of a DC microgrid and its implementation in a non-interconnected region located in the Cauca Pacific (Colombia), specifically in the area of Chacón Playa (Timbiquí). In this context, it is of vital importance to ensure energy supply for food conservation, since the main source of economic livelihood in this area derives from fishing activities. Thus, our work's creation and evaluation of the DC microgrid considers the essential inclusion of a DC load (*e.g.*, refrigerators) for food preservation. This analysis will be complemented with the implementation of a control system based on the incremental conductance algorithm, with the purpose of optimizing and efficiently managing the microgrid.

The key contributions of this paper are as follows:

- **Evaluation of the technical feasibility of food preservation in non-interconnected zones.** This paper shows that DC microgrids are an effective and stable solution for critical energy needs, specifically the refrigeration of fish products in isolated communities. This contribution is fundamental because it addresses the socioeconomic problems of a region that depends on fishing for its livelihood but currently lacks a reliable electricity service to preserve its food.
- **Design and validation of an optimal control system through simulation.** This research develops a detailed configuration that uses a radial topology and an maximum power point tracking (MPPT) control system. Through simulations in MATLAB-Simulink with real solar radiation and temperature data, it is confirmed that the system can maintain a constant voltage of 24 V and supply the necessary power (288 W) to operate four DC refrigerators—even in the face of climatic changes and periods deprived of sunlight—thanks to battery backup.
- **Promoting the energy transition and sustainability in rural areas.** Our study provides technical evidence that supports the migration from diesel generator-based systems (which account for 85% of the energy in the rural areas of Colombia) to renewable sources integrated into DC microgrids. This implementation not only reduces dependence on fossil fuels and CO_2 emissions but also offers a more efficient system with lower initial costs than traditional AC microgrids, laying the groundwork for future regulatory frameworks in these regions.

The structure of this article is as follows. Section 2 provides general details on DC microgrids, highlights their advantages compared to AC microgrids, and explores their future directions. Section 3 details the methodology employed in this research. Section 4 is devoted to presenting and analyzing the results obtained, and, finally, Section 5 presents the conclusions drawn from our findings.

2. Overview and trends in DC microgrids

A microgrid is an electrical system that encompasses a variety of generation components, mostly based on renewable sources, but also conventional ones, as well as storage centers, loads, power electronics, management, and communication and control systems. Unlike the traditional power grid, a microgrid operates on a smaller scale, and its main objective is to provide a constant supply of high-quality and reliable energy to a community with a low dispersion index who live close to the generation center (*i.e.*, distributed generation). Microgrids are located in the vicinity of consumption centers and can operate in two main modes: connected to the AC grid or in islanded mode. When operating in interconnected mode, there is a flow of energy between the generation systems within the microgrid, its components, and the traditional electrical grid. On the other hand, in islanded mode, energy is generated and stored only through the generation systems and internal components of the microgrid [15].

A microgrid manages two types of configurations, which are classified depending on the type of current in the main bus connection.

2.1. AC operation

In this configuration, the main connection bus operates with AC, which makes it directly compatible with the common connection point of the large-scale grid, also known as the *traditional AC grid*. The microgrid is designed to be able to transmit power over long distances, benefiting from the ease of transforming AC voltage at different levels. In [16], the authors provide a comprehensive review of the operation of these systems, and they propose a nonlinear control strategy combined with an efficient energy flow management algorithm for a low-voltage AC microgrid integrating a wind turbine, a PV system, and a battery energy storage system (BESS). A comprehensive mathematical model of the system is developed, and backstepping-based controllers are designed to achieve the control objectives, including the maximization of renewable energy extraction, battery storage management, and power factor correction at the grid interface. Simulation results confirm that the proposed strategy significantly improves energy efficiency, system stability, and dynamic performance under variable load and generation conditions.

2.2. DC operation

In this configuration, the main connection bus operates with DC, which simplifies the integration of renewable generation sources thanks to the reduced use of power converters. This system enables the connection to the electrical grid through an inverter for bidirectional electrical flow between the DC bus of the microgrid and the conventional grid. This technology has positioned itself as an excellent alternative due to the multiple advantages compared to AC microgrids. Below are some advantages and disadvantages of this type of technology.

- From a protection perspective, the main advantage of DC microgrids over AC microgrids lies in their simpler and more predictable system behavior, resulting from the absence of frequency, reactive power, and phase-angle dynamics, which facilitates fault detection, protection coordination, and the implementation of adaptive protection schemes [17].
- In [18], the authors mention some advantages of DC microgrids from the perspective of control systems. The paper investigates super-twisting sliding mode controllers for dynamic DC microgrid voltage regulation. The proposed control approach aims to enhance robustness against disturbances and load variations while mitigating the chattering effects inherent to classical sliding mode control, thereby maintaining stable DC bus voltage under dynamic operating conditions.
- Much of the renewable generation systems and storage facilities (*e.g.*, batteries) supply DC power, which simplifies their integration with a DC main bus when compared to an AC main bus, which may lead to synchronization difficulties [19].

- The DC microgrid exhibits superior reliability in contrast to its AC counterpart. This is due to the ability to adjust the DC bus to the system requirements as the number of components increases [16]. In addition, these systems have a greater ability to operate in islanded mode, which improves their reliability.
- In [20], the authors presented an intelligent energy management system (EMS) for a hybrid microgrid incorporating multiple generation sources, and they examined its technical viability and economic performance. The EMS integrates control strategies and multilevel grid interface conversion to manage energy flows, enhance power quality, and reduce operating costs, demonstrating the benefits of coordinated generation, storage, and control in microgrid operation.
- Regarding the implementation, the size of a DC microgrid tends to be significantly smaller compared to an AC microgrid. This is due to the decrease in the required conversion components [20].
- In systems operating via DC, imbalances in the circulation of electric current are prevented through a conductor, thus avoiding the phenomenon known as *skin effect*, which manifests itself in the transport of AC [21].
- A significant proportion of electronic loads require DC as a voltage source to operate, whereas, for interconnection to an AC system, they rely on an internal rectifier which can negatively impact their efficiency. In contrast, DC microgrids offer a direct power supply, which results in reduced costs and higher efficiency [22].
- In a DC microgrid, the quality of power transmission can experience significant improvements since reactive power and frequency must not be regulated, factors that influence system performance. In addition, DC microgrids are free of phase imbalance and harmonics, which contributes to a more efficient transmission [23].

The current development of research works and applications of DC microgrids reflects their numerous advantages over AC microgrids, given the technological advances, the increase in DC equipment and devices—such as the direct integration of renewable energy systems—, and the obvious technical advantages. However, these systems also come with challenges and disadvantages that require attention in future research and applications. Some of them are listed below:

- DC microgrids have not undergone an extensive development and research as their AC counterparts. This translates into a lack of standardization in voltage levels and regulatory frameworks that are essential to defining technical aspects. This lack becomes a significant obstacle for a faster transition to the implementation of DC microgrids [22].
- In a bidirectional power flow, protection techniques continue to be a challenge due to the complexity of fault management and the lack of standardization and coordination, problems that arise due to the intermittency of renewable generation sources. Likewise, DC microgrids generate constant current in only one direction, which means that there are no zero crossing cycles, as occurs in AC microgrids. This feature complicates the natural extinction of the electric arcs that can be generated when contacts are opened in protective devices such as circuit breakers [24].

- Microgrids, which on renewable generation sources, often face voltage swings and variations. Power generation can be intermittent due to climatic factors and the availability of the main resource. Over time, this can complicate the regulation of the power supplied. This implies the need to implement backup and advanced management systems to mitigate this variability [22].

The paragraphs above discussed the main advantages and limitations of DC microgrids. Although several challenges remain in their large-scale deployment, the reported benefits indicate that these systems are increasingly being regarded as promising solutions for a wide range of applications. Driven by ongoing research efforts and technological advancements, recent studies on DC microgrids have focused on the integration of advanced energy storage technologies such as supercapacitors and high-performance lithium-based batteries [25]. These developments allow DC microgrids to efficiently exploit weather-dependent renewable energy sources, including solar and wind power, as primary generation resources. Consequently, reliance on diesel-based generators is significantly reduced, leading to lower CO_2 emissions and mitigating negative environmental impacts, including ecosystem degradation and adverse effects on human and animal health.

Furthermore, the growing adoption of DC-compatible loads and the direct interfacing of traditionally AC-based devices without extensive power conversion stages contribute to reduced system complexity, lower investment costs, and decreased energy losses [22]. In parallel, the emergence of smart grid technologies and advances in automation support a more effective operation and management of DC microgrids. Intelligent energy management and control systems enable real-time decision-making regarding energy generation, storage, and distribution, thereby enhancing system stability and reliability [26]–[28].

Additionally, a clear trend towards the deployment of DC generation systems at the household and building levels is observed, allowing end-users to manage energy locally and participate more actively in electricity markets [29]. This decentralization paradigm is particularly relevant for NIZ, where the installation of standalone DC microgrids facilitates access to electricity, supports basic community needs, and enables the development of productive activities in remote areas, overcoming the limitations of conventional centralized infrastructure [30]. Finally, the interconnection of multiple microgrids is being explored as a means to improve energy management and configure hybrid systems that combine renewable and conventional generation sources, thereby reducing environmental impacts while expanding electricity coverage in a coordinated manner [28].

In the future, the enactment of new laws and technical standards is expected to foster an increased adoption of DC power systems at the local and rural levels, allowing industries and businesses to manage energy more efficiently and mitigate the impact of power outages on continuous production.

Another area of research and continued growth involves the integration of electric vehicles in the context of DC microgrids. These vehicles operate on DC, where microgrids are ideal for charging them, which not only provides a convenient form of charging, but also allows their batteries to be used as energy storage devices for the grid. This can be essential for balancing demand and power generation in real time [31]. In addition, this trend extends to electric marine vehicles, which can take advantage of DC microgrids through systems for lighting or cooling needs, DC motors powered by renewable generation sources, or DC charging systems [32].

These trends reflect the potential growth of DC microgrids thanks to significant advances in research and technological development, in response to an energy transition that seeks to reduce environmental impacts while expanding energy availability. This not only improves efficiency in urban areas but also meets the needs of rural areas and contributes to their social development and access to electricity.

3. METHODOLOGY

This section first describes the NIZ of the department of Cauca, for which the proposed microgrid was designed, emphasizing the main challenges associated with the lack of access to reliable and high-quality electricity services. In Colombia, the Pacific is one of the regions with the highest concentration of NIZ. Within this area, the department of Cauca features three municipalities, *i.e.*, Timbiquí, López de Micay, and Guapi, which are particularly affected by limited or intermittent electricity supply [33], [34].

Along the Pacific coast of Cauca, the municipality of Timbiquí stands out as one of the areas with the highest number of households without access to electricity in the department. According to the telemetry report issued by the Institute for Planning and Promotion of Energy Solutions for NIZ (IPSE) in 2024, approximately 2196 users in Timbiquí lack access to electricity. The municipality also includes the township of Chacón Playa, where the absence of continuous and high-quality electricity service has resulted in significant social and economic challenges. The following subsection provides a brief characterization of the municipality and this NIZ, highlighting the main issues associated with inadequate energy access.

3.1. Description of the municipality of Timbiquí

Timbiquí is located in the western part of the department of Cauca, at approximately 230 km from the departmental capital, Popayán. Its territory extends for 1813 km^2 and has an estimated population of about 27 182 inhabitants, according to projections made by DANE from the 2018 census. About 74% of its residents live in rural areas, while the remaining percentage corresponds to urban population. The predominant economic activities in Timbiquí focus on fishing, agriculture, mining, and timber exploitation, making it a municipality with an economy based on extractive and primary sectors [35]. In 2017, the municipal capital of Timbiquí was interconnected through the San Bernardino-Guapi-Olaya Herrera electrical interconnection line at 115 000 V, from the San Bernardino substation in Popayán to the

Guapi substation. However, the conditions of the layout have imply suboptimal service conditions for this population.

3.2. Description and main problems at the Chacón Playa-Timbiquí district

Chacón Playa is one of the smallest of the townships in terms of population and geographic extension, but it faces profound challenges due to the lack of access to essential public services. It is inhabited by about 570 people who reside in the rural areas of the municipality of Timbiquí. Chacón Playa's main economic activity corresponds to fishing and agriculture. The population is deeply rooted to its environment, as it is highly dependent on it for survival.

Chacón Playa faces difficulties in terms of the availability of essential services for community development. The quality of the electricity service is poor and currently relies on a 56 kW diesel-fueled generation plant. According to the telemetry report provided by the IPSE in July 2023, there is limited availability of electricity. The average daily electricity supply is limited to approximately five hours and 56 minutes in the Chacón region [36]. This limitation is evidence of persistent difficulties in accessing quality electricity. These problems can be attributed to a number of factors, including price fluctuations in the fuel supply, the challenging geographic conditions of the area, and the technical limitations of its power generation system. All of these highlight the marked dependence on fossil fuels in regional power generation and, as a consequence, the shortages in electricity supply. This dependence on fuels has a negative impact on the environment, especially in the Pacific Ocean and the region as a whole.

In addition to the environmental implications, the lack of electrical power poses significant challenges for the social and economic development of the local community. The absence of refrigerators makes it difficult to preserve food, which is a crucial source of economic livelihood. It also results in literacy problems due to lack of access to quality education and inadequate healthcare. The lack of reliable energy services has led to increased deforestation, as firewood is used as a source of energy for cooking. The community is also forced to rely heavily on fuel for transportation and electricity generation. These issues continue to perpetuate the precarious living conditions in the Chacón region and reflect the urgent need to address and improve access to quality electricity, in order to promote sustainable development and improve the quality of life of its inhabitants.

3.3. Selection of pressing need in the Chacón Timbiquí area

The availability of refrigeration equipment is essential, since it keeps food products in optimal conditions by ensuring adequate temperatures, thus preventing spoilage caused by bacteria and pathogens. In the case of foods, it is crucial to keep them at adequate temperatures to preserve their nutrients and avoid the proliferation of microorganisms that can affect their quality [37].

Fisheries play a fundamental role in the economic development of the region and in the livelihood of the local community. Therefore, the conservation of these foods takes on even greater importance.

Fish products can be prone to contamination by parasites, which can be controlled by using refrigerators and maintaining appropriate temperatures, ensuring that they can be sold in perfect conditions [38].

In addition to benefiting food preservation, the availability of electrical power and refrigeration systems is also crucial for the proper storage of vaccines and medicines. This is essential to improving the quality of life in the area and contribute to the general well-being of the community.

3.4. Topology of the DC microgrid

Once the energy needs of the selected NIZ had been identified, an isolated DC microgrid topology was selected to address the urgent need for a reliable and high-quality electricity supply. These microgrids can be deployed in close proximity to load centers, which facilitates the integration of distributed renewable energy resources. The literature reports several DC microgrid topologies for different applications, with their selection depending on key factors such as system security, fault resilience, scalability, operational complexity, and overall reliability, all of which must be tailored to the specific requirements of the context [13].

DC microgrid topologies can be classified according to their structural complexity and reliability, including single-bus, radial, ring-loop, mesh, and zonal configurations [19], [22]. The selection of a given topology is primarily influenced by its capacity to withstand faults and ensure continuity of service. Table I summarizes the main characteristics of these topologies and their typical applications. Among them, the single-bus topology exhibits the lowest structural complexity, as all generation units, energy storage systems, and loads are connected to a common DC bus. While this configuration offers simplicity in installation and operation, it presents reduced reliability due to its high vulnerability to component failures [38].

In contrast, the zonal topology provides the highest level of reliability, given its ability to establish interconnected zones that enable multiple power supply paths to the loads. Additionally, this topology allows interconnection with conventional AC grids, offering enhanced flexibility in fault management and system reconfiguration. However, these benefits come at the expense of increased installation complexity and higher implementation costs [19].

Table I. Characteristics and applications for DC microgrid topologies

Criteria/topology	Single-bus	Radial	Ring-Loop	Meshed	Zonal
Difficulty of installation	Low	Low	Average	High	High
Difficulty of maintenance	Low	Low	Average	High	High
Reliability	Low	Average	Average	High	Very high
Cost	Low	Low	Average	High	High
Dependability	Low	high	High	High	Average
Reconfiguration	No	No	Yes	Yes	Yes
Response to Failures	Low	Low	Average	High	High
Expansion to multiple buses	X				
Applications	Small buildings and villas, isolated systems, low voltage loads	Low voltage domestic applications, small villages and isolated systems	Small towns, DC distribution systems	Distribution systems, large cities	Ships, on-board systems

Based on the characteristics of the different topologies presented in Table I, and considering the needs of this project, which seeks to analyze the technical feasibility of DC networks in NIZ, as is the case with Chacón, Timbiquí, a radial topology was selected. This is because the region is geographically isolated and has limitations regarding communication, as well as limited access to electricity due to its dependence on diesel energy sources and its lack of connection to the national interconnected system. In this context, a system of less complexity and easier maintenance is recommended. A radial topology constitutes an excellent option for isolated systems and low-voltage domestic applications [40]. In addition, it offers the possibility of expanding to multiple buses through series or parallel connections, which significantly improves its reliability. This topology is versatile and can initially operate with a single bus, but it can be expanded to multiple buses, which allows sharing power between them and working with different voltage levels [39].

The choice of this topology is based on its low installation complexity, ease of maintenance, affordability, and suitability for applications in rural areas. It is also important to highlight its ability to establish connections with AC grids and its extension to multiple buses and points for renewable DC generation.

4. RESULTS

After selecting the topology, a DC microgrid was developed which employs a PV source and a storage center based on batteries. To this effect, it was essential to verify if the area of the village of Chacón in Timbiquí had any availability of primary resources. To carry out this verification, the NASA Data Access Viewer was used, which, thanks to the collection of data over several years and its historical record, allows evaluating the hours of greatest solar irradiance in the study area throughout the year. UMPE solar maps were also used to obtain the average annual radiation.

The data are listed below by database consulted.

- NASA Data Access Viewer:
- Peak Solar Hour PSH = 4.02Kwh/m^2, evaluated between 2021 and 2022.
- UPME solar maps: Average annual radiation = 3.8 Kwh/m^2

Based on the above-presented data, the study area exhibits a significant solar radiation potential, which supports the analysis of microgrids powered by PV generation with energy storage systems as backup sources. Accordingly, solar irradiance and ambient temperature data were collected to characterize the operating conditions and simulate a DC microgrid using real environmental data. Daily irradiance and temperature profiles were obtained from the Photovoltaic Geographical Information System (PVGIS). Fig. 1 shows that solar irradiance is available between approximately 06:00 and 18:00, which is consistent with the expected sunrise and sunset times for the analyzed location. The global irradiance curve exhibits a smooth bell-shaped profile, reaching its maximum value around solar noon (12:00-13:00), with peak values close to 700-750 W/m². This behavior reflects the effective alignment of the tracking plane with the sun's apparent motion, maximizing the incident radiation during the central hours of the day.

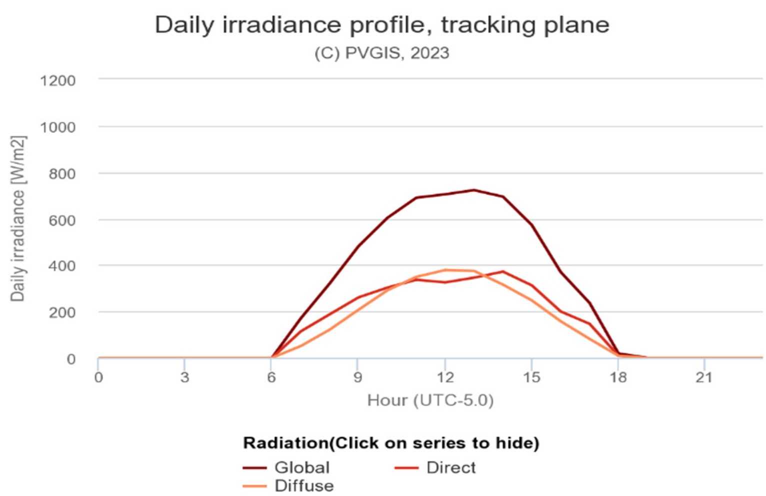

Figure 1. Daily irradiance data for Chacón Playa, Timbiquí

Source: [39]

Fig. 2 illustrates the hourly evolution of the daily average ambient temperature, as obtained from the PVGIS database. The temperature profile exhibits a clear diurnal pattern, with relatively stable values during nighttime hours and a gradual increase after sunrise, followed by a peak in the early afternoon. From a PV performance perspective, this temperature profile is particularly relevant, as higher ambient temperatures coincide with periods of maximum solar irradiance. This overlap may lead to increased module operating temperatures and, consequently, to a reduction in conversion efficiency.

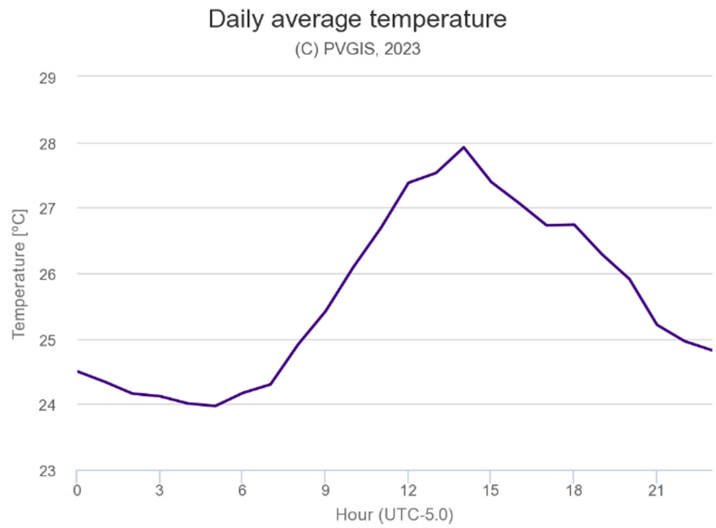

Figure 2. Daily temperature data for Chacón, Timbiquí

Source: [39]

Once the solar irradiance and temperature data had been collected, we selected the actual generation equipment for the DC microgrid. The details of the solar panels and batteries obtained from the datasheets and considered in the simulation are given below.

Polycrystalline Solar Module CS6C-145P

- Brand: Canadian Solar CS6C-145 P
- Maximum power: Pmax = 145 W
- Optimum operating voltage: Vmp = 17.9 V
- Optimum operating current: Imp = 8.09 A
- Open-circuit voltage: Voc = 22.2 V
- Short-circuit current: Isc = 8.65A
- Cells per polycrystalline module: Ncell = 36
- Operating temperature: -40℃ ~+ 85℃
- Power tolerance: ± 3%

Lithium Battery LFP12V100 12V 100 Ah deep cycle

- Nominal voltage = 12.8 V
- Nominal capacity = 100 Ah
- Cycles at 100% = 2000
- Cycles at 80% = 3600
- Energy = 1280 Wh

- Maximum depth of discharge = 80%
- Maximum output current = 100 A

The proposed microgrid is primarily intended to address one of the most pressing needs of the area, which is to provide energy for food preservation. Therefore, a DC solar freezer was selected as the load to be powered by the DC microgrid. This choice is due to the microgrid's focus on operating in isolation and with DC loads, which allows evaluating its technical feasibility.

The technical data of the DC freezer are presented below.

Solar horizontal freezer 430 liters 24V

- System voltage = 24 VDC
- Input voltage range = 21.3 to 31.5 V
- Deep discharge protection = 22.8 V
- Power = 72 W
- Recommended fuse = 7.5 A

Based on the above-presented information, the DC microgrid was designed. The key components of this microgrid include a solar PV generation system, composed of four solar panels connected in series and in parallel; a storage center based on two batteries connected in series; a DC-DC boost converter; a bidirectional DC-DC converter; and the specific load to be fed, which, in this case, consisted of four DC solar chillers. Fig. 3 shows the microgrid design, which was used to conduct our simulations.

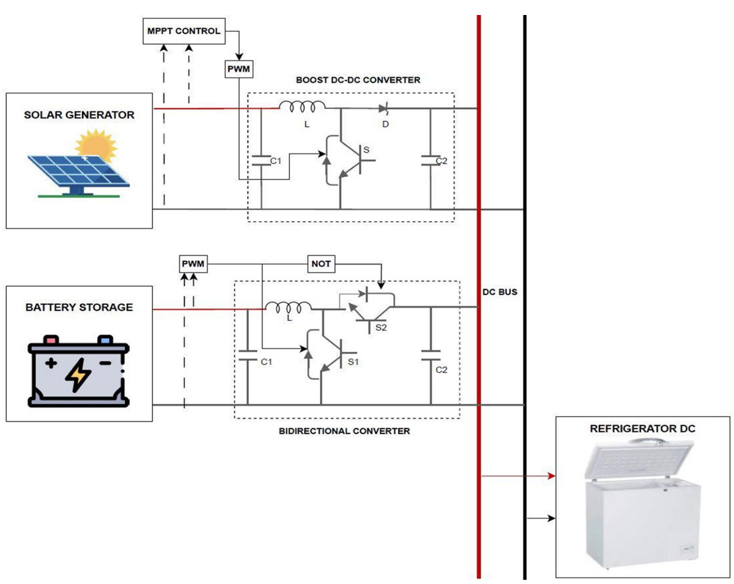

Figure 3. DC microgrid design

After developing the microgrid structure, it was essential to ensure a constant power flow to the four selected chillers. To this effect, the microgrid had to be equipped with a power electronics system comprising converters and their corresponding control systems. These components are vital to maintaining proper voltage and current levels in the DC bus, allowing each of the chillers to be adequately powered. The boost converter was entrusted with raising the voltage of the solar generation source to the values required by the microgrid. On the other hand, the bidirectional converter was responsible for supplying controlled energy to the batteries and, if necessary, delivering it to the microgrid. In this role, the bidirectional converter can act as a step-down buck converter or as a boost converter depending on the specific demands of the microgrid.

The objective was to power four 72 W chillers, which requires supplying a total power of 288 W. The system was configured to maintain a constant voltage of 24 V on the DC bus to power the load, since the microgrid was set at 24 V. To achieve this, it was essential to properly size the DC-DC converters (both boost and bidirectional), which had to be able to handle the total power of 288 W and guarantee a constant 24 V.

The calculations for the electrical circuit components of each converter were conducted under the standard procedures and equations presented below [40], [41]:

$$L = \frac{Vi * \left(Vo - Vi\right)}{\Delta I_l * Fs * Vo} \tag{1}$$

$$C = \frac{Io * 1 - \frac{Vi}{Vo}}{Fs * \Delta Vo} \tag{2}$$

$$D = \frac{Vo - Vi}{Vo} \tag{3}$$

First, parameters were defined according to the technical datasheet of modules, batteries and frezzer presented above. The calculation of the electrical components of the DC-DC boost converter of the solar array was conducted using the following equations, which are presented with their corresponding results:

$$P = 4 * Pmax = 4 * 145W = 580W \tag{4}$$

$$Vi = Vmp = 17.9V \tag{5}$$

$$Fs = 10KH_z \tag{6}$$

$$Vo = 24V \tag{7}$$

$$Io = \frac{P}{Vo} = 24.17\,A \tag{8}$$

$$\Delta I_L = 0.01 * Io * \frac{Vo}{Vi} = 0.3240 \tag{9}$$

$$\Delta Vo = 0.01 * Vo = 0.24 \tag{10}$$

$$L = \frac{Vi * (Vo - Vi)}{\Delta I_l * Fs * Vo} = 0.0014\,H \tag{11}$$

$$C = \frac{Io * 1 - \frac{Vi}{Vo}}{Fs * \Delta Vo} = 0.0026\,F \tag{12}$$

$$P = \#modulos * Pmax = 4 * 145W = 580W \tag{13}$$

$$Vi = (2 * 12)V * 0.9 = 21.6V \tag{14}$$

$$Fs = 10KH_z \tag{15}$$

$$Vo = 24V \tag{16}$$

$$Io = \frac{P}{Vo} = 24.17\,A \tag{17}$$

$$\Delta I_L = 0.01 * Io * \frac{Vo}{Vi} = 0.2685 \tag{18}$$

$$\Delta Vo = 0.01 * Vo = 0.24 \tag{19}$$

$$L = \frac{Vi * (Vo - Vi)}{\Delta I_l * Fs * Vo} = 8.044 * 10^{-4}\,H \tag{20}$$

$$C = \frac{Io * 1 - \frac{Vi}{Vo}}{Fs * \Delta Vo} = 0.0010\,F \tag{21}$$

In these calculations, we emphasized that the variable parameter is the input voltage Vi, which is equivalent to 90% of the nominal battery voltage. The main purpose of the bidirectional converter in this configuration is to maintain a constant voltage of 24 V in the microgrid and, if necessary, to take advantage of the battery as a complementary power supply. Performing these calculations is essential, as it allows determining the precise inductance and capacitance values required to ensure the optimal operation of the bidirectional converter for the microgrid and the load requirements.

Once the sizing of the converters had been completed, it became essential to implement a controller to measure the duty cycles of these converters, with the aim of monitoring and optimizing their efficiency. To this effect, MPPT control was adopted, which is based on the incremental conductance algorithm. The purpose of this strategy was to keep the solar system operating at its maximum power point, even in the face of variations in solar irradiance or temperature. We mainly aimed to improve efficiency in the conversion of the energy absorbed by the solar system. This algorithm focuses on adjusting the voltage of the solar system while considering the derivative of the power with respect to the converter voltage—this is achieved by constant measurements of the current and voltage in the system. The above can be explained with the following equation and the incremental conductance algorithm diagram shown in Fig. 4.

$$\frac{dP}{dV} = \frac{d(IV)}{dV} = I + \frac{dI}{dV}V \tag{22}$$

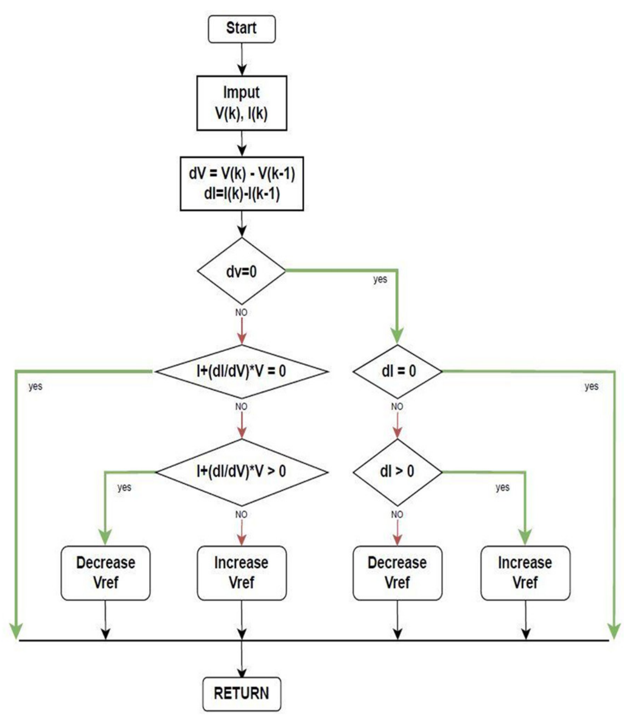

Figure 4. MPPT incremental conductance algorithm

Source: inspired by [41]

The algorithm operates as follows. First, the controller receives the initial values of current and voltage from the solar system. Next, the power is calculated, and the converter connected to the PV system is initialized to the optimum operating voltage. Then, the variations in current and voltage in the converter are calculated. Afterwards, the derivative of power with respect to the converter voltage is calculated. Depending on whether this derivative is equal to, greater than, or less than zero, the converter output voltage is adjusted to operate near the maximum power point. If the derivative of power with respect to voltage is not greater than zero, the output voltage is increased. Conversely, if it is greater than zero, the voltage is reduced. This algorithm operates in a continuous cycle to keep the converter output as close as possible to the maximum power point.

Once the MPPT control system had been defined, we simulated the microgrid using MATLAB-Simulink software and its Simscape complement. A diagram showing our proposal's structure and its different components is shown in Fig. 5.

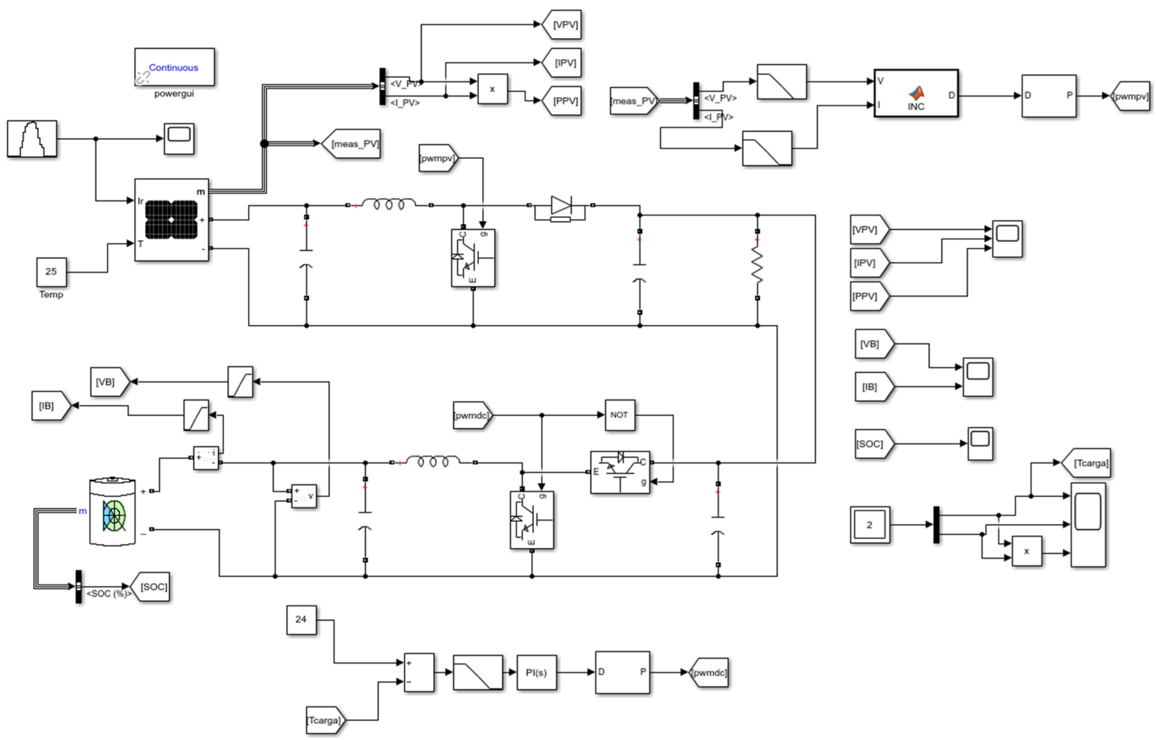

Figure 5. Implementation of our DC microgrid in Simulink

A commercial PV module was selected from the Simulink library, specifically the Canadian Solar CS6C-145P, whose electrical characteristics were presented above. The PV array was configured using four modules arranged in two series-connected modules per string and two parallel strings.

Simulink also enabled the selection of an energy storage system based on predefined characteristic curves. In this study, two lithium iron phosphate ($LiFePO_4$) batteries—model LFP12V100 (12 V, 100 Ah)—were employed and connected in series to form the battery bank. The load was modeled as a constant DC load with an active power demand of 288 W, representing the operation of four DC coolers.

A boost converter and a bidirectional DC-DC converter were incorporated into the system. The inductance and capacitance values of both converters were calculated analytically and implemented in the model. The solar irradiance and ambient temperature inputs to the PV module were defined using a step function and a constant value, respectively, based on the data obtained from the PVGIS platform for the Chacón-Timbiquí region.

To enhance the efficiency of the power converters, appropriate control strategies were implemented. An incremental-conductance MPPT algorithm was applied to the boost converter and developed using a MATLAB function. The initial reference voltage was set to 0 V, with a maximum voltage limit defined according to the module's optimal operating voltage of 17.9 V and a reference value close to 15 V. For the bidirectional converter, a proportional-integral (PI) controller was employed to regulate the DC bus voltage, with the proportional and integral gains set to 0.001 and 0.1, respectively.

The remaining components of the microgrid, including the switches, filters, measurement blocks, DC-DC PWM generators, and comparison elements, were implemented using standard Simulink blocks. Once the system architecture had been completed, simulations were conducted to evaluate the technical feasibility and dynamic response of the microgrid under the specified operating conditions. The objective was to maintain a regulated DC bus voltage of 24 V while supplying a constant power of 288 W to the DC load.

Said simulations were performed over a 24-hour period using time-varying irradiance profiles derived from PVGIS data and assuming an average ambient temperature of 25 °C for the studied location.

The simulation results can be seen in Figs. 6, 7, 8 and 9, respectively.

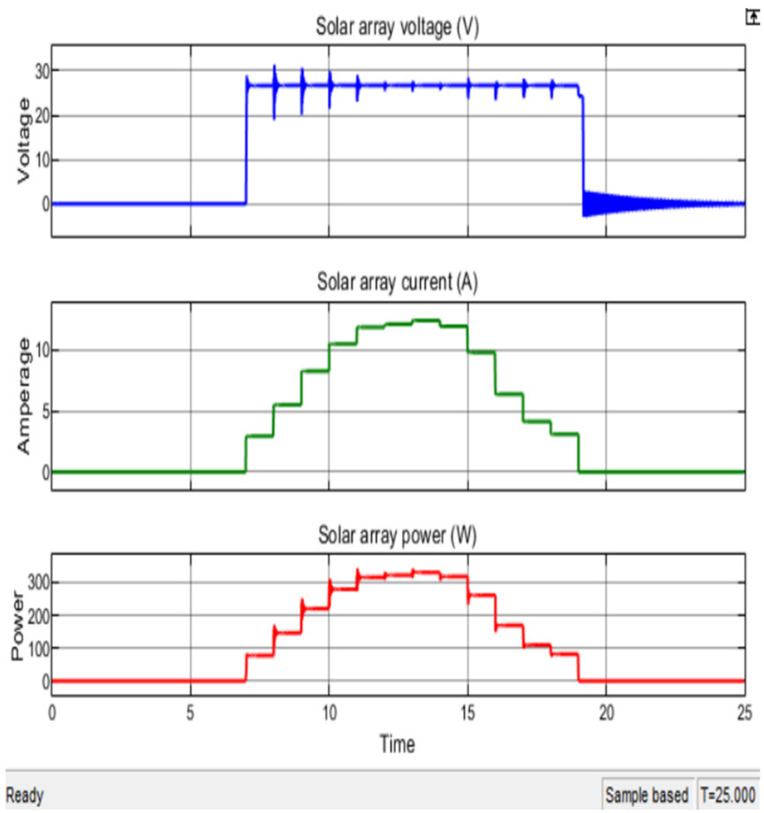

Figure 6. PV system response

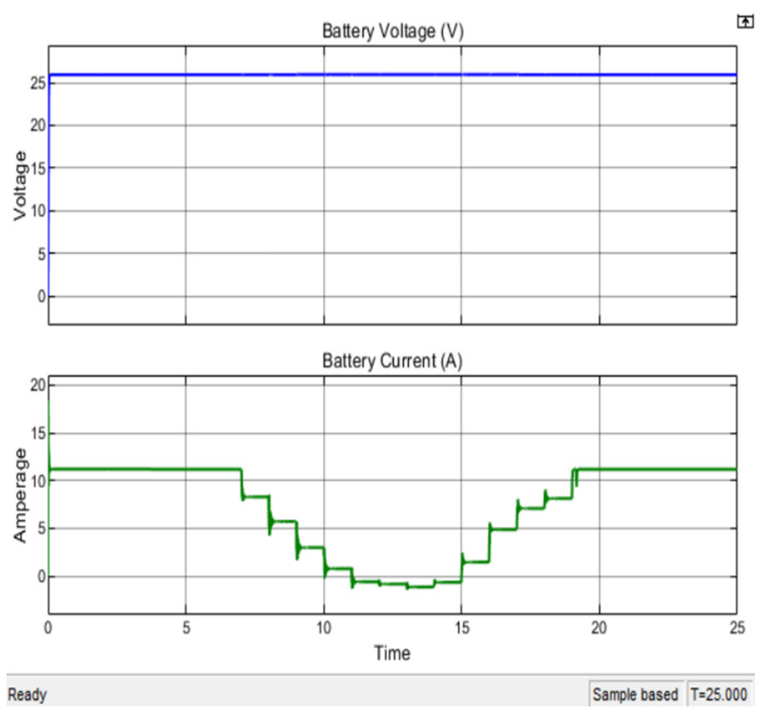

Figure 7. Battery response

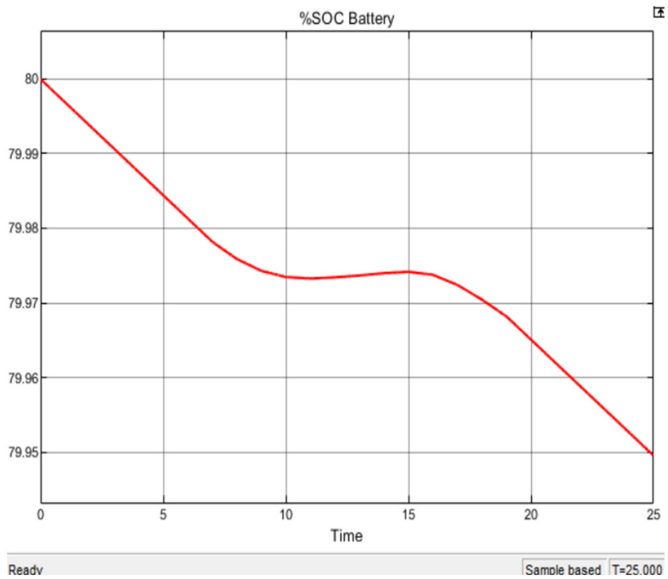

Figure 8. %SOC response

The simulation and the behavior of the microgrid must be adapted to the variations in the global irradiance, which was previously shown in Figure 1. In this graphical representation, it is observed that the irradiance is zero from 12 am to 6 am. Between 7 am and 7 pm, a variation in irradiance is recorded, reaching its maximum value at 1 pm with a total of 722 W/m^2. Subsequently, between 8 pm and 11 pm, the irradiance returns to zero. It is essential that the system is able to operate efficiently under these conditions.

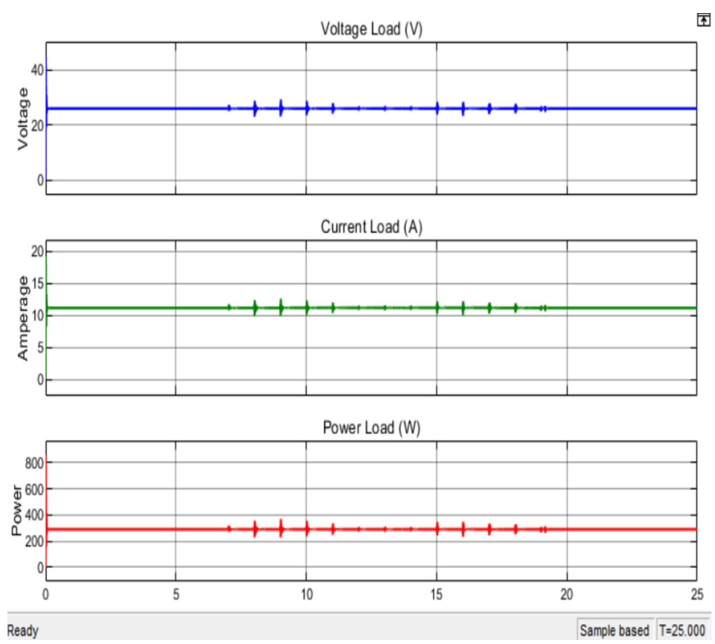

Figure 9. DC chiller load response

Fig. 6 illustrates the response of the solar array during these changes in irradiance. During periods of high irradiance, the system, with the help of the boost converter and its corresponding controller, maintains the voltage close to 24 V, where the current varies according to the fluctuations in irradiance. This naturally affects the power delivered by the solar array, which also varies according to these changes.

When irradiance is low or zero, the solar array provides little or no power. At these times, the batteries come into play as a storage source, wherein the supplied voltage is also maintained at a constant 24 V throughout the operation. Here, the current is also adjusted according to the presence or absence of irradiance, as shown in Fig. 7. The batteries play a crucial role in supplementing the microgrid during hours of low or no solar irradiance, serving as a backup source to maintain optimal levels of power supplied to the load.

Fig. 8 provides a glimpse of the charging and discharging behavior of the batteries, which start at 80% charge. In the absence of solar radiation, the batteries gradually discharge by supplying power to the microgrid. When solar radiation is present again, the batteries are recharged.

Fig. 8 shows how the four DC coolers are provided with a constant voltage of 24 V, with a current of approximately 10 A and a power output of about 288 W. This guarantees their operation and demonstrates the technical feasibility of the microgrid to meet the voltage and current demands of the chillers in response to changes in solar radiation, with the aim of supplying the demanded power.

This system evidences the potential of DC microgrids to meet the energy needs in the region, especially in non-interconnected areas such as Chacón-Timbiquí in the department of Cauca. The simulation supports the technical feasibility of providing a reliable and essential energy supply in response to the priorities of this area.

5. CONCLUSIONS

This paper demonstrates that DC microgrids constitute a technically superior solution for supplying electricity in NIZ, as their architecture reduces the number of power conversion stages, resulting in more compact, efficient, and cost-effective systems compared to their AC counterparts. By eliminating the need for frequency regulation and reactive power management, DC microgrids provide high-quality and reliable electricity supply, particularly suitable for geographically dispersed rural communities. The results show that a significant reduction in diesel generator dependence—up to 85%—can be achieved, thereby mitigating fuel transportation costs and CO_2 emissions. The integration of PV generation with battery energy storage systems enables remote communities, such as Chacón Playa, to achieve energy autonomy and maintain service continuity even under low or zero solar irradiance conditions. Furthermore, the proposed DC microgrid supports critical local economic and healthcare activities by enabling reliable food and medical supply preservation through DC loads such as refrigeration systems. System feasibility was validated through simulations using the incremental conductance algorithm, ensuring stable 24 V regulation to protect refrigeration equipment. The adoption of a radial topology facilitates deployment in hard-to-access areas due to its reduced installation complexity, ease of maintenance, and inherent scalability, allowing expansion to multiple buses as community demand increases without compromising system stability. Finally, the findings provide technical evidence to support the development of regulatory frameworks that promote the adoption of DC microgrids as a reliable and sustainable alternative, contributing to national objectives of universal electricity access and social development in remote regions of Colombia.

The future of DC microgrids is shaped by several research and technological development directions aimed at addressing current challenges related to standardization, efficiency, and system reliability. A key priority involves the development of regulatory frameworks and technical standards that define standardized voltage levels and operational requirements to enable the safe and accelerated deployment of DC microgrids in isolated and remote areas. Advances in energy storage technologies, including high-performance lithium-based batteries and supercapacitors, are expected to enhance the integration of variable renewable energy sources such as solar and wind power. In parallel, the incorporation of intelligent energy management and automation through smart grid technologies will enable the real-time control of generation, storage, and load dispatch, thereby improving system reliability and operational efficiency. Additionally, a trend towards increased decentralization is anticipated, with DC-based generation systems being deployed at the household and building levels, allowing end-users to manage energy autonomously and participate in electricity markets. The interconnection of multiple DC microgrids to form hybrid systems is also envisioned as a means to increase renewable penetration, expand coverage, and reduce environmental impacts in a coordinated manner. Finally, future research must address the development of advanced protection schemes capable of managing bidirectional power flows and fault conditions in DC systems, particularly considering the absence of natural current zero crossings, which complicates arc extinction in protection devices.

Author contributions

Iván Felipe Muñoz Sarria: investigation, conceptualization, software, formal analysis, writing (original draft).

Maximiliano Bueno López: Investigation, conceptualization, methodology, formal analysis, writing (review and editing).

Conflict of interest

The authors declare that there is no conflict of interest that could inappropriately influence the results obtained.

Declaration of Generative AI and AI-assisted technologies in the writing process

During the elaboration of this work, the authors did not employ any technologies associated with artificial intelligence.

References

[1] F. De La Cruz and C. Avila, "Sistemas fotovoltaicos: solución energética en las comunidades aisladas," *Rev. Cien. Ing.*, vol. 9, no. 2, 2022.

[2] M. I. Torres Villamizar, "Caracterización de soluciones para comunidades en zonas no interconectadas al sistema eléctrico en Colombia," Jul. 2022, [Online]. Available: http://hdl.handle.net/1992/59144

[3] M. Castaneda, P. Yanguas, F. Corral, E. Ángel-Sanint, F. Palacios, D. Gómez, R. Ávila, J. D. Cortés, P.-Y. Oei, S. Zapata, and I. Dyner, "Achieving a 100% renewable electricity supply in Colombia by 2030: Dream or feasible possibility?," *Sustain. Futures*, vol. 10, Art. no. 101468, 2025. https://doi.org/10.1016/j.sftr.2025.101468

[4] I. Granit, "What makes Colombia's indigenous peoples adopt microgrids? Social acceptance and financial constraints in renewable energy diffusion," *Energy Res. Soc. Sci.*, vol. 101, Art. no. 103132, Jul. 2023. https://doi.org/10.1016/j.erss.2023.1031

[5] F. Ojeda Peña, "Revisión de contenido teórico sobre microrredes y estudios previos Colombia," Universidad Santo Tomas, 2022. [Online]. Available: http://hdl.handle.net/11634/49251

[6] G. Liu, Z. Li, Y. Xue, and K. Tomsovic, "Microgrid assisted design for remote areas," *Energies*, vol. 15, no. 10, Art. no. 3725, May 2022. https://doi.org/10.3390/en15103725

[7] UPME, "Plan Indicativo de Expansión de Cobertura de Energía Eléctrica," 2019. [Online]. Available: https://www1.upme.gov.co/siel/PIEC/2019-23/2019/Informacion_Base_PIEC_Dic302019.pdf

[8] J. A. Cerón, E. Gómez-Luna, and J. C. Vasquez, "Driving the Energy Transition in Colombia for Off-Grid Regions: Microgrids and Non-Conventional Renewable Energy Sources," *Energies*, vol. 18, no. 4, Art. no. 1010, Feb. 2025. https://doi.org/10.3390/en18041010

[9] T. Mosetlhe, A. Yusuff, T. Ayodele, and A. Ogunjuyigbe, "Sustainable rural electrification through micro-grids in developing nations—A review of recent development," *Energy Reports*, vol. 13, pp. 1171–1177, 2025. https://doi.org/10.1016/j.egyr.2024.11.040

[10] F. Randibarnas, K. S. Gautama, E. Agustian, T. Ardriani, J. Furqani, and A. Rizqiawan, "A distributed PCS based DC microgrid system for rural electrification," in *Proc. 5th Int. Conf. Power Eng. Renew. Energy (ICPERE)*, 2022, pp. 1–6. https://doi.org/10.1109/ICPERE56870.2022.10037531

[11] D. Li and C. N. M. Ho, "A module-based plug-n-play DC microgrid with fully decentralized control for IEEE Empower a Billion Lives competition," *IEEE Trans. Power Electron.*, vol. 36, no. 2, pp. 1764–1776, Feb. 2021. https://doi.org/10.1109/TPEL.2020.3009631

[12] N. Wang, Y. Jiang, Y. Wang, D. Mou, Y. Liu, and W. Hu, “Advanced operation and control schemes of retired batteries in DC microgrid for secondary usage,” *IEEE Trans. Smart Grid*, vol. 16, no. 4, pp. 3155–3166, Jul. 2025. https://doi.org/10.1109/TSG.2025.3555181

[13] B. Modu, M. P. Abdullah, M. A. Sanusi, and M. F. Hamza, “DC-based microgrid: Topologies, control schemes, and implementations,” *Alexandria Eng. J.*, 2023. https://doi.org/10.1016/j.aej.2023.02.021

[14] A. Bastidas and A. Pantoja, “Análisis técnico-económico de una microrred DC en un edificio universitario,” Sep. 2023, pp. 1–11. https://doi.org/10.26507/paper.3209

[15] A. Valencia-Díaz, E. M. Toro, and R. A. Hincapié, "Optimal planning and management of the energy–water–carbon nexus in hybrid AC/DC microgrids for sustainable development of remote communities," *Applied Energy*, vol. 377, pt. B, Art. no. 124517, 2025. https://doi.org/10.1016/j.apenergy.2024.124517

[16] K. El Mezdi, A. El Magri, A. Watil, I. El Myasse, N. El Aadouli, and P. Kumar, "Efficient energy management of a low-voltage AC microgrid with renewable and energy storage integration using nonlinear control," *Sci. Rep*, vol. 15, no. 1, Art. no. 38651, 2025. https://doi.org/10.1038/s41598-025-22473-6

[17] N. Peter, P. Gupta, and N. Goel, "Intelligent strategies for microgrid protection: A comprehensive review," *Appl. Energy*, vol. 379, Art. no. 124901, 2025. https://doi.org/10.1016/j.apenergy.2024.124901

[18] S. Anbuchandran, M. Arumuga Babu, D. Silas Stephen, and M. Thinakaran, "Dynamic voltage regulation in DC microgrids using super-twisting sliding mode controllers," *Electr Eng*, vol. 107, no. 11, pp. 14205–14227, 2025. https://doi.org/10.1007/s00202-025-03256-8

[19] M. Fotopoulou, D. Rakopoulos, D. Trigkas, F. Stergiopoulos, O. Blanas, and S. Voutetakis, "State of the art of low and medium voltage direct current (DC) microgrids," *Energies*, vol. 14, no. 18, Art. no. 5595, Sep. 2021. https://doi.org/10.3390/en14185595

[20] S. Jayaprakash, B. Gopi, M. G. Raj, S. Sujith, S. Deepa, and S. Swapna, “Development of Energy Management System for Micro Grid Operation,” *Comp. Syst. Sci. Eng.*, vol. 45, no. 3, pp. 2537–2551, 2023. https://doi.org/10.32604/csse.2023.032038

[21] S. Coffey, V. Timmers, R. Li, G. Wu, and A. Egea-Àlvarez, "Review of MVDC applications, technologies, and future prospects," *Energies*, vol. 14, no. 24, Art. no. 8294, Dec. 2021. https://doi.org/10.3390/en14248294

[22] V. F. Pires, A. Pires, and A. Cordeiro, “DC Microgrids: Benefits, Architectures, Perspectives and Challenges,” *Energies (Basel)*, vol. 16, no. 3, Feb. 2023. https://doi.org/10.3390/en16031217

[23] V. Srimathi and D. Vijayakumar, "Design and Implementation of Power Management System in Multi-String Solar-Interfaced DC Microgrid With Energy Storage System," *IEEE Access*, vol. 13, pp. 140012-140027, 2025. https://doi.org/10.1109/ACCESS.2025.3595594

[24] Z. Ali *et al.*, “Fault Management in DC Microgrids: A Review of Challenges, Countermeasures, and Future Research Trends,” *IEEE Access*, vol. 9, pp. 128032–128054, 2021. https://doi.org/10.1109/ACCESS.2021.3112383

[25] A. Baqar, M. B. Camara, and B. Dakyo, “Supercapacitors Fast Ageing Control in Residential Microgrid Based Photovoltaic/Fuel Cell/Electric Vehicle Charging Station,” *Energies (Basel)*, vol. 16, no. 13, p. 5084, Jun. 2023. https://doi.org/10.3390/en16135084

[26] S. S. Rangarajan, R. Raman, A. Singh, C. K. Shiva, R. Kumar, P. K. Sadhu, E. R. Collins, and T. Senjyu, "DC Microgrids: A Propitious Smart Grid Paradigm for Smart Cities," *Smart Cities*, vol. 6, no. 4, pp. 1690–1718, Jul. 2023. https://doi.org/10.3390/smartcities6040079

[27] J. A. G. Archetti *et al.*, “Real time validation of a control system for microgrids with distributed generation and storage resources,” *Elec. Power Syst. Res.*, vol. 223, Oct. 2023, https://doi.org/10.1016/j.epsr.2023.109683

[28] B. Aljafari, S. Vasantharaj, V. Indragandhi, and R. Vaibhav, "Optimization of DC, AC, and Hybrid AC/DC Microgrid-Based IoT Systems: A Review," *Energies*, vol. 15, no. 18, Art. no. 6813, Sep. 2022. https://doi.org/10.3390/en15186813

[29] J. Kang, B. Hao, Y. Li, H. Lin, and Z. Xue, “The Application and Development of LVDC Buildings in China,” *Energies (Basel)*, vol. 15, no. 19, Art. no. 7045, Oct. 2022, https://doi.org/10.3390/en15197045

[30] M. Nasir, S. Iqbal, H. A. Khan, J. C. Vasquez, and J. M. Guerrero, “Sustainable rural electrification through solar PV DC microgrids—An architecture-based assessment,” *Processes*, vol. 8, no. 11, pp. 1–23, Nov. 2020, https://doi.org/10.3390/pr8111417

[31] H. M. Mohan and S. K. Dash, “Renewable Energy-Based DC Microgrid with Hybrid Energy Management System Supporting Electric Vehicle Charging System,” *Systems*, vol. 11, no. 6, p. 273, May 2023, https://doi.org/10.3390/systems11060273

[32] S. Azizi, M. H. Asemani, N. Vafamand, S. Mobayen, and A. Fekih, “Adaptive Neural Network Linear Parameter-Varying Control of Shipboard Direct Current Microgrids,” *IEEE Access*, vol. 10, pp. 75825–75834, 2022, https://doi.org/10.1109/ACCESS.2022.3191385

[33] J. Díaz , “Propuesta metodológica para el análisis integral de la factibilidad de la implementación de microrredes para zonas no interconectadas (ZNI) colombianas,” Universidad de los Andes, 2023. [Online]. Available: http://hdl.handle.net/1992/69629

[34] Y. L. Correa, I. F. Muñoz, F. Franco Obando, and M. Bueno Lopez, "Computational comparison of AC and DC motors to hydrodynamic changes in marine fishing vessels," *TecnoL*, vol. 26, no. 56, Art. no. e2442, 2023. https://doi.org/10.22430/22565337.2442

[35] M. Bueno Lopez, M. T. Rengifo Ordoñez, D. Chacón Campo, J. Tocancipá-Falla, and A. Osorio Arias, "Energy Transition for rural development: A preliminary case study in Colombia for improving artisanal fishing," *Sci. Tech*, vol. 29, no. 2, pp. 89–96, 2024. https://doi.org/10.22517/23447214.24944

[36] IPSE, “Informe Mensual de telemetría,” 2023. [Online]. Available: https://ipse.gov.co/cnm/informes-de-operacion/

[37] K. Jithin, P. P. Haridev, N. Mayadevi, R. Hari Kumar, and V. P. Mini, "A Review on Challenges in DC Microgrid Planning and Implementation," *J. Mod. Power Syst. Clean Energy*, vol. 11, no. 5, pp. 1375–1395, Sep. 2023. https://doi.org/10.35833/MPCE.2022.000053

[38] T. Castillo-Calzadilla, M. A. Cuesta, C. Olivares-Rodriguez, A. M. Macarulla, J. Legarda, and C. E. Borges, "Is it feasible a massive deployment of low voltage direct current microgrids renewable-based?

A technical and social sight," *Renew. Sustain. Energy Rev.*, vol. 161, Art. no. 112198, Jun. 2022. https://doi.org/10.1016/j.rser.2022.112198

[39] PVGIS, "Solar radiation," 2022. [Online]. Available: https://re.jrc.ec.europa.eu/pvg_tools/en/#MR

[40] J. F. Franco Martínez and B. S. Laserna Murcia, " Diseño y simulación de controladores por aprendizaje reforzado para convertidores de potencia utilizados en micro redes de corriente directa.," Universidad Antonio Nariño, 2023. [Online]. Available: http://repositorio.uan.edu.co/handle/123456789/8263

[41] H.-Y. Lu, C.-E. Ye, H.-Y. Tsai, and Y.-P. Huang, "Enhanced harmony search for MPPT control in solar systems," *Results Eng*, vol. 25, Art. no. 104274, 2025. https://doi.org/10.1016/j.rineng.2025.104274

Iván Felipe Muñoz

He received his degree in Industrial Automation Engineering from Universidad del Cauca, with a specialization in Project Management from the Universidad Autónoma de Occidente. He has professional experience in projects within the electrical sector, including alternative energy initiatives and advanced metering systems. His academic interests include technological innovation, applied research, and the development of alternative energy sources.

Maximiliano Bueno López

He received a Bachelor's and a Master's degree in Electrical Engineering from Universidad Tecnológica de Pereira, Colombia, as well as a PhD in Engineering from Universidad Nacional Autónoma de México. He served as a postdoctoral researcher at the Norwegian University of Science and Technology (NTNU), in the Department of Engineering Cybernetics. He currently serves as an associate professor at Universidad Tecnológica de Pereira, Pereira, Colombia. Email: m.bueno3@utp.edu.co.edu.co

UNIVERSIDAD DISTRITAL
FRANCISCO JOSÉ DE CALDAS

Ingeniería

https://revistas.udistrital.edu.co/index.php/reving/issue/view/1320

DOI: https://doi.org/10.14483/23448393.22514

Research

Comparative Analysis of the Standards ANSI/IEEE C.37 and 141 and IEC 60909 for Short-Circuit Calculation in Industrial Systems

Análisis comparativo de las normas ANSI/IEEE C.37 y 141 e IEC 60909 para el cálculo de cortocircuitos en sistemas industriales

John Muñoz-Goez[1], Joseph C. Sosapanta-Salas[1], and Jhon Noguera-Jiménez[2]

[1]Institución Universitaria Pascual Bravo, Medellín, Colombia
[2]Unidad Central del Valle del Cauca, Tuluá, Colombia

Abstract

Context: Calculating short-circuit currents is key to equipment sizing and protection coordination in electrical power systems. However, methodological differences between ANSI/IEEE C.37 and 141 and IEC 60909 create uncertainty when selecting the most appropriate approach. This study addresses this problem through a comparative analysis based on computer simulations that evaluate both methodologies under equivalent conditions.

Method: An industrial system with 44 busbars is modeled in ETAP (version 20.0), considering grid connection, local generation, and rotating loads. Short-circuit currents are calculated while following the procedures of both standards, and five representative fault points are analyzed. The evaluation includes six parameters: symmetrical inrush current, half-cycle closing current, peak fault current, interrupting current, asymmetrical breaking current, and steady-state current.

Results: The IEC method yields values between 5 and 10% higher than those obtained with ANSI/IEEE in most cases. The greatest differences are observed at busbars near generators and higher-power rotating machines, reaching up to 9.34% in the inrush current. These variations are mainly associated with the treatment of the X/R ratio and the voltage factor c applied in IEC.

Conclusions: The IEC 60909 standard offers more conservative estimates for demanding designs, while ANSI/IEEE is useful in preliminary analyses, providing practical criteria for selecting the standard based on system criticality.

Keywords: electrical system modeling, electrical transient analyzer program (ETAP), load flows, protection coordination

Article history

Received:
July 22nd, 2024

Modified:
December 28th, 2025

Accepted:
February 23rd, 2026

Ing, vol. 31, no. 1, 2026, e22514

* Correspondence: j.sosapantasa@pascualbravo.edu.co

Resumen

Contexto: El cálculo de corrientes de cortocircuito es clave para el dimensionamiento de equipos y la coordinación de protecciones en sistemas eléctricos de potencia. Sin embargo, las diferencias metodológicas entre las normas ANSI/IEEE C.37 y 141 e IEC 60909 generan incertidumbre al seleccionar el enfoque más adecuado. Este estudio aborda esta problemática mediante un análisis comparativo basado en simulaciones computacionales que evalúan ambas metodologías bajo condiciones equivalentes.
Método: Se modela un sistema industrial de 44 barras en ETAP (versión 20.0), considerando conexión a la red eléctrica, generación local y cargas rotativas. Las corrientes de cortocircuito se calculan siguiendo los procedimientos de ambas normas y se analizan cinco puntos de falla representativos. La evaluación incluye seis parámetros: corriente inicial simétrica, corriente de cierre de medio ciclo, corriente pico de falla, corriente de interrupción, corriente de ruptura asimétrica y corriente en estado estable.
Resultados: El método IEC presenta valores entre un 5 y un 10% superiores a los obtenidos con ANSI/IEEE en la mayoría de los casos. Las mayores diferencias se observan en barras cercanas a generadores y máquinas rotativas de mayor potencia, alcanzando hasta un 9.34 % en la corriente de cierre. Estas variaciones se asocian principalmente con el tratamiento de la relación X/R y el factor de voltaje c aplicado en IEC.
Conclusiones: La norma IEC 60909 ofrece estimaciones más conservadoras para diseños exigentes, mientras que ANSI/IEEE resulta útil en análisis preliminares, proporcionando criterios prácticos para seleccionar la norma según la criticidad del sistema.

***Palabras clave*:** modelado de sistemas eléctricos, programa de analizador de transitorios eléctricos (ETAP), flujos de carga, coordinación de protecciones

Contents

I. Introduction

An accurate calculation of short-circuit currents is essential in ensuring the safety and efficiency of electrical systems, as it directly influences equipment sizing and protection coordination [1]. International guidelines such as the ANSI/IEEE standards (C37.5, C37.13, C37.010, and 141) and IEC 60909 address these calculations. However, they differ in their methodologies and parameters. These discrepancies have generated ongoing debate regarding which standard provides more accurate and suitable results under different system conditions [1], [2], [3]. The literature also highlights that variations in calculated short-circuit currents can affect protection coordination and equipment design, impacting both system safety and operating costs [4].

This study aims to compare the methodologies of both standards by performing short-circuit simulations in an industrial distribution system using the electrical transient analyzer program (ETAP), version 20.0. The analysis will identify key differences between the standards and evaluate their impact on electrical design, providing recommendations to support the selection of the most appropriate standard for specific industrial applications. This comparison is motivated by the need to support engineers in selecting the most suitable standard depending on equipment requirements and study objectives. ANSI/IEEE standards are often preferred for circuit breaker duty and protection coordination studies, while IEC 60909 is commonly applied when standardized calculation assumptions are required.

Several studies and technical standards provide methodologies for calculating short-circuit currents, among which the ANSI/IEEE and IEC approaches stand out. These standards differ significantly in terms of accuracy and applicability, which has motivated a wide range of comparative research, assessing their effectiveness in different contexts. Several comparative studies [4], [5], [6], [7], [8] have conducted detailed evaluations of the IEC 60909 and ANSI/IEEE 141-4 standards, using simulation tools such as DigSILENT PowerFactory to identify key differences in the results yielded by both methods. This complements previous research [9], [10], [11], [12], [13], which has also examined the accuracy of ANSI and IEC methodologies in industrial environments and highlights their corresponding strengths and limitations. Additionally, subsequent studies [6] have investigated the applicability of IEC-based results in arc-flash calculations according to IEEE 1584, enabling a more comprehensive assessment of the risks associated with electrical faults.

Research focused on 33-11 kV substations [14] has emphasized the importance of selecting an appropriate standard to obtain accurate short-circuit current calculations in complex systems. These studies, along with other analytical works [8], [9], demonstrate the applicability and limitations of each standard across different industrial scenarios. Overall, the reviewed literature highlights the need for further studies that comprehensively assess the differences between ANSI/IEEE and IEC short-circuit calculation approaches. This research aims to contribute to this discussion by providing a comparative analysis that supports engineers in selecting the most suitable standard based on the technical requirements of each system and its specific operating conditions.

This article provides a detailed comparative analysis of the ANSI/IEEE C37 and 141 standards and IEC 60909 for short-circuit current calculations, with a specific focus on identifying discrepancies and similarities in their methodologies and results. Unlike previous studies that focus on a single standard or present non-comparative analyses, this research offers a comprehensive evaluation based on practical case studies and simulations performed using ETAP 20.0. The main technical contributions of this work include the identification of key methodological differences, an assessment of their impact on system safety and reliability, and the development of tools to improve commonly used calculation procedures through the analysis of real-world case studies.

There are methodological and parametric differences between the ANSI/IEEE and IEC standards for calculating short-circuit currents. However, their practical impact on the design and operation of industrial electrical systems has not been sufficiently investigated. Recent updates to both regulations introduce new elements that have not yet been comparatively examined in the existing literature, making it difficult to make an informed selection of the most appropriate approach. This lack of detailed and contextualized analysis creates uncertainty for engineers, particularly regarding the selection of protection devices, equipment settings, and protection coordination, all of which are critical to ensuring the safety and reliability of power systems. This research aims to address this gap by conducting a comparative analysis of both standards, using simulation tools to evaluate and document discrepancies in their results and assess their relevance in specific industrial applications.

This paper is organized as follows. Section II presents a theoretical comparison of short-circuit calculation methods, detailing the technical basis for analyzing alternating-current (AC) and direct-current (DC) components as well as network configuration. Section III describes the methodology, including the data collection process and the general procedure used to compare the standards. Section IV presents the practical case study of an industrial system, including calculations, figures, and results. Section V analyzes the results in terms of the different fault current types and the behavior of the ANSI/IEEE and IEC methods. Finally, Section VI presents the conclusions, and Section VII lists the references consulted for this research.

II. Comparison of short-circuit methods

The following subsections present a general comparison between the ANSI/IEEE C.37, ANSI/IEEE 141, and IEC 60909 standards.

A. General considerations

In ANSI/IEEE standards C37.5, C37.13, C37.010, and 141, short-circuit calculations and equipment impedance values are primarily based on parameters provided by manufacturers, with tolerance margins applied to obtain conservative fault current estimates. As for short-circuit calculations in IEC 60909, a correction factor is applied to synchronous machines and transformers in order to account for nominal operating conditions [15], [16], [17], [18].

B. Pre-fault voltage

The calculated short-circuit currents are proportional to the pre-fault voltages. The ANSI/IEEE standard assumes a maximum operating voltage, typically ranging from 100% to 105% of the nominal system voltage [2]. Therefore, the equivalent source voltage corresponding to the pre-fault condition is computed as follows:

$$U_{pre-fault} = U_{nom} = 1\, p.u. \tag{1}$$

On the other hand, the IEC standard uses a correction factor c multiplied by the nominal bus voltage and specifies its range for different voltage levels, with 1.1 being the maximum value across all voltage levels. Therefore, the equivalent voltage at the fault location is computed as follows:

$$U_{eq} = c\frac{U_n}{\sqrt{3}} \tag{2}$$

where U_{eq} denotes the equivalent voltage source, U_n is the nominal voltage of the system, and c signifies multiplicative factor.

C. Decay of AC components

ANSI/IEEE favors the adjustment of machine reactance to calculate symmetrical interrupting currents. For induction machines and synchronous motors, the decay of AC short-circuit contributions is modeled using different reactance values for the first cycle and for the system network, spanning 1.5-4 cycles. In the case of synchronous generators, different multipliers are applied to the short-circuit current depending on the electrical distance between the machine and the fault location [15], [19], [20], [21].

In contrast, the IEC recommends considering the proximity of the machine to the short-circuit, the system configuration, and the separation time. For a given fault location, system configuration and source contributions can be classified as *single-supply short-circuits*, *non-meshed network short-circuits*, and *meshed network short-circuits*. When the short-circuit occurs away from the generator, the AC decay is neglected. However, when the short-circuit is close to the generator, the AC decay is calculated based on the interruption time, the machine size, and its short-circuit contribution to the fault [6].

In this study, synchronous motors and induction machines were incorporated by assigning short-circuit current contributions according to their rated capacity and electrical proximity to the faulted bus. The transient decay was modeled using the corresponding sub-transient, transient, and steady-state reactance values, as recommended by each standard, in order to represent the time-dependent reduction of machine contributions during the interruption interval.

D. Decay of DC components

ANSI/IEEE recommends applying multipliers to symmetrical fault currents in order to calculate asymmetrical currents. A key concept in this standard for modeling the decay of DC components is the X/R ratio at the fault location. The standard requires the use of the reactance network to determine the equivalent reactance at the fault point, along with a separate resistance network to calculate the equivalent resistance. In contrast, the IEC standard is not restricted to a single X/R ratio and generally considers more than one. This approach is applicable when the fault is supplied by several independent sources [9], [22], [23], [24].

E. Network configuration

ANSI/IEEE provides a systematic approach for all types of system configurations, whether they be meshed or non-meshed. This simplifies the calculation procedure. IEC offers different approaches to AC and DC decay for single-supply, meshed, and non-meshed systems. This classification refers to a given fault location.

III. Methodology

An industrial network was modeled while including the necessary elements for a short-circuit study, adjusting the parameters in accordance with the specifications of the studied standards (ANSI/IEEE C.37 and 141 and IEC 60909) [2], [3].

A. Data collection for modeling

The data required to perform a short-circuit study include the following:

- Utility interconnection points and the corresponding fault MVA levels (both three-phase and line-to-ground) to determine the equivalent grid impedance.
- Generation data and rotating load data, including synchronous and induction motors, both individual and aggregated.

- Data for static system equipment, such as transformers, cables, reactors, overhead lines, bus ducts, and other electrical components.
- Impedance values of electrical components.

B. General procedure

The procedure required to determine the short-circuit analysis is illustrated in Fig. 1.

IV. Case study

The short-circuit study was conducted on a typical 44-bus industrial system to illustrate the required calculations and resulting outcomes. This system, shown in Fig. 2, includes circuits at multiple voltage levels, local generation, a utility interconnection, and a variety of rotating machines. The utility operates at 69 kV, while the plant generators operate at 13.8 kV. Both the utility connection and the generators are assumed to be supplying power, and the rotating loads are considered to be operating near their full capacity. The system includes both induction and synchronous motors, and its general information is shown in Table I [5].

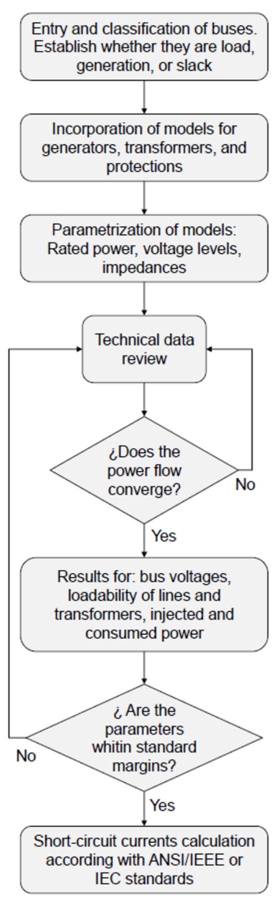

Figure 1. Procedure schematic

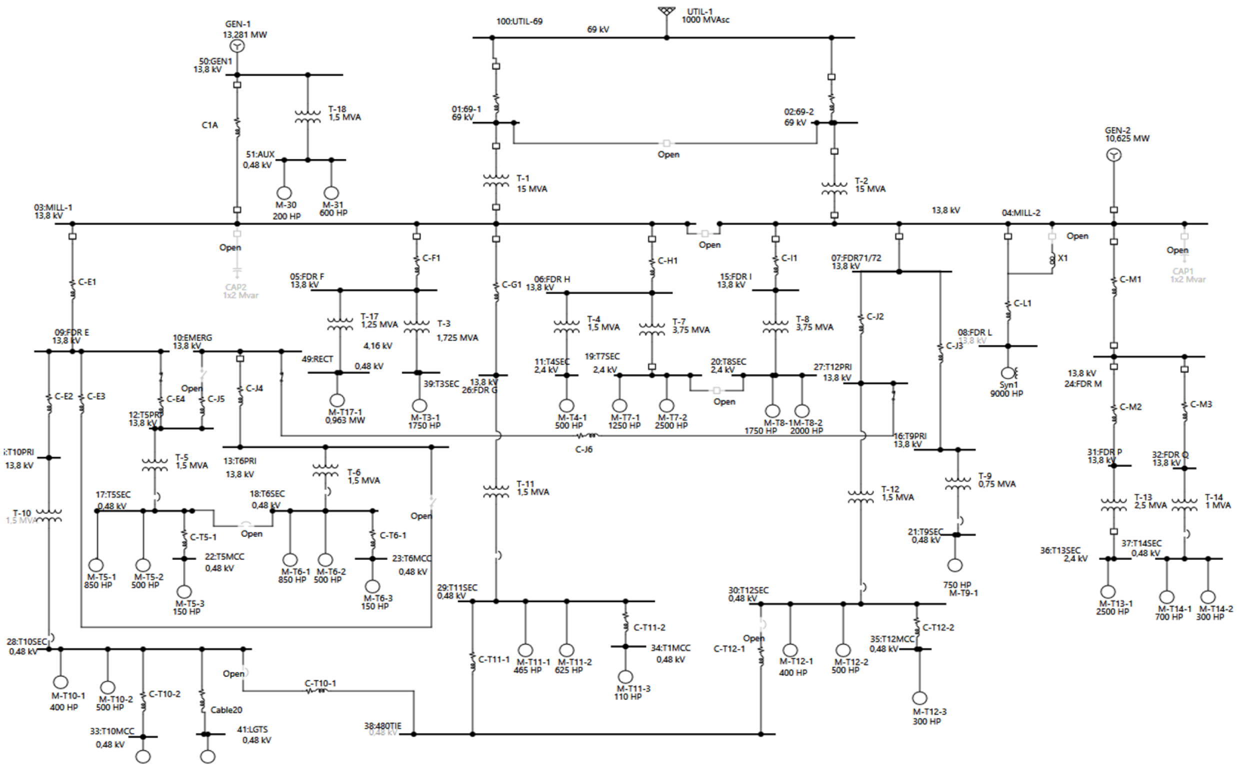

Figure 2. 44-bus industrial system

Table I. General information

Buses	44
Branches	43
Generators	2
Transmission lines	1
Loads	30
Load-MW	21.766
Load-MVAR	9.009
Generation-MW	21.919
Generation-MVAR	9.969
Losses-MW	0.156
Losses-MVAR	0.961

Considering the network topology and the base study presented in [9], the buses with the highest connected loads and the greatest fault current contributions, according to the short-circuit and load flow simulations, were selected as the fault locations, *i.e.*, 04:MILL-2, 05:FDR F, 10:EMERG, 19:T7SEC, and 50:GEN1.

V. Results analysis

The following subsections explicitly analyze the differences between the ANSI/IEEE C.37, ANSI/IEEE 141, and IEC 60909 standards. To this effect, the short-circuit modeling parameters, including the fault impedance, source representation, and X/R ratio, are assumed to be identical in order to ensure consistent results.

A. Symmetrical initial short-circuits current

ANSI/IEEE. The RMS (symmetrical) momentary short-circuit current of the first cycle for a zero-impedance fault is calculated as follows:

$$I_{mom,rms,symm} = \frac{U_f}{\sqrt{3}Z_{eq}} \quad (3)$$

where U_f is the pre-fault voltage, and Z_{eq} is the equivalent impedance at faulted bus. The latter is obtained by reducing separate networks for X and R within half-cycle.

IEC. The initial short-circuit current can be calculated using the method of symmetrical components. This approach is applicable to both meshed and non-meshed networks. For faults located close to the generator,

$$I_k^{"} = \frac{cU_n}{\sqrt{3}\,Z_k} \quad (4)$$

where Z_k denotes the equivalent impedance at the fault location. For faults far from the generator, impedance correction factors should be considered for generators (K_G) and power plant units (K_S).

The results for the initial symmetrical short-circuit currents are presented in Table II. The discrepancies largely depend on the proximity to the generators. The results show that the IEC short-circuit current values are higher than those obtained using the ANSI/IEEE approach. This difference is mainly attributed to the contribution of rotating machines located along the path between the fault sources and the fault location, which supply the momentary current. In addition, the impedance of the intervening equipment limits the fault current' contribution, affecting the calculated short-circuit currents at specific buses.

Table II. Initial symmetrical short-circuit currents

Bus	V_{nom} [kV]	ANSI/IEEE		IEC			Relative error [%]
		$\frac{X}{R}$	$I_{mon,rms,symm}$ [kA]	Factor c	$\frac{X}{R}$	$I_k^"$ [kA]	
04:MILL-2	13.8	25.169	13.598	1.1	25.2	14.7217	8.27
05:FDR F	13.8	12.439	13.630	1.1	12.5	14.8519	8.96
10:EMERG	13.8	8.881	12.684	1.1	9.0	13.7503	8.40
19:T7SEC	2.4	13.702	18.438	1.1	13.9	20.1240	9.14
50:GEN1	13.8	21.806	13.733	1.1	22.1	14.9371	8.77

B. ½ cycle short-circuit current (closing and blocking)

ANSI/IEEE. The most accurate approach is to use the asymmetrical RMS value of the momentary short-circuit current:

$$I_{mom,rms,asymm} = MF_m \cdot I_{mom,rms,symm} \tag{5}$$

where MF_m denotes the momentary multiplying factor, which is computed as

$$MF_m = \sqrt{1 + 2e^{\frac{-2\pi}{X/R}}} \tag{6}$$

The closing and blocking stress currents are asymmetric fault currents that are calculated in ½ cycle after the start of the fault [5]. ANSI/IEEE recommends the same network because, in ½ cycle, the machine model remains valid. This is performed by applying (6) with a time interval of 0.5 cycles for different X/R values.

IEC. The standard does not explicitly account for asymmetric half-cycle currents. For comparison purposes, these currents were calculated as follows:

$$I_{k\ 1/2}^" = MF_m \cdot I_k^" \tag{7}$$

The results are presented in Table III, considering that the IEC multiplying factor is set nearly identical to that of the methodology given by the ANSI/IEEE, considering the X/R ratio. The resulting short-circuit current values are very similar, with differences of less than 10%, indicating low discrepancies between the two standards. This outcome is particularly relevant for bus 19:T7SEC, a 2.4 kV node that receives contributions from two high-power motors (1250 and 2500 HP, respectively). These synchronous machines contribute significantly to the initial short-circuit current, leading to very high current values.

Table III. Closing and locking short-circuit currents

Bus	V_{nom} [kV]	ANSI/IEEE		IEC		Relative error [%]
		MF_m	$I_{mon,rms,symm}$ [kA]	MF_m	$I''_{k\,1/2}$ [kA]	
04:MILL-2	13.8	1.60	21.75	1.60	23.55	8.28
05:FDR F	13.8	1.49	20.25	1.49	22.08	9.04
10:EMERG	13.8	1.41	17.87	1.41	19.42	8.66
19:T7SEC	2.4	1.50	27.75	1.51	30.34	9.34
50:GEN1	13.8	1.58	21.71	1.58	23.64	8.90

C. Peak fault currents

ANSI/IEEE. The maximum value of the momentary short-circuit current is computed using

$$I_{mom,peak} = MF_p \cdot I_{mom,rms,symm} \tag{8}$$

where MF_p denotes the maximum multiplication factor, which is calculated as follows:

$$MF_p = \sqrt{2}\left(1 + e^{-\frac{\pi}{X/R}}\right) \tag{9}$$

IEC. The recommendation is to perform the calculation separately for each branch of the X/R ratio, and then the maximum current (I_p) is computed as follows:

$$I_p = k\sqrt{2}I''_k \tag{10}$$

where I''_k denotes initial short-circuit current, and k is a factor that depends on the system's X/R ratio at the fault location, which is obtained from Fig. 3.

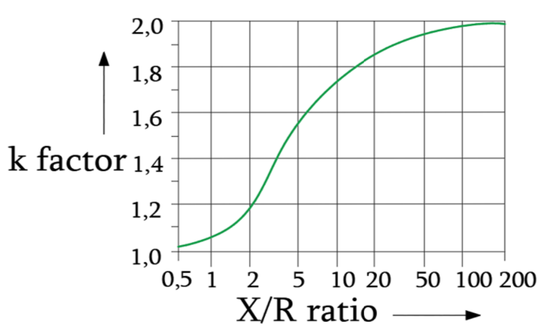

Figure 3. K-factor for series circuits as a function of $\frac{X}{R}$.

These standards describe three techniques for calculating the maximum short-circuit current in meshed networks. The c method was selected for this study [1]. Here, the equivalent impedance is calculated at the fault location using a frequency $f_c = 24$ Hz (for a nominal frequency $f = 60$ Hz). The R/X ratio is calculated as follows:

$$\frac{R}{X} = \frac{R_c}{X_c} \cdot \frac{f_c}{f} \tag{11}$$

where R_c is the real equivalent effective resistance component, and X_c denotes the imaginary equivalent effective reactance. The equivalent impedance is given by

$$Z_c = R_c + jX_c \tag{12}$$

The same calculation is applied for faults located either far from or close to the generator. In addition, impedance correction factors for generators (K_G) and/or power plant units (K_S) must be considered [11]. The results are presented in Table IV.

Table IV. Short crest and peak current

Bus	V_{nom} [kV]	ANSI/IEEE		IEC		Relative error [%]
		MF_p	$I_{mon,peak}$ [kA]	Factor k	I_p [kA]	
04:MILL-2	13.8	2.64	35.86	2.6	38.02	6.02
05:FDR F	13.8	2.47	33.65	2.5	36.89	9.64
10:EMERG	13.8	2.35	29.83	2.4	32.61	9.32
19:T7SEC	2.4	2.50	46.05	2.5	49.79	8.13
50:GEN1	13.8	2.61	35.85	2.6	38.03	6.10

D. Breakdown current

ANSI/IEEE. The interrupting currents correspond to the short-circuit currents in the time range of 1.5-4 cycles after fault inception. In this case, the contributions are considered remote, and the calculations are performed based on the total current. The symmetrical value, corrected by the factor MF_r, can be obtained as follows

$$MF_r = \sqrt{1 + 2e^{-\frac{4\pi}{X/R}t}} \tag{13}$$

where t denotes the circuit breaker contact separation time (in cycles). An alternative method is illustrated in Fig. 4.

E. Setting the interrupting current

The real multiplication factor (AMF_i) is determined using the $NCAD$ relationship.

$$AMF_i = MF_l + NCAD \tag{14}$$

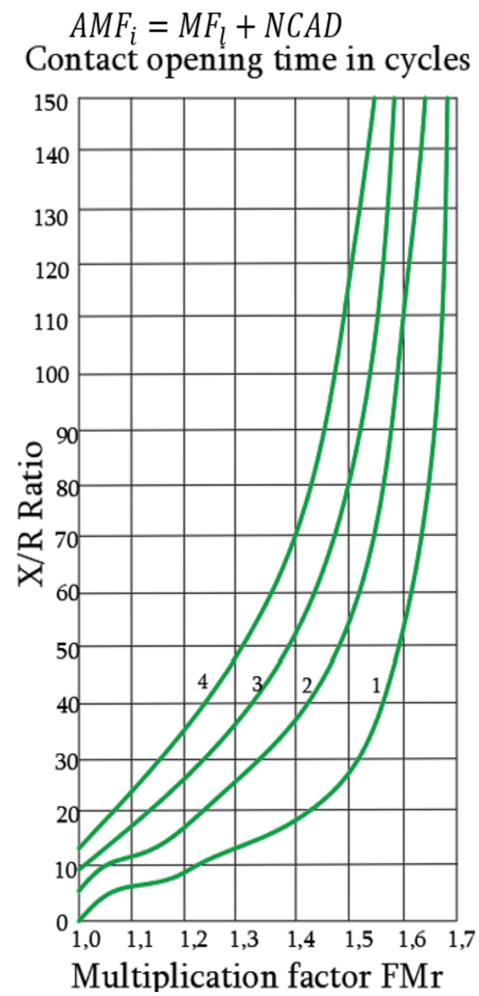

Figure 4. Remote multiplication factor.

For symmetrically rated circuit breakers, the adjusted RMS interrupting short-circuit current is calculated using

$$I_{int,rms,adj} = \frac{AMF_i \cdot I_{int,rms,symm}}{S} \tag{15}$$

where $NCAD$ represents the remote contributions to the total short-circuit current. The variable S is the correction factor that considers the AC high voltage switch.

IEC. The breaking current is used to determine the breaking capacity of automatic switches. For faults located far from the generator, it is expressed as follows:

$$I_b = I"_k \tag{16}$$

For faults near the generator, the DC component of the short-circuit current is given by

$$I_{dc} = I"_k \sqrt{2} e^{\left(\frac{-2\pi f t_{min}}{\frac{X}{R}}\right)} \tag{17}$$

where f is the natural frequency, and t_{min} denotes the minimum response time of the protection device. This standard determines the calculation of the breakdown current by the type of machine [12], [25], [26]. This approach involves the calculation of synchronous machines as given by

$$I_b = \mu \cdot I"_k \tag{18}$$

where μ is decrement factor, $I"_k$ represents the initial short-circuit current, and I_b denotes the symmetrical cutting current. The factor μ is calculated as follows, depending on the minimum delay time, the ratio $\frac{I"_{kG}}{I"_{rG}}$, and the nominal generator current:

$$\mu = 0.84 + 0.26 \cdot e^{-0.26\frac{I"_{kG}}{I"_{rG}}} \quad t_{min} = 0.02s \quad \mu = 0.71 + 0.51 \cdot e^{-0.30\frac{I"_{kG}}{I"_{rG}}} \quad t_{min} = 0.05s \quad \mu = 0.62 + 0.72 \cdot e^{-0.32\frac{I"_{kG}}{I"_{rG}}} \quad t_{min} = 0.10s \quad \mu = 0.56 + 0.94 \cdot e^{-0.38\frac{I"_{kG}}{I"_{rG}}} \quad t_{min} \geq 0.25s \tag{19}$$

The factor μ can also be obtained from Fig. 5.

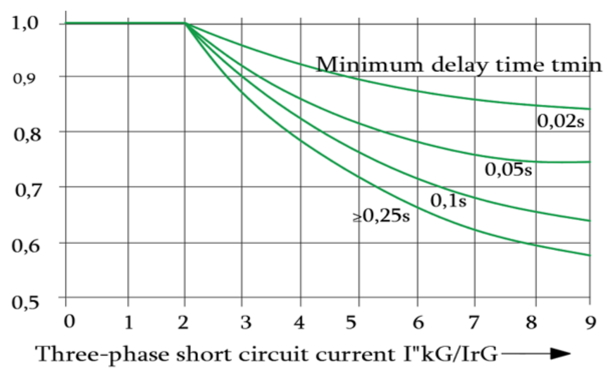

Figure 5. Factor μ for calculating short-circuit breaker current

F. Asymmetric opening current

During the closing or opening of switches, it is necessary to calculate the current flowing at the instant when the contacts separate. Therefore, the asymmetric breaking current must be determined. Starting from the symmetric breaking current I_b of the AC component, and by applying the superposition theorem, the DC component current I_{dc}, evaluated at the same instant, is added [10]. Thus, the breaking current is given by

$$I_{b,asymm} = \sqrt{I_b^2 + I_{dc}^2} \tag{20}$$

where I_{basymm} is the RMS asymmetric breaking current, I_b the RMS symmetric current of the AC component, and I_{dc} the DC component. A more detailed calculation technique involves determining the symmetrical breakdown current while considering the exact opening time, the type of machine, and its proximity to the short-circuit. For this example, the calculation is performed using a breaking time of 0.1 s, the time defined in the simulations. A detailed report of the results is presented in Table V.

Table V. Breaking and interruption current

Bus	V_{nom} [kV]	ANSI/IEEE			IEC			Relative error [%]
		X/R ratio	M_{Fr}	$I_{adj,symm}$ [kA]	I_{dc}	$I_{b,sym}$	$I_{b,asym}$	
04:MILL-2	13.8	24.832	1.067	13.314	4.049	12.205	12.859	3.42
05:FDR F	13.8	12.844	1	12.897	1.520	12.104	12.199	5.41
10:EMERG	13.8	9.242	1	11.684	0.488	11.603	11.614	0.60
19:T7SEC	2.4	13.265	1	16.661	1.537	17.019	17.088	2.57
50:GEN1	13.8	22.644	1.038	13.528	3.591	12.010	12.535	7.34

Note that, except for the generators, the effective reactances used in IEC are generally lower than those of ANSI/IEEE for short compensation times. Although IEC assumes higher pre-fault voltages, the reactance adjustment becomes the dominant factor, explaining the difference from other comparisons with higher IEC values.

G. ANSI/IEEE's time delay current vs. IEC's steady-state currents

Both the IEC and ANSI/IEEE procedures assume that transient effects have decayed by the time the steady-state current occurs and are therefore not considered in the modeling.

IEC. The amplitude of the permanent short-circuit current I_k depends on the saturation state of the magnetic circuit. For faults located far from the generator, it is computed as follows:

$$I_k = I''_k \tag{21}$$

For faults close to the generator, the maximum and minimum fault currents in the steady state under the highest and lowest excitations of the synchronous generator are given by

$$I_{kmax} = \lambda_{max} \cdot I_{rG} \; I_{kmin} = \lambda_{min} \cdot I_{rG} \tag{22}$$

where I_{kmax} is the maximum fault current, I_{kmin} the minimum current in the steady state, λ_{max} the maximum scaling coefficient, and λ_{min} the minimum scaling coefficient, which depends on the saturation inductance and the nominal generator current [11]. The values of λ_{max} and λ_{min} are obtained from Fig. 6.

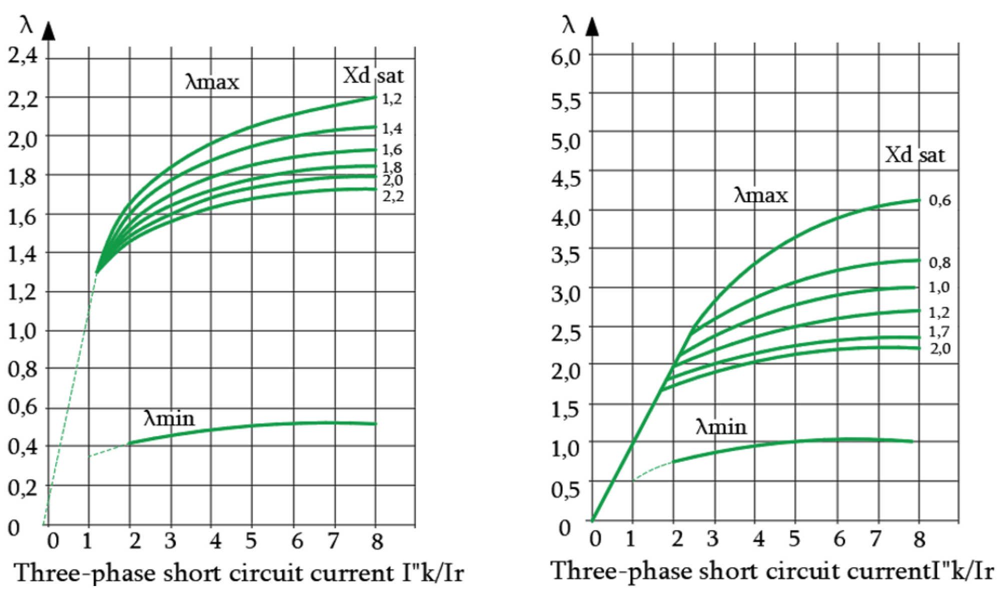

Figure 6. λ_{max} and λ_{min} factors for turbogenerators

ANSI/IEEE. The contributions of all motors are ignored, and only generators contributing to the fault are considered. The DC component is zero in a 30-cycle network. The steady-state reactance of the network components is used to calculate the fault current and the steady-state short-circuit current:

$$I_{est,rms,symm} = \frac{U_f}{\sqrt{3}Z_{eq}} \tag{23}$$

where Z_{eq} denotes the equivalent impedance at the fault point (generators and passive equipment). The permanent and delay short-circuit currents are presented in Table VI.

Table VI. Permanent and delay short-circuit currents

Bus	V_{nom} [kV]	ANSI/IEEE	IEC	Relative error [%]
		$I_{est,rms,sym}$ [kA]	I_k [kA]	
04:MILL-2	13.8	11.455	12.148	6.05
05:FDR F	13.8	11.736	12.089	3.01
10:EMERG	13.8	10.961	11.467	4.61
19:T7SEC	2.4	13.701	14.294	4.33
50:GEN1	13.8	11.921	12.199	2.33

According to ANSI/IEEE standards, the network model includes only generators, which are represented by either their transient reactance or a higher reactance value [5]. ANSI/IEEE uses the transient reactance of the machines. In contrast, IEC assumes that the motors no longer contribute to the short-circuit current. Therefore, the differences between both methods are mainly attributed to the reactance values applied.

VI. Conclusions

The results reveal significant differences in the short-circuit currents calculated using the IEC and ANSI/IEEE standards, mainly due to their distinct methodological approaches. In general, IEC yields higher short-circuit current values, particularly at buses electrically close to generators. This behavior is consistent with the findings of [4], who emphasize that the IEC standard considers more sustained contributions from rotating machines, leading to more conservative results in complex industrial systems.

Regarding asymmetric closing and blocking currents, the differences between IEC and ANSI/IEEE were below 10%, which supports the equivalence reported in previous studies [1]. This similarity suggests that both standards rely on comparable modeling principles. However, IEC adjusts reactance values according to compensation time, whereas ANSI/IEEE applies transient reactance assumptions. As highlighted by Bandaru [12], this IEC-specific approach becomes particularly relevant in systems where rapid response times are critical.

Regarding the X/R ratio, ANSI/IEEE tends to apply higher reactance multipliers, which generally results in lower calculated short-circuit currents compared to IEC. This discrepancy reinforces the importance of selecting the most appropriate standard based on the characteristics and criticality of the electrical system. While IEC may provide a more conservative perspective that is suitable for highly demanding environments, ANSI/IEEE may be preferable in applications where different assumptions about transient behavior are more representative. The literature consistently indicates that a clear understanding of these methodological differences can support better protection coordination and improve overall system efficiency.

The results confirm the expected behavior in which IEC-based calculations consistently produce higher short-circuit currents than those obtained under ANSI/IEEE criteria. This outcome can be explained by the influence of system topology, particularly the electrical proximity to generation sources and the interconnection paths between buses, as well as by the contribution of rotating machines, whose inertia and transient response are represented differently. These differences are not only relevant from a numerical perspective; they also have direct practical implications for protection coordination, since they affect relay settings, interrupting duties, and equipment withstand capabilities. Consequently, understanding why IEC yields more conservative currents becomes essential for ensuring adequate breaker selection, reliable protection performance, and overall system safety in industrial networks.

This study contributes to a deeper understanding of how IEC and ANSI/IEEE standards influence short-circuit calculations in industrial systems through simulations performed in ETAP 20.0. The accurate modeling of a 44-bus industrial network enabled the evaluation of multiple fault scenarios and a detailed comparison between both regulations. The results also confirmed the high consistency between ETAP simulations and manual calculations, reinforcing the usefulness of software tools in system planning and protection design. Nevertheless, since the analysis was limited to a single industrial configuration, future work should extend the comparison to different voltage levels, network topologies, and additional international standards, including scenarios with emerging generation and storage technologies.

Availability of data and materials

The data presented in this study are available from the corresponding author upon request.

Funding

This research received no external funding.

CRediT author contribution statement

J. Muñoz-Goez: conceptualization, methodology, validation, writing (review and editing).

J. Sosapanta-Salas: methodology, research, formal analysis, writing (review and editing).

J. Noguera-Jiménez: supervision, conceptualization, methodology, validation, writing (original draft, review, and editing).

Declaration of competing interest

The authors declare that they have no known competing financial interests or personal relationships that could appear to have influenced the study reported in this paper.

Use of artificial intelligence (AI)

During this work, the authors did not employ any technologies associated with artificial intelligence.

References

[1] I. C. Choachi Gómez and Á. J. López Loaiza, "Estudio comparativo de las normas IEC 60909-0 y ANSI/IEEE 141-4 para el cálculo de corrientes de cortocircuito en instalaciones eléctricas de uso final empleando los simuladores Digsilent PowerFactory y ETAP," Undergraduate thesis, Univ. Tecnológica de Pereira, Pereira, Colombia, 2017. [Online]. Available: https://hdl.handle.net/11059/8426

[2] IEEE Power and Energy Society, "IEEE application guide for AC high-voltage circuit breakers >1000 Vac rated on a symmetrical current basis," *IEEE Std C37.010-2016*, 2016. https://doi.org/10.1109/IEEESTD.2017.7906465

[3] International Electrotechnical Commission, "Short-circuit currents in three-phase a.c. systems – Part 0: Calculation of currents," *IEC 60909-0*, 2016. [Online]. Available: https://webstore.iec.ch/en/publication/24100

[4] R. Chelluri and M. D. Mohapatra, "Comparison of ANSI–IEC short circuit methods," *Int. J. Adv. Res. Electr. Electron. Instrum. Eng.*, vol. 8, no. 9, pp. 2182–2188, Sep. 2019. https://doi.org/10.1109/28.297928

[5] S. J. Muñoz Goez and P. Mesa Beleño, "Análisis comparativo de las normas ANSI/IEEE Std C37.010-2016, IEEE Std C37.13-2015, IEEE Std C37.5-1979, IEEE Std 141-1993 and IEC 60909-2016 para el cálculo de corrientes de cortocircuito," Undergraduate thesis, Institución Universitaria Pascual Bravo, Medellín, Colombia, 2024..https://repositorio.pascualbravo.edu.co/handle/pascualbravo/2536

[6] J. Catagua and A. Valdivieso, "Análisis de cortocircuito en un sistema industrial bajo normativas ANSI e IEC, simulados en Digsilent PowerFactory," Undergraduate thesis, Univ. Politécnica Salesiana, Ecuador, 2024. [Online]. Available: http://dspace.ups.edu.ec/handle/123456789/28685

[7] J. C. Das, *Power system analysis: Short-circuit load flow and harmonics*, 2nd ed. Boca Raton, FL, USA: CRC Press, 2017. https://doi.org/10.1201/b11021

[8] H. Arboleda, “Aplicación del análisis de flujos de carga y cortocircuito a la optimización del diseño de un sistema eléctrico industrial,” Undergraduate thesis, Univ. del Valle, Cali, Colombia, 2017. https://hdl.handle.net/20.500.14330/TES01000759661

[9] M. Brenna and Y. A. M. Mohammed, “Short-circuit fault level calculation on 33/11 kV substation by using ETAP simulator according to the IEC 60909 standard,” MS thesis, Politec. di Milano, Milan, Italy, 2020. https://www.politesi.polimi.it/handle/10589/166274

[10] IEEE, “IEEE recommended practice for conducting short-circuit studies and analysis of industrial and commercial power systems,” *IEEE Std 3002.3-2018*, 2019. https://doi.org/10.1109/IEEESTD.2019.8672198

[11] R. Luo, A. Majd, and M. Devadass, “Comprehensive overview and comparisons of ANSI *vs.* IEC short-circuit calculations,” presented at 2018 *IEEE Petrol. Chem. Ind. Tech. Conf. (PCIC)*, 2019. https://doi.org/10.1109/PCIC31437.2018.9080479

[12] D. Bandaru, S. R. Sura, J. K. Bokam, and K. A. Kumar, “Methods for Short Circuit Analysis in ANSI and IEC Standards,” *Int. J. Mech. Eng.*, vol. 7, no. 2, 5487–5493, 2022. https://doi.org/10.1109/TIA.2019.2919479

[13] D. Brankovic and R. Schuerhuber, “Short-circuit current of a hydropower plant with consideration of constant switching and fault arc voltages,” *IET Gener., Transm. Distrib.*, vol. 18, pp. 3476-3486, 2024. https://doi.org/10.1049/gtd2.13297

[14] A. Heyduk and J. Joostberens, “Comparative analysis of European and American standards for maximum fault current calculations on medium voltage mine power networks,” *Elektron. Elektrotech.*, vol. 22, no. 2, pp. 13–20, 2016. https://doi.org/10.5755/j01.eie.22.2.14608

[15] S. N. Afifi and M. Darwish, “Impact of hybrid distributed generation allocation on short circuit currents in distribution systems,” PhD dissertation, Brunel Univ., London, UK, 2017. https://doi.org/10.1109/UPEC.2014.6934697

[16] P. A. Salvatierra Villavicencio, “Simulación de una red soterrada de distribución de energía eléctrica de potencia bajo la norma IEC 60909/ANSI,” Master’s thesis, Universidad Politécnica Salesiana, Ecuador, 2021. [Online]. Available: http://dspace.ups.edu.ec/handle/123456789/20185

[17] Y. N. Lafta, N. A. Shalash, Y. N. Abd, and A. A. Al-Lami, “IEC 60909 and ANSI standards comparison with ASCC-based fault calculations of Iraqi power system,” *Cogent Eng.*, vol. 6, no. 1, Art. no. 1559545, Jan. 2019. https://doi.org/10.1080/23311916.2019.1705654

[18] B. Niersbach, I. Ghourabi, B. Braun, and J. Hanson, “Advanced modelling of inverter-based generators for short-circuit current calculations based on IEC 60909-0:2016,” in *Proc. IEEE PowerTech*, Milan, Italy, 2019, pp. 1–6. http://dx.doi.org/10.34890/837

[19] H. Peláez Velásquez, “Análisis comparativo de las fallas simétricas aplicando las normas ANSI/IEEE C37.10 e IEC 60909 con el paquete computacional NEPLAN,” Undergraduate thesis, Universidad Tecnológica de Pereira, Pereira, Colombia, 2015. [Online]. Available: https://hdl.handle.net/11059/6033

[20] O. Álvarez Lastra, “Simulación de cortocircuitos en sistemas eléctricos de potencia usando métodos tradicionales y normativas,” Undergraduate thesis, Univ. Politécnica Salesiana, 2020. https://dspace.ups.edu.ec/handle/123456789/19339

[21] W. D. Mendoza Pardo and J. P. Samaniego Avalos, "Validación del programa ATP para estudios de cortocircuitos en sistemas eléctricos de potencia," Undergraduate thesis, Universidad Politécnica Salesiana, Ecuador, Apr. 2023. [Online]. Available: http://dspace.ups.edu.ec/handle/123456789/24681

[22] Y. Zhang *et al.*, "The adaptability of IEC 60909-0-2016 to power grid with voltage levels above 400 kV," *J. Phys. Conf. Ser.*, vol. 2276, no. 1, art. 012018, May 2022. https://doi.org/10.1088/1742-6596/2276/1/012018

[23] J. C. Barrantes Quesada, "Estudio de cortocircuito y coordinación de protecciones en CVG ALUNASA," *undergraduate thesis*, Universidad de Costa Rica, San José, Costa Rica, 2014.https://ruie.ucr.ac.cr/catalogo/Record/INII-UIR-CD-13557

[24] V. J. V. Bojórquez, "Estudio comparativo de las normas IEC y ANSI para cálculo de corto circuito," Master's thesis, Instituto Politécnico Nacional, Escuela Superior de Ingeniería Mecánica y Eléctrica, México, D.F., México, Sept. 2007. [Online]. Available: https://www.zlibrary.to/dl/estudio-comparativo-de-las-normas-iec-y-ansi-para-calculo-de-corto-circuito

[25] S. Lakshmi Sankar and M. Mohamed Iqbal, "ANSI and IEC standards based short circuit analysis of a typical 2 × 30 MW thermal power plant," *Middle-East J. Sci. Res.*, vol. 23, no. 8, pp. 1617–1625, 2015.

[26] D. Schulz, Ed., *Proceedings of the NEIS 2020 Conference on Sustainable Energy Supply and Energy Storage Systems*. Berlin, Germany: VDE Verlag, 2020. [Online]. Available: https://www.researchgate.net/publication/361927719

UNIVERSIDAD DISTRITAL
FRANCISCO JOSÉ DE CALDAS

Ingeniería

https://revistas.udistrital.edu.co/index.php/reving/issue/view/1320

DOI: https://doi.org/10.14483/23448393.23090

Research

Assessing the Efficacy of Optimization Algorithms, P&O and MPC in MPPT for Photovoltaic Systems: A Comparative Study

Evaluación de la eficacia de los algoritmos de optimización, P&O y MPC en MPPT para sistemas fotovoltaicos: Un estudio comparativo

Jose Mena-Palomeque[1] *, Juan E. Zabala-Daza[2], Jhon A. Gómez P.[1], Jaime A. Ramírez-Ospina[1]

[1]IU Digital, Medellín, Colombia
[2]ITM, Medellín, Colombia

Abstract

Context: The need for efficient energy harvesting in photovoltaic (PV) systems requires advanced maximum power point tracking (MPPT) techniques. Traditional methods like perturb and observe (P&O) exhibit limitations under varying conditions, leading to less efficient energy extraction.
Method: This study compares a model-predictive controller (MPC) combined with optimization algorithms such as the particle swarm optimizer (PSO), the vortex search algorithm (VSA), and the salp swarm algorithm (SSA) to improve MPPT performance in PV systems. These algorithms are tested under different irradiance conditions to assess their efficiency and adaptability.
Results: The results show that PSO, when used with MPC, greatly enhances energy extraction compared to the conventional P&O method. Additionally, VSA and SSA also perform well in adapting to rapid irradiance changes, ensuring an optimal power output.
Conclusions: Optimization-based MPPT methods, especially those using PSO, offer significant efficiency improvements for PV systems, making them strong alternatives to traditional techniques.
Keywords: Solar Power System, Partial Shading, PS, PV, Power Converter, MPPT, MPC, Optimization Algorithms, Energy Efficiency.

Article history

Received: February 26th, 2025

Modified: December 10th, 2025

Accepted: February 3rd, 2026

Ing, vol. 31, no. 1, 2026. e23090

* **Correspondence:** Jose.mena@prof.iudigital.edu.co

Resumen

Contexto: La creciente demanda de extracción eficiente de energía en sistemas fotovoltaicos (PV) requiere técnicas avanzadas de seguimiento del punto de máxima potencia (MPPT). Métodos tradicionales como *perturb and observe* (P&O) enfrentan limitaciones bajo condiciones ambientales variables, conlleva una extracción subóptima de energía.

Método: Este estudio presenta un análisis comparativo de un controlador predictivo de modelos (MPC) integrado con varios algoritmos de optimización, incluyendo la optimización por enjambre de partículas (PSO), el algoritmo de búsqueda de vórtices (VSA) y el algoritmo de enjambre de salpas (SSA), para mejorar el rendimiento del MPPT en sistemas PV. Los algoritmos fueron evaluados bajo diferentes perfiles de irradiancia para determinar su eficiencia y adaptabilidad.

Resultados: Los resultados indican que PSO, cuando se combina con MPC, mejora significativamente la eficiencia de extracción de energía en comparación con el método convencional P&O. Además, VSA y SSA también demuestran un rendimiento superior al adaptarse a cambios rápidos en la irradiancia, asegurando una salida de potencia óptima.

Conclusiones: Los métodos MPPT basados en optimización, particularmente aquellos que utilizan PSO, ofrecen mejoras sustanciales en la eficiencia de los sistemas PV, lo que los posiciona como alternativas viables a las técnicas MPPT tradicionales.

Palabras clave: Sistema de energía solar, Sombreado parcial, PS, PV, Convertidor de potencia, MPPT, MPC, Algoritmos de Optimización, P&O, Eficiencia Energética.

Contents

1 Introduction

The rapid rise in global population density has significantly increased the demand for energy, food, and natural resources [1]. Fossil fuels, including oil, coal, and natural gas, are the world's primary energy sources [2–4], but its reliance on them raises concerns about depletion and environmental impact [5]. In response, renewable energy has become pivotal in the global transition [6].

Photovoltaic (PV) systems stand out as a promising alternative since they convert solar energy into electricity. With components like power converters, PV panels, and electrical loads, they require coordination to operate efficiently [7, 8]. Bypass diodes protect PV panels from reverse currents, preventing shading effects that reduce efficiency and lifespan [9].

PV systems use DC/DC and DC/AC converters to adapt to load needs [10], monitoring current and voltage for optimal energy management [11]. Maximum power point tracking (MPPT) strategies maximize energy extraction by adapting to environmental variations [12], adjusting the output voltage to optimize conversion efficiency [13].

MPPT techniques include approaches based on P&O [14], incremental conductance (INC) [15, 16], MPPT-current (MPPT-I) [17], MPPT-voltage (MPPT-V) [18], neural networks [19], and genetic algorithms [20–22]. Still, some challenges remain in achieving precise, rapid MPPT adaptation to environmental changes, with methods like P&O often leading to oscillations under fluctuating irradiance [23, 24]. Complex controllers must respond to shading conditions [25], though the high costs of advanced methods and hardware pose barriers [13]. Thus, PV systems require DC/DC or DC/AC converters to consistently supply energy to loads, ensuring efficiency across operating conditions [26].

1.1 State of the art

The specialized literature presents numerous studies on the MPPT search problem regarding PV panels, highlighting the widespread use of the P&O algorithm, often combined with proportional-integral-derivative (PID) controllers, model-predictive control (MPC), sliding mode control, and more. This study focuses on validating and comparing various MPPT algorithms with MPC controllers, in order to identify the approach that maximizes power extraction under variable irradiance scenarios.

The MPPT problem has been widely solved in the specialized literature [14,15,27–33], using methods based on artificial intelligence (AI), such as neural networks (NNs), genetic algorithms (GAs), and fuzzy logic to improve efficiency and accuracy under different environmental and irradiance conditions. In addition, hybrid techniques have been developed which combine multiple algorithms to obtain a more robust and accurate response to different operational contexts.

In [30], the authors review MPPT algorithms, classifying them by key performance indicators to aid the selection of suitable algorithms for PV systems. This study highlights challenges in control strategies, including poor performance under partial shading, steady-state oscillations, slow convergence, implementation complexity, and limited use of real data or experiments.

The work by [14] introduces SOFT-MPPT, an MPPT algorithm for P&O-based PV systems that employs an adaptive modulation factor to correlate PV current measurements with irradiance, aiming to enhance energy extraction efficiency. Although the authors claim high efficiency, their study lacks data to fully substantiate these assertions. The proposed comparative analysis of MPPT techniques does not quantitatively validate the algorithm's performance in terms of maximum power or point tracking accuracy. Furthermore, no comparisons with standard MPPT strategies are provided, nor is the algorithm tested under variable weather or partial shading conditions.

The study by [15] proposes a control algorithm that combines unit vector template (UVT) and power balance theory (PBT) for a PV system implementing an MPPT strategy to enhance power stability. Although an appropriate evaluation of the MPPT strategy is conducted, the authors do not perform a comparative analysis with other MPPT methods, making it challenging to assess the efficiency of the proposed solution for time-varying systems. Additionally, while the authors assert that the solution's performance was evaluated in terms of DC voltage regulation quality and mains current harmonic mitigation under linear and nonlinear load conditions, no results or data supporting these claims are provided, limiting the proper validation of the study's findings.

In [27], an MPPT strategy based on the Mayfly optimization algorithm for PV systems under variable conditions is proposed. The authors test the approach in Matlab/Simulink, comparing it to the PSO algorithm. However, limitations arise since evidence for MPPT success under dynamic conditions is insufficient, with no demonstration of irradiance variation or a direct comparison of power output between methods. Additionally, details on convergence to the MPPT voltage reference are unclear, necessitating further evaluation to clarify algorithm performance and confirm the authors' claims.

The authors of [28] propose a fuzzy logic-based driver coupled with an MPPT algorithm inspired by the IFFO (*i.e.*, farmland fertility method), aiming to optimize PV system controller parameters under different climate scenarios, achieving over 99% efficiency in both uniform irradiation (UI) and power supply (PS) contexts. However, limitations arise from the lack of discussion on the method's constraints and the algorithm's performance under variable conditions. Additionally, the power curves do not fully capture energy fluctuations, and there is minimal information on voltage reference points within the MPPT process, raising questions about the method's applicability across varying PV generation profiles and its reproducibility in achieving stated efficiencies.

In [29], the authors propose a reinforcement deep learning-based MPPT control for PV systems under partial shading conditions. They use deep reinforcement learning (DRL) algorithms, specifically Deep Q-Network (DQN) and Deep Deterministic Policy Gradient (DDPG), to optimize the MPPT control strategy. This approach is compared against the conventional P&O method and evidences higher energy production as well as better tracking performance, especially in scenarios where global MPPT cannot be obtained. However, the authors do not provide information on the statistical validations used to ensure that the experiment performed is repeatable and applicable to other PV panel curves, which does not allow scaling the implementation to other test cases.

The work by [31] presents a fuzzy logic-based controller that integrates the grey wolf optimizer (GWO) into its MPPT strategy to enhance energy extraction in PV systems. The authors employ opposition-based learning (BLO) to accelerate the search for the optimal solution and simulate partial shading conditions to better reflect real-world scenarios. However, this article lacks detailed results—including specific data, graphs, or tables—to support the effectiveness of the proposed method. Additionally, it does not provide comparative analyses with existing methods or discuss potential limitations, necessitating further evidence to substantiate its claims.

In [32], the authors propose a fuzzy logic-based controller that incorporates the GWO within its MPPT strategy to enhance energy extraction in PV systems. They use the BLO method to expedite the search for the optimal solution. Additionally, they suggest a PV energy conversion system using a boost converter and digital filtering within the controller to improve signal quality, optimizing MPPT through the P&O algorithm. However, this article lacks clarity with regard to its methodology, making replication and validation challenging. Although experimental results are mentioned, specific numerical values and procedural details are absent. The study also omits comparisons with other MPPT techniques and does not use statistical tests to validate solution quality, which could impact result interpretation and generalizability.

The authors of [33] authors propose an MPPT method that uses system identification (SI) with an adaptive reference voltage (AVR) and a proportional-integral (PI) controller while incorporating a polynomial model. This approach, designed for simplicity, is compared against MPPT techniques such as P&O, IC, CVR, ANN, and a nonlinear AVR-SI method. However, the study lacks in-depth descriptions of these MPPT strategies, statistical analyses, and a discussion of the limitations.

Additionally, variable climatic conditions affecting PV generation and the lack of comparative analyses between algorithms highlight gaps in existing research. To address these gaps, our study proposes a methodology for comparing various MPPT algorithms via a cost function to characterize MPC within a PV system with a boost converter and a battery. The aim is to identify the algorithm that optimally extracts power under varying irradiance. For comparison, P&O and optimization algorithms, *i.e.*, the particle swarm optimizer (PSO), the vortex search algorithm (VSA), and the salp swarm algorithm (SSA), are considered.

Our choice of PSO, VSA, and SSA was supported by recent literature on PV MPPT, where optimization and swarm-based techniques are widely used to improve efficiency and energy extraction under varying and partial shading conditions. In particular, the use of the SSA for MPPT to optimize the duty cycle of a DC/DC converter and maximize power extraction has been reported, demonstrating the applicability of bio-inspired optimization techniques in PV systems [34]. Likewise, hybrid and metaheuristic optimization methods that combine swarm intelligence with conventional MPPT strategies have been shown to enhance tracking performance when compared to traditional techniques [35].

1.2 Scope and main contributions

This study compares different MPPT algorithms implemented in a DC/DC boost converter connected to a PV panel and a battery using an MPC controller with the aim of achieving maximum power extraction. Strategies such as P&O, PSO, VSA, and SSA are used, evaluating an objective function with respect to the voltage of the system.

The main contributions in this study are presented below.

- The development of a comparison methodology between different optimization algorithms in order to achieve maximum power extraction.
- The simulation of variable irradiance conditions for a PV panel within a 24-hour scenario.
- A comparison between the results obtained with the P&O algorithm and those of other optimization techniques widely used in the specialized literature, including PSO, VSA, and SSA. This comparison is based on the maximum power extraction of the system and how these algorithms reach the desired benchmarks, implementing irradiance scenarios on an average day and critical irradiance cases.
- The implementation of an MPC controller for a PV system comprising a DC/DC converter and a battery while using optimization algorithms, in order to compare the results in terms of maximum energy extraction.

  To summarize, this article presents an approach for MPP tracking using an MPC controller within a PV system linked to a boost converter and a battery. Two irradiance scenarios are considered: an average day and a fluctuating day under critical conditions. This study compares the P&O algorithm against PSO, VSA, and SSA to determine the most effective method for maximizing energy extraction through MPPT.

1.3 Structure of the paper

This paper is organized as follows. Section 2 details the mathematical formulation, circuit diagrams, technical specifications, and MPC controller configuration. Section 3 describes the algorithms and the objective function for MPPT. Section 4 covers the simulation stage, experimental voltage and current data, and MPC implementation in Matlab, including the representation of maximum energy extraction. The results of each algorithm are analyzed in terms of energy extraction percentage by integrating areas under power curves. Finally, Section 5 presents the main conclusions of our work.

2 Mathematical Formulation

This section presents the mathematical modeling for the PV system and the boost DC/DC converter connected to a battery. The MPC controller with the MPPT algorithms (P&O, PSO, SSA, and VSA) is implemented on these models. All of this is done with the objective of tracking the maximum power point and validating which algorithm enables the highest power transfer.

2.1 Mathematical model of the PV panel

A PV panel converts solar radiation into electrical energy via p-n junction semiconductors, with its power output varying according to solar irradiance and ambient temperature. This variability can be accurately modeled using the single-diode model (SDM), as shown in Eq. (1), which is highly valued for both accuracy and simplicity. Additionally, the PV panel can be represented by an equivalent circuit comprising a current source in parallel with a diode and two resistors connected in parallel and series (Fig. 1).

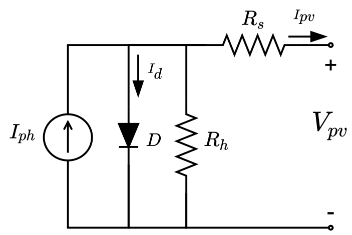

Figura 1. Equivalent circuit for the SDM

$$I_{pv} = I_{ph} - I_d \left[e^{\left(\frac{V_{pv}+R_s I_{pv}}{\eta \frac{N_s k T}{q}} \right)} - 1 \right] - \left(\frac{V_{pv} + R_s I_{pv}}{R_h} \right) \tag{1}$$

Eq. (1) represents the output current of the panel I_{pv}, the photo-induced current I_{ph}, the reverse saturation current of the diode I_d, the electron charge q, the output voltage V_{pv}, the ideality factor η_1, the Boltzmann constant k, and the panel temperature T.

$$I_{ph} = \left(\frac{G}{G_{ref}} \right) \cdot (I_{ph,ref} + \mu \cdot (T_c - T_{ref})) \tag{2}$$

Although Eq. (2) is a simplified model adapted for use cases and modeling involving power converters, I_{ph} is proportional to the solar irradiance G, which is given in Watts per square meter (W/m^2). The term G/G_{ref} represents the ratio between the current irradiance and a reference irradiance G_{ref}, which is generally $1000\ W/m^2$ under standard conditions. $\mu \cdot (T_c - T_{ref})$ accounts for the effect of temperature on the current generated by the panel. Here, T_c denotes the current temperature of the PV panel, T_{ref} is the reference temperature $(25C)$, and the coefficient μ indicates the variation between the current for each degree of change in the temperature.

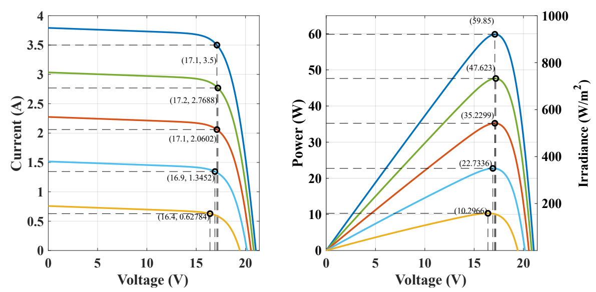

Figura 2. Profile of V_{pv} *vs.* P_{pv} and V_{pv} *vs.* I_{pv} under standard test conditions

By using this equation or the electrical circuit, a representation of the PV profiles under any uniform condition of irradiance and temperature can be obtained. It is necessary to understand that the representation of the profiles or the characteristic curves of a PV panel has a maximum power point (MPP), which is determined by the product between the voltage at the maximum point (V_{mpp}) and the current at the maximum point (I_{mpp}). At this point, the highest power is extracted from the panel (P_{mpp}) (Fig. 2).

2.2 Modeling the PV system for control purposes

To integrate a PV panel, a DC/DC converter, and a battery, it is necessary to establish the effective control point of the converter using pulse-width modulation (PWM). This control focuses on the precise definition of the duty cycles (D), which are constantly adjusted to find the system's optimal operating point. This work typical when dealing with energy generation systems, such as PV panels, which require the constant production of the maximum power point (MPP).

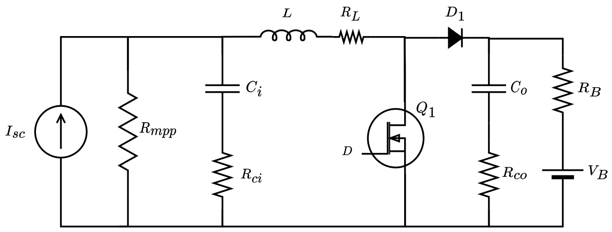

Figura 3. Circuit model for the PV system with converter boost and battery

It should be noted that, in this study, it is necessary to mathematically model the system, which consists of a PV panel, a DC/DC converter, and a battery. To this effect, the PV panel is simplified using the Norton equivalent (Fig. 3). The current source I_{SC} and the resistance R_{MPP} represent the short-circuit current and the instantaneous impedance of the PV panel. The DC/DC converter is represented by an inductor L and the inductor losses R_L. In addition, R_B denotes the battery resistance, R_{on} is the MOSFET (Q_1) connection resistance, V_f is the diode (D_1) forward voltage, and V_B is the battery's open-circuit voltage. C_i and C_o denote the input and output capacitance of the converter, with their equivalent series resistances R_{ci} and R_{co}, respectively.

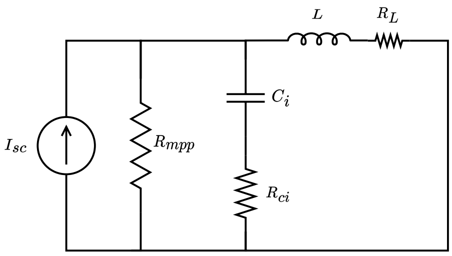

Figura 4. Activation state of the boost converter: Q_1 ON and D_1 OFF

The resulting equations for the state of Q_1 on and D_1 off (Fig. 4) are determined using Kirchhoff's voltage and current laws, yielding (3)-(6), which represent the currents in the capacitors C_i and C_o, which make up Eqs. (3) and (4), respectively.

$$I_{Ci} = \lambda \cdot I_{SC} - \frac{V_{Ci}}{R_{MPP} + R_{Ci}} \lambda I \tag{3}$$

$$I_{Co} = \frac{V_B}{R_B + R_{Co}} - \frac{V_{Co}}{R_B + R_{Co}} \tag{4}$$

The voltage across the inductor is represented in Eq. (5), where I represents the current flowing through the inductor, V_{Ci} is the voltage across capacitor C_i, and V_{Co} is the voltage across capacitor C_o. Finally, the voltage of the PV panel V_{pv} is obtained via Eq. (6).

$$V_L = \lambda \cdot V_{Ci} + \beta \cdot I_{SC} - (R_L + R_{on} + \beta) \cdot I \quad (5)$$

$$V_{PV} = \lambda \cdot V_{Ci} + \beta \cdot I_{SC} - \beta I \quad (6)$$

On the other hand, to provide a better understanding of the equations mentioned above, it is necessary to expand the parameters λ and β using Eqs. (7) and (8).

$$\lambda = \frac{R_{MPP}}{R_{MPP} + R_{Ci}} \quad (7)$$

$$\beta = \frac{R_{Ci} \cdot R_{MPP}}{R_{MPP} + R_{Ci}} \quad (8)$$

Continuing with the equations for mathematically modeling the converter, the next state of the circuit occurs when Q_1 is off and D_1 is on (Fig. 5). The resulting equations are (9) and (10).

$$I_{Co} = \theta \cdot I + \frac{V_B}{R_B + R_{Co}} - \frac{V_{Co}}{R_B + R_{Co}} \quad (9)$$

$$V_L = \lambda \cdot V_{Ci} + \beta \cdot I_{SC} - (R_L + \gamma + \beta) \cdot I - V_f - \theta \cdot V_{Co} - \sigma \cdot V_B \quad (10)$$

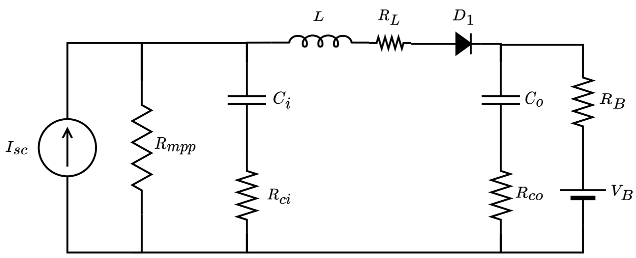

Figura 5. Activation state of the boost converter: Q_1 OFF and D_1 ON

It is worth noting that these equations are a bit lengthy because the entire converter was calculated while considering the losses of each element. This makes the system of equations robust. Therefore, parameters or variables are linked to reduce its size. These parameters are described in Eqs. (11), (12), and (13), which allow for a representation of γ, θ, and σ.

$$\gamma = \frac{R_B \cdot R_{Co}}{R_B + R_{Co}} \quad (11)$$

$$\theta = \frac{R_B}{R_B + R_{Co}} \quad (12)$$

$$\sigma = \frac{R_{Co}}{R_B + R_{Co}} \quad (13)$$

As part of the final system of equations, the system dynamics at any operating point must be defined. For this purpose, a volt-second balance is applied to the inductor, and a charge balance is applied to each capacitor (C_i, C_o). The resulting equations are presented in (14), (15), and (16).

$$\begin{aligned} L\frac{dI}{dt} =& \lambda \cdot V_{Ci} + \beta \cdot I_{SC} - (R_L + d \cdot R_{on} + \beta + (1-d) \cdot \gamma) \cdot I \\ &- (1-d) \cdot V_f - (1-d) \cdot \theta \cdot V_{Co} - (1-d) \cdot \sigma \cdot V_B \end{aligned} \tag{14}$$

$$C_i \frac{dV_{Ci}}{dt} = \lambda \cdot I_{SC} - \frac{V_{Ci}}{\alpha} - \lambda I \tag{15}$$

$$C_o \frac{dV_{Co}}{dt} = (1-d) \cdot \theta \cdot I - \frac{V_{Co}}{\delta} + \frac{V_B}{\delta} \tag{16}$$

Where:

$$\alpha = R_{MPP} + R_{Ci} \tag{17}$$

$$\delta = R_{Co} + R_B \tag{18}$$

Based on the equations that describe the behavior of the system at any operating point throughout the mathematical model, it is possible to implement linear or nonlinear control techniques that allow taking the behavior of the plant to a desired point of operation. This work uses a linear control technique to validate the behavior of the system under different environmental conditions.

In order to apply a linear control technique to the plant, it is necessary to linearize the system at a given operating point. This is adjusted in the equations by applying the Jacobian [36], with the aim of representing all the equations in the state space based on the Characteristic Equations (19) and (20).

$$\dot{X} = AX + BU \tag{19}$$

$$Y = CX + EU \tag{20}$$

Here, X represents the state of the system, U denotes the control inputs, Y signifies the system outputs, and A, B, C, and E are the matrices used to perform the state-space representation of the plant, which is given by Eqs. (21), (22), (23), and (24). It should be noted that the state variables used herein are V_{Ci}, I and V_{Co}. In addition, the input variables are I_{SC} and V_B.

$$X = \begin{bmatrix} V_{Ci} \\ I \\ V_{Co} \end{bmatrix}, \quad U = \begin{bmatrix} I_{SC} \\ V_B \\ d \end{bmatrix}, \quad Y = \begin{bmatrix} V_{pv} \end{bmatrix} \tag{21}$$

$$A = \begin{bmatrix} -\frac{1}{C_i \alpha} & -\frac{\lambda}{C_i} & 0 \\ \frac{\lambda}{L} & -\frac{R_L + \beta + (1-D)\gamma + DR_{on}}{L} & -\frac{(1-D)\theta}{L} \\ 0 & \frac{(1-D)\theta}{C_o} & -\frac{1}{C_o \delta} \end{bmatrix} \tag{22}$$

$$B = \begin{bmatrix} -\frac{\lambda}{C_i} & 0 & 0 \\ \frac{\beta}{L} & -\frac{(1-D)\sigma}{L} & \frac{V_f - (R_{on} - \gamma)I + \sigma V_B + \theta V_{Co}}{L} \\ 0 & \frac{1}{C_o \delta} & \frac{I\theta}{C_o} \end{bmatrix} \tag{23}$$

$$C = \begin{bmatrix} \lambda & -\beta & 0 \end{bmatrix} \tag{24}$$

$$E = \begin{bmatrix} \beta & 0 & 0 \end{bmatrix} \tag{25}$$

Starting from these equations, the implementation and validation of the MPC is carried out. It should be noted that the specifications of the entire system are defined in Table I.

Table I. Test system parameters and specifications

Parameter	Symbol	Value
Solar Panel Parameters at STC		
Maximum power	P_{mpp}	85 W
Voltage at P_{max}	V_{mpp}	18 V
Current at P_{max}	I_{mpp}	4.72 A
Short-circuit current	I_{SC}	5 A
Open-circuit voltage	V_{OC}	22.1 V
Temperature coefficient of I_{SC}	α_I	0.065%/°C
Temperature coefficient of the voltage	α_V	-80 mV/°C
Converter Parameters		
Input capacitor	C_i	22 μF
Output capacitor	C_o	22 μF
Inductor	L	330 μH
Inductor resistance	R_L	60 mΩ
ON resistance Mosfet 1	R_{ON1}	35 mΩ
ON resistance Mosfet 2	R_{ON2}	35 mΩ
DC Load Parameters		
DC load equivalent resistance	R_B	60 mΩ
DC load voltage	V_B	24 V

2.3 Model-predictive control (MPC)

After defining the mathematical models, MPC can be applied as a modern control technique that uses the system model to predict future behaviors under varying conditions. MPC aims to determine an optimal sequence of control signals that minimizes a cost function over a finite prediction horizon while adhering to input and output constraints [37].

2.3.1 Formulating the optimization problem

At the core of MPC is a quadratic optimization problem solved at each sampling instant, with the purpose of finding the optimal control input sequence that minimizes a quadratic cost function while respecting the system's technical and operational constraints on states, inputs, and outputs.

2.3.2 Cost function

The objective function for MPC is defined as $J(U, x(t))$, which consists of the summation of various terms affecting the system, ensuring that, at each time instant, the MPC can solve the problem through quadratic optimization, as shown in Eq. (26).

$$J(U, x(t)) = \sum_{k=0}^{N_p-1} (x(k|t) - r(k))^T \, Q \, (x(k|t) - r(k)) + \Delta u(k|t)^T R \Delta u(k|t) \tag{26}$$

Here, $x(k+1|t) = Ax(k|t) + Bu(k|t)$ is the predicted state, $u(k|t)$ represents the control input at time instant k, U is the sequence of control inputs to be optimized, Q and R are weighting matrices, N_p is the prediction horizon, N_u is the control horizon, and E and G are matrices defining constraints on states and inputs, respectively. Finally, f_x and f_u represent vectors defining constraints on the states and inputs, respectively. It is worth highlighting that all elements provide the predicted state at time instant k in order to provide information at time instant t.

2.3.3 System constraints

The constraints considered herein prioritize limiting the control signals, states, and outputs of the system, as shown in Eqs. (27) and (28).

- **Input constraints**:

$$Gu(k) \leq f_u \tag{27}$$

- **States constraints**:

$$Ex(k) \leq f_x \tag{28}$$

2.4 Prediction and control horizon

Once the system equations and their restrictions have been defined, it is necessary to determine the parameters of the system.

2.4.1 Prediction horizon

The prediction horizon is defined as N_p and focuses on defining the number of future time steps over which the behavior and progress of the system will be predicted. In other words, the MPC seeks to predict the behavior of the states and outputs of the system over future steps.

2.4.2 Control horizon

In MPC, the control horizon functions similarly to the prediction horizon, with each time step enabling the determination of an optimal control sequence for the next N_u steps. This process iteratively applies optimal inputs, where performance depends on horizon lengths: a shorter horizon limits constraint handling, while a longer one enhances foresight. For the Matlab configuration, see [38]. Algorithms like P&O and optimization methods such as PSO, VSA, and SSA are also suggested for effective reference tracking.

3 Maximum Power Point Tracking Algorithms

With an understanding of PV panel behavior, the MPC controller must be considered in relation to the DC/DC converter. The maximum power point (MPP) shifts with changes in irradiance and temperature, necessitating continuous tracking to maintain an optimal energy transfer. To address this issue, we will explore the various algorithms analyzed in this paper.

3.1 Perturb and observe algorithm ($P\&O$)

P&O, one of the most well-known algorithms, is used to maximize energy transmission from a PV panel by continuously tracking the MPP. For a clearer understanding, the reader may consult Figure 1, which depicts the complete flowchart of the P&O algorithm's behavior, detailing how the MPPT is conducted when using this technique.

Algorithm 1 Perturb and observe MPPT algorithm

Data: Initial reference voltage V_{ref}, Step size for voltage perturbation Δ_V, Initial voltage reading V_{prev}, Initial power reading P_{prev}

Measure current voltage V Measure current power P **if** $P > P_{prev}$ **then**
    if $V > V_{ref}$ **then**
        $V_{\text{ref}} = V_{\text{ref}} + \Delta_V$
    end
    else
        $V_{\text{ref}} = V_{\text{ref}} - \Delta_V$
    end
end
else if $P < P_{prev}$ **then**
    if $V > V_{ref}$ **then**
        $V_{\text{ref}} = V_{\text{ref}} - \Delta_V$
    end
    else
        $V_{\text{ref}} = V_{\text{ref}} + \Delta_V$
    end
end
$P_{\text{prev}} = P$ $V_{\text{prev}} = V$ Apply new reference voltage V_{ref} to the system

The process starts by setting the parameter $P(k-1)$, representing the initial voltage change (perturbation), to identify the MPP. The system then reads the voltage $V(k)$ and current $I(k)$ to compute the power $P(k)$ of the PV panel. The P&O algorithm iteratively adjusts the panel's operating voltage by a value dV, either increasing or decreasing it. After each adjustment, the algorithm calculates the resulting power by comparing the new voltage-current product to the previous power $P(k)$. If the power increases, the next adjustment follows the same direction; if it decreases, the direction reverses. This cycle allows P&O to continuously fine-tune the panel's output, ensuring that it consistently operates at peak power despite changing conditions.

3.2 Optimization techniques

Optimization algorithms are commonly used for tracking the MPP through a forward method that stores critical data, including objective function updates and derived individuals. This research compares the P&O algorithm against optimization methods like PSO, SSA, and VSA, in order to determine which one maximizes energy transfer, guiding cost-effective MPPT and MPC combinations.

3.2.1 The particle swarm optimizer (PSO)

The PSO algorithm is a bio-inspired optimization method based on the social behavior of bird flocks and fish schools. It begins by randomly distributing particles throughout the solution space. Each particle then adjusts its position while following an advancement method, as shown in Eq. (29), which depends on its velocity and both personal and swarm experiences.

$$v_i(t+1) = w \cdot v_i(t) + c_1 \cdot r_1 \cdot (p_i - x_i(t)) + c_2 \cdot r_2 \cdot (p_g - x_i(t)) \tag{29}$$

By utilizing each particle's memory and the swarm's collective knowledge, PSO identifies promising candidate solutions. This collective intelligence allows the swarm to converge to an optimal solution, making PSO ideal for engineering problems that require intelligent algorithms and a clear objective function [39].

3.2.2 The vortex search algorithm (VSA)

Inspired by the dynamics of vertically stirred fluids, VSA explores the solution space through Gaussian distributions. With each iteration, the vortex diameter narrows, steering particles toward the most promising solution. VSA's progression relies on calculating the vortex center (μ) and radius (r), with the initial center set by Eq. (30) and the radius adjusted iteratively by Eq. (31).

$$\mu_0 = (x_{\max} + x_{\min})/2 \tag{30}$$

$$r_{t+1} = \sigma_0 \left(1 - \frac{t}{t_{\max}}\right) \epsilon^{-at_{\max}} \tag{31}$$

These equations incorporate the solution search space bounds, the iteration count, and a constant that dictates the radius reduction rate. As the algorithm generates new populations, it evaluates and adjusts individuals based on the solutions obtained, recalibrating the vortex center around the best solution found to ensure a steady convergence to the optimum [40].

3.2.3 The salp swarm algorithm (SSA)

The SSA algorithm, inspired by marine salps moving in chain-like swarms, balances exploration and exploitation by mimicking salp chain dynamics. A leading salp drives exploration, while follower salps focus on local exploitation, adjusting their positions based on the leader's guidance. As the algorithm evaluates the objective function for each salp's position, it continually updates leader and follower roles and positions. This is governed by Eq. (32).

$$X_i\,(t+1) = X_i\,(t) + d \cdot e^{(-\lambda \cdot t)} \cdot \cos\,(2\pi \cdot t) \tag{32}$$

In this equation, $(X_i(t))$ represents the particles' current position, (d) is the distance to the lead salp, and (λ) is a damping parameter. This structure allows the SSA to effectively tackle complex, non-linear, and non-convex optimization problems [41].

Algorithm 2 MPPT using optimization algorithms

Data: Input parameters Vpv and Ipv

Result: The best position $Vmpp = gbest\_position$

begin
- Initialize parameters PSO, SSA, VSA **if** *positions is empty* **then**
  - Initialize random positions within the voltage limits $Vmin$ and $Vmax$ Initialize initial parameters for each algorithm (PSO, VSA, SSA) Set initial $pbest$ values to infinity and positions Set $gbest$ value to infinity and take the first particle position
- Compute solar panel power: $Ppv = Vpv \times Ipv$ **for** *particle i in the population* **do**
  - Compute power for particle using its position and Ipv Adjust the objective function Update the particle's $pbest$ if the new objective function is better Update $gbest$ if the new objective function is better
- **for** *particle i in the population* **do**
  - Adjust according to the advancement method of each optimization algorithm (PSO, VSA, SSA) Constrain position within voltage limits $Vmin$ and $Vmax$

3.3 Objective function

To track the maximum power point with optimization algorithms, voltage and current readings from the PV panel are essential, as in the P&O method. This is encapsulated in the objective function, where the absolute difference between the particles' computed power and the actual PV panel power is calculated. This is shown in Eq. (33).

$$f(x) = |power - P_{pv}| + |X(i) - V_{ref}| \tag{33}$$

The variable $power$ arises from the product of the particles $(X(i))$ and the current (I_{pv}). It is worth noting that $(X(i))$ represents voltages randomly generated by each of the optimization algorithms, each of which employs distinct advancement methods for individual creation. The actual power of the PV panel, denoted as (P_{pv}), is computed from the PV panel voltage (V_{pv}) and (I_{pv}).

To minimize MPPT calculation error and ensure particle proximity to the reference voltage, the objective function establishes a power-voltage relationship, as shown in Eq. (33). This function reflects the closeness between calculated and actual power, aiming to balance PV power matching with reference voltage tracking for MPPT. The absolute differences in power and voltage are given by $|X(i) - V_{ref}|$.

4 Simulations and results

To validate the process, Matlab/Simulink was used to integrate the DC/DC converter (with losses), the PV panel, and the MPPT controllers, as shown in Fig. 6. This setup emulated realistic behavior similar to non-ideal physical testing conditions.

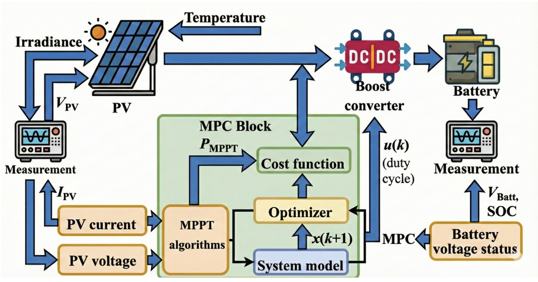

Figura 6. Experimental setup of a Simulink to validate the results

For improved clarity, Fig. 6 explicitly illustrates the interaction between the MPPT algorithm and the MPC controller. The MPPT block generates the PV voltage reference associated with the maximum power point, which is then provided to the MPC controller. The MPC uses this reference to compute the duty cycle required by the DC/DC converter.

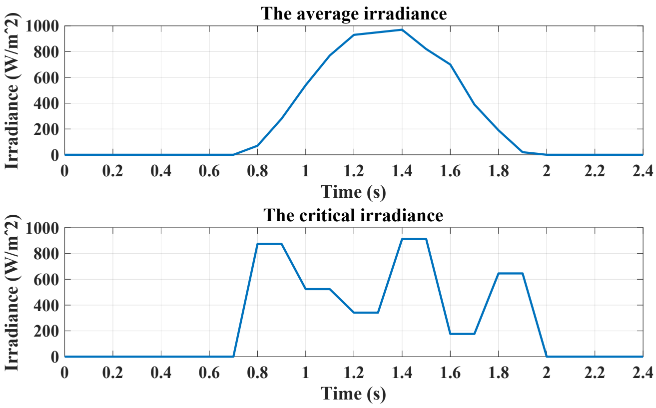

Figura 7. Testing under average and critical conditions

Furthermore, Fig. 7 presents the irradiance profiles to which the controllers and the converter are subjected. It is worth highlighting the inclusion of a critical scenario and an average PV generation curve for the city of Medellín. This is done to validate whether the analyzed optimization algorithms can perform MPPT when using MPC as the controller for the boost DC/DC converter.

4.1 MPC configuration

The MPC is constructed using the state-space representation of the system, as depicted in Eqs. 22 and 23. It is configured using the following parameters:

- Prediction horizon: 2
- Control horizon: 1
- Manipulated variables (MV): Converter's duty cycle (Duty)
- Measured disturbances (MD): Input voltage (V_B) and solar panel current (I_{pv})
- Limits for the manipulated variables:
  - MV min: -0.25
  - MV max: 0.75

Additionally, to implement the controller in software like Matlab/Simulink, it is essential to incorporate the parameters defined in Table II.

Table II. MPC parameters for the boost converter

Parameter	Value
Prediction horizon	2
Control horizon	1
Lower limit of Duty	-0.25
Upper limit of Duty	0.75
Sampling frequency (Ts)	$10e^{-6}$ s

These parameters, set for the controller's use, should be implemented in Matlab code as follows:

```
% System model creation
Boost = ss(A, B, C, D);
% MPC controller configuration
Ts = 10e-6;
% Sampling time
Boost.InputGroup.MV = 3;
% Manipulated variables
Boost.InputGroup.MD = [1 2];
% Measured disturbances
Boost.OutputGroup.MO = 1;
% Manipulated outputs
MPCobj = mpc(Boost, Ts);
% MPC control object
MPCobj.PredictionHorizon = 2;
% Prediction horizon
MPCobj.ControlHorizon = 1;
% Control horizon
MPCobj.ManipulatedVariables.Min = -0.25;
% Lower limit of manipulated variables
MPCobj.ManipulatedVariables.Max = 0.75;
% Upper limit of manipulated variables
```

Listing 1. Configuración del controlador MPC para el convertidor boost.

In the proposed control structure, the MPC is not responsible for reference generation. The voltage reference corresponding to the MPP is generated by the MPPT algorithm. The MPC receives this voltage reference and computes the converter duty cycle (expressed as a percentage) required to drive the PV voltage towards the reference value.

It should be clarified that the MPC controller is designed using a linearized model around an operating point defined by an initial duty cycle $d_0 = 0.25$. Therefore, the control input is expressed as a deviation variable $\Delta d = d - d_0$. The limits reported in Table II correspond to this deviation variable. When mapped to the physical domain, these limits ensure that the actual duty cycle remains within the feasible range $0 \leq d \leq 1$.

4.2 Test scenarios and considerations

In this section, we analyze the results obtained by the MPC with the optimization algorithms in comparison with the P&O. The aforementioned algorithms were employed in this study to address the challenge of tracking the maximum power point in a PV system. This was achieved using the MPC controller and a boost DC/DC converter while considering critical irradiation and irradiance test scenarios on an average day in the city of Medellín, Colombia. All simulations were conducted in MATLAB $R2023a$ ® on a Dell Precision Tower 5810 workstation equipped with an Intel(R) Xeon(R) CPU E5-1660 v3 @ 3.00GHz, 16 GB of RAM, a 480-GB SSD, and Windows 10.

4.3 Tests under critical operating conditions

One of the primary objectives within this analysis was to ascertain which algorithm allows for maximum power transfer while simultaneously tracking the MPP. The secondary objective was to validate how the MPC controller adapts to the behaviors of the test scenarios in relation to the MPPT algorithms. To determine the maximum energy transfer, we employed the trapezoidal integral [42]. In this data context, time *vs.* power was used. The trapezoidal integral was utilized to estimate the total energy contained within a signal, as shown in Eq. (34).

$$\text{Trapezoidal Integral} = \frac{h}{2}\sum_{i=1}^{n}\left(y_{(i-1)} + y_{(i)}\right) \tag{34}$$

Here, (h) is the difference in the time interval value, (n) is the number of intervals, and $(y_{(i-1)})$ and $(y_{(i)})$ are the power values at consecutive points. It should be noted that the maximum power extracted from the system is derived from the area under the curve of the power generated by the PV panel, in comparison with that obtained by each algorithm.

Table **III** presents the results obtained by the algorithms for the critical irradiance test scenario. This includes the area under the curve achieved by implementing the trapezoidal integral and the maximum percentage of energy extracted.

Table III. Results obtained with algorithms based on the MPC controller under a scenario of variable average irradiance (critical)

Area under the power curve				
PV panel	**P&O**	**PSO**	**SSA**	**VSA**
56.355	43.594	54.065	53.597	53.716
Percentage of power extracted				
PV panel	**P&O**	**PSO**	**SSA**	**VSA**
100	85.101	95.937	95 .106	95.317

In this analysis, consolidated results are presented for the various optimization algorithms in comparison with the P&O algorithm. All algorithms under review successfully extract power from a PV panel under varying irradiance levels.

This study found that the PSO algorithm achieved the highest power extraction, with a performance of 95.937% relative to the PV panel power. Fig. 8 illustrates the reference and calculated voltages, as well as reference and extracted power for PSO. VSA algorithm followed with 95.317% power extraction (Fig. 9). Both algorithms, with their iterative processes and particles, exhibit optimal MPPT responses when tuned under identical conditions. SSA ranked third with 95.106% extraction, as displayed in Fig. **10**. Lastly, P&O achieved 85.101%, with Figure **11** showing significant variations in voltage and power due to the algorithm's inherent behavior.

These results were obtained under varying irradiance conditions over time. To determine the algorithm with the highest power extraction, the system was simulated under critical irradiance variations, representing an average 24-hour day compressed into 2.4 seconds in Matlab/Simulink, with each 0.1 second corresponding to an hour of operation.

It should be clarified that, at the beginning of the simulation, the PV array operates under zero solar irradiation, according to the selected irradiation profile. Under this condition, the PV system naturally exhibits the open-circuit voltage when no power conversion is active. However, since the MPPT algorithm imposes a voltage reference associated with the expected MPP, the PV array is unable to sustain this voltage due to energy unavailability. Consequently, the PV voltage decreases and tends toward zero until the solar irradiance level increases.

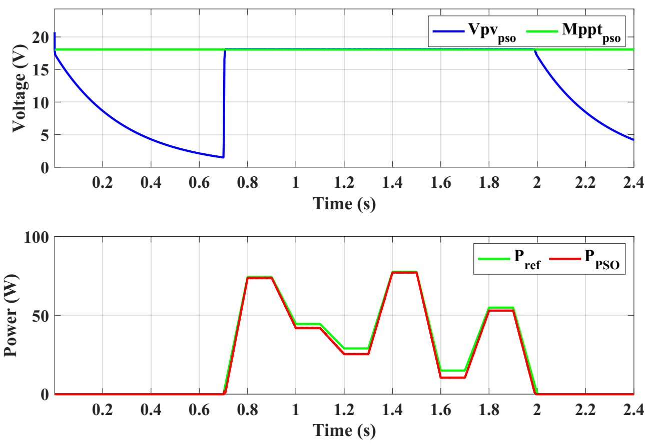

Figura 8. Variation in power demand and generation under average daily irradiance, as determined by the PSO

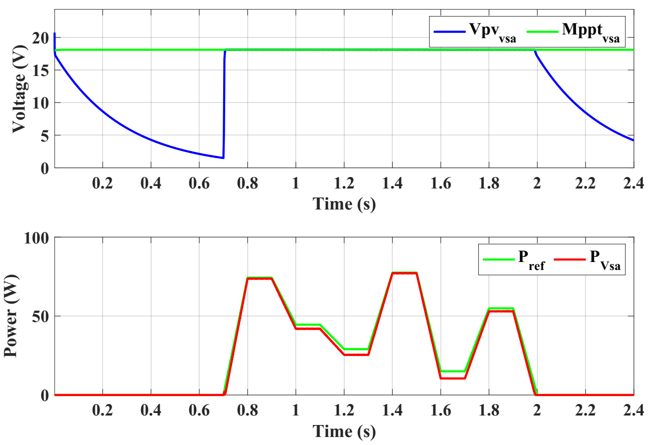

Figura 9. Variation in power demand and generation under average daily irradiance, as determined by the VSA

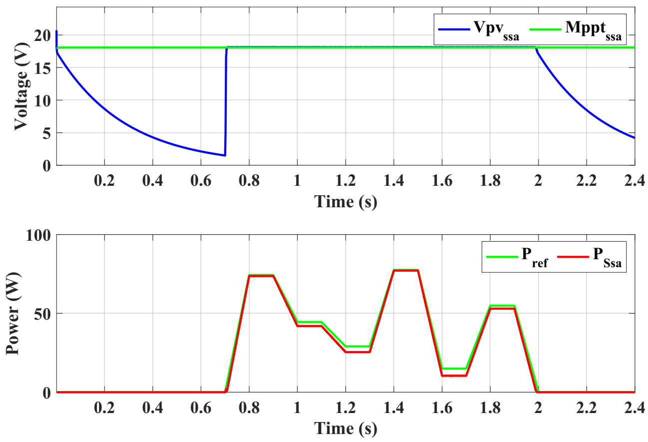

Figura 10. Variation in power demand and generation under average daily irradiance, as determined by the SSA

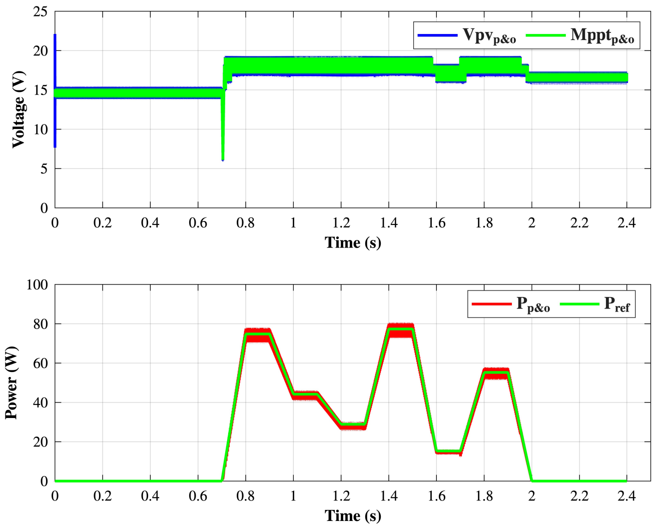

Figura 11. Variation in power demand and generation under average daily irradiance, as determined by the P&O algorithm

4.4 Tests under mean operating conditions

On the other hand, for an average scenario (Table IV), the results are presented in the same manner as in Table III. Here, under an average irradiance curve, note how the algorithms manage to extract maximum power.

To validate the test systems, an average daily irradiance condition was applied. According to the results, the PSO algorithm achieved the highest power extraction, with 94.538% relative to PV panel power, as shown in Fig, 12 alongside the corresponding voltage variations. The VSA followed with 94.218% power extraction (Fig. 13). In third place, SSA achieved 94.118%, exhibiting a similar behavior

Table IV. Results obtained with algorithms based on the MPC controller under a scenario of average irradiance

Area under the power curve				
PV panel	**P&O**	**PSO**	**SSA**	**VSA**
56	42.671	52.941	52 .706	52.762
Percentage of power extracted				
PV panel	**P&O**	**PSO**	**SSA**	**VSA**
100	84.056	94.538	94 .118	94.218

to other optimization algorithms (Fig. 14). Finally, P&O reached 84.056%, with Figure 15 highlighting pronounced variations in voltage and power due to its nature.

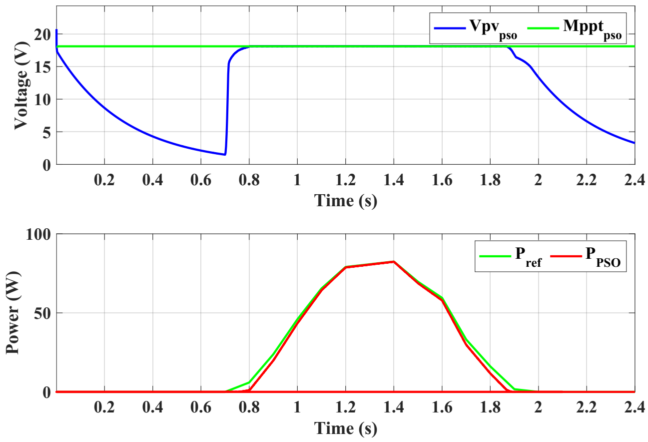

Figura 12. Variation in power demand and generation under critical daily irradiance, as determined by the PSO

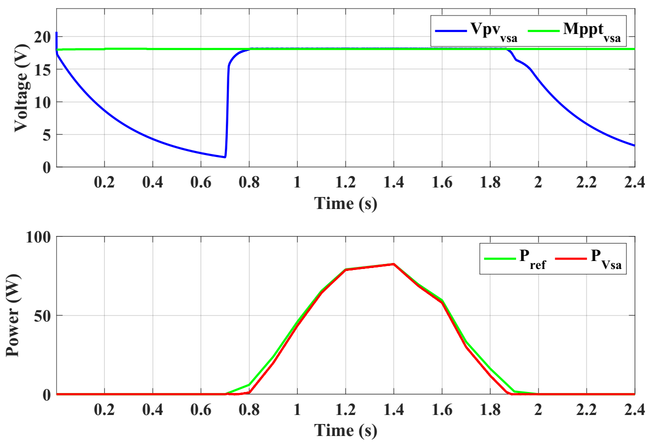

Figura 13. Variation in power demand and generation under critical daily irradiance, as determined by the VSA

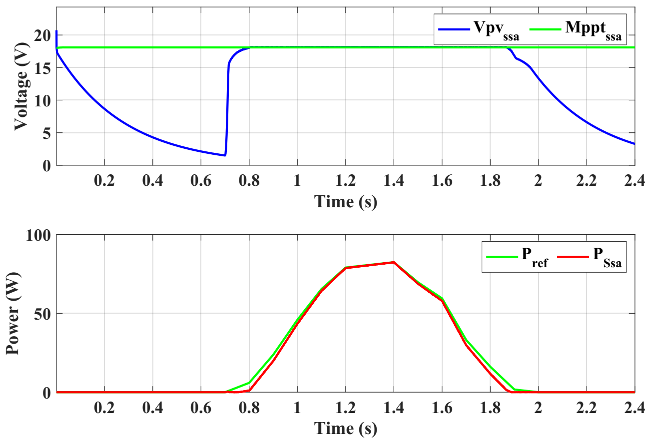

Figura 14. Variation in power demand and generation under critical daily irradiance, as determined by the SSA

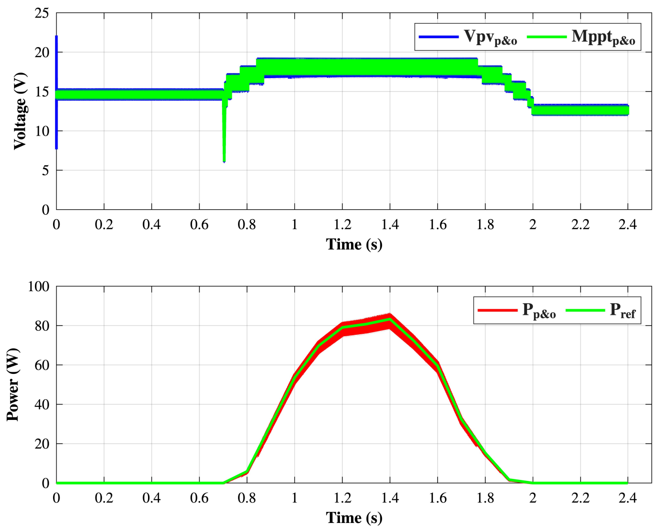

Figura 15. Variation in power demand and generation under critical daily irradiance, as determined by the P&O algorithm

During the simulation of these systems, various tests were conducted under different irradiance levels over a test period of 2.4 s. This allowed observing the way in which optimization algorithms are capable of extracting more power in response to system changes under any irradiance profile compared to P&O. It was evident that the algorithm that enables maximum power extraction is PSO. In the critical scenario, an average power of 91.615% was obtained by the algorithms, and, on an average day, 91.733% of the power was extracted.

5 Conclusions

This study presented a comprehensive analysis of four MPPT algorithms, *i.e.*, P&O, PSO, SSA, and VSA, focused on maximizing power extraction from a PV panel. Emphasis was placed on the objective function and algorithm efficiency under varying irradiance levels, including both average daily and critical conditions. Using Matlab/Simulink, complex scenarios that reflect real-world PV configurations were simulated. The analysis used a trapezoidal integral to evaluate the area under the power curve, showing that PSO achieved approximately 95.937% and 94.538% of power extraction under critical and average conditions, respectively. The remaining algorithms followed in order: VSA, SSA, and P&O. Visual representations further illustrated system responses, providing a clearer understanding of voltage-power relationships. Given its high efficiency, PSO emerges as a strong candidate for future PV system applications, particularly in scenarios with partial and total shading. Additionally, the MPC controller demonstrated adaptability, effectively adjusting the boost DC/DC converter to maintain MPPT under variable irradiance conditions. This adaptability highlights MPC's potential for future PV implementations that encounter fluctuating environmental conditions. Future work aims to develop a DMPPT platform to support series-connected PV systems. This would include integrating monitoring systems with energy storage, enabling optimal management and stability under conditions with varying irradiance and improving system efficiency for different PV applications.

6 Author contributions

Conceptualization: Jhon Anderson Gómez Pemberty, Jaime Alberto Ramírez Ospina.
Methodology: Jose Mena, Juan Esteban Zabala.
Software: Jose Mena, Jhon Anderson Gómez Pemberty.
Validation: Jose Mena, Juan Esteban Zabala.
Formal analysis: Jose Mena, Jhon Anderson Gómez Pemberty.
Investigation: Jose Mena, Jhon Anderson Gómez Pemberty.
Resources: Juan Esteban Zabala.
Data curation: Jose Mena.
Writing – original draft: Jose Mena.
Writing – review and editing: Jose Mena, Juan Esteban Zabala.
Visualization: Jose Mena.
Supervision: Juan Esteban Zabala, Jaime Alberto Ramírez Ospina.
Project administration: Jhon Anderson Gómez Pemberty.
Funding acquisition: Institución Universitaria Digital de Antioquia.

7 Conflicts of Interest

The authors declare no conflicts of interest.

8 Declaration of generative AI and AI-assisted technologies in the writing process

During the preparation of this work, the authors used ChatGPT to improve the writing. After using this tool, the authors reviewed and edited the content as needed and take full responsibility for the content of this publication.

References

[1] T. Ahmad and D. Zhang, "A critical review of comparative global historical energy consumption and future demand: the story told so far," *Energy Rep.*, vol. 6, pp. 1973–1991, 2020.

[2] K. Makieła, B. Mazur, and J. Głowacki, "The impact of renewable energy supply on economic growth and productivity," *Energies*, vol. 15, no. 13, p. 4808, 2022.

[3] Y. Zhu and C. Huo, "The impact of agricultural production efficiency on agricultural carbon emissions in china," *Energies*, vol. 15, no. 12, p. 4464, 2022.

[4] M. Khezri, M. S. Karimi, J. Mamkhezri, R. Ghazal, and L. Blank, "Assessing the impact of selected determinants on renewable energy sources in the electricity mix: the case of ASEAN countries," *Energies*, vol. 15, no. 13, p. 4604, 2022.

[5] P. Zhang and D. Hao, "Enterprise financial management and fossil fuel energy efficiency for green economic growth," *Resour. Policy*, vol. 84, p. 103763, 2023.

[6] C. Tudor and R. Sova, "On the impact of GDP per capita, carbon intensity and innovation for renewable energy consumption: worldwide evidence," *Energies*, vol. 14, no. 19, p. 6254, 2021.

[7] A. Bughneda, M. Salem, A. Richelli, D. Ishak, and S. Alatai, "Review of multilevel inverters for PV energy system applications," *Energies*, vol. 14, no. 6, p. 1585, 2021.

[8] I. Jagadeesh and V. Indragandhi, "Comparative study of DC-DC converters for solar PV with microgrid applications," *Energies*, vol. 15, no. 20, p. 7569, 2022.

[9] M.-H. Hwang, Y.-G. Kim, H.-S. Lee, Y.-D. Kim, and H.-R. Cha, "A study on the improvement of efficiency by detection solar module faults in deteriorated photovoltaic power plants," *Appl. Sci.*, vol. 11, no. 2, p. 727, 2021.

[10] S. A. Gorji, H. G. Sahebi, M. Ektesabi, and A. B. Rad, "Topologies and control schemes of bidirectional DC–DC power converters: an overview," *IEEE Access*, vol. 7, pp. 117 997–118 019, 2019.

[11] L. Zhang, Z. Wang, S. Li, S. Ding, and H. Du, "Universal finite-time observer based second-order sliding mode control for DC-DC buck converters with only output voltage measurement," *J. Franklin Inst.*, vol. 357, no. 16, pp. 11 863–11 879, 2020.

[12] M. Mao, L. Cui, Q. Zhang, K. Guo, L. Zhou, and H. Huang, "Classification and summarization of solar photovoltaic MPPT techniques: a review based on traditional and intelligent control strategies," *Energy Rep.*, vol. 6, pp. 1312–1327, 2020.

[13] R. B. Bollipo, S. Mikkili, and P. K. Bonthagorla, "Hybrid, optimal, intelligent and classical PV MPPT techniques: a review," *CSEE J. Power Energy Syst.*, vol. 7, no. 1, pp. 9–33, 2020.

[14] S. Bhattacharyya, D. S. P. Kumar, S. Samanta, and S. Mishra, "Steady output and fast tracking MPPT (SOFT-MPPT) for P&O and InC algorithms," *IEEE Trans. Sustain. Energy*, vol. 12, no. 1, pp. 293–302, 2021.

[15] P. Kumar and I. Srikanth, "Power quality performance enhancement by PV-based distribution static compensator under incremental conductance maximum power point tracking algorithm," *Cleaner Energy Syst.*, vol. 4, p. 100062, 2023.

[16] F. J. Diez, A. Martínez-Rodríguez, L. M. Navas-Gracia, L. Chico-Santamarta, A. Correa-Guimaraes, and R. Andara, "Estimation of the hourly global solar irradiation on the tilted and oriented plane of photovoltaic solar panels applied to greenhouse production," *Agronomy*, vol. 11, no. 3, p. 495, 2021.

[17] J. A. Qahouq, Y. Jiang, and W. Huang, "Load-voltage-based single-sensor MPPT controller for multi-channel PV systems," in *Proc. IEEE Appl. Power Electron. Conf. Expo. (APEC)*, 2014, pp. 3451–3454.

[18] A. Ortiz, E. Mendez, I. Macias, and A. Molina, "Earthquake algorithm-based voltage referenced MPPT implementation through a standardized validation frame," *Energies*, vol. 15, no. 23, p. 8971, 2022.

[19] M. Jiang, M. Ghahremani, S. Dadfar, H. Chi, Y. N. Abdallah, and N. Furukawa, "A novel combinatorial hybrid SFL–PS algorithm based neural network with perturb and observe for the MPPT controller of a hybrid PV-storage system," *Control Eng. Pract.*, vol. 114, p. 104880, 2021.

[20] S. Hadji, J.-P. Gaubert, and F. Krim, "Real-time genetic algorithms-based MPPT: study and comparison (theoretical and experimental) with conventional methods," *Energies*, vol. 11, no. 2, p. 459, 2018.

[21] M. H. Zafar, N. M. Khan, A. F. Mirza, and M. Mansoor, "Bio-inspired optimization algorithms based maximum power point tracking technique for photovoltaic systems under partial shading and complex partial shading conditions," *J. Cleaner Prod.*, vol. 309, p. 127279, 2021.

[22] R. Mas, A. Berastain, A. Antoniou, L. Angeles, S. Valencia, and C. Celis, "Genetic algorithms-based size optimization of directly and indirectly coupled photovoltaic-electrolyzer systems," *Energy Convers. Manag.*, vol. 270, p. 116213, 2022.

[23] A. G. Abo-Khalil, I. I. El-Sharkawy, A. Radwan, and S. Memon, "Influence of a hybrid MPPT technique, SA-P&O, on PV system performance under partial shading conditions," *Energies*, vol. 16, no. 2, p. 577, 2023.

[24] M. A. Hafeez, A. Naeem, M. Akram, M. Y. Javed, A. B. Asghar, and Y. Wang, "A novel hybrid MPPT technique based on harris hawk optimization (HHO) and perturb and observer (P&O) under partial and complex partial shading conditions," *Energies*, vol. 15, no. 15, p. 5550, 2022.

[25] M. Rastogi, A. Ahmad, and A. H. Bhat, "Performance investigation of two-level reduced-switch D-STATCOM in grid-tied solar-PV array with stepped P&O MPPT algorithm and modified SRF strategy," *J. King Saud Univ. Eng. Sci.*, 2021.

[26] K. Ali, L. Khan, Q. Khan, S. Ullah, S. Ahmad, S. Mumtaz, F. W. Karam, and Naghmash, "Robust integral backstepping based nonlinear MPPT control for a PV system," *Energies*, vol. 12, no. 16, p. 3180, 2019.

[27] S. Mo, Q. Ye, K. Jiang, X. Mo, and G. Shen, "An improved MPPT method for photovoltaic systems based on mayfly optimization algorithm," *Energy Rep.*, vol. 8, pp. 141–150, 2022.

[28] T. Hai, J. Zhou, and K. Muranaka, "An efficient fuzzy-logic based MPPT controller for grid-connected PV systems by farmland fertility optimization algorithm," *Optik*, vol. 267, p. 169636, 2022.

[29] B. C. Phan, Y.-C. Lai, and C. E. Lin, "A deep reinforcement learning-based MPPT control for PV systems under partial shading condition," *Sensors*, vol. 20, no. 11, p. 3039, 2020.

[30] M. L. Katche, A. B. Makokha, S. O. Zachary, and M. S. Adaramola, "A comprehensive review of maximum power point tracking (MPPT) techniques used in solar PV systems," *Energies*, vol. 16, no. 5, p. 2206, 2023.

[31] A. Almutairi, A. G. Abo-Khalil, K. Sayed, and N. Albagami, "MPPT for a PV grid-connected system to improve efficiency under partial shading conditions," *Sustainability*, vol. 12, no. 24, p. 10310, 2020.

[32] S. Angadi, U. R. Yaragatti, Y. Suresh, and A. B. Raju, "System parameter based performance optimization of solar PV systems with perturbation based MPPT algorithms," *Energies*, vol. 14, no. 7, p. 2007, 2021.

[33] A. Gündoğdu, "System identification based ARV-MPPT technique for PV systems under variable atmospheric conditions," *IEEE Access*, vol. 10, pp. 51 325–51 342, 2022.

[34] L. Tightiz, S. Mansouri, F. Zishan, J. Yoo, and N. Shafaghatian, "Maximum power point tracking for photovoltaic systems operating under partially shaded conditions using SALP swarm algorithm," *Energies*, vol. 15, no. 21, p. 8210, 2022.

[35] Z.-K. Fan, A. Setianingrum, K.-L. Lian, and S. Suwarno, "A hybrid approach for photovoltaic maximum power tracking under partial shading using honey badger and genetic algorithms," *Energies*, vol. 17, no. 16, p. 3935, 2024.

[36] L. A. T. Grisales, C. A. Ramos-Paja, and A. J. Saavedra-Montes, "Techniques for modeling photovoltaic systems under partial shading," *Tecnura*, vol. 20, no. 48, pp. 171–183, 2016.

[37] A. Gómez and R. Correa, "Implementación de un sistema de control predictivo multivariable en un horno," *Dyna*, vol. 76, no. 157, pp. 195–203, 2009.

[38] MathWorks, "Model predictive control toolbox," 2023, https://la.mathworks.com/products/model-predictive-control.html (accessed Jun. 21, 2023). [Online]. Available: https://la.mathworks.com/products/model-predictive-control.html

[39] J. Kennedy and R. Eberhart, "Particle swarm optimization," in *Proc. IEEE Int. Conf. Neural Netw. (ICNN)*, vol. 4, 1995, pp. 1942–1948.

[40] B. Doğan and T. Ölmez, "A new metaheuristic for numerical function optimization: vortex search algorithm," *Inf. Sci.*, vol. 293, pp. 125–145, 2015.

[41] J. Montano, A. F. T. Mejia, A. A. R. Muñoz, F. Andrade, O. D. G. Rivera, and J. M. Palomeque, "Salp swarm optimization algorithm for estimating the parameters of photovoltaic panels based on the three-diode model," *Electronics*, vol. 10, no. 24, p. 3123, 2021.

[42] S. S. Dragomir, P. Cerone, and A. Sofo, "Some remarks on the trapezoid rule in numerical integration," *RGMIA Res. Rep. Collect.*, vol. 2, no. 5, 1999.

Jose Mena

from Medellín, Antioquia, Colombia, earned his Bachelor's degree in Mechatronics Engineering from Instituto Tecnológico Metropolitano (ITM) in 2017. He is currently pursuing a Master's degree in Automation and Industrial Control at ITM and works as a lecturer in the Department of Mechatronics at Institución Universitaria Digital de Antioquia. His research interests include renewable energy systems, power electronics, smart grids, photovoltaic systems optimization, fault diagnosis in photovoltaic panels, intelligent energy storage management, prototyping, microelectronics, and embedded systems.
Email: jose.mena@prof.iudigital.edu.co

Juan Esteban Zabala-Daza

from Medellín, Antioquia, Colombia, earned his Bachelor's degree in Mechatronics Engineering from Instituto Tecnológico Metropolitano (ITM). He is currently a researcher focused on control systems and photovoltaic energy applications. His research interests include model-predictive control, optimization algorithms, renewable energy systems, and advanced control strategies applied to power electronics.
Email: juanzabala1110@correo.itm.edu.co

Jhon A. Gómez P.

from Medellín, Antioquia, Colombia, earned his Bachelor's degree in Mechatronic Engineering from Instituto Tecnológico Metropolitano (ITM) in 2017. He earned a Specialist's degree in Project Formulation and Evaluation at Institución Universitaria Digital de Antioquia. His research interests include renewable energy systems, power electronics, photovoltaic systems optimization, fault diagnosis in electronic systems, prototyping, microelectronics, PLC programming, and embedded systems.
Email: jhon.gomez95@est.iudigital.edu.co

Jaime A. Ramírez-Ospina

from Itagüí, Antioquia, Colombia, earned his Bachelor's degree in Instrumentation and Control Engineering from Politécnico Jaime Isaza Cadavid in 2013. He has professional experience in industrial automation and is currently pursuing a Master's degree in Innovation and Technology at Universidad El Bosque. He also works as a lecturer in the Department of Mechatronics at Institución Universitaria Digital de Antioquia. His research interests include industrial automation, industrial process optimization, renewable energy systems, photovoltaic systems optimization, intelligent energy storage management, and educational innovation in engineering.
Email: jaime.ramirez@iudigital.edu.co

UNIVERSIDAD DISTRITAL
FRANCISCO JOSÉ DE CALDAS

Ingeniería

https://revistas.udistrital.edu.co/index.php/reving/issue/view/1320

DOI: https://doi.org/10.14483/23448393.23305

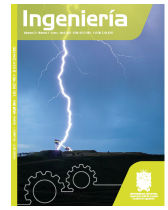

Research

Classification of Transient Signals Produced by Direct Impacts of a Lightning Strike on a Medium Voltage Network in the Frequency Domain Using a Deep Learning Neural Network

Clasificación de las señales transitorias producidas por el impacto directo de un rayo en una red de media tensión en el dominio de la frecuencia mediante una red neuronal de aprendizaje profundo

Luis Eduardo Perdomo Orjuela[1, 2, *], Francisco Santamaria[2], and Nelson Enrique Vera[2]

[1]Universidad Nacional de Colombia, (Bogotá, Colombia)
[2]Universidad Distrital Francisco José de Caldas, (Bogotá, Colombia)

Abstract

Context: This research presents two main results: (i) the application of deep learning networks for the classification of transient overvoltage in the frequency domain, and (ii) the physical-mathematical formulation for the coupling of atmospheric electrical discharges in polarized media in the frequency domain.
Method: Initially, transient overvoltage records resulting from atmospheric electrical discharges were obtained from simulations in EMTP-ATP software, using the IEEE 13-node distribution network as a reference. Each transient overvoltage was transformed from the time domain to the frequency domain via the Fast Fourier Transform. Subsequently, the neural networks were trained, and their results were compared. For indirect lightning strikes, a complex-variable analysis of permittivity and permeability was performed. These variables were applied to the lightning coupling model in distribution lines or networks.
Results: Classification accuracies of 80 and 89.99% were achieved for transient overvoltage using the GoogLeNet and Python-ChatGPT neural networks, respectively. Furthermore, this work presents the coupling expression for atmospheric electrical discharges in polarized media.
Conclusions: The classification of transient overvoltage records using deep-layer neural networks and the physical-mathematical expression for lightning coupling in the frequency domain through complex variables allows for a broader understanding of the network response to this type of natural phenomenon.

Keywords: artificial intelligence, lightning, polarized media, frequency domain, deep neural networks.

Article history

Received:
March 4th, 2025

Modified:
October 17th, 2025

Accepted:
November 27th, 2025

Ing, vol. 31, no. 1, 2026, e23305

* Correspondence: leperdomoo@unal.edu.co

Resumen

Contexto: Esta investigación presenta dos resultados principales: (i) la aplicación de redes de aprendizaje profundo para la clasificación de sobretensiones transitorias en el dominio de la frecuencia y (ii) la formulación fisicomatemática para el acoplamiento de descargas eléctricas atmosféricas en medios polarizados en el dominio de la frecuencia.
Método: Inicialmente, se obtuvieron registros de sobretensiones transitorias producto de descargas eléctricas atmosféricas, a partir de simulaciones en el *software* EMTP-ATP, tomando como referencia la red de distribución IEEE de 13 nodos. Las sobretensiones transitorias fueron transformadas del dominio del tiempo al dominio de la frecuencia mediante la aplicación de la transformada rápida de Fourier. Posteriormente, se entrenaron las redes neuronales y se compararon sus resultados. Para descargas eléctricas por impacto indirecto, se realizó un manejo en variable compleja de la permitividad y la permeabilidad, las cuales fueron aplicadas al modelo de acoplamiento de rayos en líneas o redes de distribución.
Resultados: Se alcanzó una exactitud de 80 y 89.99 % en la clasificación de sobretensiones transitorias para las redes neuronales GoogLeNet y Python-ChatGPT respectivamente. Por otra parte, este trabajo presenta la expresión de acoplamiento de descargas eléctricas atmosféricas en medios polarizados.
Conclusiones: La clasificación de sobretensiones transitorias mediante redes neuronales de capa profunda y la expresión fisicomatemática de acoplamiento del rayo en el dominio de la frecuencia mediante variables complejas permite ampliar la comprensión de la respuesta de la red ante este tipo de fenómenos naturales.

Palabras clave: inteligencia artificial, descarga eléctrica atmosférica, medios polarizados, dominio de la frecuencia, redes de aprendizaje profundo

Contents

1. Introduction

Transient overvoltage in medium-voltage networks occurs due to direct or indirect lightning strokes [1]-[12]. Direct strokes on any phase conductors are caused by the absence of guard cables in the grid or by low-intensity lightning currents for which the attraction radius of said cables is insufficient. On the other hand, indirect strokes occur due to the coupling of the wave propagating through the air to the network. The physical-mathematical expression for this can be found in the scientific literature [13]-[24].

The classification of direct lightning strokes on medium-voltage networks allows developing appropriate investment and maintenance plans. This allows optimizing the CAPEX/OPEX of companies, utilities, and other related entities. On the other hand, improving the shielding of medium-voltage networks in rural areas, as well as implementing comprehensive lightning protection systems, has a positive impact on the service quality for end-users with sensitive loads. Improving the design of comprehensive lightning protection systems based on the characterization of surge records allows improving operation and maintenance processes, making the installation safe for network operators.

The purpose of this work is to continue with the analysis of previously conducted research detailing the composition of the IEEE 13-node test feeder, specifically the lightning current generator, the surge arresters, and the grounding system, among others [18], [25]-[30]. The second section of this article provides a brief description of said feeder in order to contextualize the progress made. GoogLeNet, Python, and ChatGPT were used to classify transient overvoltage records taken the head of the feeder (*i.e.*, on the secondary side of the 34.5/13.2 kV transformer), as presented in the third section. The reader may consult additional works conducted with artificial intelligence techniques in [13]-[16], [31]-[35]. The fourth and fifth sections detail the methodology and the analyses conducted regarding the accuracy and results obtained with our neural network-based approach. The sixth part of this research presents the physical-mathematical contribution to the coupling of atmospheric lightning discharges in polarized media. Throughout this section, the authors provide a detailed formulation of complex permittivity and permeability, together with a new proposal for its application within the Taylor model [23]. The final part of this document presents the conclusions drawn from our work.

2. Testing system

Our evaluation of the frequency response resulting from lightning captured at the head of the medium-voltage (MV) grid covers the frequency spectrum up to 4 kHz.

2.1 IEEE test feeder

The IEEE 13-node test feeder was taken as a reference to characterize the transient overvoltage resulting from direct lightning strokes in MV networks. Fig. 1 shows the system implemented in the EMTP-ATP software.

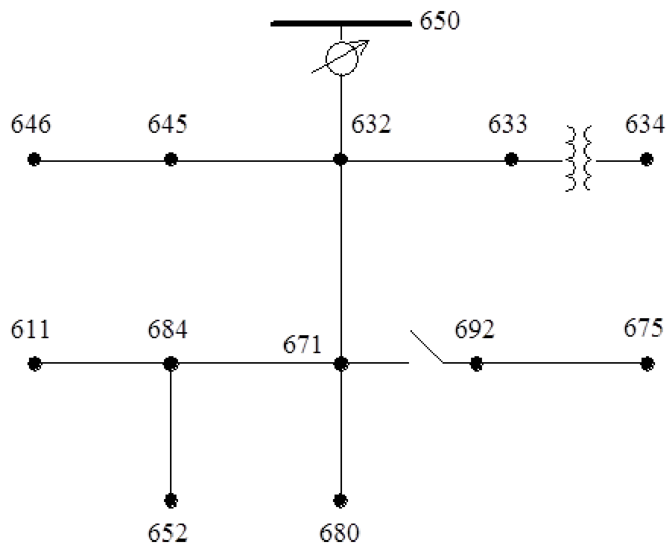

Figure 1. IEEE 13-node test feeder

In order to adequately assess the transient overvoltage transfer, the high-frequency model of the network's constituents was included. As an example, the capacitive coupling model between transformer windings had a value of 5 pF. On the other hand, to assess flashover in the network due to dielectric stress, the insulation coordination model in the medium voltage structures considered the basic insulation level (BIL) and the critical flashover (CFO). For the specific case of the selected region of Colombia, the BIL value included the altitude correction factor, considering an altitude of 2600 m above sea level. In addition, we included correction for environmental pollution, rated as moderate to high, and a grounding system, which considered an impedance at neutral bushing for the HV/MV transformers. Therefore, the BIL values were 95-170 kV [36]. The surge arresters were only located in the transformers [5], [37]-[44].

Direct lightning strokes were distributed along sections 632-633, 671-680, and 632-671. Section 632-671 was divided into ten parts, with strokes covering 10, 50, and 90% of the network.

The point of registration for transient overvoltage resulting from direct lightning strokes was the transformer head, located between nodes 650 and 632 on the secondary side, with a voltage level of 13.2 kV.

2.2 Current pulse generator

Lightning has an 8/20 μs waveform, with peak currents of 3, 10, 20, 50, 80, and 100 kA. The direct strokes on the IEEE 13-node network occurred in phases A and C. Fig. 2 present the generated current waveform.

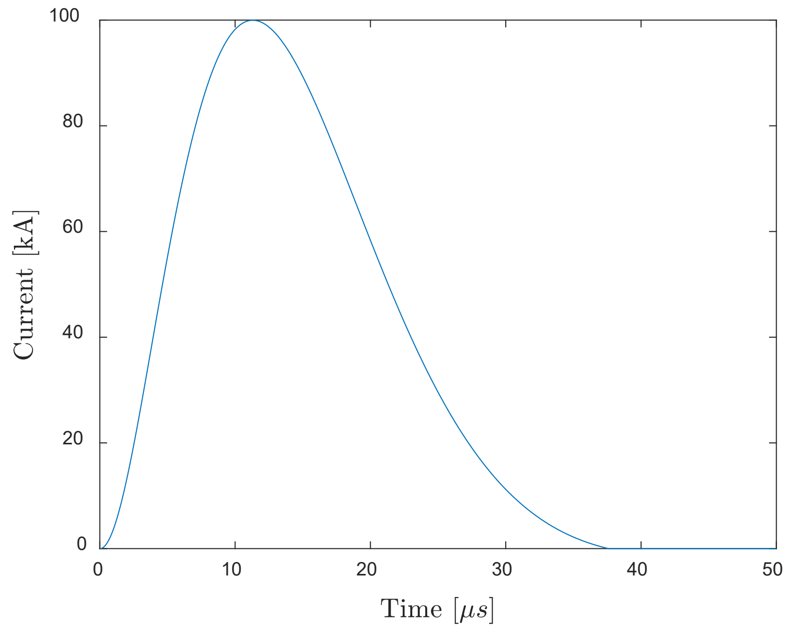

Figure 2. Current transient signal with an 8/20 μs waveform

The selection of the previously listed current magnitudes was based on the CIGRE and IEEE stroke current probability curves (Fig. 3), thereby ensuring that our study covered the spectrum of possible magnitudes in the analyzed geographic area [6], [45]-[47].

The IEEE 1410-2010 standard presents the statistical distribution of measurements obtained from towers, with a mean value of 31 kA [45], [48]. In IEEE 998-2012, the mean value ranges from 24 to 31 kA, and, in IEEE 1243-1997, the normalized mean value is 31 kA. This value is 31.1 kA in CIGRE 63 [49]-[51].

Throughout the Colombian territory, the distribution of positive and negative discharges is 31 and 69% with respect to the total lightning strokes [36]. It is noteworthy that 50% of the cloud-to-ground lightning equals or exceeds the value of 35 kA.

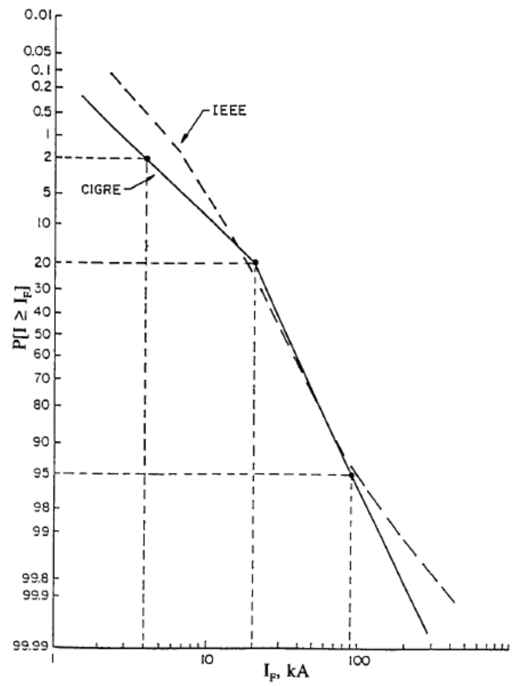

Figure 3. CIGRE and IEEE stroke current probability curves, first stroke Negative downward flash [4].

3. GoogLeNet, Python, and ChatGPT

The GoogLeNet deep learning neural network was implemented in MATLAB's Deep Network Designer, with a depth of 22, a size of 27 MB, seven million parameters, and an image input size of 224 x 224 pixels. The dataset used in this research contained RGB-type images, so we had to condition them to a size of 224 x 224 x 3 as an input parameter for the network. Fig. 4 depicts the architecture of the neural network.

Figure 4. GoogLeNet neural network architecture in MATLAB

The final blocks of GoogLeNet were adapted, ensuring a correct response to the number of classes entered. The ClassOutput layer (*i.e.*, the last one) and the FullyConnected layer were replaced to support five classes. Fig. 5 shows the replaced layers.

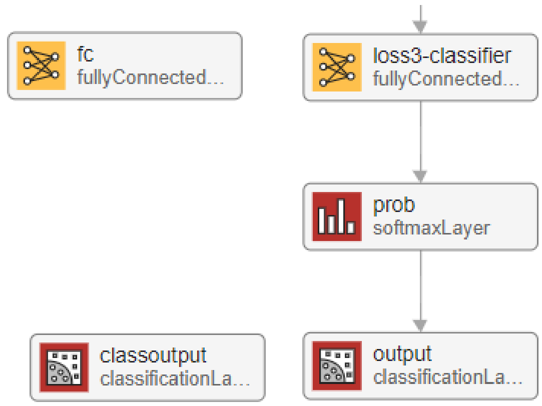

Figure 5. Replaced GoogLeNet layers

Table I presents the pseudocode for our neural network, which was developed in collaboration with ChatGPT [52]. The optimal hyperparameters are as follows: filters_1: 64, kernel_size_1: 4, conv_layers: 3, filters_2: 96, kernel_size_2: 5, units: 320, learning_rate: 0.001, filters_3: 32, kernel_size_3: 3, filters_4: 80, kernel_size_4: 3.

Table I. Pseudocode for the Python neural network developed in collaboration with ChatGPT

Input: Image dataset distributed into five classes.
Output: trained and validated neural network for image classification

|1| **Mount Google Drive**|
|2| Import necessary libraries: pandas, tensorflow, sklearn.model_selection|
|3| Define dataset_path|
|4| Define function create_dataframe_from_images(dataset_path) |
|5| Call create_dataframe_from_images(dataset_path) and assign it to image_df|
|6| Print image_df.head()|
|7| Import matplotlib.pyplot and cv2|
|8| Define function visualize_dataset_per_class(df, num_samples)|
|9| Call visualize_dataset_per_class(image_df, num_samples=5)|
|10| Define datagen|
|11| Define train_generator|
|12| Define validation_generator|
|13| Import keras, layers, kerastuner|
|14| Define function model_builder(hp) |
|15| Define tuner|
|16| Define class ClearTrainingOutput(tf.keras.callbacks.Callback)|
|17| Execute tuner.search() with specified arguments and callbacks|
|18| Get the best hyperparameters with tuner.get_best_hyperparameters(num_trials=1)[0]|
| 19| Print best hyperparameters|
|20| Import EarlyStopping and define early_stopping|
|21| Build model with tuner.hypermodel.build(best_hps)|
|22| Train the model with the specified parameters and callbacks|

4. Methodology

Initially, the IEEE 13-node feeder was modeled in the EMTP-ATP software, in order to record the transient overvoltage from direct lightning strokes at the head of the network. Subsequently, the records were converted from the time domain to the frequency domain using the MATLAB software.

Once the five dataset classes with transient signals in the frequency domain had been constructed, the neural networks were performed in MATLAB and Python-ChatGPT. Fig. 6 presents the transformation of the transient signal. The transient signal in the time domain has no scaling regarding the overvoltage magnitude. Fig. 6 shows the records of direct lightning stroke, measured at the head of the feeder (20 kA at L632-671, 10% distance from L632 node).

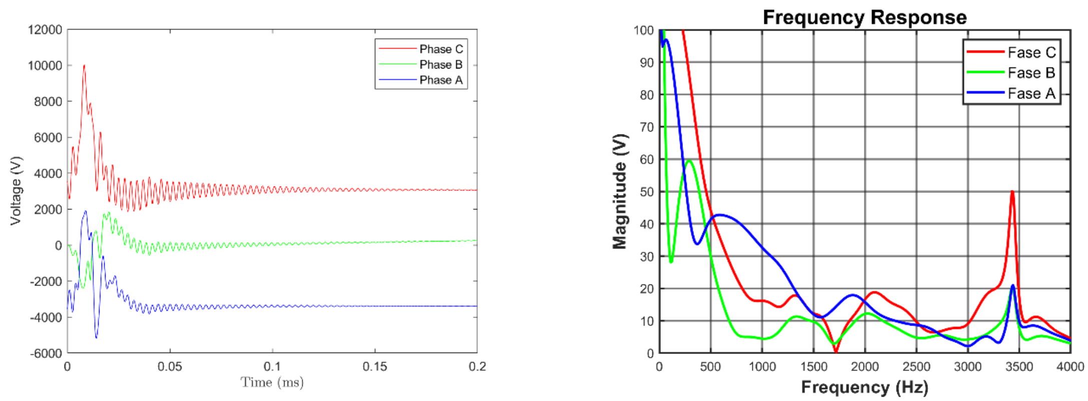

Figure 6. Transient signals in the time and frequency domains

5. Analysis of the results

The dataset was composed of 60 records of transient overvoltage in the frequency domain. As an example, Fig. 7 shows the frequency response of nine records with return stroke currents of 3, 50, and 100 kA and a waveform of 8/20 μs in phase C. The impact points with records of 13.2 kV at the feeder head are L632-633, L632-671 (50% distance from L632 node), and L671-680.

The format of the transient overvoltage records was PNG (Portable Network Graphics) format. The distribution of the dataset was 70% for training and 30% for testing in GoogLeNet. As for Python-ChatGPT, the distribution was 80% for training and 20% for testing.

Fig. 7 shows that, as the distance from the lightning stroke to the measurement point increases, frequencies above 1 kHz are attenuated. Therefore, the system behaves like a low-pass filter, which is consistent with the capacitive model of MV networks, the operation of surge arresters, and the electrical disruption of the insulator chain (pin insulator) of the poles supporting the MV overhead conductors, among other aspects.

On the other hand, frequencies below 1 kHz experience an increase in magnitude in some cases, given the reflection caused by changes in the characteristic impedance along the different branches of the MV system.

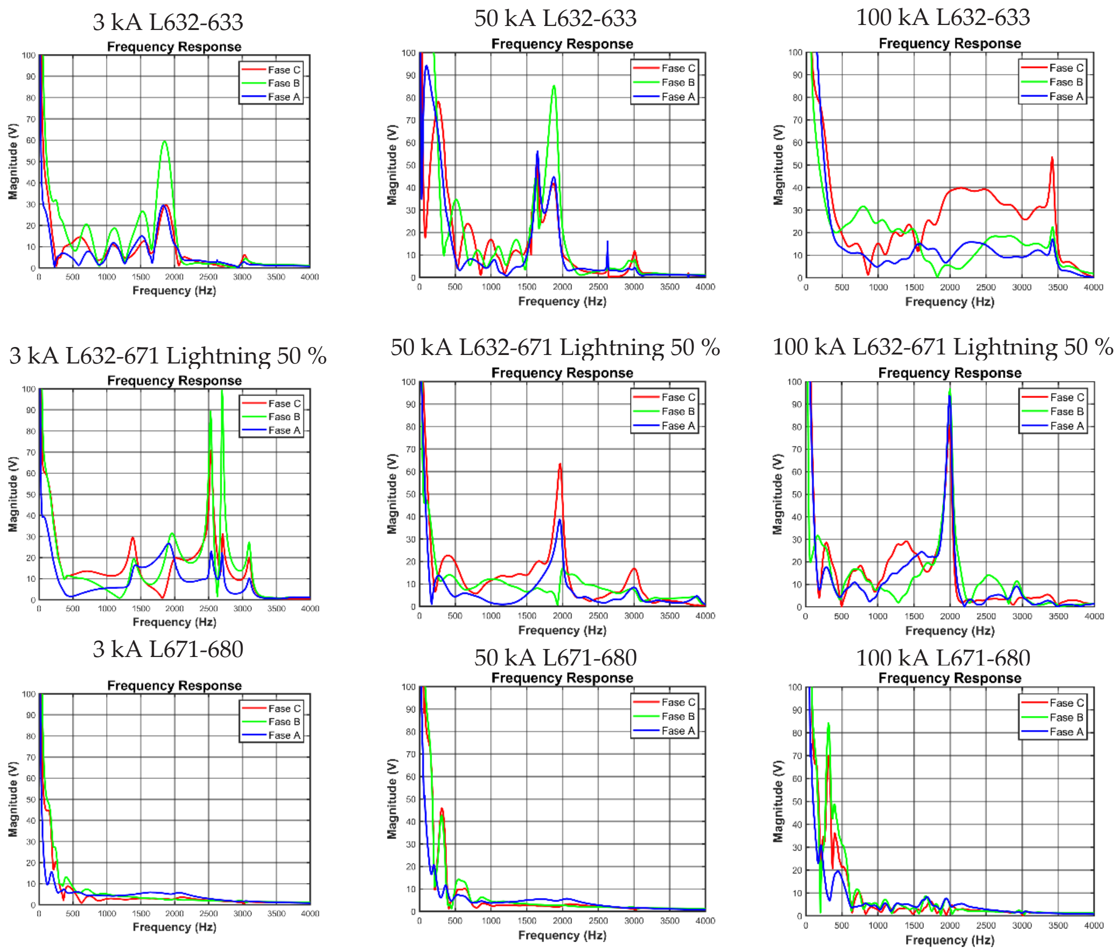

Figure 7. Frequency-domain transient overvoltage records from the feeder head

Table II presents the parameterization of each trained instance of GoogLeNet along with its accuracy. The best results were obtained by Network 3, with a value of 80%.

Table II. Summary of the parameters used for our instances of the GoogLeNet deep learning network

Trained network	Validation frequency	*Max* epochs	*MiniBatch* size	Validation accuracy [%]
E1	1	200	12	**60**
2	10	150	10	**50**
3	1	200	24	**80**
4	1	200	36	**60**
5	**24**	**150**	**24**	**75**

trainedNetwork_5 and trainedNetwork_6 reported accuracies of 85 and 45%, respectively. These are the pretrained neural networks with the best and worst results. The difference in their parameterization corresponds to the *MiniBatch* size: 12 for trainedNetwork_5 and 24 for trainedNetwork_6. All neural networks were trained with the Adam solver, selecting the best evaluation point.

Four images from the dataset were evaluated to appropriately classify the frequency transient overvoltage measured at the 13.2 kV feeder head. The results of said classification show an adequate response when it comes to identifying direct lightning strokes with a peak value of 20 kA. Fig. 8 (1:1) shows a direct stroke in network segment L632-633. The (1:2) image reports a direct stroke in network segment L632-671, covering 90% of the line. The (2:1) image shows a direct stroke in network segment L632-671, covering 10% of the line, and the (2:2) image reports a direct stroke in network segment L671-680.

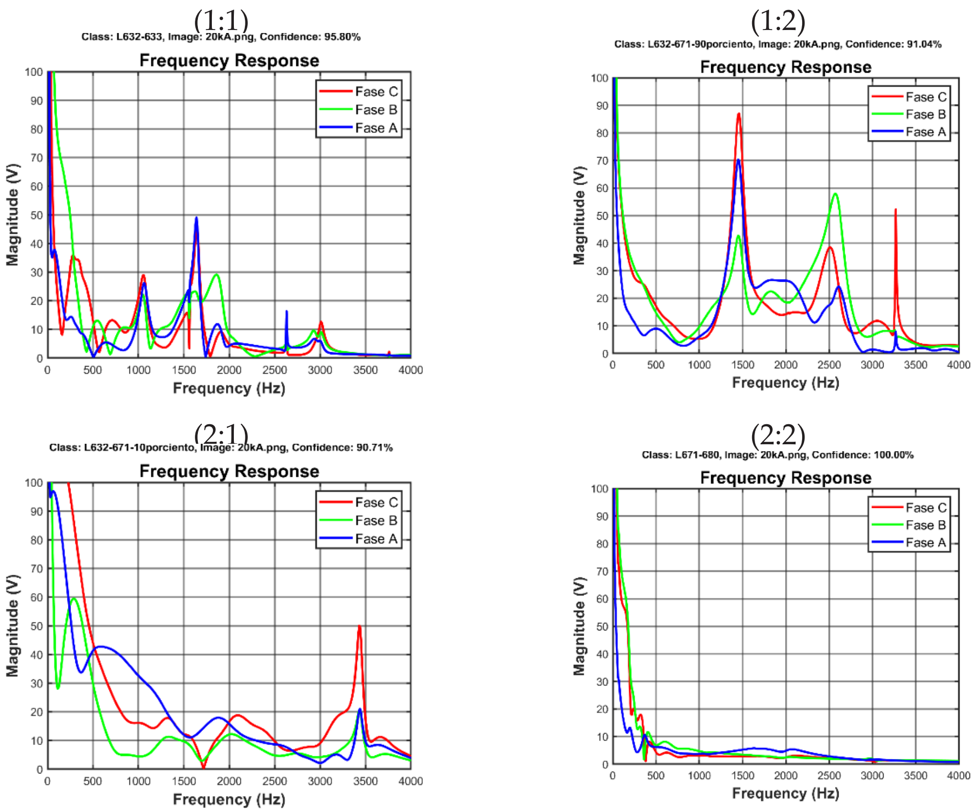

Figure 8. Image classification of the dataset

Fig. 9 presents the CDF and PDF of the confidence analysis for each of the segments containing the frequency response images. It should be highlighted that segments L671-680 and L632-671 exhibit the highest confidence during image classification, with values above 90%. Sections L632-671 (10%) and L632-633 (50%), with similar characteristic impedances for MV networks, tend to compromise confidence. However, a confidence percentage above 70% can be estimated for L632-633, L632-671 (10 and 90%), and L761-680 when classifying the frequency response.

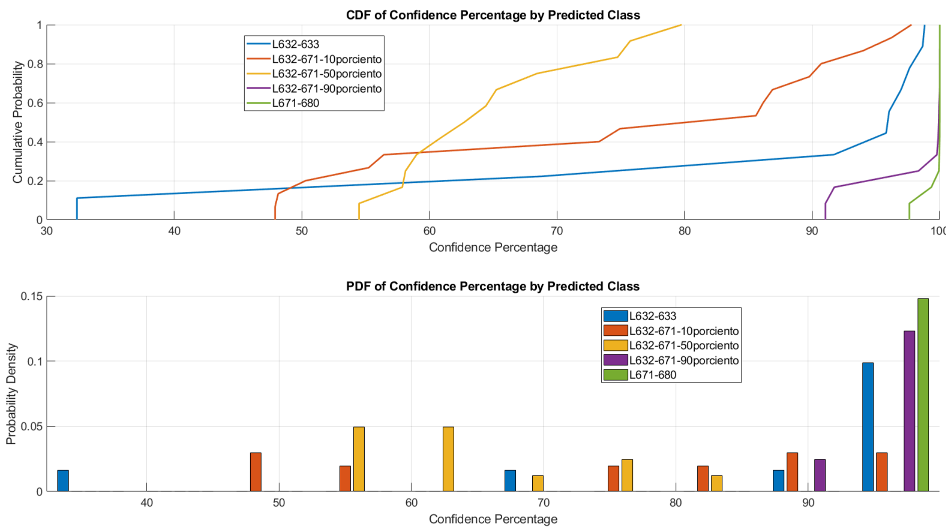

Figure 9. CDF and PDF of the confidence analysis of the segments

Proper modeling of a MV network, which includes the PI model of the network and the surge arresters, the capacitive impedances of transformers, the frequency response of the grounding system, the capacitive model of the underground cables (*e.g.*, section L692-675), and the tuning (or not) of the characteristic impedances, allows filtering multiples of the system's fundamental component. For example, the PI model of the transmission line behaves as a second-order filter for signal filtering. Therefore, at impact points far from the head of the MV circuit, where the transient overvoltage is recorded, it exhibits a better response for the classification of frequency response images.

When evaluating the confidence results for sections L632-671 and L632-633, considering the impact of a 20 kA atmospheric electrical discharge on phases A and C, note that the classification is compromised since they have very similar reflection coefficients, which is caused by changes in characteristic impedance.

Figs. 10 and 11 present the evolution of the loss and accuracy variables for each epoch for the neural network developed using with ChatGPT, which was implemented in the Google Colab Python environment. The maximum overfitting values for accuracy and loss are 0.3237 at epoch 6 and 0.3585 at epoch 35. The average overfitting values are 0.1269 and 0.1128, respectively.

From a maintenance, construction, and design engineering perspective, identifying the lightning impact point would enable a faster restoration of the power supply and positively impact service quality indicators such as the SAIDI/SAIFI [53]. Some studies have shown that the impacts of atmospheric electrical discharges on the shield wires of the transmission lines can deteriorate optical ground wires (OPGWs) (on average, 36 pairs of fiber optic cables) [54], [55], which enable communication for various substation services (*e.g.*, channel 85 for line differentials; the acceleration of tripping zones in the backup functions 21/21N in POTT schemes, which have a zone 2 comparison; and 67N, with directional comparison; among others) [56], [57]. This type of communication is structured using single-mode fiber optic, and some fibers that are not active—also known as *dark fibers*—are arranged in pair organizers in the substation [56]-[72].

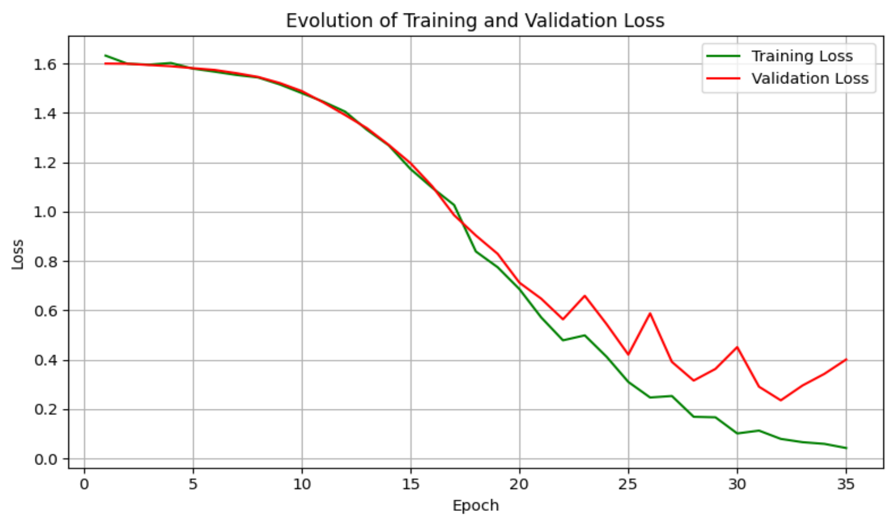

Figure 10. Evolution of the loss variable with respect to each epoch

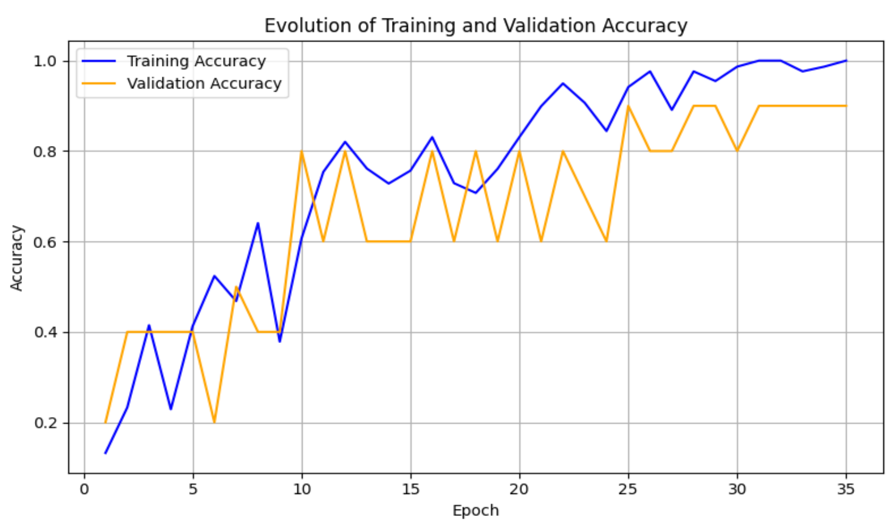

Figure 11. Evolution of the accuracy variable with respect to each epoch

Some illuminated fiber optic pairs are used for communication between the substation and the telecontrol (SCADA) center. The information transmitted through these channels is structured in frames following the IEC 60870-5-104 standard, which is supported by TCP/IP addressing. Before leaving the substation, the structured frame is formed in the gateway, which functions as a translator from the IEC

61850/DNP3 (distributed network protocol) standard to IEC 60870-5-104 [73]-[76]. Subsequently, it is routed through the substation firewall-router via multimode fiber. Finally, it is arranged in the optical distribution frame's (ODF) fiber optic pair before exiting the substation through the transmission line [67]-[70].

Failures in the illuminated fiber optic pairs require lighting dark fibers, thus reducing the availability of single-mode optical fibers. For example, in some communication architectures, it is possible to use equipment for data transmission serialization/multiplexing. This helps to reduce the physical occupation of communication channels [78]-[81]. On the other hand, the characterization of transient overvoltage resulting from direct lightning strokes allows designing adequate electrical infrastructure to favor operation and ensure safety and health conditions for network operators.

6. Mathematical contribution to electromagnetic coupling

The authors propose two physical-mathematical contributions in the frequency domain. The first one enhances the complex expression for permittivity and permeability, with applications in transverse electromagnetic (TEM) fields with arbitrary propagation, which was initially introduced in [84]. The second contribution applies complex permittivity and permeability expressions to the coupling of lightning on transmission lines.

Initially, the authors stated [84] that all media incur losses, both conductive and dielectric-polarization losses. Therefore, for linear isotropic media, constitutive relations are given by the following differential equations for the fields $\overline{E}$ and $\overline{H}$:

$$\overline{D} = \varepsilon\overline{E} + \varepsilon_1 \frac{\partial \overline{E}}{\partial t} + \varepsilon_2 \frac{\partial^2 \overline{E}}{\partial t^2} + \cdots \tag{1}$$

$$\overline{B} = \mu\overline{H} + \mu_1 \frac{\partial \overline{H}}{\partial t} + \mu_2 \frac{\partial^2 \overline{H}}{\partial t^2} + \cdots \tag{2}$$

Eqs. (1) and (2) can be expressed as presented below:

$$\overline{D} = \varepsilon\overline{E} + jw\varepsilon_1\,\overline{E} - w^2\varepsilon_2\,\overline{E} - jw^3\varepsilon_3\,\overline{E} + \cdots \tag{3}$$

$$\overline{B} = \varepsilon\overline{H} + jw\mu_1\,\overline{H} - w^2\mu_2\,\overline{H} - jw^3\mu_3\,\overline{H} + \cdots \tag{4}$$

The complex permittivity $\dot{\varepsilon}_{(w)}$ and the complex permeability $\dot{\mu}_{(w)}$ are defined as follows:

$$\dot{\varepsilon}_{(w)} = \varepsilon'(w) - j\varepsilon''(w) \tag{5}$$

$$\dot{\mu}_{(w)} = \mu'(w) - j\mu''(w) \tag{6}$$

Thus, the constitutive relations take the following complex form:

$$\overline{D} = \varepsilon^{\cdot}_{(w)}\,\overline{E} = \varepsilon'_{(w)}\,\overline{E} - j\varepsilon''_{(w)}\,\overline{E} \tag{7}$$

$$\overline{B} = \mu^{\cdot}_{(w)}\,\overline{H} = \mu'_{(w)}\,\overline{H} - j\mu''_{(w)}\,\overline{H} \tag{8}$$

Maxwell's equations in complex form are as follows:

$$\overline{\nabla} x \overline{E} = -jw\mu^{\cdot}_{(w)}\,\overline{H} = -jw\mu'_{(w)}\,\overline{H} - w\mu''_{(w)}\,\overline{H} \tag{9}$$

$$\overline{\nabla} x \overline{H} = jw\varepsilon^{\cdot}_{(w)}\,\overline{E} + \sigma\overline{E} + \overline{J} = jw\varepsilon'_{(w)}\,\overline{E} + w\varepsilon''_{(w)}\,\overline{E} + \sigma\overline{E} + \overline{J} \tag{10}$$

$$\overline{\nabla} \cdot \varepsilon^{\cdot}_{(w)}\overline{E} = \overline{\nabla} \cdot \left(\varepsilon'_{(w)} - j\varepsilon''_{(w)}\right)\overline{E} = \rho \tag{11}$$

$$\overline{\nabla} \cdot \mu^{\cdot}_{(w)}\overline{H} = \overline{\nabla} \cdot \left(\mu'_{(w)} - j\mu''_{(w)}\right)\overline{H} = 0 \tag{12}$$

For a conductive medium, σ and $w\varepsilon''_{(w)}$ are factors of the same type. Eq. 10 can be rewritten in the same way:

$$\overline{\nabla} x \overline{H} = jw\varepsilon^{\cdot}_{(w)}\,\overline{E} + \sigma\overline{E} + \overline{J} = jw\varepsilon'_{(w)}\,\overline{E} + w\varepsilon''_{(w)}\,\overline{E} + \sigma\overline{E} + \overline{J} \tag{13}$$

$$\overline{\nabla} x \overline{H} = jw\varepsilon'_{(w)}\,\overline{E} + jw\left(-j\varepsilon''_{(w)} - j\frac{\sigma}{w}\right)\overline{E} + \overline{J} \tag{14}$$

$$\overline{\nabla} x \overline{H} = jw\left(\varepsilon'_{(w)} - j\varepsilon''_{(w)} - j\frac{\sigma}{w}\right)\overline{E} + \overline{J} \tag{15}$$

where

$$\varepsilon^{\cdot}_{(w)} = \varepsilon'_{(w)} - j\left(\varepsilon''_{(w)} + \frac{\sigma}{w}\right) \tag{16}$$

The loss tangent is

$$tan\delta = \frac{w\varepsilon'' + \sigma}{w\varepsilon'} \tag{17}$$

In a lossy medium, the complex wave equations (Helmholtz equations) are

$$\overline{\nabla}^2\,\overline{E} + w^2\mu^{\cdot}_{(w)}\left[\varepsilon'_{(w)} - j\left(\varepsilon''_{(w)} + \frac{\sigma}{w}\right)\right]\overline{E} = 0 \tag{18}$$

$$\overline{\nabla}^2\,\overline{H} + w^2\mu^{\cdot}_{(w)}\left[\varepsilon'_{(w)} - j\left(\varepsilon''_{(w)} + \frac{\sigma}{w}\right)\right]\overline{H} = 0 \tag{19}$$

From this point onward, the authors will decompose the complex permeability expression in order to explicitly identify the phase and attenuation coefficients, as shown in Eqs. (20)-(23):

$$\left|\overline{k}\right| = w\sqrt{\mu^{\cdot}_{(w)}\,\varepsilon^{\cdot}_{(w)}} \tag{20}$$

$$\left|\overline{k}\right| = w\sqrt{\mu^{\cdot}_{(w)}\,\varepsilon^{\cdot}_{(w)}} = w\sqrt{\mu^{\cdot}_{(w)}\left(\varepsilon'_{(w)} - j\left(\varepsilon''_{(w)} + \frac{\sigma}{w}\right)\right)} \tag{21}$$

$$\left|\overline{k}\right| = w\sqrt{\left(\mu'_{(w)} - j\mu''_{(w)}\right)\left(\varepsilon'_{(w)} - j\left(\varepsilon''_{(w)} + \frac{\sigma}{w}\right)\right)} \tag{22}$$

$$\left|\overline{k}\right| = w\sqrt{\left(\mu'_{(w)}\varepsilon'_{(w)} - j\mu'_{(w)}\left(\varepsilon''_{(w)} + \frac{\sigma}{w}\right) - j\mu''_{(w)}\varepsilon'_{(w)} - \mu''_{(w)}\left(\varepsilon''_{(w)} + \frac{\sigma}{w}\right)\right)} \tag{23}$$

As

$$\overline{\gamma} = j\left|\overline{k}\right| = \alpha + j\beta \tag{24}$$

$$\left|\overline{k}\right| = \beta - j\alpha \tag{25}$$

Where each expression corresponds to the propagation coefficient $\overline{\gamma}$, the attenuation coefficient α , and the phase coefficient β . This is shown in Eqs. (26)-(35).

$$\left|\overline{k}\right|^2 = (\beta - j\alpha)^2 = \beta^2 - j\alpha\beta - j\alpha\beta - \alpha^2 \tag{26}$$

$$\left|\overline{k}\right|^2 = (\beta^2 - \alpha^2) - 2j\alpha\beta \tag{27}$$

$$\left|\overline{k}\right|^2 = w^2\left[\mu'_{(w)}\varepsilon'_{(w)} - \mu''_{(w)}\left(\varepsilon''_{(w)} + \frac{\sigma}{w}\right)\right] - jw^2\left[\mu'_{(w)}\left(\varepsilon''_{(w)} + \frac{\sigma}{w}\right) + \mu''_{(w)}\varepsilon'_{(w)}\right] \tag{28}$$

$$(\beta^2 - \alpha^2) = w^2\left[\mu'_{(w)}\varepsilon'_{(w)} - \mu''_{(w)}\left(\varepsilon''_{(w)} + \frac{\sigma}{w}\right)\right] \tag{29}$$

$$2\alpha\beta = w^2\left[\mu'_{(w)}\left(\varepsilon''_{(w)} + \frac{\sigma}{w}\right) + \mu''_{(w)}\,\varepsilon'_{(w)}\right] \tag{30}$$

$$\left|\left|\overline{k}\right|^2\right| = \sqrt{w^4\left[\left[\mu'_{(w)}\,\varepsilon'_{(w)} - \mu''_{(w)}\left(\varepsilon''_{(w)} + \frac{\sigma}{w}\right)\right]^2 + \left[\mu'_{(w)}\left(\varepsilon''_{(w)} + \frac{\sigma}{w}\right) + \mu''_{(w)}\,\varepsilon'_{(w)}\right]^2\right]} \tag{31}$$

$$\left|\left|\overline{k}\right|^2\right| = w^2\left[\mu'_{(w)}\,\varepsilon'_{(w)} - \mu''_{(w)}\left(\varepsilon''_{(w)} + \frac{\sigma}{w}\right)\right]\sqrt{\left[1 + \frac{\left[\mu'_{(w)}\left(\varepsilon''_{(w)}+\frac{\sigma}{w}\right)+\mu''_{(w)}\,\varepsilon'_{(w)}\right]^2}{\left[\mu'_{(w)}\,\varepsilon'_{(w)}-\mu''_{(w)}\left(\varepsilon''_{(w)}+\frac{\sigma}{w}\right)\right]^2}\right]} \tag{32}$$

$$\left|\left|\overline{k}\right|^2\right| = \sqrt{(\beta^2 - \alpha^2)^2 + (2\alpha\beta)^2} = \sqrt{\beta^4 - 2\beta^2\alpha^2 + \alpha^4 + (2\alpha\beta)^2} \tag{33}$$

$$\left|\left|\overline{k}\right|^2\right| = \sqrt{(\beta^4 + \alpha^4) + (2\alpha^2\beta^2)} = \sqrt{(\alpha^2 + \beta^2)^2} = \alpha^2 + \beta^2 \tag{34}$$

$$Re\left(\left|\overline{k}\right|^2\right) = \beta^2 - \alpha^2 = w^2\left[\mu'_{(w)}\,\varepsilon'_{(w)} - \mu''_{(w)}\left(\varepsilon''_{(w)} + \frac{\sigma}{w}\right)\right] \tag{35}$$

Therefore,

$$\left|\left|\overline{k}\right|\right| + Re\left(\left|\overline{k}\right|^2\right) = 2\beta^2 = w^2\left[\mu'_{(w)}\,\varepsilon'_{(w)} - \mu''_{(w)}\left(\varepsilon''_{(w)} + \frac{\sigma}{w}\right)\right]\cdot\left[1 + \sqrt{1 + \frac{\left[\mu'_{(w)}\left(\varepsilon''_{(w)}+\frac{\sigma}{w}\right)+\mu''_{(w)}\,\varepsilon'_{(w)}\right]^2}{\left[\mu'_{(w)}\,\varepsilon'_{(w)}-\mu''_{(w)}\left(\varepsilon''_{(w)}+\frac{\sigma}{w}\right)\right]^2}}\right] \tag{36}$$

The phase coefficient is determined by Eq. (37):

$$\boldsymbol{\beta} = \frac{w}{\sqrt{2}}\sqrt{\left[\mu'_{(w)}\,\varepsilon'_{(w)} - \mu''_{(w)}\left(\varepsilon''_{(w)} + \frac{\sigma}{w}\right)\right]} \cdot \sqrt{\left[1 + \sqrt{1 + \frac{\left[\mu'_{(w)}\left(\varepsilon''_{(w)}+\frac{\sigma}{w}\right)+\mu''_{(w)}\,\varepsilon'_{(w)}\right]^2}{\left[\mu'_{(w)}\,\varepsilon'_{(w)}-\mu''_{(w)}\left(\varepsilon''_{(w)}+\frac{\sigma}{w}\right)\right]^2}}\right]} \quad (37)$$

In addition,

$$\left|\left|\overline{\boldsymbol{k}}\right|^2\right| - \boldsymbol{Re}\left(\left|\overline{\boldsymbol{k}}\right|^2\right) = \left(\alpha^2+\beta^2\right) - \left(\beta^2-\alpha^2\right) = 2\alpha^2 \quad (38)$$

$$2\alpha^2 = \boldsymbol{w}^2\left[\mu'_{(w)}\varepsilon'_{(w)} - \mu''_{(w)}\left(\varepsilon''_{(w)}+\frac{\sigma}{\boldsymbol{w}}\right)\right] \cdot \sqrt{1+\frac{\left[\mu'_{(w)}\left(\varepsilon''_{(w)}+\frac{\sigma}{\boldsymbol{w}}\right)+\mu''_{(w)}\varepsilon'_{(w)}\right]^2}{\left[\mu'_{(w)}\varepsilon'_{(w)}-\mu'_{(w)}\left(\varepsilon''_{(w)}+\frac{\sigma}{\boldsymbol{w}}\right)\right]^2}} - \boldsymbol{w}^2\left[\mu'_{(w)}\varepsilon'_{(w)} - \mu''_{(w)}\left(\varepsilon''_{(w)}+\frac{\sigma}{\boldsymbol{w}}\right)\right] \quad (39)$$

The attenuation coefficient is determined by Eq. (40):

$$\alpha = \frac{\boldsymbol{w}}{\sqrt{2}}\sqrt{\left[\mu'_{(w)}\varepsilon'_{(w)} - \mu''_{(w)}\left(\varepsilon''_{(w)}+\frac{\sigma}{\boldsymbol{w}}\right)\right]} \cdot \sqrt{\sqrt{1+\frac{\left[\mu'_{(w)}\left(\varepsilon''_{(w)}+\frac{\sigma}{\boldsymbol{w}}\right)+\mu''_{(w)}\varepsilon'_{(w)}\right]^2}{\left[\mu'_{(w)}\varepsilon'_{(w)}-\mu'_{(w)}\left(\varepsilon''_{(w)}+\frac{\sigma}{\boldsymbol{w}}\right)\right]^2}} - 1} \quad (40)$$

In a lossy medium, the wave impedance also becomes complex, as shown in Eq. (41).

$$\dot{\eta} = \sqrt{\frac{\mu'_{(w)} - \boldsymbol{j}\mu''_{(w)}}{\varepsilon'_{(w)} - \boldsymbol{j}\left(\varepsilon'' + \frac{\sigma}{\boldsymbol{w}}\right)}} \quad (41)$$

The authors propose implementing complex-valued expressions for permittivity and permeability within the lightning-coupling model (Fig. 12).

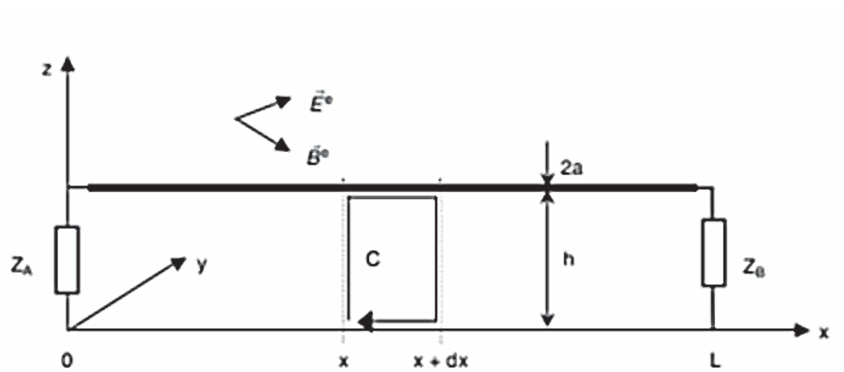

Figure 12. Lightning-coupling model [85]

As presented in the previous sections in both integral and differential forms, as shown in Eqs. (42) and (43).

$$\overline{\nabla} x \overline{E} = -jw\mu^{\cdot}_{(w)}\overline{H} = -jw\mu^{'}_{(w)}\overline{H} - jw\mu^{''}_{(w)}\overline{H} = -jw\overline{B} \tag{42}$$

$$\oint \overline{E} \cdot dl = -\int jw\mu^{\cdot}_{(w)\overline{H}} \cdot d\overline{s} = -\int jw\overline{B} \cdot d\overline{s} \tag{43}$$

The above is determined for contour CCC (differential form with Ax):

$$\int_0^h \overline{E}_{(x,z)} \cdot d\overline{z} - \int_0^h \overline{E}_{(x+\Delta x,z)} \cdot d\overline{z} + \int_x^{x+\Delta x} \overline{E}_{(x,h)} \cdot d\overline{x} - \int_x^{x+\Delta x} \overline{E}_{(x,0)} \cdot d\overline{x} = -jw\int_0^h \int_x^{x+\Delta x} \overline{B}_{(x,z)} \cdot dxdz\overline{ay} \tag{44}$$

$$\int_0^h \overline{E}_{(x,z)} \cdot d\overline{z} - \int_0^h \overline{E}_{(x+\Delta x,z)} \cdot d\overline{z} + \int_x^{x+\Delta x} \overline{E}_{(x,h)} \cdot d\overline{x} - \int_x^{x+\Delta x} \overline{E}_{(x,0)} \cdot d\overline{x} = -jw\int_0^h \int_x^{x+\Delta x} \overline{B}_{(x,z)} \cdot dxdz\overline{ay} \tag{45}$$

$$-\int_0^h \left[\left|\overline{E}_{z(x+\Delta x,z)}\right| - \left|\overline{E}_{z(x,z)}\right|\right] dz + \int_x^{x+\Delta x} \left[\left|\overline{E}_{x(x,h)}\right| - \left|\overline{E}_{x(x,0)}\right|\right] dx = -jw\int_0^h \int_x^{x+\Delta x} \left|\overline{B}_{y(x,z)}\right| dxdz \tag{46}$$

Taking the partial derivative with respect to x on both sides of the equation yields the following expression:

$$-\frac{\partial}{\partial x}\int_0^h \left[\left|\overline{E}_{z(x+\Delta x,z)}\right| - \left|\overline{E}_{z(x,z)}\right|\right] dz = -jw\int_0^h \left|\overline{B}_{y(x,z)}\right| dz \tag{47}$$

On the other hand, from Faraday's law (quasi-static fields), it is possible to obtain Eq. (48):

$$V(x) = -\int \overline{E} \cdot d\overline{l} = -\int_0^h \left[\left|\overline{E}_{z(x+\Delta x,z)}\right| - \left|\overline{E}_{z(x,z)}\right|\right] dz \tag{48}$$

And then Eqs. (49) and (50):

$$\frac{\partial}{\partial x}\left[V(x)\right] = -jw\int_0^h \left|\overline{B}_{y(x,z)}\right| dz \tag{49}$$

$$\frac{\partial}{\partial x}\left[V(x)\right] = -jw\int_0^h \left|\overline{B}^{e}_{y(x,z)}\right| dz - jw\int_0^h \left|\overline{B}^{s}_{y(x,z)}\right| dz \tag{50}$$

From earlier derivations in both integral and differential form, it is possible to express the following:

$$\overline{\nabla} x \overline{Hs} = \overline{Js} + jw\varepsilon^{\cdot}_{(w)}\overline{E} = jw\left(\varepsilon^{'}_{(w)} - j\varepsilon^{''}_{(w)} - j\frac{\sigma}{w}\right)\overline{E} + \overline{J} \tag{51}$$

$$\overline{\nabla} x \overline{Hs} = jw\overline{D} + \overline{J} \tag{52}$$

$$\int \overline{Hs}\cdot d\overline{l} = \int \overline{J}\cdot d\overline{s} + jw\int \overline{Ds}\cdot d\overline{s} \tag{53}$$

The inductance of the conductor can be determined using the following procedure:

$$\int \overline{H}\cdot d\overline{l} = \int \overline{J}\cdot d\overline{s} = Ience \tag{54}$$

$$\left|\overline{B_{\varphi}}\right| = \dot{\mu}_{(w)} \frac{Ience}{2\pi\rho} \tag{55}$$

$$\int \overline{B}\cdot d\overline{s} = L'\cdot Ience\int dz \tag{56}$$

The inductance per unit length can be expressed as presented below.

$$\int \left|\overline{B}\right| d\rho = L'\cdot Inece \tag{57}$$

Now, assuming the following expression:

$$\int\int \overline{B}\cdot d\overline{s} = \int\int \frac{\dot{\mu}_{(w)}}{2\pi\rho} Ience\cdot d\rho dz \tag{58}$$

If this is multiplied by $j\omega$, and we assume that ω does not vary with respect to ρ and z, Eq. (59) is obtained.

$$jw\int\int \overline{B}\cdot d\overline{s} = jw\int \frac{\dot{\mu}_{(w)} Ience\cdot d\rho}{2\pi\rho}\int dz \tag{59}$$

The scattered field can be expressed as follows:

$$\int jw\int \left|\overline{B}\right| d\rho dz = \frac{jw\dot{\mu}_{(w)}}{2\pi\rho} Ience \ln\frac{d2}{d1}\int dz = jwL\cdot Ience\int dz \tag{60}$$

Returning to Eqs. (49) and (50), this research implements the subscript s for the scattered field and the subscript e for the excitation field, in order to obtain the telegrapher's equation:

$$\int_{x}^{x+x\Delta} \frac{\partial}{\partial x}\left[V(x)\right] dx = -jw\int_{0}^{h}\int_{x}^{x+\Delta x} \left|\overline{B}_{y(x,z)}\right| dxdz \tag{61}$$

$$\int_{x}^{x+x\Delta} \frac{\partial}{\partial x}\left[V\left(x\right)\right]dx = -\int_{x}^{x+\Delta x} jw\int_{0}^{h}\left|\overline{B}_{y(x,z)}^{s}\right|dzdx - \int_{x}^{x+\Delta x} jw\int_{0}^{h}\left|\overline{B}_{y(x,z)}^{e}\right|dzdx \tag{62}$$

$$\int_{x}^{x+x\Delta} \frac{\partial}{\partial x}\left[V\left(x\right)\right]dx = -\int_{x}^{x+\Delta x} jwL'I_{(x)}dx - \int_{x}^{x+\Delta x} jw\int_{0}^{h}\left|\overline{B}_{y(x,z)}^{e}\right|dzdx \tag{63}$$

$$\frac{\partial}{\partial x}\left[V\left(x\right)\right] + jwL'I_{(x)} = -jw\int_{0}^{h}\left|\overline{B}_{y(x,z)}^{e}\right|dz \tag{64}$$

On the other hand, Maxwell's equations can be expressed in pointwise (differential) form:

$$\overline{\nabla} x\overline{H} = \overline{J} + jw\varepsilon_{(w)}^{\cdot}\overline{E} \tag{65}$$

$$\overline{\nabla} x\overline{H} = \overline{J} + jw\overline{D} \tag{66}$$

$$\overline{\nabla} x\overline{H} = \left(\frac{\partial\left|\overline{H}_{z}\right|}{\partial y} - \frac{\partial\left|\overline{H}_{y}\right|}{\partial z}\right)\overline{ax} - \left(\frac{\partial\left|\overline{H}_{z}\right|}{\partial x} - \frac{\partial\left|\overline{H}_{x}\right|}{\partial z}\right)\overline{ay} + \left(\frac{\partial\left|\overline{H}_{y}\right|}{\partial x} - \frac{\partial\left|\overline{H}_{x}\right|}{\partial y}\right)\overline{az} \tag{67}$$

For the z -component,

$$\left(\frac{\partial\left|\overline{H}_{y}\right|}{\partial x} - \frac{\partial\left|\overline{H}_{x}\right|}{\partial y}\right)\overline{az} = \overline{J} + jw\varepsilon_{(w)}^{\cdot}\overline{E}_{(x,z)} \tag{68}$$

Since the medium is insulating, it follows that $\sigma_{isolation} = 0$. Therefore,

$$jw\overline{E}_{(x,z)} = \left(\frac{d\left|\overline{H}_{y}\right|}{dx} - \frac{d\left|\overline{H}_{x}\right|}{dy}\right)\cdot\frac{1}{\varepsilon_{(w)}^{\cdot}} \tag{69}$$

By integrating along the z -axis from 0 to h, we obtain the following for the scattered field and the excitation:

$$jw\int_{0}^{h}\left|\overline{E}_{(x,z)}\right|dz = -jwV\left(x\right) \tag{70}$$

$$jw\int_{0}^{h}\left|\overline{E}_{(x,z)}\right|dz = \frac{1}{\varepsilon_{(w)}^{\cdot}\,\mu_{(w)}^{\cdot}}\int_{0}^{h}\left[\frac{\partial\overline{B}_{y(x,z)}^{e}}{\partial x} - \frac{\partial\overline{B}_{x(x,z)}^{e}}{\partial y}\right]dz + \frac{1}{\varepsilon_{(w)}^{\cdot}\,\mu_{(w)}^{\cdot}}\int_{0}^{h}\left[\frac{\partial\overline{B}_{y(x,z)}^{s}}{\partial x} - \frac{\partial\overline{B}_{x(x,z)}^{s}}{\partial y}\right]dz \tag{71}$$

The excitation field and the scattered field are defined as follows:

$$jw\int_0^h \left|\bar{E}^e_{(x,z)}\right| dz = \frac{1}{\varepsilon^{\cdot}_{(w)}\,\mu^{\cdot}_{(w)}} \int_0^h \left[\frac{\partial \bar{B}^e_{y(x,z)}}{\partial x} - \frac{\partial \bar{B}^e_{x(x,z)}}{\partial y} \right] dz \tag{72}$$

$$jw\int_0^h \left|\bar{E}^s_{(x,z)}\right| dz = \frac{1}{\varepsilon^{\cdot}_{(w)}\,\mu^{\cdot}_{(w)}} \int_0^h \left[\frac{\partial \bar{B}^s_{y(x,z)}}{\partial x} - \frac{\partial \bar{B}^s_{x(x,z)}}{\partial y} \right] dz \tag{73}$$

From the derivation for quasi-static fields, it is possible to obtain the following:

$$Q = \int \left|\bar{D}\right| \cdot d\bar{s} = \int \rho_v dv \tag{74}$$

$$\left|\bar{E}\right| = \frac{Q}{2\pi\rho\varepsilon^{\cdot}_{(w)} l} \tag{75}$$

$$C = \frac{Q}{V_{ab}} = \frac{\pi\varepsilon^{\cdot}_{(w)} l}{\ln \frac{d}{r}} \tag{76}$$

Therefore,

$$V = -\int \bar{E} \cdot d\bar{l} = \frac{Q}{C} \tag{77}$$

$$C'V_{ab} = -C'\int \bar{E} \cdot d\bar{l} \tag{78}$$

$$jwC'V_{ab} = -jwC'\int \bar{E} \cdot d\bar{l} \tag{79}$$

Thus,

$$-jwV(x) = jw\int_0^h \left|\bar{E}^e_{(x,z)}\right| dz + jw\int_0^h \left|\bar{E}^s_{(x,z)}\right| dz \tag{80}$$

$$-jwC'V(x) = jwC'\int_0^h \left|\bar{E}^e_{(x,z)}\right| dz + jwC'\int_0^h \left|\bar{E}^s_{(x,z)}\right| dz \tag{81}$$

$$-jwC'\int_0^h \left|\bar{E}^e_{(x,z)}\right| dz = jwC'V(x) + \frac{C'}{\varepsilon^{\cdot}_{(w)}\mu^{\cdot}_{(w)}} \int_0^h \left[\frac{\partial \bar{B}^s_{y(x,z)}}{\partial x} \right] dz \tag{82}$$

$\bar{B}^{s}_{x(x,z)} = 0$ since a TEM wave is present. Therefore,

$$-jwC'\int_0^h \left|\bar{E}^{e}_{(x,z)}\right| dz = jwC'V(x) + \frac{C'}{\varepsilon^{\bullet}_{(w)}\mu^{\bullet}_{(w)}} \frac{\partial[L' \cdot I]}{\partial x} \tag{83}$$

This can be expressed as follows, given that $L'C' = \varepsilon^{\bullet}_{(w)}\mu^{\bullet}_{(w)}$:

$$-jwC'\int_0^h \left|\bar{E}^{e}_{(x,z)}\right| dz = jwC'V(x) + \frac{\partial[I]}{\partial x} \tag{84}$$

low is the definition of the circuit with complex-field coupling. The original expression for electric and magnetic coupling can still be employed. However, it should be noted that permittivity and permeability are expressed in the complex domain and are frequency-dependent. Under the present notation, it is important to emphasize that the field e is equal to the field i in Fig. 13.

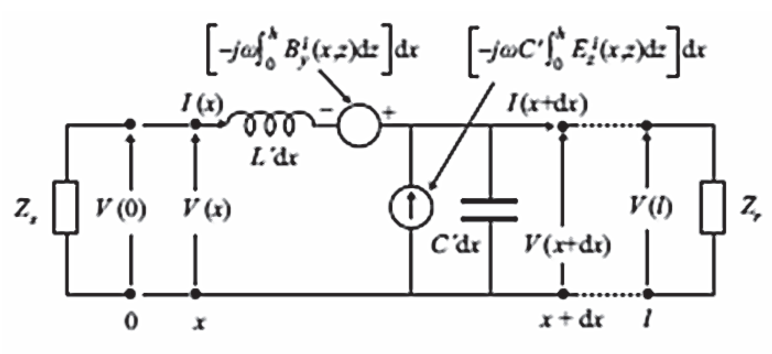

Figure 13. Equivalent circuit of TEM coupling [23]

7. Conclusions

Our implementation of neural networks based on GoogLeNet, Python, and ChatGPT for the classification of transient overvoltage resulting from direct lightning strokes in the frequency domain for branched radial networks showed an acceptable response, with accuracy values of 80 and 89.99%. The average overfitting of the network developed in collaboration with ChatGPT was 0.1269 for accuracy and 0.1128 for losses.

Furthermore, our review of 12 records of transient overvoltage due to lightning strokes on the L671-680 section shows close to 100% confidence in image classification using a pre-trained instance of GoogLeNet. The classification for the L632-633 section, under a direct lightning strike of 20 kA on phase A, reported a confidence of 32.38%, which was the worst result obtained.

The 60 frequency response images analyzed exhibited a confidence level above 70% for branches L632-633, L632-671 (10 and 90%), and L671-680.

The new mathematical formulation for the coupling of electromagnetic fields in polarized media improves upon the version proposed by Taylor (1965) [23], [85]. The authors considered the permeability and permittivity coefficients as complex quantities in order for the new coupling model to be applied to materials such as dielectrics (dry air, gas-insulated switchgear, arc chambers), ferroelectrics, and magnetic media (ferrites, cores, shielding), among others.

8. Author contributions

Luis Eduardo Perdomo Orjuela: conceptualization, data curation, formal analysis, investigation, validation, visualization, writing
Francisco Santamaria Piedrahita: conceptualization, data curation, formal analysis, investigation, supervision, validation, writing
Nelson Enrique Vera Parra: conceptualization, data curation, formal analysis, investigation, supervision, validation, writing

9. Acknowledgements

The authors would like to thank the members of the GISE3 and EMC-UN groups, attached to Universidad Distrital Francisco José de Caldas and Universidad Nacional de Colombia, respectively, for the support provided during this research.

10. Conflict of interest

The authors declare that they have no known competing financial interests or personal relationships that could appear to have influenced the study reported in this paper.

11. Use of artificial intelligence

During this work, the authors did not employ any technologies associated with artificial intelligence.

References

[1] V. Cooray, *The Lightning Flash*. London, U.K.: Institution of Engineering and Technology, 2014. https://doi.org/10.1049/PBPO069E

[2] V. Cooray, *An Introduction to Lightning*. New York, NY, USA: Springer, 2016. https://doi.org/10.1007/978-94-017-8938-7

[3] V. Cooray, *Lightning Protection*. London, U.K.: Institution of Engineering and Technology, 2010. https://doi.org/10.1049/PBPO058E

[4] A. R. Hileman, *Insulation Coordination for Power Systems*. Boca Raton, FL, USA: CRC Press, 1999.

[5] E. Kuffel, W. S. Zaengl, and J. Kuffel, *High Voltage Engineering: Fundamentals*, 2nd ed. Oxford, U.K.: Newnes, 2000.

[6] J. Martínez, *Coordinación de aislamiento en redes eléctricas de alta tensión*. Madrid, Spain: McGraw-Hill, 2007.

[7] IEC 60071-1, Insulation Co-ordination—Part 1: Definitions, Principles and Rules. Geneva, Switzerland: International Electrotechnical Commission, 2019.

[8] IEC 60071-2, Insulation Co-ordination—Part 2: Application Guidelines. Geneva, Switzerland: International Electrotechnical Commission, 2018.

[9] IEC TR 60071-4, Insulation Co-ordination—Part 4: Computational Guide to Insulation Co-ordination and Modelling of Electrical Networks. Geneva, Switzerland: International Electrotechnical Commission, 2004.

[10] IEC 60071-5, Insulation Co-ordination—Part 5: Procedures for High-Voltage Direct Current (HVDC) Converter Stations. Geneva, Switzerland: International Electrotechnical Commission, 2014.

[11] M. S. Naidu and V. Kamaraju, *High Voltage Engineering*. New York, NY, USA: McGraw-Hill, 1995.

[12] C. L. Wadhwa, *High Voltage Engineering*. New Delhi, India: New Age International (P) Ltd., 2007.

[13] Q. Wen *et al*., "Lightning overvoltage identification in distribution line based on relevance vector machine," in *Proc. China Int. Conf. Electr. Distrib. (CICED)*, 2018, pp. 1206–1210. https://doi.org/10.1109/CICED.2018.8592419

[14] D. Lin, D. Bin, S. Wenxia, C. Weigen, and L. Jing, "Identifying the overvoltage in distribution networks based on support vector machine," in *Proc. Int. Conf. High Volt. Eng. Appl. (ICHVE)*, 2008, pp. 677–680. https://doi.org/10.1109/ICHVE.2008.4774025

[15] A. L. Antunes De Sa and R. A. Marshall, "Lightning Distance Estimation Using LF Lightning Radio Signals via Analytical and Machine-Learned Models," *IEEE Trans. Geosci. Remote Sens.*, vol. 58, no. 8, pp. 5892–5907, 2020. https://doi.org/10.1109/TGRS.2020.2972153

[16] H. Karami, A. Mostajabi, M. Azadifar, M. Rubinstein, C. Zhuang, and F. Rachidi, "Machine Learning-Based Lightning Localization Algorithm Using Lightning-Induced Voltages on Transmission Lines," *IEEE Trans. Electromagn. Compat.*, vol. 62, no. 6, pp. 2512–2519, 2020. https://doi.org/10.1109/TEMC.2020.2978429

[17] J. A. Martinez-Velasco, *Power System Transients: Parameter Determination*. Boca Raton, FL, USA: CRC Press/Taylor & Francis Group, 2010.

[18] L. Perdomo, A. Alfonso, F. Santamaria, and F. Roman, "Sensitivity Study of Induced Transient Overvoltages on Distribution Networks," in *Proc. 20th Int. Symp. High Voltage Eng. (ISH 2017)*, Buenos Aires, Argentina, 2017, pp. 1–6. [Online]. Available: https://www.e-cigre.org/publications/detail/ish2017-482-sensitivity-study-of-induced-transient-overvoltages-on-distribution-networks.html.

[19] V. Cooray, F. Rachidi, and M. Rubinstein, *Lightning Electromagnetics, vol. 1: Return Stroke Modelling and Electromagnetic Radiation*. London, U.K.: Institution of Engineering and Technology, 2022. https://doi.org/10.1049/PBPO127F

[20] V. Cooray, F. Rachidi, and M. Rubinstein, *Lightning Electromagnetics, vol. 2: Electrical Processes and Effects*. London, U.K.: Institution of Engineering and Technology, 2022. https://doi.org/10.1049/PBPO127G

[21] A. Piantini, *Lightning Interaction with Power Systems, vol. 1: Fundamentals and Modelling*. London, U.K.: Institution of Engineering and Technology, 2020. https://doi.org/10.1049/PBPO172F

[22] A. Piantini, *Lightning Interaction with Power Systems, vol. 2: Applications*. London, U.K.: Institution of Engineering and Technology, 2020. https://doi.org/10.1049/PBPO172G

[23] Y. Baba and V. A. Rakov, *Lightning-Induced Effects in Electrical and Telecommunications Systems*. London, U.K.: Institution of Engineering and Technology, 2020. https://doi.org/10.1049/PBPO114E

[24] P. Chowdhuri, *Electromagnetic Transients in Power Systems*. Taunton, U.K.: John Wiley & Sons, Inc., 1996.

[25] L. E. Perdomo Orjuela, F. Santamaría, and F. Román, "Transient overvoltage in distribution networks in rural areas," in *Proc. 33rd Int. Conf. Lightning Protection (ICLP)*, Estoril, Portugal, 2016, pp. 1–6. https://doi.org/10.1109/ICLP.2016.7791433

[26] L. E. Perdomo Orjuela, F. Santamaría Piedrahita, and F. Román Campos, *Prototipo para el registro de sobretensiones transitorias estándar de 1.2/50 μs*, Master's thesis, Maestría en Ingeniería Eléctrica, Universidad Nacional de Colombia, Bogotá, Colombia, 2019. [Online]. Available: https://repositorio.unal.edu.co/handle/unal/69632

[27] L. Perdomo, A. Alfonso, and F. Santamaría, *Prototipo para el registro de sobretensiones transitorias en redes de tensión menor a 1 kV*. Bogotá, Colombia: Universidad Distrital Francisco José de Caldas, 2014.

[28] A. Alfonso, L. Perdomo, F. Santamaría, F. Amórtegui, and F. Román, "Integrity analysis of the signal transmitted to a 4G LTE module," in *Proc. Eur. Conf. Circuit Theory Design (ECCTD)*, Catania, Italy, 2017, pp. 1–4. https://doi.org/10.1109/ECCTD.2017.8093345

[29] L. Perdomo, A. Alfonso, F. Santamaría, and F. Román, "Development and Characterization of a Transient Overvoltage Recorder in Distribution Networks," in *Proc. 21st Int. Symp. High Voltage Eng. (ISH 2019)*. Cham, Switzerland: Springer, 2020, pp. 157–170. https://doi.org/10.1007/978-3-030-31676-1_16

[30] A. Alfonso, L. Perdomo, F. Santamaría, and C. Gómez, "Transient surges analysis in low voltage networks," *Tecnura*, vol. 18, no. Spec. Issue Doctorate, pp. 41–50, 2014. https://doi.org/10.14483/22487638.9241

[31] L. Li, R. Che, and H. Zang, "A fault cause identification methodology for transmission lines based on support vector machines," in *Proc. IEEE PES Asia-Pacific Power Energy Eng. Conf. (APPEEC)*, Xi'an, China, 2016, pp. 1430–1434. https://doi.org/10.1109/APPEEC.2016.7779725

[32] N. Harnzah, F. H. Anuwar, Z. Zakaria, and N. M. Tahir, "Classification of transient in power system using support vector machine," in *Proc. 5th Int. Colloq. Signal Process. Appl. (CSPA)*, Kuala Lumpur, Malaysia, 2009, pp. 418–422. https://doi.org/10.1109/CSPA.2009.5069263

[33] A. Adekitan and M. Rock, "Application of Machine Learning to Lightning Strike Probability Estimation," in *Proc. Int. Conf. Electr., Telecommun. Comput. Eng. (ICELTICs)*, Beirut, Lebanon, 2020, pp. 1–9. https://doi.org/10.1109/ICELTICs50595.2020.9315398

[34] R. Tervo, J. Karjalainen, and A. Jung, "Short-Term Prediction of Electricity Outages Caused by Convective Storms," *IEEE Trans. Geosci. Remote Sens.*, vol. 57, no. 11, pp. 8618–8626, 2019. https://doi.org/10.1109/TGRS.2019.2921809

[35] R. Tervo, J. Karjalainen, and A. Jung, "Predicting Electricity Outages Caused by Convective Storms," in *Proc. IEEE Data Sci. Workshop (DSW)*, Lausanne, Switzerland, 2018, pp. 145–149. https://doi.org/10.1109/DSW.2018.8439906

[36] H. Torres Sánchez, *Protección contra rayos*. Bogotá, Colombia: Universidad Nacional de Colombia and ICONTEC, 2010.

[37] A. Küchler, *High Voltage Engineering: Fundamentals, Technology and Applications*. Berlin, Germany: Springer Vieweg, 2018. https://doi.org/10.1007/978-3-642-11993-4_7

[38] J. C. Das, *Transients in Electrical Systems: Analysis, Recognition, and Mitigation*. New York, NY, USA: McGraw-Hill, 2010.

[39] W. Hauschild and W. Mosch, *Statistical Techniques for High-Voltage Engineering*. London, U.K.: Institution of Engineering and Technology, 1992. https://doi.org/10.1049/PBPO013E

[40] R. E. Jaimes and Q. Su, *Condition Assessment of HV Insulation in Power System Equipment*. London, U.K.: Institution of Engineering and Technology, 2008. https://doi.org/10.1049/PBPO053E

[41] H. M. Ryan, *High-Voltage Engineering and Testing*. London, U.K.: Institution of Engineering and Technology, 2013. https://doi.org/10.1049/PBPO066E

[42] M. Brignone *et al*., "Lightning-Induced Voltages on Overhead Distribution Lines Computed through Analytical Expressions for the Electromagnetic Fields," in *Proc. 35th Int. Conf. Lightning Protection (ICLP) and XVI Int. Symp. Lightning Protection (SIPDA)*, Colombo, Sri Lanka, 2021, pp. 1–6. https://doi.org/10.1109/ICLPandSIPDA54065.2021.9627387

[43] J. Guo, M. Rubinstein, V. Cooray, and F. Rachidi, "Lightning-Induced Voltage on an Overhead Transmission Line Terminated with Non-Vertical Risers," in *Proc. 35th Int. Conf. Lightning Protection (ICLP) and XVI Int. Symp. Lightning Protection (SIPDA)*, Colombo, Sri Lanka, 2021. https://doi.org/10.1109/ICLPandSIPDA54065.2021.9627332

[44] A. Haddad and D. Warne, *Advances in High Voltage Engineering*, 2nd ed. London, U.K.: Institution of Engineering and Technology, 2004. https://doi.org/10.1049/PBPO040E

[45] K. Arreaza, "Curso de Especialización Coordinación de Aislamiento," *Inel Engineering Education*. [Online]. Available: https://inelinc.com/curso/coordinacion-de-aislamiento-uwfam

[46] H. Rojas, L. Morales, and A. Santa, *Sistemas de medición indirecta de rayos*. Bogotá, Colombia: Universidad Distrital Francisco José de Caldas, 2026. https://doi.org/10.69740/UD.9789587879186.9789587879209

[47] L. Perdomo, A. Alfonso, B. Anillo, F. Santamaria, and N. Vera, "Classification of Direct Lightning Stroke According to Its Polarity in Medium Voltage Networks Based on Deep Learning Neural Networks," in *Proc. 37th Int. Conf. Lightning Protection (ICLP)*, Dresden, Germany, 2024, pp. 932–937. [Online]. Available: https://ieeexplore.ieee.org/document/10832625

[48] K. Arreaza and J. Videla, "Curso de Especialización Cálculos Avanzados en Líneas de Transmisión," *Inel Engineering Education*. [Online]. Available: https://inelinc.com/curso/calculos-avanzados-en-lineas-de-transmision-btwlx

[49] IEEE Power and Energy Society Substations Committee, *IEEE Guide for Direct Lightning Stroke Shielding of Substations*. New York, NY, USA: Institute of Electrical and Electronics Engineers, 2012. [Online]. Available: https://standards.ieee.org/ieee/998/1376/

[50] IEEE Power and Energy Society Transmission and Distribution Committee, *IEEE Guide for Improving the Lightning Performance of Transmission Lines*. New York, NY, USA: Institute of Electrical and Electronics Engineers, 1997. [Online]. Available: https://standards.ieee.org/ieee/1243/1891/

[51] IEEE Power and Energy Society Transmission and Distribution Committee, *IEEE Guide for Improving the Lightning Performance of Electric Power Overhead Distribution Lines*. New York, NY, USA: Institute of Electrical and Electronics Engineers, 2011. [Online]. https://standards.ieee.org/ieee/1410/4720/

[52] S. Hernández, "Inteligencia Artificial y Deep Learning desde Cero en Python," *Udemy*. [Online]. https://www.udemy.com/course/deep-learning-desde-cero-en-python

[53] IEEE Power and Energy Society Transmission and Distribution Committee, *IEEE Guide for Electric Power Distribution Reliability Indices (IEEE Std 1366-2012)*. New York, NY, USA: Institute of Electrical and Electronics Engineers, 2012. [Online]. https://standards.ieee.org/ieee/1366/4602/

[54] E. Gonzalez, F. Jurado, G. Jose, and M. Julio, "Extreme testing of guard cables with fiber optics: A case study," *Ingeniería*, vol. 29, no. 3, p. 21, 2024. https://doi.org/10.14483/23448393.21483

[55] A. Mishra, "Signal Integrity Basics to Advanced & Simulations – EsteemPCB," *Udemy*. [Online]. https://www.udemy.com/course/signal-integrity-basics-to-advanced-simulations-esteempcb

[56] P. Jiménez, "Programa de Especialización Parametrización, Configuración y Operación de Relés ABB," *Inel Engineering Education*. [Online]. https://inelinc.com/curso/programa-especializacion-parametrizacion-configuracion-operacion-reles-abb-hitachi-u6i6y

[57] P. Jiménez, "Programa de Especialización Parametrización, Configuración y Operación de Relés General Electric," *Inel Engineering Education*. [Online]. https://inelinc.com/curso/programa-de-especializacion-parametrizacion-configuracion-y-operacion-de-reles-general-electric-6ylkr

[58] A. T. Johns and S. K. Salman, *Digital Protection for Power Systems*. London, U.K.: Institution of Electrical Engineers, 2022.

[59] *Criterios Generales de Protección de los Sistemas Eléctricos Insulares y Extrapeninsulares*. Madrid, Spain: ENDESA–Red Eléctrica de España (REE), 2005.

[60] Comité de Operación Económica del Sistema Interconectado Nacional (COES), *Criterios de Ajuste y Coordinación de los Sistemas de Protección del SEIN*. Lima, Perú: COES-SINAC, 2022.

[61] A. G. Phadke and J. S. Thorp, *Computer Relaying for Power Systems*. Chichester, U.K.: John Wiley & Sons, 2009. https://doi.org/10.1002/9780470749722

[62] IEEE Power System Relaying and Control Committee, *IEEE Standard Inverse-Time Characteristic Equations for Overcurrent Relays (IEEE Std C37.112-2018)*. New York, NY, USA: Institute of Electrical and Electronics Engineers, 2019. [Online]. https://standards.ieee.org/ieee/C37.112/7036/

[63] A. R. van C. Warrington, *Protective Relays: Their Theory and Practice*. Norwich, U.K.: Chapman & Hall Ltd., 1968.

[64] J. M. Gers and E. J. Holmes, *Protection of Electricity Distribution Networks*. London, U.K.: Institution of Engineering and Technology, 2022. https://doi.org/10.1049/PBPO180E

[65] R. Mason, *The Art and Science of Protective Relaying*. General Electric.

[66] S. H. Horowitz, A. G. Phadke, and J. K. Niemira, *Power System Relaying*. Chichester, U.K.: John Wiley & Sons, 2013.

[67] H. L. Willis and M. H. Rashid, *Protective Relaying: Principles and Applications*. Boca Raton, FL, USA: CRC Press/Taylor & Francis Group, 2006.

[68] W. A. Elmore, *Protective Relaying: Theory and Applications*. New York, NY, USA: Marcel Dekker, Inc., 2004.

[69] Q. Wu, Z. Lu, and T. Ji, *Protective Relaying of Power Systems Using Mathematical Morphology*. London, U.K.: Springer, 2009.

[70] P. M. Anderson and P. Rush, *Network Protection and Automation Guide*. Barcelona, Spain: AREVA T&D Automation & Information Systems, 2005.

[71] P. M. Anderson, *Power System Protection*. New York, NY, USA: Institute of Electrical and Electronics Engineers, 1999.

[72] IEEE Industry Applications Society Industrial and Commercial Power Systems Department Committee, *IEEE Recommended Practice for Protection and Coordination of Industrial and Commercial Power Systems*. New York, NY, USA: Institute of Electrical and Electronics Engineers, 2001. [Online]. https://standards.ieee.org/ieee/242/426

[73] J. D. McDonald, *Electric Power Substations Engineering*. Boca Raton, FL, USA: CRC Press, 2012.

[74] A. M. Sleva, *Protective Relay Principles*. Boca Raton, FL, USA: CRC Press, 2009.

[75] K. Arreaza, "Curso de Especialización Automatización de Subestaciones IEC 61850," *Inel Engineering Education*. [Online]. https://inelinc.com/curso/automatizacion-de-subestaciones-iec-61850-l9kaf

[76] P. B. Nair and Nirmal-Kumar C., *IEC 61850: Principles and Applications to Electric Power Systems*. 2023.

[77] Y. Yuan and Y. Yang, *IEC 61850-Based Smart Substations: Principles, Testing, Operation and Maintenance*. Beijing, China: China Electric Power Press, 2019.

[78] A. Apostolov, *IEC 61850: Digitizing the Electric Power Grid*. Norwood, MA, USA: Artech House, 2023.

[79] M. S. Thomas and J. D. McDonald, *Power System SCADA and Smart Grids*. Boca Raton, FL, USA: CRC Press, 2015.

[80] J. Luo, Y. Hao, Q. Ye, Y. Hao, and L. Li, "Development of Optical Fiber Sensors Based on Brillouin Scattering and FBG for On-Line Monitoring in Overhead Transmission Lines," *J. Lightwave Technol.*, vol. 31, no. 10, pp. 1559–1565, 2013. https://doi.org/10.1109/JLT.2013.2252882

[81] G. Ma, C. Li, J. Quan, J. Jiang, and Y. Cheng, "A Fiber Bragg Grating Tension and Tilt Sensor Applied to Icing Monitoring on Overhead Transmission Lines," *IEEE Trans. Power Deliv.*, vol. 26, no. 4, pp. 2163–2170, 2011. https://doi.org/10.1109/TPWRD.2011.2157947

[82] K. T. V. Grattan and T. Sun, "Fiber Optic Sensor Technology: An Overview," *Sens. Actuators A Phys.*, vol. 82, nos. 1–3, pp. 40–61, 2000. https://doi.org/10.1016/S0924-4247(99)00368-4

[83] K. Fidanboylu and H. Efendioğlu, "Fiber Optic Sensors and Their Applications," in *Proc. 5th Int. Adv. Technol. Symp. (IATS'09)*, Karabük, Turkey, 2009.

[84] K. Zhang and D. Li, *Electromagnetic Theory for Microwaves and Optoelectronics*. Beijing, China: Springer, 2008.

[85] F. Rachidi and S. Tkachenko, *Electromagnetic Field Interaction with Transmission Lines: From Classical Theory to HF Radiation Effects*. Southampton, U.K.: WIT Press, 2008. https://doi.org/10.2495/978-1-84564-063-7

Authors and biographies

Luis Eduardo Perdomo Orjuela received a BSc degree in Electrical Engineering from Universidad Distrital Francisco José de Caldas in 2014 and subsequently earned a MSc degree in Electrical Engineering from Universidad Nacional de Colombia in 2019. He is currently pursuing a second MSc in Information and Communication Sciences at Universidad Distrital Francisco José de Caldas. With more than ten years of professional experience in the electrical, electronics, and ICT sectors, he has developed advanced expertise in the maintenance of medium- and high-voltage substations, digital substations, protection and control systems, and data analytics, among other areas. In this role, he has been responsible for ensuring the reliability and operational integrity of power systems, in addition to managing maintenance activities in power, control, protection and digital substations. He has also verified power system designs, including substations and transmission lines. He currently works at Ingeniería y Soluciones Especializadas (ISES), performing factory acceptance tests (FAT), site acceptance tests (SAT), system integration tests (SIT), stability tests, and functional tests, as part of witness testing and commissioning activities for substation control, protection, and telecommunications systems, among other technical evaluations.
Email: leperdomoo@unal.edu.co, leperdomoo@udistrital.edu.co.

Francisco Santamaria Piedrahita received his BSc, MSc, and PhD degrees in Electrical Engineering from Universidad Nacional de Colombia in 2002, 2007, and 2013. In 2010 he joined the staff of the Department of Electrical Engineering at Universidad Distrital Francisco Jose de Caldas, where he currently works as a full professor and member of the research group on Electrical Systems and Energy Efficiency (GISE3). His research interests include lightning protection, electromagnetic interference, electric vehicles, and energy management systems.
Email: fsantamariap@udistrital.edu.co

Nelson Enrique Vera Parra is a full professor and former head of the Research Office of the Universidad Distrital Francisco José de Caldas. He is an Electronics Engineer with an MSc in Information and Communication Sciences and a PhD in Engineering. He also serves as a researcher in the GICOGE group (International Group in Computing and Communications for Knowledge Management), focusing on high-performance computing, data science, artificial intelligence, and bioinformatics.
Email: neverap@udistrital.edu.co

UNIVERSIDAD DISTRITAL
FRANCISCO JOSÉ DE CALDAS

Ingeniería

https://revistas.udistrital.edu.co/index.php/reving/issue/view/1320

DOI: https://doi.org/10.14483/23448393.23625

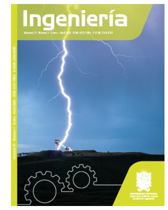

Review Article

Empowering the Community: Development and Validation of a Participatory Tool for Road Safety Assessment on Colombian Tertiary Roads

Empoderamiento de la comunidad: desarrollo y validación de una herramienta participativa para la evaluación de la seguridad vial en las carreteras terciarias colombianas

Erik S. Vidal[1], Yesi N. López[1], Carlos A. Calero[1], Aldemar J. González[1], and Víctor Uribe[2]

[1]Universidad del Cauca (Popayán, Colombia)
[2]Universidad Politécnica de Puerto Rico (Orlando, Puerto Rico)

Abstract

Context: Crash rates on Colombia's tertiary road network exceed the national averages, largely due to the lack of instruments for systematic data collection and the limited involvement of local communities in risk identification. This study aimed to design a road safety diagnostic tool that can be applied by the community, tailored to rural contexts and validated with local stakeholders in the department of Cauca, Colombia.
Method: A literature review was conducted to identify the key risk factors affecting road safety on Colombia's tertiary roads. The KABCO scale was incorporated due to its simplicity and suitability for collaborative work. Based on these inputs, a diagnostic tool and a user guide were developed. Finally, a pilot study was implemented through participatory workshops, during which georeferenced points and risk assessments were collected.
Results: The pilot's application of the tool enabled the identification and georeferencing of seven critical points along a road segment in the municipality of Popayán. In these locations, speed was identified as one of the most influential factors in the road crashes reported by the community. The tool demonstrated clarity and feasibility of use by participants without prior technical training.
Conclusions: The developed tool provides a replicable method that allows rural communities to identify and manage road safety risks, generating valuable data for the formulation of maintenance plans and prevention policies. Its implementation can optimize resource allocation and strengthen collaboration between communities and the responsible authorities.

Keywords: Local rural roads, Rural roads, Safety

Article history

Received:
November 2nd, 2024

Modified:
December 9th, 2025

Accepted:
March 2nd, 2026

Ing, vol. 31, no. 1, 2026, e23625

* Correspondence: erikvid@unicauca.edu.co

Resumen

Contexto: Las tasas de siniestralidad en la red vial terciaria de Colombia superan los promedios nacionales, en gran parte debido a la falta de instrumentos para la recolección sistemática de datos y a la limitada participación de las comunidades locales en la identificación de riesgos. Este estudio tuvo como objetivo diseñar una herramienta de diagnóstico de seguridad vial que pueda ser aplicada por la comunidad, adaptada a contextos rurales y validada con actores locales en el departamento del Cauca, Colombia.
Método: Se realizó una revisión de literatura para identificar los principales factores de riesgo que afectan la seguridad vial en las vías terciarias de Colombia. Se incorporó la escala KABCO por su simplicidad y su idoneidad para el trabajo colaborativo. A partir de estos insumos, se desarrolló una herramienta de diagnóstico y una guía de usuario. Finalmente, se implementó un estudio piloto mediante talleres participativos, durante los cuales se recolectaron puntos georreferenciados y evaluaciones de riesgo.
Resultados: La aplicación piloto de la herramienta permitió identificar y georreferenciar siete puntos críticos a lo largo de un tramo vial en el municipio de Popayán. En estos lugares, la velocidad fue identificada como uno de los factores más influyentes en los siniestros viales reportados por la comunidad. La herramienta demostró claridad y viabilidad de uso por parte de participantes sin formación técnica previa.
Conclusiones: La herramienta desarrollada ofrece un método replicable que permite a las comunidades rurales identificar y gestionar los riesgos de seguridad vial, generando datos valiosos para la formulación de planes de mantenimiento y políticas de prevención. Su implementación puede optimizar la asignación de recursos y fortalecer la colaboración entre las comunidades y las autoridades responsables.

Palabras clave: Vías rurales locales, Vías rurales, Seguridad

Contents

1. Introduction

Road crashes on rural tertiary roads in Colombia far exceed the national levels, mainly due to the absence of standardized instruments for data collection and the limited involvement of communities in risk identification. Annually, approximately 1.19 million people die in road crashes worldwide [1], and Colombia leads Latin America in mortality rates, with a 26% increase in the number of fatalities between 2021 and 2023, particularly on rural roads [2], [3], [4].

Tertiary roads account for 70% of the national road network and ensure rural connectivity. However, they have experienced significant deterioration due to the lack of maintenance and climatic and geographical challenges [5], [6], [7]. This deterioration restricts access to essential services such as education, healthcare, and food, and it further widens the urban-rural gap, contributing to higher poverty rates in these communities [8], [9].

One major challenge is the lack of crash records on the tertiary road network by the competent authorities, which prevents proper diagnostics. The National Road Safety Observatory (ONSV) does not provide a complete municipal breakdown for tertiary roads. Moreover, in the case of the Department of Cauca, only five of the 42 existing municipalities have reported official data on tertiary infrastructure, leaving 88% of the territory without information. The absence of this data generates bias in intervention efforts, as investments are allocated to areas that do report information, while vulnerable areas are neglected.

In this context, our study proposes the development of a community-based road safety diagnostic tool for rural tertiary roads. Designed to actively engage local communities in the Department of Cauca, the tool integrates technical criteria (the KABCO scale) with participatory protocols for the collection of georeferenced data. Thus, this study seeks to close the information gap and strengthen collaboration between users and institutions, improving the accuracy of the diagnosis and enhancing the effectiveness of interventions both in Colombia and other rural contexts across Latin America.

Methodology

This study employed a sequential mixed-methods design, which was carried out through four interconnected phases to develop and validate a community-based road safety assessment tool for tertiary roads (Fig. 1).

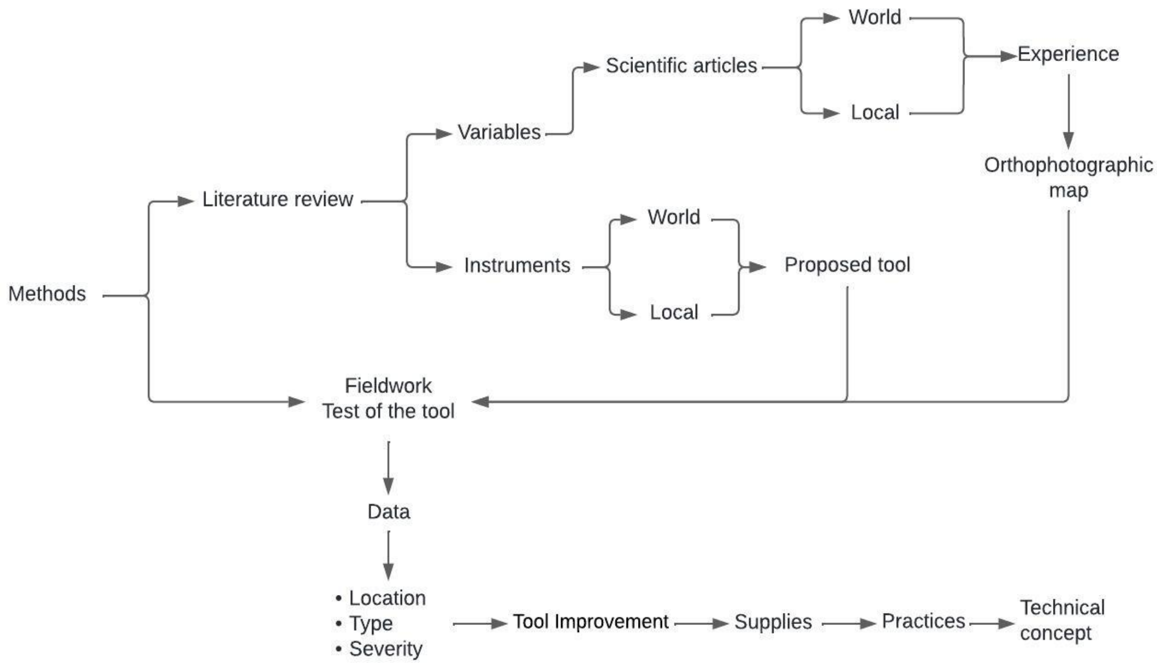

Figure 1. Methodology

Phase 1: systematic literature review

The literature review was conducted in two complementary stages, following the principles of the PRISMA guidelines (preferred reporting items for systematic reviews and meta-analyses).

Stage 1: identification of factors through a systematic review

An initial systematic search was carried out to identify risk factors affecting road safety on rural roads. The search was conducted in the Scopus, Web of Science, SciELO, and Google Scholar databases, using search strings that combined keywords such as "road traffic crashes," "rural roads," "road safety," "crash rate," and "human factors," together with Boolean operators to refine the results. The search period was limited to publications between 2019 and 2025, in order to ensure up-to-date and relevant information.

The inclusion criteria covered studies focused on road safety on rural tertiary roads. We excluded studies addressing only urban roads or highways, as well as documents without full access or with information not applicable to the Latin American context.

From the selected literature, information on factors affecting road safety was systematically extracted and classified into five main categories based on the Highway Safety Manual [10] and expanded to the Colombian rural context. The factors were originally grouped into human, roadway, and vehicle factors according to the HSM (2009), with the addition of the environmental factor—which varies by road section and may influence road safety—and the institutional factor—state actions that, in theory, should be implemented to ensure an adequate level of road safety but are often absent.

To assess and prioritize these factors during the community-based application of the tool, the KABCO scale was integrated. This scale is a standardized classification system that categorizes the severity of risks according to their observed potential for harm in a crash and includes the following levels:

- K: killed (fatality)
- A: incapacitating injury
- B: non-incapacitating injury
- C: possible injury
- O: no injury

This scale was selected due to its conceptual simplicity and its compatibility with the empirical knowledge of rural communities, allowing users without specialized technical training to assess and classify the risks identified in their territories. Furthermore, it was validated through pilot testing.

Stage 2: factor-specific literature review

Once the risk factors had been identified in Stage 1, a targeted literature search was conducted to document the specific scientific evidence supporting the influence of each factor on rural road safety. This stage aimed to consolidate a robust evidence base for each individual factor.

For each factor identified, targeted searches were carried out, using the factor name as the main term, combined with road safety-related keywords and rural context terms.

The bibliographic information for each factor was managed in a structured matrix, linking each factor to its specific references. This approach made it possible to trace the available evidence for each identified factor and to assess the robustness of the existing knowledge base.

Note that a PRISMA diagram is not presented for Stage 2, as it consisted of multiple targeted searches rather than a single systematic review. The PRISMA diagram in Fig. 2 exclusively documents Stage 1.

The factors identified in Stage 1 and validated with specific evidence in Stage 2 were subsequently submitted to evaluation by the expert panel (described in Phase 2) to determine their relevance and specific applicability to the context of tertiary roads in the Department of Cauca.

Phase 2: validation by an expert panel

A panel of four road safety experts was established to validate and refine the identification of critical factors according to the original article. The experts included in the study each have more than 15 years of experience in projects related to the subject matter and teach road safety courses in postgraduate programs at Colombian universities. This ensures the reliability of the opinions provided, as well as their relevance and equal weighting.

The assessment was conducted through structured and independent interviews. Each participant was first contextualized regarding the findings from the literature in relation to the specific conditions of the region. Based on this information, by assigning scores, each expert evaluated the relevance and applicability of the identified variables in the context of tertiary roads.

Using the collected information, a final consensus was reached through validations based on convergent expert knowledge. This ensured the identification of critical factors via the integration of individual perspectives and their collective and systematic validation.

Phase 3: tool development

Based on the factors validated by the experts, a tool was designed as a practical instrument to assess road safety on tertiary roads through the identification of risk factors, the recording of structured data, and the prioritization of interventions. Its application is participatory, incorporating local community knowledge of road incidents in contexts where official data are unavailable.

The tool was designed while considering the sociodemographic characteristics of rural communities and their educational standards [9], employing an approach that offers an informed understanding of the problem and facilitates the selection of the most influential factors for road safety on tertiary roads in Cauca.

The tool differs from traditional methodologies in its adaptability to the sociodemographic context surrounding tertiary roads in Cauca, its participatory approach, and the use of accessible technological resources such as georeferencing and orthophotography via smartphones. The application was developed in three interconnected stages: (i) the identification of the study section through detailed inspection, in order to recognize existing risk factors; (ii) the recording of information in a standard format that allowed for the systematic structuring of findings and the georeferencing of critical points; and (iii) the prioritization of risks, classifying them according to the KABCO scale based on their impact on road safety.

Phase 4: pilot testing and community validation

For the pilot implementation, we selected a 1 km segment of the road between La Tetilla and Puente Zaté in the municipality of Popayán, Department of Cauca. The reasons for our choice included compliance with geometric design standards and the verification of road safety, traffic conditions, and environmental considerations. The characteristics of the segment include an average width of 4.5 m, an average longitudinal slope of 5%, the absence of basic drainage infrastructure and sewer networks, and alternative routes that allow for traffic continuity without full closures.

From a geological and geomorphological perspective, the section is located on the Cauca-Patía inter-Andean plateau, characterized by volcanic deposits and erosion processes differentiated by their temporality. The area exhibits tectonic activity, with geological faults that influence ground stability, generating mass movements and erosion. The predominant soils are of alluvial origin and highly susceptible to erosion, affecting maintenance activities and road safety.

Community participation was sought by assessing 21% of the households adjacent to the road and within a 2 km radius of the segment. These households were selected through convenience sampling in order to evaluate the effectiveness and applicability of the initial tool. The participants received a two-hour training session on basic road safety concepts and the evaluation methodology prior to the process. In addition, three complementary site visits were scheduled over a six-week period to collect and verify relevant information.

These activities included a systematic environmental analysis using standardized technical forms to document geographical and climatic characteristics; structured road inspections using checklists to identify deficiencies related to geometric design, visibility, and surface conditions; and community input collected through three-hour participatory workshops employing social cartography techniques and semi-structured interviews to understand perceived problems and critical points. Data was recorded in digital formats and validated through triangulation between technical observations and community perceptions.

The tools employed included drones to capture high-resolution orthophotographs, which were processed with Agisoft Metashape; georeferencing of critical points using Google Earth; and heat maps to represent the spatial distribution of road safety issues.

After applying the tool and analyzing the collected data, adjustments were made to improve the accuracy and relevance of the information gathered. The pilot test and subsequent refinements enhanced the tool's structure, sequence, and clarity, allowing users to collect reliable data to support the technical understanding of the specific risks associated with the analyzed roadway.

Results

Systematic review and characterization of influential factors

Stage 1: identification of factors through a systematic review

The information search was conducted using a structured strategy that included recognized scientific databases and complementary sources, in order to ensure a broad and relevant coverage of the study topic. First, the Scopus, Web of Science, and SciELO databases were consulted due to their relevance in indexing high-quality scientific literature and their coverage of studies related to road safety, infrastructure, and risk factor analysis. As a result of this search, 76 database records were identified: 47 documents from Scopus, 16 from Web of Science, and 13 from SciELO.

Additional information sources were included to complement the scientific evidence, including manual searches in specialized journals and gray literature, which comprised theses, technical reports, and relevant institutional documents. Together, these strategies made it possible to identify a total of 83 documents that were potentially relevant to this study.

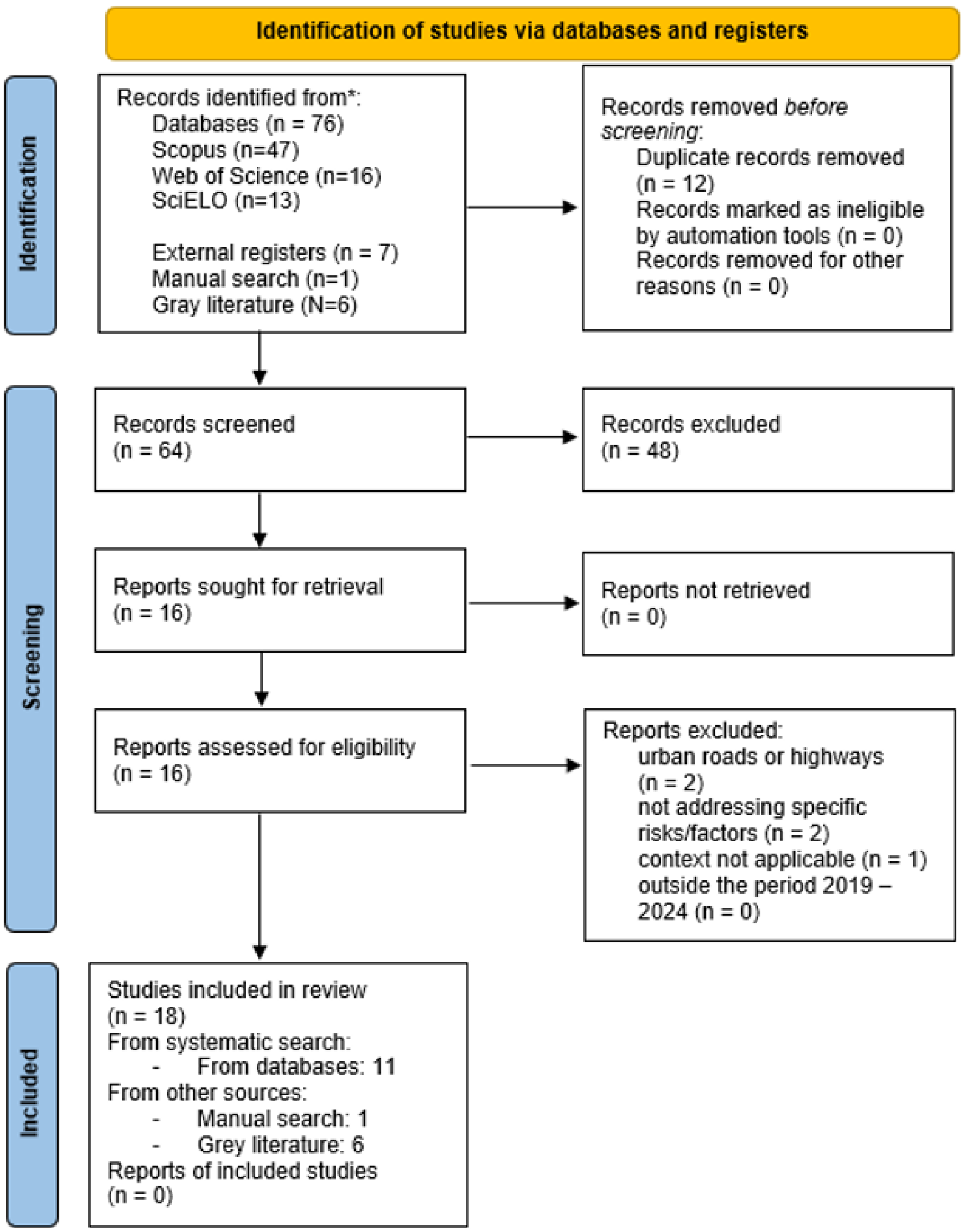

Figure 2. PRISMA flow diagram

The systematic literature review made it possible to identify a total of 47 risk factors associated with road crashes on rural roads, prioritizing information from studies conducted in rural areas and low-traffic local roads. The distribution of these factors by category is presented in Fig. 3, showing a significant concentration in human and roadway factors, which, together, account for 85% of the identified factors.

The five main risk factor categories, based on international literature and adapted to the Colombian context, were distributed as follows:

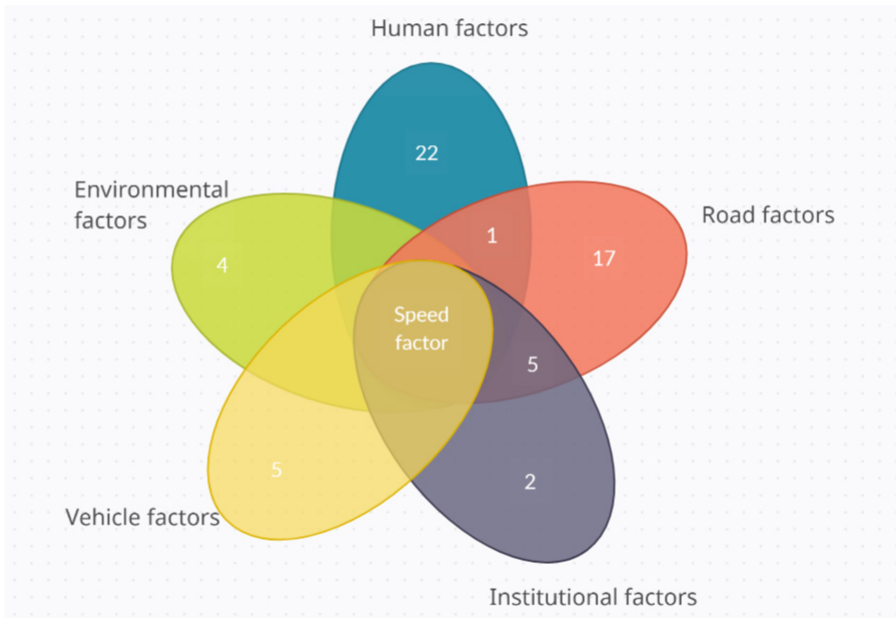

Figure 3. Interaction of concurrent factors in road crashes

Human factors (23 factors, 49%). This category comprises the largest number of identified variables, including driver behaviors that generate unsafe conditions such as speeding, alcohol and psychoactive substance consumption, non-compliance with safety protocols, distracted driving, inadequate reaction time, physical and mental conditions, experience, andage, among others.

Road factors (23 factors, 49%). These are related to deficiencies in road infrastructure safety, including the absence of signage, deterioration of the running surface, inadequate road geometry, pavement conditions, curve density, sight distance, geometric alignment, vertical grade, lighting, intersections, the International Roughness Index (IRI), access points, and cross-section characteristics.

Institutional factors (five factors, 11%). These include the lack of traffic regulation and enforcement, the absence of preventive maintenance plans, non-compliance with regulations, deficiencies in safety barriers, and the inadequate management of surface friction.

Vehicle factors (five factors, 11%). These are related to the mechanical conditions and proper functioning of vehicles, including the use of poorly maintained vehicles, brake failures, worn tires, maintenance deficiencies, and inadequate technical-mechanical conditions.

Environmental factors (four factors, 9%). These consider the influence of climate on terrain conditions and their direct relationship with road crashes, including erosion or slippery surfaces due to rainfall, surrounding terrain types, land use, and adverse weather conditions.

Stage 2: factor-specific literature review

For each of the factors identified in Stage 1, a targeted literature search was conducted with the aim of consolidating the evidence base to support their influence on road safety on rural roads.

The factor-specific review resulted in the identification of more than 40 additional bibliographic references, each providing evidence on the relationship between specific factors and road safety in rural contexts. The complete account of factors with and their corresponding references is presented in Table I.

The targeted search revealed different levels of bibliographic availability depending on the factor category.

- **Human factors.** Multiple references were identified for each factor. Factors such as speed, alcohol consumption, and distraction are supported by extensive international documentation.
- **Roadway factors.** The documentation was consistent for factors related to road geometry and surface conditions, with more limited availability for factors specific to tertiary or rural roads.
- **Vehicle factors.** The identified literature focused mainly on general mechanical conditions rather than on specific characteristics of vehicles used in rural contexts.
- **Environmental factors.** A smaller body of literature specific to rural contexts was identified, highlighting this category as an area requiring further research.
- **Institutional factors.** The available documentation was comparatively limited, particularly for developing countries, reflecting the emerging nature of this approach in rural road safety.

Table I. List of identified risk factors with supporting bibliographic evidence

List of factors	Category	Author
Evasive actions	Human factor	[11]
Acceleration/deceleration	Human factor	[12]
Attention	Human factor	[13], [12]
Information processing capacity	Human factor	[10]
Driver's ability to adapt to the geometry of the track/trajectory used	Human factor	[14]
Unsafe behaviors	Human factor	[15]

List of factors	Category	Author
Precondition for unsafe behavior	Human factor	[15]
Physical conditions of the driver	Human factor	[11]
Mental conditions	Human factor	[11]
Use of psychoactive substances	Human factor	[16], [17]
Distractions	Human factor	[18]
Age	Human factor	[10], [19], [20]
Experience	Human factor	[10], [18]
Driver skill	Human factor	[11], [13]
Driving time	Human factor	[21]
Inappropriate lateral position	Human factor	[13]
Drowsiness	Human factor	[22]
Insecure monitoring	Human factor	[23]
Perception-response time	Human factor	[24]
Type of driver	Human factor	[25]
Violation of regulations	Human factor	[26]
Vision	Human factor	[11]
Vehicle conditions	Vehicle factor	[11]
Vehicle design and manufacture	Vehicle factor	[10], [27], [28]
Maintenance	Vehicle factor	[10], [29]
Vehicle ratio	Vehicle factor	[21], [30]
Vehicle type	Vehicle factor	[15], [31], [32]
Geometric alignment	Roadway factor	[33]
Paved and unpaved berm width	Roadway factor	[34]
Berm soundtracks	Roadway factor	[35]
Overtaking lane	Roadway factor	[36], [37], [38]
Track category	Roadway factor	[39], [40]
Running surface condition	Roadway factor	[41]
Curve density	Roadway factor	[13], [42], [14], [43], [44]
Visibility distance	Roadway factor	[45]
Track geometry horizontal curves	Roadway factor	[42], [14], [13]
Vertical gradient	Roadway factor	[46]
Lighting	Roadway factor	[45]
Intersections	Roadway factor	[43], [47], [26]
International roughness index (IRI)	Roadway factor	[48]
Segment length	Roadway factor	[49]
Access points	Roadway factor	[49]
Cross section	Roadway factor	[50]

List of factors	Category	Author
Controlled and split access main road	Roadway factor	[10]
Climate	Environmental factor	[21]
Type of terrain – environment	Environmental factor	[47]
Average daily traffic	Environmental factor	[51], [52], [30]
Land use	Environmental factor	[49], [51]
Traffic control devices	Institutional factor	[53]
Technical-mechanical review	Institutional factor	[47]
Visibility	Road/human factor	[54]
Surface friction	Road/ institutional factor	[48]
Number of accesses	Road/ institutional factor	[10]
Presence of safety barriers	Road/ institutional factor	[34]
Presence of separator	Road/ institutional factor	[47]
Signage	Road/ institutional factor	[49], [43]
Speed	Human factor, vehicle, road, environmental, institutional factor	[21], [50], [35], [44], [13], [12], [54], [24], [51]

Validation by expert panel

The road safety expert panel led to the consolidation of 43 critical variables from the 47 initially identified factors, reflecting the complexity of the topic and the need for specific approaches to assess safety on rural roads. The reduction in factors was based on criteria of specific relevance to Colombian tertiary roads, the feasibility of assessment by rural communities, and the applicability in contexts with limited official data reporting.

The factors validated as most influential by the expert panel are presented in Table II, organized by category and prioritized according to their potential impact on tertiary road safety. This validation process allowed refining the assessment instrument while ensuring that it included only variables that could be effectively identified and evaluated by local communities.

Table II. List of factors classified by the expert panel as contributing to road safety incidents on tertiary roads

Factor	**Category**
Weather	Environmental factor
Type of terrain – environment	
Land Use	
Evasive actions	Human factor
Attention	
Information processing capacity	
Ability of the driver to adapt to the geometry/trajectory of the road used	
Unsafe behaviors	
Precondition for unsafe behaviors	
Physical condition of the driver	
Mental condition	
Psychoactive substance/alcohol use	
Distractions	
Age	
Experience	
Drowsiness	
Insecure monitoring	
Perception-response time	
Driving time	
Violation of regulations	
Vision	
Technical-mechanical inspection	Vehicle factor
Vehicle conditions	
Maintenance	
Vehicle ratio	
Vehicle type	

Geometric alignment	Roadway factor
Pavement Surface Conditions	
Curve density	
Visibility distance	
Road geometry: horizontal curves	
Vertical gradient	
Lighting	
Intersections	
IRI	
Access points	
Cross section	
Visibility	Roadway/human factor
Surface friction	Roadway/institutional factor
Number of access points	
Presence of safety barriers	
Signage	
Speed	Human/vehicle/ roadway/environmental/ institutional factor

Tool development

As a result of the methodological development, a structured tool adapted to the context of rural tertiary roads in the Department of Cauca was obtained, which was aimed at the collection and analysis of road safety information with community participation. The final tool was organized as a practical guide, structured into eight chapters and three interconnected modules, which sequentially reflect the methodology, covering a range aspects from conceptual and contextual elements to operational formats for the identification, recording, and analysis of road crashes. The structure includes clearly defined sections for roadway segment recognition and the characterization of risk factors associated with the road, the vehicle, the human factor, and the environment, as well as the systematic recording of crash events through interviews conducted with the local community.

In designing the tool, specific criteria for our adaptation to the Colombian rural context were implemented, prioritizing clear language, simplified formats, and procedures accessible to individuals without technical training in road safety. These criteria were defined based on a review of national and international guidelines and the characterization of the pilot segment, considering the geometric, topographic, climatic, and operational particularities of tertiary roads, *e.g.*, non-uniform cross-sections, the absence of signage, drainage limitations, and the predominance of motorcycle traffic. As a result of this process, 43 of the risk factors that were previously validated by an expert panel were incorporated and organized into field forms designed for practical application by non-specialist users.

As part of the tool's development, a specific user manual was prepared and integrated into the guide, with the purpose of providing clear and sequential guidance for the correct application of the proposed methodology. This manual includes detailed instructions for each phase of the process, facilitating implementation by the community and ensuring consistency in data collection. In addition, standardized data recording forms were designed to systematize the information obtained during community interviews, incorporating variables related to the individuals involved, the factors associated with the crash, the characteristics of the road segment, geographic coordinates, injury severity, and relevant observations.

Furthermore, a coding system was implemented to organize and clean the collected data, including the numerical identification of participants, the verification of duplicate reported events, and the standardized classification of crash severity. In this context, the integration of the KABCO scale constituted a central component of the tool since it was incorporated as a prioritization system for classifying the severity of injuries associated with road crashes. The application was carried out through contextualized and easily understandable descriptions for rural communities, facilitating the identification of the K, A, B, C, and O categories based on the information provided during interviews and ensuring consistency in the interpretation and analysis of the recorded events.

During the pilot, the events reported by the community were initially located using printed maps and subsequently georeferenced using conventional mobile devices, allowing for the collection of precise geographic coordinates. Additionally, standardized photographic recording protocols were established, facilitating the generation of orthophotographs and heat maps, from which spatial patterns of road crashes were identified, revealing a significant concentration of events on horizontal curves along the pilot segment.

As part of the validation process, preliminary usability tests were conducted during the pilot of the guide on the selected road segment, in order to assess the comprehensibility of the formats, the clarity of the instructions, and the feasibility of the data collection process by the community. Based on this experience, adjustments were made to the wording of the questions, the organization of the forms, and the sequence of application, with the aim of improving process coherence and reducing potential ambiguities during completion.

Finally, the development of the tool incorporated specific adjustments derived from the conditions of the Colombian rural context, such as the limited availability of official traffic data, the absence of vehicle counting stations, and the need to complement technical information with local community knowledge. These adjustments made it possible to consolidate a flexible, operational, and contextualized tool aimed at supporting the identification and prioritization of road safety risks on tertiary roads, which serves as an input for technical decision-making by specialized professionals.

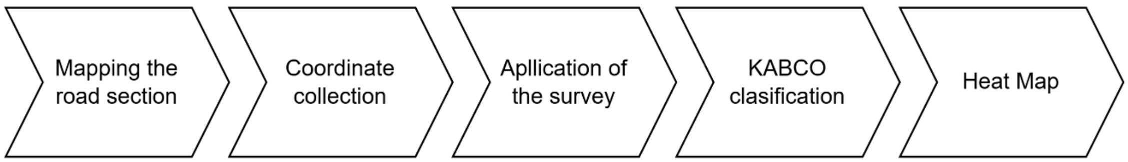

Figure 4. Phases of the tool's application

Pilot application and community validation

Characterization of the studied section

The pilot was implemented in an approximately 1 km-long section of the tertiary road called *La Tetilla-Puente Zaté*, enabling a practical and context-specific application of the proposed tool. This section features an average carriageway width of 4.5 m, a mean longitudinal gradient of approximately 5%, an unpaved surface composed of granular material, and the absence of basic drainage infrastructure and sewer networks—conditions representative of the rural tertiary road network in the Department of Cauca.

The pilot's application involved the participation of 15 members of the local community, aged between 25 and 45 years, with an average educational level corresponding to secondary education (high school). Prior to data collection, a structured community training process was conducted in two sessions: an initial three-hour session focused on understanding the analysis scales—particularly severity classification using the KABCO system—and a second session of approximately thirty minutes focused on the general use of the final tool and the completion of the data collection forms. The pilot was assessed over a single day, during which data were collected through face-to-face interviews, the recording of crash events reported by the community, the identification of risk factors associated with the road section, and the georeferencing of critical points. This process made it possible to validate the clarity of the formats, the participants' understanding of the instructions, and the operational feasibility of the tool in a real-world context, ensuring its coherence with the technical and social conditions of the studied section.

Figure 5. Satellite image of the studied section, coordinates: 2°31′21.96″ N, 76°41′14.03″ W

Identification and georeferencing of critical points

The application of the tool by the local community resulted in the identification and georeferencing of seven critical points distributed along the studied section. Each critical point was classified according to the KABCO scale and categorized by the predominant type of risk factor, generating a systematic database to support the prioritization of interventions.

Table III. Geographic coordinates of the reported road traffic crashes

Reporting individual	Roadway element where the crash occurred	Latitude	Longitude
41	Curve	2°31′18.32″ N	76°61′16.77″ W
42	Curve	2°31′14.71″ N	76°41′23.91″ W
44	Curve	2°31′19.76″ N	76°41′16.10″ W
46-1	Curve	2°31′16.43″ N	76°41′15.22″ W
46-2	Curve	2°31′32.09″ N	76°41′3.68″ W
46-4	Curve	2°31′46.31″ N	76°40′57.89″ W
5-1	Curve	2°31′19.73″ N	76°41′13.73″ W
62-1	Curve	2°31′18.62″ N	76°41′16.92″ W
62-2	Curve	2°31′18.35″ N	76°41′15.20″ W
62-3	Curve	2°31′28.99 N	76°41′12.32″ W
62-5	Curve	2°31′20.98″ N	76°41′11.31 W
65	Curve	2°31′15.66″ N	76°41′23.81″ W
68	Curve	2°31′44.21″ N	76°41′2.17″ W

The spatial analysis of road traffic crashes, conducted through the generation of heat maps, showed a significant concentration of events in the curved sections of the studied segment, particularly those with smaller curvature radii, in contrast to the straight sections of the roadway. This spatial pattern suggests a direct relationship between road geometry and the increased risk of crash occurrence, with a greater impact on motorcycle users, who represent the main type of traffic along the analyzed segment.

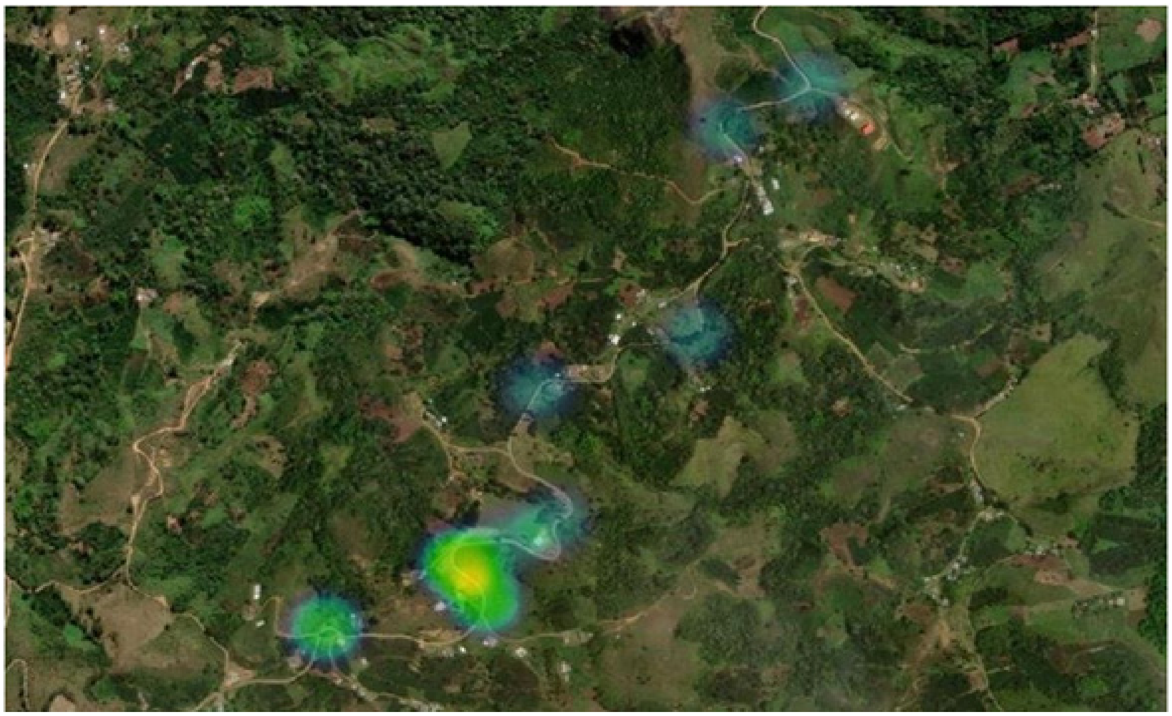

Figure 6. Heat map of road traffic crashes along the segment.

Additionally, the information collected during community interviews made it possible to identify that human behavior constitutes a determining factor in the occurrence of the recorded events, mainly associated with the speeds that are inadequate for the geometric and operational conditions of the roadway. The combination of unfavorable geometric design of curves and risky driving behaviors increases the likelihood of vehicle loss of control, especially in the context of limited road infrastructure.

Likewise, variations were observed in the intensity of the critical points among the different curves identified, suggesting that specific factors such as curvature radius, superelevation, visibility conditions, and roadway surface conditions influence the level of risk associated with each segment in a differentiated manner. These factors, when interacting with driver behavior, particularly travel speed—contribute to the generation of conditions conducive to road traffic crashes.

Complementarily, the analysis of injury severity, classified using the KABCO scale, showed a correspondence between areas with higher crash density and the occurrence of more severe injuries.

In particular, the critical points with the highest concentration of events predominantly coincided with crashes classified in Category A (incapacitating injuries), which supports the prioritization of these segments as critical areas for the formulation and implementation of intervention measures aimed at improving road safety on rural tertiary roads.

Figure 7. Distribution of crash classification according to the KABCO scale

Analysis by factor categories

The main findings identified in each category during the pilot application were as follows:

Human factors. Speeding was the factor identified by community participants as the most recurrent behavior among motorcyclists, present at six out of seven critical points. Additionally, during the site visit, the presence of pedestrians traveling on the roadway was documented, which increases the risk of crashes. The inadequate use of personal protective equipment by motorcyclists and reckless driving behaviors on curves with reduced radii were also identified.

Vehicle factors. During the site visit, motorcycles operating with overloads and in poor mechanical condition were observed, affecting braking capacity and stability on curves. The absence of preventive vehicle maintenance in the rural area was a recurrent factor identified by the community.

Road factors. The absence of signage on sharp curves, the loss of granular material on the roadway, and deficiencies in drainage capacity were observed, contributing to the formation of critical areas that are prone to crashes. Inadequate roadway geometry was identified as a high-risk factor at three specific points.

Environmental factors. We identified areas with active erosion and accumulation of sediments on the roadway due to runoff, causing instability of the running surface. We also identified adverse weather conditions during rainy periods as factors that exacerbate other risk conditions.

Institutional factors. The absence of traffic enforcement personnel and the lack of road safety education campaigns within the community were confirmed, negatively impacting compliance with road safety regulations. The lack of systematic maintenance plans was identified as an underlying critical factor.

Effectiveness evaluation of the tool: community validation of results

The evaluation of the tool's effectiveness was conducted through a validation process that involved the participating community, considering specific metrics related to its applicability and comprehension. The average time required to complete the thorough assessment of the segment was approximately two hours. This demonstrates the operational viability of the tool in rural contexts where time and resources are limited.

Regarding comprehension, community users exhibited a high level of understanding of the tool's content, instructions, and formats. This result can be attributed to the use of plain language, the sequential structuring of the methodological process, and the support of graphical and cartographic elements. Such understanding was evidenced by the accurate execution of risk identification stages, crash classification, and the georeferencing of critical points (black spots).

Furthermore, total consistency was observed among the different community evaluators, achieving 100% inter-rater reliability in the generated reports, in both the identification of critical points and their classification via the KABCO scale. This homogeneity in the results confirms the replicability of the instrument and its capacity to mitigate the variability associated with subjective interpretation.

Finally, the results derived from the community application showed strong alignment with the risk factors previously defined from a technical standpoint. This validated the relevance of the collected data as a reliable input for subsequent analysis by road safety professionals. This community validation process confirms the effectiveness of the developed participatory assessment tool as a mechanism for identifying and prioritizing road risks on rural tertiary roads.

Main validated contributions

Systematization of community data. The tool enabled the collection of information that had not been documented in official records, validating the importance of local participation in road safety assessment. 100% of the risks identified by the community were not present in previous institutional databases.

Georeferencing of critical points. Segments with a higher concentration of risks were identified, facilitating the prioritization of infrastructure interventions. The georeferencing precision achieved through mobile devices proved sufficient for territorial planning purposes.

Adaptability to the rural context. Unlike other methodologies, the tool was designed while considering specific environmental and social variables, which enabled its application in environments with scarce official data. The tool demonstrated to be comprehensible and applicable by users with diverse educational levels.

Future work

Based on the results obtained in this study, we identified several lines of future work aimed at strengthening, validating, and expanding the scope of the developed tool for the participatory assessment of road safety on rural tertiary roads. First, we recommend expanding the sample of test segments, incorporating roads with different geometric, topographic, and operational characteristics, as well as collecting information at different times and under varying weather conditions. This would allow for the evaluation of result stability and the establishment of replicability metrics in rural contexts with similar conditions.

Additionally, it is pertinent to conduct a comparative analysis between the proposed tool and traditional road safety diagnostic methodologies, in order to evaluate differences in terms of implementation time, the level of detail of the information obtained, and technical requirements. In this regard, the pilot experience demonstrated that the community application of the tool can be completed in an average time of two hours, representing a significant reduction compared to the times associated with conventional evaluations carried out exclusively by specialized technical teams.

As a complement, we propose the implementation of a continuous monitoring system based on periodic community feedback, allowing for the update of information on crash rates and emerging risks. The feedback obtained during the pilot's application suggests a positive perception of the tool's usability, highlighting the clarity of the formats, the ease of application, and understanding of the generated results—aspects that support its potential sustained adoption over time.

Furthermore, there is an identified need to strengthen coordination with government entities, non-governmental organizations, and institutional actors linked to road safety to guarantee larger-scale implementation, as well as the allocation of resources for its updating and maintenance. In this context, future studies could incorporate a cost-effectiveness analysis, comparing the community application of the tool with traditional technical methods, considering variables such as operating costs, specialized personnel requirements, and territorial coverage.

Finally, we recommend conducting a comparative study that follows the intervention proposed by *CDT Vial* on the test segment, enabling the evaluation of changes in crash levels and injury severity, thereby verifying the impact of the implemented improvement alternatives. Together, these lines of future work consolidate the tool as a structured, replicable, and cost-effective mechanism for monitoring and improving road safety on rural tertiary roads.

Synthesis of results by phase

The sequential implementation of the four methodological phases enabled the systematic construction of a tool validated both technically and by the community. Phase 1 established the theoretical foundation by identifying 47 risk factors. Phase 2 refined this set to 43 critical factors through expert validation. Phase 3 materialized these factors into a practical tool adapted to the rural context. Finally, Phase 4 demonstrated the applicability and effectiveness of the instrument through its successful community implementation in identifying seven georeferenced critical points.

Discussion

The results of this study demonstrate that road safety on tertiary roads in the department of Cauca is influenced by multiple factors, among which infrastructure deficiencies, adverse environmental conditions, and the lack of institutional regulation stand out. The validation of risk factors with an expert panel enabled the consolidation of a total of 43 critical variables, reflecting the complexity of the problem and the need for specific approaches to evaluate safety on rural roads. Furthermore, the field application of the tool allowed detecting risks that were undocumented in official records, highlighting the fundamental role of community participation in identifying road issues.

When comparing these findings against those of previous studies on road safety in rural areas [37], we confirmed that the lack of signaling, deficient drainage, and poor road conditions are recurrent factors contributing to the occurrence of crashes. Previous research has indicated that inadequate infrastructure and the accelerated deterioration of roads create high-risk conditions, especially in regions with frequent rainfall and erodible soils [47], as is the case in Cauca. However, unlike traditional methodologies that rely exclusively on official databases, the tool developed in this study integrates empirical data collected with the community, allowing for a more detailed and contextualized characterization of local risks.

Conclusions

Due to the lack of institutional presence in rural areas of Colombia, the community adjacent to the selected rural road became the primary source of information for the development of a database aimed at analyzing road safety in this area. The tool presented herein represents an initial structured approach to extracting information from the community and translating it into terms easily understood by them, facilitating analysis and decision-making in the subsequent stages of road interventions by the competent authorities. Based on the review of the expert panel, the risk factors with the greatest impact on the safety of tertiary roads were synthesized. Its field application demonstrated the tool's capacity to systematically identify these risks, providing reliable data in a context where the underreporting of incidents remains a recurrent issue.

The findings confirm the need for accessible and structured tools for data collection regarding crashes on tertiary roads, as official records are limited and do not accurately reflect the reality of road safety. The implementation of road safety measures, infrastructure improvements, and road education are fundamental for reducing the incidence and severity of crashes. In this sense, the proposed tool facilitates the identification of critical points and provides clear instructions for its application, allowing for its replication in other rural environments with similar characteristics.

While this study represents an advancement in the evaluation of road safety on tertiary roads, we acknowledge the importance of comparing the effectiveness of the tool with conventional risk analysis methodologies. Future studies could focus on establishing objective performance metrics and evaluating their impact on crash reduction. Additionally, the tool can be used to monitor improvements in road infrastructure, allowing for safety assessments before and after interventions, which makes it a potential instrument for longitudinal studies on rural road safety. Our results strengthen the understanding of risk factors on tertiary roads and lay the foundation for the creation of road safety strategies adapted to these environments. The combination of a participatory approach, expert validation, and the use of georeferencing tools reinforces the potential of this methodology to contribute to the planning and management of road safety in rural communities.

Acknowledgments

To the Technological Development Center (CDT) of Universidad del Cauca, which provided the section data and the orthophotography on which the tool was evaluated for this study. This information has been instrumental in conducting the tests and analysis of this research.

Author contributions

Author 1: writing (original draft, review, and editing).
Author 2: writing (original draft, review, and editing).

Author 3: methodology, formal analysis.
Author 4: methodology.
Author 5: Methodology, formal analysis, writing (original draft, review, and editing).

Statement on artificial intelligence

During the elaboration of this work, the authors used Claude by Anthropic to improve the organization and clarity of the text. The authors reviewed and edited all AI-generated content and took full responsibility for the accuracy and integrity of the final manuscript.

Conflict of interest

The authors declare that they have no conflicts of interest that could have influenced the research process.

Data availability statement

The tool developed in this study is available for consultation and use by researchers, public policymakers, and professionals interested in improving road safety in rural areas. This resource provides structured guidelines for identifying risk factors on tertiary roads and facilitates data collection in regions with limited official records. To access the tool and related documentation, please visit the following link: https://drive.google.com/drive/folders/1MLCgQVB0BJQZKh6yYwE-_JWNOsc7V-99?usp=sharing

References

[1] World Health Organization, "*Global status report on road safety 2023*," Geneva, 2023. Accessed: Feb. 23, 2025. [Online]. Available: https://iris.who.int/bitstream/handle/10665/375016/9789240086517-eng.pdf?sequence=1

[2] G. Castañeda-Millán and J. Eslava-Schmalbach, "Tendencias en la mortalidad por accidentes de tránsito en motocicleta en Colombia, 2008-2021," *Rev. Panam. Salud Pública*, vol. 48, p. 1, Apr. 2024. https://doi.org/10.26633/RPSP.2024.44.

[3] Agen. Nac. de Seg. Vial, "*Víctimas por Siniestros Viales Clasificadas por Tipo de Vía*." Accessed: Feb. 23, 2025. [Online]. Available: https://ansv.gov.co/es/observatorio/estadísticas/victimas-por-siniestros-viales-clasificadas-por-tipo-de

[4] D. Mohan, G. Tiwari, M. Khayesi, and F. M. Nafukho, "*Road traffic injury prevention training manual*," 2006. Accessed: Feb. 27, 2025. [Online]. Available: https://iris.who.int/bitstream/handle/10665/43271/9241546751_eng.pdf

[5] Dep Nac de Plan, "*Política para la gestión de la red terciaria: presupuesto informado por resultados*." Accessed: Feb. 27, 2025. [Online]. Available: https://colaboracion.dnp.gov.co/CDT/Prensa/Presentaciones/RED%20TERCIARIA%20CCI%20-%20DNP.pdf

[6] J. Cárdenas Grisales, *Diseño geométrico de carreteras*, 2da Edición. 2013.

[7] L. Narvaez, "Vías terciarias: motor del desarrollo económico económico rural," *Rev. Ing.*, vol. 45 2017. https://doi.org/10.16924/revinge.45.11.

[8] L. V. Juan and M. Ramírez, "*Infraestructura regional y pobreza rural*," 2014. Accessed: Feb. 27, 2025. [Online]. Available: https://www.repository.fedesarrollo.org.co/handle/11445/234

[9] Laboratorio de Economía de la Educación (LEE) - Pontificia Universidad Javeriana., "*Informe No. 79: Características y retos de la educación rural en Colombia*." Accessed: Feb. 23, 2025. [Online]. Available: https://www.javeriana.edu.co/recursosdb/5581483/8102914/Informe-79-Educación-rural-en-Colombia-%28F%29oct.pdf

[10] AASHTO, *Highway Safety Manual*, vol. 1. Washington, DC, USA: AASHTO, 2009.

[11] T. Ishida and N. Kanda, "An analysis of human factors in traffic accidents," *Transp. Res. Part F: Traffic Psychol. and Behav.*, vol. 2, no. 3, pp. 181–193, 1999. https://doi.org/10.1016/S0389-4304(98)00065-4

[12] D. Babić and T. Brijs, "Low-cost road marking measures for increasing safety in horizontal curves: A driving simulator study," *Accid. Anal. Prev.*, vol. 153, p. 106013, 2021. https://doi.org/10.1016/j.aap.2021.106013

[13] P. Lemonakis, N. Eliou, y T. Karakasidis, "Investigation of speed and trajectory of motorcycle riders at curved road sections of two-lane rural roads under diverse lighting conditions", *J. Safety Res.*, vol. 78, pp. 138-145, sep. 2021. https://doi.org/10.1016/j.jsr.2021.05.009

[14] R. Elvik, "Which is the more important for road safety—road design or driver behavioural adaptation?", *Traffic Saf. Res.*, vol. 2, p. 000009, ago. 2022. https://doi.org/10.55329/pvir7839

[15] Y. Zhang, T. Liu, Q. Bai, W. Shao, y Q. Wang, "New systems-based method to conduct analysis of road traffic accidents", *Transp. Res. Part F Traffic Psychol. Behav.*, vol. 54, pp. 96-109, abr. 2018. https://doi.org/10.1016/j.trf.2018.01.019

[16] S. Athanaselis, A. Dona, S. Papadodima, G. Papoutsis, C. Maravelias, y A. Koutselinis, "The use of alcohol and other psychoactive substances by victims of traffic accidents in Greece", *Forensic Sci. Int.*, vol. 102, no. 2, pp. 103-109, jun. 1999. https://doi.org/10.1016/S0379-0738(99)00053-5

[17] H. Gjerde, A. S. Christophersen, P. T. Normann, y J. Mørland, "Toxicological investigations of drivers killed in road traffic accidents in Norway during 2006–2008", *Forensic Sci. Int.*, vol. 212, No. 1, pp. 102-109, oct. 2011. https://doi.org/10.1016/j.forsciint.2011.05.021

[18] P. J. Knight, D. Iverson, y M. F. Harris, "Early driving experience and influence on risk perception in young rural people", *Accid. Anal. Prev.*, vol. 45, pp. 775-781, mar. 2012. https://doi.org/10.1016/j.aap.2011.10.005

[19] H. I. Castellucci, G. Bravo, P. M. Arezes, y M. Lavallière, "Are interventions effective at improving driving in older drivers?: A systematic review", *BMC Geriatr.*, vol. 20, No. 1, p. 125, abr. 2020. https://doi.org/10.1186/s12877-020-01512-z

[20] C. Lyon et al., "Age and road safety performance: Focusing on elderly and young drivers", *IATSS Res.*, vol. 44, no. 3, pp. 212-219, oct. 2020. https://doi.org/10.1016/j.iatssr.2020.08.005

[21] M. Tanishita y B. van Wee, "Impact of vehicle speeds and changes in mean speeds on per vehicle-kilometer traffic accident rates in Japan", *IATSS Res*., vol. 41, no. 3, pp. 107-112, oct. 2017. https://doi.org/10.1016/j.iatssr.2016.09.003

[22] C. Papadelis et al., "Monitoring sleepiness with on-board electrophysiological recordings for preventing sleep-deprived traffic accidents", *Clin. Neurophysiol*., vol. 118, no. 9, pp. 1906-1922 sep. 2007. https://doi.org/10.1016/j.clinph.2007.04.031

[23] Y. Zhang, L. Jing, C. Sun, J. Fang, y Y. Feng, "Human factors related to major road traffic accidents in China", *Traffic Inj. Prev*., vol. 20, no. 8, pp. 796-800, nov. 2019. https://doi.org/10.1080/15389588.2019.1670817

[24] D. Pavlou, G. Christodoulou, y G. Yannis, "The impact of weather conditions and driver characteristics on road safety on rural roads", *Transp. Res. Proc*., vol. 72, pp. 4081-4088, ene. 2023, https://doi.org/10.1016/j.trpro.2023.11.369

[25] C.-D. Rosas-López, C.-A. Gaviria-Mendoza y C.-A. Calero-Valenzuela, "Clasificación del comportamiento del conductor en curvas horizontales de caminos rurales de dos carriles", *Rev. Fac. Ing*., vol. 30, no. 57, p. e13410, ago de 2021, https://doi.org/10.19053/01211129.v30.n57.2021.13410

[26] O. H. Kwon, W. Rhee, y Y. Yoon, "Application of classification algorithms for analysis of road safety risk factor dependencies", *Accid. Anal. Prev*., vol. 75, pp. 1-15, feb. 2015, https://doi.org/10.1016/j.aap.2014.11.005

[27] A. Mendoza Díaz, F. L. Quintero Pereda, and E. F. Mayoral Grajeda, *Seguridad vial en carreteras*, Publicación Técnica No. 224. Sanfandila, Qro., México: Secretaría de Comunicaciones y Transportes, Instituto Mexicano del Transporte, 2003. [Online]. Available: https://imt.mx/archivos/Publicaciones/PublicacionTecnica/pt224.pdf

[28] C. Marín-Ruíz and J. Sánchez-Tapiero, *Estudio de las tecnologías de seguridad pasiva y activa presentes en los vehículos vendidos en Colombia*. Bogotá, Colombia: Universidad Católica de Colombia, 2022. [Online]. Available: https://hdl.handle.net/10983/27135

[29] S. Repin, S. Evtiukov, y S. Maksimov, "A method for quantitative assessment of vehicle reliability impact on road safety", *Transp. Res. Proc.,* vol. 36, pp. 661-668, ene. 2018, https://doi.org/10.1016/j.trpro.2018.12.128

[30] I. Ashraf, S. Hur, M. Shafiq, y. Park, "Catastrophic factors involved in road accidents: Underlying causes and descriptive analysis", *PLoS ONE*, vol. 14, no. 10, p. e0223473, oct. 2019, https://doi.org/10.1371/journal.pone.0223473

[31] L. M. Martín-de-los Reyes, V. Martínez-Ruiz, P. Lardelli-Claret, E. Moreno-Roldán, D. Molina-Soberanes, y E. Jiménez-Mejías, "Asociación del tipo de vehículo con el riesgo de provocar una colisión entre vehículos", *Gac. Sanit*., vol. 34, no. 4, pp. 350-355, jul. 2020, https://doi.org/10.1016/j.gaceta.2018.10.007

[32] J. Galindo, "Perfil epidemiológico de los accidentes de tránsito en México," *Horiz. Sanit*., vol. 22, no. 1, 2019, https://doi.org/10.19136/hs.a22n1.5038

[33] M. Atashafrazeh and M. M. Yadollahi, “Geometric design consistency model based on speed and safety in rural highways in some European countries: A review,” *Int. J. Struct. Civ. Eng. Res*., 2013. [Online]. Available: www.ijscer.com

[34] V. Gitelman, E. Doveh, R. Carmel, y S. Hakkert, "The influence of shoulder characteristics on the safety level of two-lane roads: A case-study", *Accid. Anal. Prev*., vol. 122, pp. 108-118, ene. 2019, https://doi.org/10.1016/j.aap.2018.10.003

[35] I. Kučina, D. Babić, M. Fiolić, y D. Babić, "Application of road signs and road markings to increase safety in horizontal curves on rural roads", *Transp. Res. Proc.*, vol. 73, pp. 186-194, ene. 2023, https://doi.org/10.1016/j.trpro.2023.11.907

[36] L. Ye y T. Yamamoto, "Evaluating the impact of connected and autonomous vehicles on traffic safety", *Phys. A Stat. Mech. Appl*., vol. 526, p. 121009, jul. 2019, https://doi.org/10.1016/j.physa.2019.04.245

[37] J. P. Gooch, V. V. Gayah, y E. T. Donnell, "Safety performance functions for horizontal curves and tangents on two lane, two way rural roads", *Accid. Anal. Prev*., vol. 120, pp. 28-37, nov. 2018, https://doi.org/10.1016/j.aap.2018.07.030

[38] H. Mirzahossein, H. Adibi, A. Khishdari, S. Afandizadeh, y A. Severino, "Evaluating Geometric Design Characteristics of Two-Lane Two-Way Rural Roads on Crash Frequencies Occurrences", *Iran. J. Sci. Technol. Trans. Civ. Eng*., vol. 47, n.o 4, pp. 2497-2506, ago. 2023, https://doi.org/10.1007/s40996-023-01072-3

[39] Instituto Nacional de Vías y Ministerio de Transporte, *Manual de Diseño Geométrico de Carreteras*. Bogotá, Colombia, 2008.

[40] MQ Ghadi , " Análisis multinivel de la frecuencia de accidentes de tráfico: El impacto de la categoría de la vía ", *Int. J. Transp. Dev. Integr*., vol. 7, no. 2, pp. 123-130, 2023. https://doi.org/10.18280/ijtdi.070207

[41] M. G. Karlaftis y I. Golias, "Effects of road geometry and traffic volumes on rural roadway accident rates", *Accid. Anal. Prev*., vol. 34, n.o 3, pp. 357-365, may 2002, https://doi.org/10.1016/S0001-4575(01)00033-1.

[42] F. Hisam, M. Halim, N. Naharudin, and N. Hashim, “GIS analysis on road accident and road safety: A case study of road geometry in Kajang, Selangor,” *Int. J. Geoinformatics*, vol. 18, no. 4, pp. 45–50, 2022, https://doi.org/10.52939/ijg.v18i4.2257

[43] S. Mićić, R. Vujadinović, G. Amidžić, M. Damjanović, y B. Matović, "Accident Frequency Prediction Model for Flat Rural Roads in Serbia", *Sustainability*, vol. 14, n.o 13, p. 7704, jun. 2022, https://doi.org/10.3390/su14137704

[44] S. Gaca y M. Kiec, "Speed Management for Local and Regional Rural Roads", *Transp. Res. Proc.*, vol. 14, pp. 4170-4179, ene. 2016, https://doi.org/10.1016/j.trpro.2016.05.388

[45] S. Das, X. Sun, y M. Sun, «Rule-based safety prediction models for rural two-lane run-off-road crashes», *Int. J. Transp. Sci. Technol*., vol. 10, no. 3, pp. 235-244, sep. 2021, https://doi.org/10.1016/j.ijtst.2020.08.001

[46] R. Fu, Y. Guo, W. Yuan, H. Feng, y Y. Ma, "The correlation between gradients of descending roads and accident rates", *Saf. Sci*., vol. 49, no. 3, pp. 416-423, mar. 2011, https://doi.org/10.1016/j.ssci.2010.10.006

[47] A. Arévalo-Támara, M. Orozco-Fontalvo, and V. Cantillo, “Factors influencing crash frequency on Colombian rural roads,” *Promet - Traffic Transp.*, vol. 32, no. 4, 2020, https://doi.org/10.7307/ptt.v32i4.3385

[48] R. Elvik y E. Strandvik Haugvik, "Safety of horizontal curves on rural two-lane roads in Norway", *Traffic Saf. Res.*, vol. 4, p. e000026, abr. 2023, https://doi.org/10.55329/hkbk3638

[49] M. Haghani, R. Jalalkamali, y M. Berangi, "Assigning crashes to road segments in developing countries", *Proc. Inst. Civ. Eng. - Transp.*, vol. 172, n.o 5, pp. 299-307, mar. 2018, https://doi.org/10.1680/jtran.17.00099

[50] C. Polidori, X. Cocu, A. Volckaert, T. Teichner, K. Lemke, P. Saleh, and P. Pokorny, *Safety Prevention Manual for Secondary Roads: For the International Training of Road Safety Inspectors and Auditors, Complying with the European Directive 2008/96/EC*. June 2012. [Online]. Available: http://www.aipss.it/documents/manual-en.pdf

[51] A. Mohammadnazar, I. Mahdinia, N. Ahmad, A. J. Khattak, y J. Liu, "Understanding how relationships between crash frequency and correlates vary for multilane rural highways: Estimating geographically and temporally weighted regression models", *Accid. Anal. Prev.*, vol. 157, p. 106146, jul. 2021, https://doi.org/10.1016/j.aap.2021.106146

[52] E. Norza, S. Useche, and J. Moreno, “Componentes descriptivos y explicativos de la accidentalidad vial en Colombia: incidencia del Human factor,” *Rev. Psicol.*, 2013.

[53] H. Safarpour, D. Khorasani-Zavareh, y R. Mohammadi, "The common road safety approaches: A scoping review and thematic analysis", *Chin. J. Traumatol.*, vol. 23, n.o 2, pp. 113-121, abr. 2020, https://doi.org/10.1016/j.cjtee.2020.02.005

[54] A. Matírnez, D. A. Mántaras, y P. Luque, "Reducing posted speed and perceptual countermeasures to improve safety in road stretches with a high concentration of accidents", *Saf. Sci.*, vol. 60, pp. 160-168, dic. 2013, https://doi.org/10.1016/j.ssci.2013.07.003

Authors and biographies

Erik Santiago Vidal Lara is a final-year Civil Engineering student at Universidad del Cauca, Colombia. In 2024, he presented his research at the 8th Interinstitutional Meeting of Research Seedbeds. His interests focus on civil engineering and research development.
Contact: erikvid@unicauca.edu.co

Yesi Natalia López Sánchez holds a degree in Environmental Engineering from Universidad del Cauca, Colombia (2023), where she conducted research on air quality under the supervision of PhD Nazly Sánchez. She received a DAAD scholarship for further studies in Germany and was recognized with a score of 95/100 at the National and International Meeting of Research Seedbeds. Currently, she is completing a Civil Engineering degree at Universidad del Cauca. Her research interests include air quality and environmental sustainability.
Contact: yesinata@unicauca.edu.co

Carlos Aníbal Calero Valenzuela holds a Civil Engineering degree from Universidad del Cauca, Colombia, and a Master's and PhD in Transportation from the University of Puerto Rico, Mayagüez Campus. He is an associate professor at Universidad del Cauca, where he conducts research on road safety, highway geometric design, geometric design consistency, and traffic engineering. His work aims to enhance road infrastructure safety and efficiency, addressing key challenges in transportation design and operation.
Contact: ccalero@unicauca.edu.co

Aldemar José González Fernández is a Civil Engineer from Universidad del Cauca, Colombia, with a specialization in Roads and a Master's in Traffic and Transportation Engineering from the same university. He serves as a full-time tenured professor there, affiliated with the Department of Roads and Transportation. He conducts development and research work in the areas of traffic engineering and road safety.
Contact: ajgonza@unicauca.edu.co

Victor M. Uribe Flórez is a civil engineer from Universidad Pontificia Bolivariana, Bucaramanga, Colombia, and he holds a master's degree in urban planning from the Universidad de Puerto Rico in Río Piedras, as well as another Master's degree and a PhD in Civil Engineering from the same university. Professor at Universidad Politécnica de Puerto Rico, Orlando Campus. His research focuses on urban and regional transportation, congestion management, urban and regional planning, and mass transit systems.
Contact: vuribe@pupr.edu